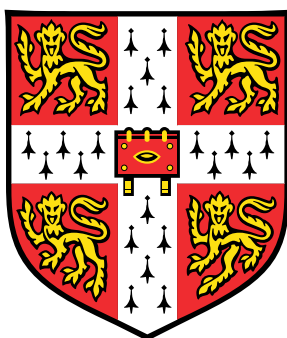


Upconversion Nanoparticles for pH Sensing and Imaging



Evaline Shin-Tin Tsai

Department of Chemical Engineering and Biotechnology

University of Cambridge

This dissertation is submitted for the degree of

Doctor of Philosophy

Peterhouse

April 2019

Declaration

This dissertation is the result of my own work and includes nothing which is the outcome of work done in collaboration except as declared in the Preface and specified in the text.

It is not substantially the same as any that I have submitted, or, is being concurrently submitted for a degree or diploma or other qualification at the University of Cambridge or any other University or similar institution except as declared in the Preface and specified in the text. I further state that no substantial part of my dissertation has already been submitted, or, is being concurrently submitted for any such degree, diploma or other qualification at the University of Cambridge or any other University or similar institution except as declared in the Preface and specified in the text

This dissertation contains 41,348 words and 78 figures. As such, it does not exceed the Engineering Degree Committee's prescribed word limit of 65,000 words, including appendices, footnotes, tables, and equations, and does not contain more than 150 figures, excluding the bibliography.

Evaline Shin-Tin Tsai
April 2019

Evaline Tsai

Upconversion Nanoparticles for pH Sensing and Imaging

Abstract

Drug development studies and other applications in diagnostics/therapeutics require pH measurement down to the micro or nanoscale to provide relevant subcellular information, but the most widely used optical pH sensors (fluorescent dyes, dye-labeled quantum dots) suffer from drawbacks of photobleaching, blinking, and limited tissue penetration. Autofluorescence is also an issue during tissue imaging in the UV-VIS excitation range of these fluorescers. The ability of upconversion nanoparticles (UCNPs) to overcome these challenges through their unique optical properties (NIR excitation, long lifetimes) motivated this work to further the understanding of interactions between particle and pH dye before applying this knowledge to the creation of a novel pH nanosensor for cellular imaging.

High-temperature coprecipitation was used to synthesize β -phase UCNPs with shell layers of different thicknesses (≤ 1 nm and 3 nm) to decrease surface quenching. The two types of particles were modified with different ligands, polyethylenimine (PEI) and poly(isobutylene-*alt*-maleic anhydride) (PMA), respectively, to enable dispersion in aqueous solutions. The effect of two anthraquinone dyes, Calcium Red and Alizarin Red S, on UCNPs was measured by spectroscopic techniques at various pHs. When the thick-shell (3 nm), PMA-coated UCNPs and dyes were mixed directly, the green emission band of the UCNPs was quenched by a pH-dependent inner filter effect while the red emission band remained unchanged and acted as the reference signal for ratiometric pH measurements. When the anthraquinones were attached onto the thin-shell (0.4 nm), PEI-coated UCNPs through electrostatic attraction, inner filter effect remained the dominant quenching mechanism compared to resonance energy transfer (RET).

Based on the above findings, UCNPs with an intermediate shell thickness of 1 nm were synthesized to simultaneously enable RET and ensure particle brightness. The PEI-coated UCNPs were attached to a dye called pHAb for pH sensing in live cells. RET was much more significant for UCNP-pHAb compared to either of the UCNP-anthraquinone combinations. Ratiometric sensing was performed with the sensitized pHAb emission and reference UCNP red emission in buffer solutions, then the nanosensors were calibrated in SH-SY5Y cells between pH 4 and 6. The UCNP-pHAb conjugates successfully measured the pH of acidic compartments (lysosomes) after clathrin-mediated endocytosis.

To the generations of scientists and engineers that came before us.
We stand on the shoulders of giants.

Acknowledgements

Firstly, I would like to thank Professor Lisa Hall for supervising my work and offering insight and clarity over the last few years. With her guidance, my PhD has grown from a smattering of small, unrelated hypotheses to a collection of intertwined works of knowledge. I have also grown tremendously as a researcher and project manager, and look forward to applying those same principles of curiosity and exploration to the rest of my career.

I would also like to thank Dr. Thomas Hirsch and his group at the University of Regensburg for use of their synthesis/characterization facilities and for their expertise in up-conversion nanoparticles and surface modification. In particular, I am grateful to Sandy Himmelstoss for help with TEM, Lisa Wiesholler for assisting with lifetime measurements and training me on nanoparticle synthesis, and Markus Buchner for working with me on surface chemistry and ICP-OES. These research visits were immensely productive and fun, and I inadvertently picked up some German along the way.

I am also thankful for the help and support from Dr. Balazs Varga, Dr. Deborah Kronenberg-Versteeg, Dr. Ragnhildur Thóra Káradóttir, and other members of the MRC Cambridge Stem Cell Institute as well as Dr. Fadwa Joud and Dr. Stefanie Reichelt of the Cancer Research UK Cambridge Institute for enabling the application of my research in cell culture and light microscopy. Further thanks goes to the NanoPhotonics Centre, in particular Dr. Anna Lombardi, Dr. Bart de Nijs, William Deacon, Junyang Huang, and Professor Jeremy Baumberg for guidance on optics and usage of their facilities.

I would also like to thank my colleagues in the Cambridge Analytical Biotechnology group and the wider Department of Chemical Engineering and Biotechnology for technical support, usage of facilities, and good-natured banter. Funding throughout my PhD from Peterhouse and NanoDTC is also greatly appreciated. Many thanks to Bianka Seres for reading thesis chapters and her insightful comments from a cell biologist's point of view. My wonderful friends from college deserve a special shout-out for making my visits back to the US incredibly memorable.

Finally, I would like to thank my mom and dad for their unwavering love and support throughout the course of my PhD.

Contents

Contents	xi
List of Figures	xv
List of Tables	xxi
1 Introduction	1
1.1 Motivation	1
1.2 Optical methods of pH measurement	3
1.2.1 Colorimetric dyes	3
1.2.2 Fluorescent dyes	5
1.2.3 PEBBLE nanosensors	8
1.2.4 Fluorescent nanomaterials for sensing	8
1.2.4.1 Inner filter effect	10
1.2.4.2 Resonance energy transfer	11
1.2.5 Disadvantages of downconversion	13
1.3 Upconversion nanoparticles	14
1.3.1 Composition and upconversion mechanisms	14
1.3.2 Synthesis methods	17
1.3.3 Photoluminescence properties	21
1.3.4 Surface modification	22
1.3.5 UC-IFE sensors	26
1.3.6 UC-RET sensors	26
1.3.7 Toxicity studies	28
1.4 Aims and objectives	30
2 Rational design of upconversion nanoparticles for sensing	33
2.1 Introduction	33
2.2 Materials and methods	35

2.2.1	Materials	35
2.2.2	Solvothermal synthesis	35
2.2.3	Thermal decomposition	36
2.2.4	Low-temperature coprecipitation	36
2.2.5	High-temperature coprecipitation	37
2.2.6	Surface modification for uncapped UCNPs	38
2.2.7	Surface modification with PEI	38
2.2.8	Surface modification with PMA	38
2.2.9	Photoluminescence spectroscopy	39
2.2.10	X-ray diffraction	39
2.2.11	Transmission electron microscopy	39
2.2.12	Scanning electron microscopy	40
2.2.13	Zeta, DLS, and ICP measurements	40
2.3	Results and discussion	40
2.3.1	UCNPs from solvothermal synthesis	40
2.3.2	UCNPs from thermal decomposition	41
2.3.3	UCNPs from low-temperature coprecipitation	50
2.3.4	UCNPs from high-temperature coprecipitation	51
2.3.5	Surface modification for biological applications	53
2.4	Conclusions	57
3	Energy transfer mechanisms from UCNPs to pH dyes	61
3.1	Introduction	61
3.2	Materials and methods	62
3.2.1	Materials	62
3.2.2	Anthraquinone attachment	62
3.2.3	Characterization methods	62
3.2.4	Spectroscopic measurements of CaR solutions	63
3.2.5	Spectroscopic measurements of ARS solutions	63
3.2.6	Spectroscopic measurements of UCNP-anthraquinone mixtures	64
3.2.7	Spectroscopic measurements of UCNP-anthraquinone nanoconjugates	64
3.2.8	Dye loading calculations	64
3.3	Results and discussions	65
3.3.1	Shell thickness selection	65
3.3.2	UCNP mixed with CaR and ARS in solution	66
3.3.3	UCNP-CaR and UCNP-ARS nanoconjugates	77
3.4	Conclusions	82

4	Ratiometric sensing of pH in live cells	85
4.1	Introduction	85
4.2	Materials and methods	86
4.2.1	Materials	86
4.2.2	Synthesis of UCNP-PEI-pHAb conjugate	87
4.2.3	Characterization of the pH nanoprobe	87
4.2.4	Multiphoton imaging of the pH nanoprobe	88
4.2.5	Multiphoton imaging of cells	88
4.2.6	Confocal laser scanning imaging of cells	89
4.2.7	Endocytosis experiments	90
4.2.8	Linearity of alamarBlue	91
4.2.9	Cell viability assay with alamarBlue	91
4.2.10	Cell viability assay with trypan blue exclusion assay	91
4.3	Results and discussions	92
4.3.1	Preparation and characterization of UCNP-pHAb sensor	92
4.3.2	Calibration of the UCNP-pHAb nanoprobe	99
4.3.3	Colocalization with lysosome indicator	110
4.3.4	Endocytosis pathway studies	113
4.3.5	Cell viability assays	118
4.4	Conclusions	121
5	Conclusions and future work	123
5.1	Summary of findings	123
5.2	Limitations and future work	125
5.3	Conclusions	127
A	Crystal structure of NaYF₄	129
B	Supplemental microscopy images of UCNP-pHAb in cells	133
C	Copyright permissions	137
	Bibliography	143

List of Figures

1.1	Structure of parent anthraquinone dye.	4
1.2	Simplified Jablonski diagram displaying the different energy levels involved in fluorescence.	5
1.3	Schematic showing electronic transitions, vibrational energy levels, and rotational energy levels for a generic organic molecule.	6
1.4	pH-dependent ionization of fluorescein in aqueous solutions.	7
1.5	Fluorescent colors from quantum dots of different sizes.	9
1.6	Simplified schematic comparing the excitation and emission of organic dyes, quantum dots, and upconversion nanoparticles.	15
1.7	Energy diagrams of a) excited state absorption and b) energy transfer upconversion.	16
1.8	Energy transfer mechanisms for upconversion processes in Er^{3+} , Tm^{3+} , and Yb^{3+} doped crystals under 980 nm laser excitation.	18
1.9	General illustration of UCNP synthesis using oil-based methods.	20
1.10	Schematic of the growth stages of $\alpha\text{-NaYF}_4\text{:Yb,Er}$ nanocrystals.	21
1.11	Heart function of zebrafish after treatment with upconversion nanoparticles versus quantum dots to visualize toxicity differences.	29
2.1	Luminescence spectra, XRD, and DLS data for UCNPs synthesized via solvothermal synthesis.	42
2.2	Luminescence spectrum, emission photo, and heat map of OA-coated, $\alpha\text{-NaLuF}_4$ UCNPs synthesized via thermal decomposition.	43
2.3	TEM image of UCNPs synthesized via thermal decomposition at 320 °C.	45
2.4	XRD data for UCNPs synthesized via thermal decomposition.	46
2.5	TEM image and SEM image of UCNPs synthesized via thermal decomposition at 340 °C.	46
2.6	Comparison of luminescence spectra of UCNPs synthesized via thermal decomposition at 320 °C and 340 °C.	47

2.7	EDXA spectrum of β -NaLuF ₄ nanoplates synthesized via thermal decomposition at 340 °C.	48
2.8	SEM image of β -NaLuF ₄ nanoplates synthesized via thermal decomposition at 340 °C overlaid with chemical mapping from EDXA to show the distribution of the different elements.	49
2.9	Luminescence spectrum and XRD pattern of UCNPs synthesized via low-temperature coprecipitation method.	50
2.10	TEM images of UCNPs synthesized via low-temperature coprecipitation	51
2.11	TEM images of (a) core NaYF ₄ : Yb, Er particles, (b) core particles with a ‘thin’ shell of NaYF ₄ , and (c) core particles with a ‘thick’ shell of NaYF ₄ from high-temperature coprecipitation.	52
2.12	Size distribution of hexagonal-phase, oleate-capped NaYF ₄ : 20% Yb, 2% Er UCNPs calculated from the transmission electron micrographs in Figure 2.11.	54
2.13	(a) XRD pattern of the UCNPs from Figure 2.11a and the reference XRD pattern of β -NaYF ₄ . (b) Emission spectra of core, core-shell (thin), and core-shell (thick) UCNPs at 1 wt%.	55
2.14	(a) Zeta potential measurement of UCNP coated with PMA and (b) intensity-weighted DLS measurements of UCNPs coated with OA in cyclohexane and PMA in water.	55
2.15	(a) TEM images of NaYF ₄ :Yb, Er nanoparticles with high molecular weight PEI and (b) the same particles at higher magnification.	57
2.16	(a) Zeta potential measurement of UCNP coated with PEI after a two-step ligand exchange process and (b) DLS measurements of UCNPs coated with PEI at different pHs.	58
3.1	Theoretical calculations of Förster distances between donor (Er ³⁺) and acceptor (dye) for (a) CaR and (b) ARS at pH 8.	66
3.2	Effect of different amounts of CaR and ARS on the luminescence spectra of UCNPs in phosphate/citrate buffer of different pH values.	67
3.3	Absorption spectra of (a) CaR and (b) ARS in solution buffered with 0.2 M phosphate/citrate at different pHs.	68
3.4	Fluorescence emission spectra of (a) CaR and (b) ARS in solution buffered with 0.2 M phosphate/citrate at different pHs.	69
3.5	pH response curve in 0.2 M phosphate/citrate buffer of (a) CaR solution at an absorbance of 533 nm and (b) ARS solution at an absorbance of 518 nm.	69

3.6	Plots showing (a) Stern-Volmer quenching for UCNP-CaR, (b) Perrin model sphere of action quenching for UCNP-CaR, (c) Stern-Volmer quenching for UCNP-ARS, and (d) Perrin model sphere of action quenching for UCNP-ARS.	70
3.7	Cut and normalized decay data of the 540 nm emission of UCNP-CaR mixture (A-C) and UCNP-CaR conjugate (D-F) in phosphate/citrate buffer solution of different pH values.	72
3.8	(a) Absorption spectra of CaR, UCNP, UCNP-CaR mixture, and the sum value of the absorbance of UCNP and CaR. (b) Absorption spectra of ARS, UCNP, UCNP-ARS mixture, and the sum value of the absorbance of UCNP and ARS.	73
3.9	(a) Absorption spectra of CaR in aqueous solutions of different pHs overlaid with the emission spectrum of the UCNP in water upon 980 nm excitation. (b) Normalized emission spectra of UCNP-CaR mixtures at pH 4.2, 5.0, and 5.8 upon 980 nm excitation.	75
3.10	(a) Absorption spectra of ARS in aqueous solutions of different pHs overlaid with the emission spectrum of the UCNP in water upon 980 nm excitation. (b) Normalized emission spectra of UCNP-ARS mixtures at pH 4.0, 5.2, and 6.4 upon 980 nm excitation.	75
3.11	Ratiometric pH-titration data measured at 540 nm and 650 nm of (a) UCNP-CaR mixture, (b) UCNP-CaR conjugate, (c) UCNP-ARS mixture, and (d) UCNP-ARS conjugate.	76
3.12	Structures of the CaR and ARS anthraquinone derivatives used in this work.	77
3.13	Schematic of the UCNP-anthraquinone conjugate sensor.	78
3.14	Schematic of UCNP crystal structure to illustrate the distribution of Er ³⁺ ions in the host lattice.	80
3.15	(a) Normalized emission spectra of UCNP-CaR conjugates in phosphate/citrate buffer solutions of pH 4.2, 5.0, and 5.8 and (b) normalized emission spectra of UCNP-ARS conjugates in phosphate/citrate buffer solutions of pH 4.0, 5.2, and 6.4 upon 980 nm excitation.	81
4.1	Molecular structure of pHAb amine reactive dye.	86
4.2	Succinimidyl ester and primary amine crosslinker chemistry.	87
4.3	Overlaid excitation/emission spectra of UCNP and pHAb. The absorption and emission spectra of pHAb are overlaid with the emission spectrum of thin-shell, PEI-coated UCNP.	93

4.4	TEM images of monodisperse, oleate-capped (a) core NaYF ₄ : 20% Yb, 2% Er and (b) core-shell NaYF ₄ : 20% Yb, 2% Er@NaYF ₄ . Histograms of the size distribution from the TEM images are shown in (c) and (d) for the core and core-shell particles, respectively.	94
4.5	Emission spectra at various pHs when UCNP-pHAb in phosphate/citrate buffer is excited at 532 nm (direct excitation of the dye).	95
4.6	Raw data and binomial smoothing of UCNP-pHAb emission spectra at different pHs.	96
4.7	Ratiometric pH titration curves of UCNP-pHAb in 0.2 M phosphate/citrate buffer.	97
4.8	UC-RET efficiency values for UCNP-pHAb at pH 4, 5, and 6.	98
4.9	Number-weighted histogram of particle diameters obtained from DLS.	99
4.10	Confocal fluorescence microscope images of the green, yellow, and red emission of UCNP-pHAb conjugate in agarose gel.	100
4.11	Multiphoton confocal microscopy images of UCNP-pHAb in nigericin-treated SH-SY5Y cells exposed to citric acid/phosphate buffer with KCl at pH 4.0 collected with 2x frame accumulation.	102
4.12	Multiphoton confocal microscopy images of UCNP-pHAb in nigericin-treated SH-SY5Y cells exposed to citric acid/phosphate buffer with KCl at pH 4.5 collected with 2x frame accumulation.	103
4.13	Multiphoton confocal microscopy images of UCNP-pHAb in nigericin-treated SH-SY5Y cells exposed to citric acid/phosphate buffer with KCl at pH 5.0 collected with 2x frame accumulation.	104
4.14	Multiphoton confocal microscopy images of UCNP-pHAb in nigericin-treated SH-SY5Y cells exposed to citric acid/phosphate buffer with KCl at pH 5.5 collected with 2x frame accumulation.	105
4.15	Multiphoton confocal microscopy images of UCNP-pHAb in nigericin-treated SH-SY5Y cells exposed to citric acid/phosphate buffer with KCl at pH 6.0 collected with 2x frame accumulation.	106
4.16	pH calibration curve of UCNP-pHAb in SH-SY5Y cells, based on the average of the ratio of yellow (I _y) to red (I _r) fluorescence intensity at each pixel of interest.	107
4.17	Ratiometric images of UCNP-pHAb in SH-SY5Y cells at pH 4.0, 4.5, 5.0, 5.5, and 6.0.	108

4.18	Pseudocolor ratiometric images of UCNP-pHAb in various intracellular compartments of SH-SY5Y cells overlaid with transmission images obtained through multiphoton confocal microscopy.	109
4.19	Images of SH-SY5Y cells incubated with UCNP-pHAb and LysoBrite. (a) shows the LysoBrite channel, (b) shows the pHAb channel, and (c) is the merged image.	110
4.20	Pixel intensities along a line drawn through a cell before and after median subtraction.	111
4.21	Schematics of (a) phagocytosis and (b) pinocytosis.	113
4.22	Fluorescence histogram of UCNP-pHAb at pH 4 and 6 from flow cytometry.	114
4.23	Illustrations of (a) clathrin-mediated endocytosis and (b) caveolae-mediated endocytosis.	115
4.24	Gating strategy for the endocytosis pathway studies (positive and negative control).	116
4.25	Gating strategy for the endocytosis pathway studies (chlorpromazine and nystatin).	117
4.26	Effects of pharmacological inhibitors on UCNP-pHAb uptake.	118
4.27	95% confidence intervals for Dunnett's multiple comparison test.	119
4.28	AlamarBlue mechanism.	119
4.29	Linearity and nonlinearity of AlamarBlue.	120
4.30	Cell viability with AlamarBlue assay.	121
4.31	Cell viability with trypan blue exclusion assay.	122
A.1	The three types of unit cells for the cubic crystal.	130
A.2	HR-TEM images of UCNPs synthesized via low-temperature coprecipitation.	130
A.3	The unit cell of the hexagonal close-packed structure.	131
B.1	Raw multiphoton confocal microscopy images of optimized UCNP-pHAb in nigericin-treated SH-SY5Y cells exposed to citric acid/phosphate buffer with KCl at pH 4.0, 4.5, 5.0, 5.5, and 6.0 collected with 2x frame accumulation.	134
B.2	Raw multiphoton confocal microscopy images of optimized UCNP-pHAb in nigericin-treated SH-SY5Y cells exposed to citric acid/phosphate buffer with KCl at pH 4.0, 4.5, 5.0, 5.5, and 6.0 collected with 1x frame accumulation.	135

List of Tables

1.1	Summary of surface modification methods.	25
2.1	Compositional analysis by EDXA of β -NaLuF ₄ nanoplates synthesized via thermal decomposition at 340 °C.	48
2.2	Average hydrodynamic diameters of thin-shell UCNPs coated with high molecular weight PEI and their respective PdIs from pH 5.0-7.0	56
3.1	Fluorescence lifetimes at 540 nm of thick-shell UCNPs, UCNP-CaR mixtures, thin-shell UCNPs, and UCNP-CaR conjugates in phosphate/citrate buffer solution of different pH values	71
3.2	Fluorescence lifetimes at 540 nm of thick-shell UCNPs, UCNP-ARS mixtures, thin-shell UCNPs, and UCNP-ARS conjugates in phosphate/citrate buffer solution of different pH values	71
3.3	Fluorescence lifetimes at 650 nm of thick-shell UCNPs, UCNP-CaR mixtures, thin-shell UCNPs, and UCNP-CaR conjugates in phosphate/citrate buffer solution of different pH values. UCNP-ARS mixture and UCNP-ARS conjugate had similar trends in their lifetime data.	71
3.4	Radii of the quenching spheres for UCNP-CaR mixtures and UCNP-ARS mixtures	74
3.5	Fraction of excess starting CaR dye on UCNPs after wash steps.	78
3.6	Fraction of excess starting ARS dye on UCNPs after wash steps.	78
3.7	Förster distances and donor quantum yields for different (donor) and anthraquinone (acceptor) distances, given a UC-RET efficiency of 0.09 calculated from the lifetime data	79
4.1	Lifetimes of 540 nm green emission of UCNPs, diluted UCNP-pHAb, and photobleached UCNP-pHAb	95
4.2	MCC values for pHAb and LysoBrite in cells after median subtraction	112
4.3	MCC values for one-tailed, one-sample t-test	113

Chapter 1

Introduction

1.1 Motivation

Biological systems are known to be highly connected to pH across a wide range of spatiotemporal scales. Due to the absorption of anthropogenic carbon dioxide from the atmosphere, oceans have become more acidic since preindustrial times,¹ with geochemical models predicting a reduction of 0.8 pH units by 2300,² which would be disastrous for coral reef ecosystems. On an organismic scale, earthworms are very sensitive to the pH of their aqueous environments, so it is not surprising that some species are limited to certain areas by the acidity of the soil.³ Finally, on a cellular level, small changes in pH can impact cellular functions, such as metabolism, muscle contraction, cell volume regulation, signaling pathways, and cellular activation, growth, and proliferation. For example, fluctuations in pH affect the charges of ionizable groups in proteins, which change the configuration of proteins and affect their activity.⁴

While measurement of pH in the first two examples can be performed with a pH electrode, the technology is not suitable in the last example where micro and nanoscale measurement within cellular compartments is needed to give relevant information. A combination pH electrode, which is by far the most widely used electrochemical method, has a reference electrode (e.g. Ag/AgCl electrode) and glass membrane electrode (measuring electrode) incorporated in the same body. The special glass material allows the protons from the surrounding test solution to equilibrate with the membrane. A pH meter measures the potential of the combination electrode, which results from the difference in proton concentration between the test solution and reference solution, and outputs the pH of the test solution based on this information. While pH electrodes are reliable and easy to use, they are limited by their size, and hence, spatial resolution. Even microelectrodes are only capable of measuring down to microliter sample size. They are not suitable for measuring the small sample

volumes required in cellular analysis, and electrode signal drift makes them unsatisfactory for long-term measurements.⁵

Due to strong interest in single cell analysis, fiber-optic optodes have significantly miniaturized since their introduction 60 years ago. In 1992, Tan et al. built a submicrometer pH optical fiber sensor with millisecond response time.⁶ Fiber optic tips can have nanometer dimensions, but the sensors still physically perturb the cell by puncturing the cellular membrane during insertion and disturbing the intracellular contents during further penetration. The integrity of the collected data depends on sensors “silently observing” without interfering with the cell’s normal behavior, so the fiber-optic probes are not ideal in this sense.⁷

The development of sensors that can accurately, affordably, and selectively measure pH down to the organelle level is important for understanding the pH distribution in cells, which can improve our knowledge of the intricacies in cell biology. These sensors should also minimally interact with the cell so that normal cellular processes are observed. Optical sensors are particularly well suited for measurement inside cells because they can be imaged down to submicrometer dimensions in near real-time using fluorescence microscopy.⁸ They are also physically insignificant compared to the size of the cell volume, so physical perturbations are minimized.⁷ Those developed over the last few decades have progressively improved on sensitivity, selectivity, and resolution, resulting in the generation of remarkable images where pH is mapped across the cell⁹ or followed temporally in endocytic vesicles.¹⁰ Tracking the pH of endosomal/lysosomal compartments in combination with degradation studies of drugs can provide insight to critical design parameters. Such measurement is needed to ensure that lysosomal degradation of the proposed drug is avoided before it reaches its target.^{11,12}

This thesis begins by covering an overview of representative work on optical pH sensors before diving into a discussion of the various challenges still faced by these techniques. It then explores how upconversion materials can be used to overcome problems, such as photobleaching, autofluorescence, and deep tissue penetration, that are commonly encountered in cellular imaging applications. Finally, a critical review of the limitations of current upconversion pH sensing studies paves the way for the fundamental studies of synthesis strategies, photophysics, and bio-interactions of upconversion nanoparticles (UCNPs) presented in this thesis. Studies like this that go beyond calibration of pH in different environments are critical to the translation of new sensing materials from academic research tools into real-world products used to track pH inside cells for drug development studies.

1.2 Optical methods of pH measurement

1.2.1 Colorimetric dyes

The simplest optical pH sensors rely on colorimetric dyes, which are organic dye molecules that change their absorption (color) properties depending on the pH of the surrounding environment. The protonated (acidic) and deprotonated (basic) forms of the molecule have different electronic structures, giving rise to a measurable change in the way it interacts with light.^{5,13}

Equilibrium exists between the acid and base forms of the dye when in solution, which in its simplest form can be described by the equations:



$$K_a = \frac{[Dye^z][H^+]}{[Hdye^{z+1}]} \quad (1.2)$$

where z is the valence number of the dye molecule in its deprotonated form. The highest sensitivity usually occurs when the pH is close to the pK_a ($-\log[K_a]$) of the dye; in other words, when the acidic and basic forms are approximately present in equal concentrations.¹³ As a result of the relationship above, the response of optical pH sensors (which is related to the concentration of either the protonated or deprotonated dye) is often sigmoidal, and their sensitivity is usually limited to $pK_a \pm 1.5$.⁵

The acid and base forms of colorimetric dyes can absorb light at different wavelengths. For example, phenol red has an absorption maximum at 560 nm from pH 8 to 11, but it exhibits a blue-shifted absorption maximum of 430 nm from pH 4 to 7.¹⁴ It is often added in tissue culture media as a visual pH indicator to allow researchers to quickly check by eye whether their culture stocks need to be replenished. Waste products from cells decrease the pH of the solution, causing it to turn from red to yellow. Paper strips can be impregnated with colorimetric dyes for quick, approximate measurements of pH (± 0.5 units) by comparing the color of the strip to a calibration chart. Shukla et al. immobilized anthocyanins on filter paper to make a pH sensor for application in intelligent packaging, which could provide a convenient and visual method for detecting food spoilage.¹⁵ The sensor changed from green to red upon contact with ammonia, which is a byproduct of meat spoilage.

For quantitative determination of pH, a spectrometer measures absorption of light at the wavelength of maximum absorption, λ_{max} , for the acidic or basic form of the dye. The

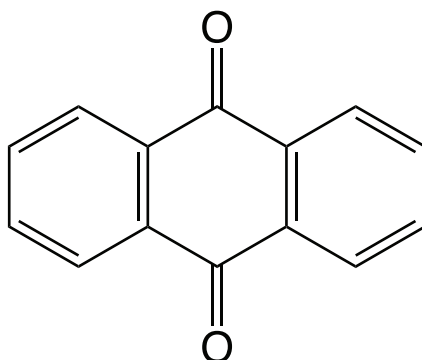


Figure 1.1: Chemical structure of parent anthraquinone dye. Created with ChemDraw based on figure from Gordon.¹⁷

Beer-Lambert law relates the absorbance, A , to the concentration of the dye, c :

$$A = \epsilon bc \quad (1.3)$$

where ϵ is the extinction coefficient of the dye and b is the path length.¹³ The ϵ value, which typically ranges from 0 to 10^6 (units of $100 \text{ cm}^2 \text{ mol}^{-1}$), indicates the probability of a particular absorption/transition. The b value describes the length of the cell or cuvette holding the solution.¹⁶

There are several ways of classifying these species that absorb visible light, including Color Index and chemical structure. Anthraquinones are one class of dye by chemical structure. They are recognized by the basic structure of two benzene rings connected by two carbonyl groups.¹⁸ The parent anthraquinone (Figure 1.1) is nearly insensitive to pH variations except in very acidic conditions (e.g. concentrated sulfuric acid). However, it changes hues and other properties in accordance with pH when substituted with various electron-donating and electron-accepting groups at different positions of the rings.¹⁷ An electron-donating group increases ϵ and λ_{max} through resonance of the lone pair electrons into the aromatic ring (similar effect as conjugation).¹⁶ Thus, the absorption spectra of anthraquinones can be quite diverse, ranging from blue and turquoise to red colors. Also, dyes with a primary amino group at the 1-position have higher pK_b than those with a primary amino group at the 2-position because the 1-position allows intramolecular hydrogen bonding with the neighboring carbonyl group to stabilize the molecule. For the same reason, 1-hydroxyanthraquinone has a higher pK_a than 2-hydroxyanthraquinone; the hydroxy group is more easily ionized when there is no intramolecular hydrogen bonding.¹⁷

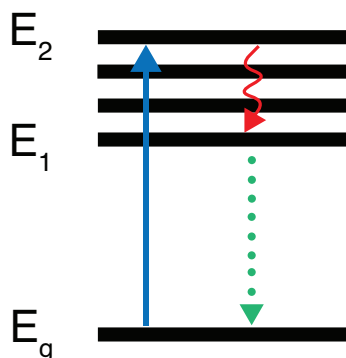


Figure 1.2: Simplified Jablonski diagram displaying the different energy levels involved in fluorescence. A molecule excited by UV light transitions from the ground state (E_g) to an excited state (E_2) (blue arrow). When the molecule loses vibrational energy (red arrow), it then drops to a lower excited state (E_1). Upon the molecule's return to E_g (green arrow), a photon is emitted.

1.2.2 Fluorescent dyes

For applications requiring high-sensitivity detection, fluorescence is more advantageous than absorbance. This is because fluorescence is measured relative to a dark background, while absorbance is compared to a bright reference beam.¹⁹ Fluorescent indicator dyes absorb light at a particular wavelength and re-emit a portion of that absorbed energy as light at a different wavelength. According to the Planck-Einstein relation, a photon of light of a certain wavelength, λ , corresponds to a certain energy, E , as described by the equation:

$$E = \frac{hc}{\lambda} \quad (1.4)$$

where h is Planck's constant and c is the speed of light. This energy promotes the molecule from the ground state, E_g , to an excited state, E_2 (Figure 1.2). Subsequent processes, such as heat loss from molecular collisions, lower the energy of the excited state to E_1 . The photon emitted has energy of $E_1 - E_g$, which is why organic dyes emit light at a longer wavelength than that at which they are excited (Stokes shift).¹³

Organic dye molecules contain electrons of varying energy levels, depending on their participation in σ bonds, π bonds, or as lone pairs.²⁰ These electronic energy levels are greater in difference than other types of energy levels, i.e. vibrational (infrared) or rotational (microwave) (Figure 1.3). Absorption bands are broad because the excited electron can go from the lowest vibrational state of the lower electronic energy level (at room temperature) to any vibrational or rotational state of a higher electronic energy level.¹⁶ The presence of a π bond in a double bond allows for delocalization to produce conjugated

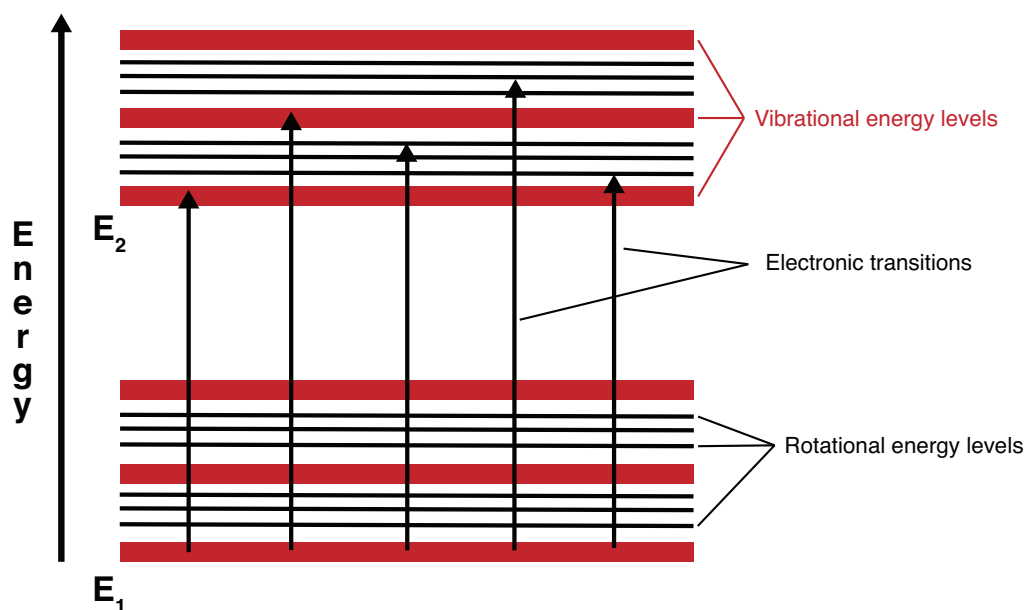


Figure 1.3: Schematic showing electronic transitions, vibrational energy levels, and rotational energy levels for a generic organic molecule. Adapted from figure in Anderson et al.¹⁶

systems responsible for fluorescence.²⁰ Systems with a higher degree of conjugation have stronger absorption bands (larger ϵ values) and longer λ_{max} .¹⁶ The non-bonding electrons of lone pairs can also delocalize depending on their proximity to such conjugated systems. In addition to these bonding and nonbonding orbitals, there are also antibonding orbitals that temporarily accept electrons when the molecule is excited. The incident photon energy is equivalent to the difference in energy of the bonding/nonbonding orbital and antibonding orbital.²⁰

There are now many commercially available pH-dependent fluorescent dyes, including derivatives of fluorescein, cyanine, and rhodamine.²¹ Fluorescein itself leaks from cells, so highly-charged derivatives, such as 2',7'-bis(2-carboxy-ethyl)-5(6)-carboxyfluorescein (BCECF), are often used instead for intracellular pH measurements. Fluorescein has many ionic forms across a wide range of pHs (Figure 1.4), but only the two anionic forms of fluorescein are fluorescent.¹⁹ While some anthraquinones are solely quenchers,²² others emit pH-dependent fluorescence.²³ The range of pK_a values covered by different anthraquinones means that there is a family of dyes that can measure pH in various types of samples. The appropriate selection of dye for a particular application depends on preferred excitation wavelength, desired emission wavelength, photobleaching characteristics, leaching potential, etc.

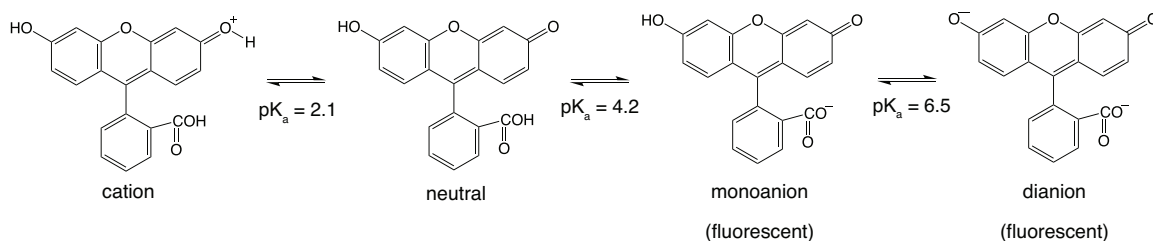


Figure 1.4: pH-dependent ionization of fluorescein in aqueous solutions. Chemical structures created with ChemDraw based on figure from Lakowicz.¹⁹

The majority of fluorescent dyes are single excitation/single emission, which simplifies the equipment needed for spectroscopic measurements but makes it difficult to quantitatively determine pH. Because the brightness depends not only on the proton concentration but also on the amount of dye that is loaded, uneven sequestration of the dye in cells complicates the measurement of an absolute value of pH. As a result, most free dye molecules can only function as qualitative sensors.⁹ Ratiometric dyes are more suitable for quantitative pH analysis because using the ratio of two fluorescent peaks rather than the absolute intensity of one peak normalizes experimental variations.²⁴ In this method, emission at one wavelength is enhanced or diminished relative to that at another based on the pH of the surrounding environment.²¹ By calibrating the ratio between these two signals, quantitative pH can be determined because variants such as excitation source fluctuation and dye concentration are taken into account.^{24,25}

Firstly, there are dual excitation dyes that are sequentially illuminated by light at two different wavelengths, and the emission is detected at one wavelength.²⁶ To illustrate, consider pH measurements with BCECF, which are made by calculating the ratio of emission intensity at 535 nm when the dye is excited at 490 nm versus 440 nm.^{27,28} However, because fluorescence images are not acquired simultaneously, it is difficult to monitor intracellular pH of cells with high temporal resolution.²⁶ In addition, the required equipment and operation are complex.²⁵ The second type, dual emission dyes, overcomes these problems through excitation at one wavelength and emission detection at two independent wavelengths. The compound 2-(4-pyridyl)-5-((4-(2-dimethylaminoethylaminocarbonyl)methoxy)phenyl)oxazole (PDMPO), commercially known as LysoSensor Yellow/Blue, is one example of this class of dye, wherein the emission ratio at 450 nm and 510 nm is determined while the dye is excited at 340 nm.^{29,30} Unfortunately, the selection of dual excitation and dual emission dyes is still very limited.

1.2.3 PEBBLE nanosensors

To overcome the fact that the majority of dyes are not ratiometric in and of themselves, Clark et al. designed probes encapsulated by biologically localized embedding (PEBBLEs).³¹ A pH-sensitive dye and an internal standard (sulforhodamine 101) was introduced into each PEBBLE, and the calibration showed a linear range between pH 6 and 7.³² These nanosensors combine multiple dyes in a protective polymer matrix to allow dual wavelength pH measurements with single excitation/single emission dyes. The matrices, which can be based on polyacrylamide, poly(decyl methacrylate), polyurethane, and sol-gel silica, are porous to allow the analyte to diffuse through the material and interact with the indicator dye, which changes fluorescence intensity based on the surrounding concentration of analyte.^{7,33} The assemblage of dyes within a matrix provides the nanosensor with advantages like higher local brightness, higher photostability, and protective shielding.³⁴ The extra layer of barrier helps to prevent nonspecific quenching from the solvent and has the added benefit of protecting the cell from any dye toxicity.⁷

One polymer matrix of the polyurethane type commonly used for pH sensing is hydrogel D4. It is stable under a wide range of pHs and soluble in 90% ethanol but not in water. Because hydrogel D4 contains hydrophilic and hydrophobic blocks, it can embed lipophilic pH indicators without covalent coupling or significant leaching.^{35,36} Peng et al. entrapped two fluorophores in hydrogel D4 to give a dual (green and red) fluorescence signal for ratiometric analysis; a pH indicator was also loaded to impart the nanogel with pH sensitivity.³⁷

Sun et al. covalently linked a pH sensitive dye (fluoresceinamine derivative) and a pH-insensitive dye (rhodamine B derivative) to a polyacrylamide matrix, producing a sensor that reliably measured pH between 5.8 and 7.2 ($pK_a = 6.6$).²⁴ In the same year, Burns et al. coated a reference-dye-rich core with a thin layer of sensor-dye-rich silica using the same dye families. In their design, fluorescein's ($\lambda_{ex} = 488$ nm, $\lambda_{em} = 520$ nm) quantum efficiency changed with pH while tetramethylrhodamine ($\lambda_{ex} = 540$ nm, $\lambda_{em} = 575$ nm) acted as the internal standard. They were able to obtain ratiometric imaging of pH in various intracellular compartments with high spatial resolution.⁹

1.2.4 Fluorescent nanomaterials for sensing

While PEBBLEs overcome multiple problems associated with free dyes, they still have several drawbacks problematic to indicator dyes in general (e.g. photobleaching, brightness). Fluorescent nanomaterials have emerged as a reliable support for pH sensing assays by providing superior optical properties, including higher fluorescence, better photostability, and wide ranges of excitation/emission wavelengths. Multiple probes can even be attached to

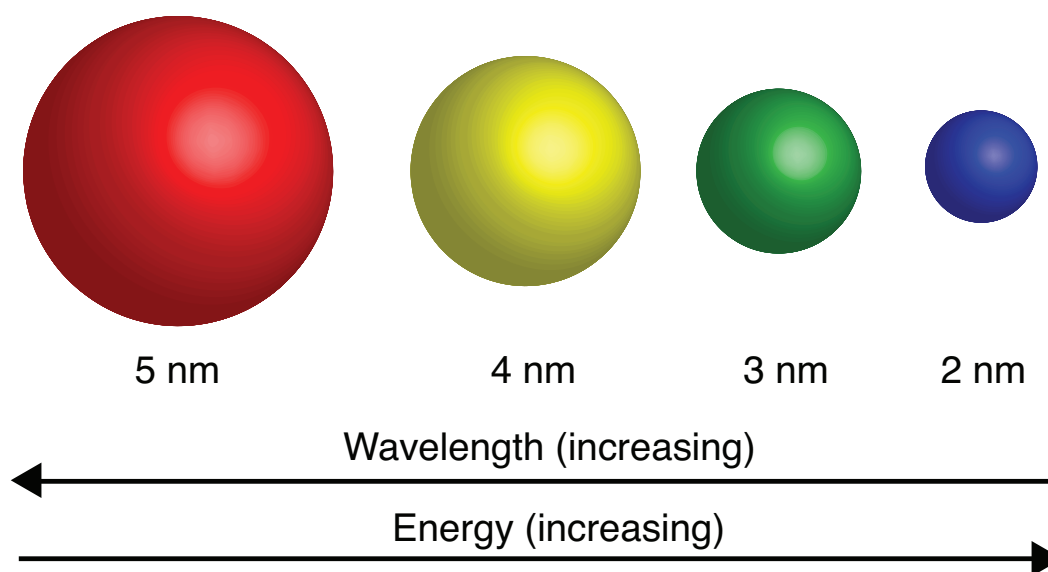


Figure 1.5: Fluorescent colors from quantum dots of different sizes. Larger dots produce fluorescence at longer wavelengths and lower energy. Smaller dots produce fluorescence at shorter wavelengths and higher energy. Adapted from figure in Elasersawi.³⁹

the nanostructure to increase the labeling ratio for improved sensitivity.³⁸

One of the most common nanoparticle types used in pH sensing is semiconductor quantum dots (QDs), which are excited at wavelengths as short as 350 nm.²³ One common type comprises a core of CdS and a shell of ZnS, which passivates and stabilizes the core.¹⁹ Due to quantum confinement, the emission wavelength of the QD can be tuned by controlling its size (Figure 1.5). Increasing the size of the CdSe/ZnS particles by a few nanometers changes the fluorescence from blue to red. The Stokes shifts of QDs are much larger than organic fluorophores such that the absorbance bands are spectrally separated from the emission bands.¹⁹

Carbon dots (CDs), mainly composed of graphene quantum dots (GQDs), carbon nanodots (CNDs), and polymer dots (PDs), have also received considerable attention for biological sensing applications. They are typically excited in the UV region (230-320 nm), and their emission wavelength has the unique property of depending on excitation wavelength. Compared to QDs, CDs experience higher emission bandwidth and less blinking.⁴⁰

GQDs consist of fewer than ten layers of graphene sheets, resulting in particles that have lateral dimensions less than 100 nm. The size of the GQDs and functionalization with different groups (e.g. $-\text{OH}$, $\text{C}=\text{O}$, COOH) can influence their fluorescence wavelength.⁴¹ CNDs must be spherical, but they do not always have a crystal lattice.⁴⁰ Similar to GQDs, CND photoluminescence can be tuned by adjusting size and surface chemistry.⁴² PDs are

made from an assembly of conjugated polymers,⁴³ and their fluorescence properties depend mostly on the chemical structure of the conjugated polymer, although size of the overall PD can also be a factor.⁴⁴ While non-conjugated polymers are known to have little fluorescence, some show good emission when aggregated or cross-linked together due to the crosslink enhanced emission effect.^{40,43}

All of these fluorescent nanoparticles can interact with the indicator dyes through two main mechanisms: inner filter effect (IFE) and fluorescence resonance energy transfer (FRET). They will be described separately in detail below.

1.2.4.1 Inner filter effect

When the absorption spectrum of an indicator dye (absorber) and the excitation and/or emission spectrum of the luminescent nanomaterial (fluorescer) overlap, a phenomenon called IFE can occur in which the nanomaterial emission is reduced by the absorber. Primary IFE occurs when the fluorescer's excitation is diminished by the absorber, and secondary IFE is when the fluorescer's emission radiation is absorbed by the dye.⁴⁵ Both are forms of radiative energy transfer. IFE was frequently considered to be a source of error in spectrofluorometry, so multiple ways of correcting for the inner filter effect were developed,⁴⁶⁻⁴⁸ of which the correction for the typical square 1 cm path length cuvette is described here.^{19,49}

The correct fluorescence intensity in this scenario can be approximated by:

$$F_{corr} = F_{obs} 10^{(OD_{ex} + OD_{em})/2} \quad (1.5)$$

where F_{corr} is the corrected maximum fluorescence intensity, F_{obs} is the measured maximum fluorescence intensity, OD_{ex} is the absorbance (optical density) at the excitation wavelength, and OD_{em} is the absorbance (optical density) at the emission wavelength.

Yet, changes in fluorescence related to variations in analyte concentrations creates the potential for an IFE-based sensing system. When the absorption of the quencher varies with analyte concentration, the emission of the inert fluorescence compound subsequently also correlates with the analyte concentration.⁵⁰ Because measured changes in the fluorescence of the nanomaterial are exponentially greater than the absorbance of the dye, the IFE analytical method achieves greater sensitivity and lower limit of detection compared to the capability of the absorber alone. Thus, the IFE sensing technique offers a simple, flexible strategy to convert a colorimetric assay into a fluorescence sensing approach without requiring any covalent linkage between nanomaterial and dye.^{45,51}

To study the pH-dependent IFE interaction between CNDs and fluorescein isothiocyanate (FITC), Liu et al. mixed different amounts of the dye with a fixed concentration of CND

solution at different pHs.⁵² To confirm that the fluorescence decrease of the CNDs by FITC was due to IFE, they confirmed that the fluorescence intensities no longer changed with increasing FITC concentration after correction with Equation 1.5. Using a double layer of sol-gel silica, Hiruta et al. immobilized two types of QDs ($\lambda_{ex} = 400$ nm, $\lambda_{em,1} = 525$ nm, $\lambda_{em,2} = 650$ nm) in the first layer and pH indicators (neutral red, methyl yellow) in the second layer.⁵³ In contrast to a single dye which has a narrow pH response range of 3-4 pH units, the combination of dyes extended the responsive range to 6 pH units (pH 4-10). The ratiometric analysis relied on the pH-dependent emission peak at 525 nm and the pH-independent reference at 650 nm. The sensor showed long-term stability even after six months of storage.

1.2.4.2 Resonance energy transfer

FRET is a non-radiative phenomenon whereby a donor fluorophore donates energy to an acceptor fluorophore via intermolecular dipole-dipole coupling.⁵⁴ There are multiple prerequisites for FRET to occur. The first relates to proximity since the efficiency is inversely proportional to the sixth power of the distance between donor and acceptor, r , as described in the following equation:

$$E = \frac{R_0^6}{R_0^6 + r^6} \quad (1.6)$$

where R_0 is the distance at which FRET efficiency is 50% (i.e. Förster radius). R_0 can be calculated by:

$$R_0 = \sqrt[6]{\frac{9 \times \ln 10 \times \kappa^2 \times Q_D \times J}{128\pi^5 \times N_A \times n^4}} \quad (1.7)$$

where κ^2 is the dipole orientation factor, Q_D is the intrinsic quantum yield of the donor alone, J is the overlap integral between the donor emission spectrum and the acceptor absorption spectrum, N_A is Avogadro's number, and n is the refractive index of the medium.⁵⁵ κ^2 is usually assumed to be 2/3 for simplicity, which is the case when the fluorophores are spherical or tumbling through all possible orientations within the span of energy transfer.^{56,57} Common values of R_0 are between 2 and 7 nm, so FRET is essentially limited to intermolecular distances of 10 nm.⁵⁸ Secondly, there must be good spectral overlap between the emission spectrum of the donor and the absorption spectrum of the acceptor.^{54,59} Thirdly, there must be favorable spatial orientation; the best case scenario occurs when the acceptor excitation dipole and the donor emission dipole are aligned parallelly. In practice, the dipoles are randomly oriented such that transfer efficiencies are less than ideal.⁵⁸

As a result of FRET, there is a decrease in donor emission and a subsequent increase in acceptor emission (i.e. sensitized emission). Special care must be taken to make sure that the emission spectra of the FRET pairs do not overlap. Cross-talk dampens ratio changes and results in poor sensitivity because an increase in sensitized emission is masked in part by a reduction in donor emission mixed in the acceptor channel.^{60–62} In addition, the fluorescence lifetime of the donor molecule is shortened because FRET provides an additional pathway for it to lose energy in the excited state. The efficiency can also be described by:

$$E = 1 - \frac{I_{DA}}{I_D} = 1 - \frac{\tau_{DA}}{\tau_D} \quad (1.8)$$

where I_{DA} and I_D are the donor fluorescence intensity with and without the acceptor present and τ_{DA} and τ_D are the donor fluorescence lifetime with and without the acceptor present.⁶³ Experimental calculation of E is preferably done with the ratio τ_{DA}/τ_D instead of I_{DA}/I_D because the former is not affected by inner-filter effects and does not require the task of rigorously maintaining the same concentrations while comparing D alone to the DA pair.⁶⁴

“Relative” FRET efficiency is given by:

$$E_{rel} = \frac{I_A}{I_D + I_A} \quad (1.9)$$

where I_A and I_D are the donor and acceptor fluorescence intensity after donor excitation. E_{rel} is not equivalent to the actual FRET efficiency and should only be used for qualitative purposes because it doesn't take into account the quantum yields of the two fluorophores.⁶⁵

Complementary to conventional steady-state fluorescence spectroscopy is time-resolved fluorescence spectroscopy. Once a fluorophore has been excited with a pulse of laser light, its fluorescence intensity at time t , $I(t)$, will decay according to the following equation:

$$I(t) = I_0 e^{-t/\tau_0} \quad (1.10)$$

where I_0 is the initial emission intensity at $t = 0$ and τ_0 is the fluorescence lifetime, which is the time required for the fluorescence intensity to decay to $1/e$ of I_0 . If there is an acceptor present that can acquire energy from the donor, there will be a short component of the lifetime, τ_1 (attributed to the quenched donor molecules), and a long component of the lifetime, τ_2 (attributed to the unquenched donor molecules). The fluorescence decay then follows a bi-exponential function:

$$I(t) = A_1 e^{-t/\tau_1} + A_2 e^{-t/\tau_2} \quad (1.11)$$

where A_1 and A_2 are the corresponding amplitudes.^{66,67} The fraction of donor molecules undergoing FRET is $A_1/(A_1 + A_2)$.⁶⁸ If the donor already shows bi-exponential behavior and is paired with a mono-exponential acceptor, four exponential decay components have to be considered.⁶⁹ Two of these describe the different donor conformations alone, and the other two describe the donor conformations undergoing FRET. Fitting time-resolved data to these complex fluorescence decay profiles is not a trivial task.⁵⁵ Such calculations require high photon counts and sophisticated data analysis.⁷⁰ In practice, it is more common to approximate complex fluorescence decay models with a mono-exponential or bi-exponential function. These fits will not give information about the proportion of donors undergoing FRET, but their average lifetimes indicate changes in the decay times, and in the case of bi-exponential decay curves, their amplitudes show changes in the contributions of different lifetime components after the acceptor is present.^{71,72}

There have been many recent reports on the use of fluorescent nanoparticles for FRET-based ratiometric pH sensors. Ruedas-Rama and Hall attached pH-dependent anthraquinones to semiconductor quantum dots (QDs) for their nanosensor using layer-by-layer modification.²³ Two of the anthraquinone derivatives, alizarin red S (ARS) and calcium red (CaR), were shown to emit light based on resonance energy transfer from the QDs based on a decrease in the emission lifetime. In a more recent study, Sumusu et al. synthesized water-soluble, blue-emitting QDs that were conjugated with FITC to construct a ratiometric pH sensor that could be further coupled to membrane localization peptides to monitor the pH of extracellular environments.⁷³ Surface modification by ligand exchange was used to minimize the hydrodynamic size of the QD sensor. They then presumed that the QDs donated energy to FITC through FRET due to the small distance between fluorophore and absorber but did not confirm its presence through lifetime measurements.

Du et al. demonstrated a pH nanosensor with FITC covalently linked onto CNDs.⁷⁴ It was the first CND-based FRET system to map an intracellular pH gradient. Chan et al. used PDs that were much brighter than QDs to develop a ratiometric pH sensor. Fluorescein was conjugated to pH-insensitive PDs then introduced into live HeLa cells to measure the pHs in the various organelles involved with the endocytic pathway.⁵⁹ Both studies supported their FRET explanations with lifetime measurements.

1.2.5 Disadvantages of downconversion

The pH nanoprobe described above all suffer from shortwave excitation, which (i) gives rise to autofluorescence in biological materials, resulting in poor signal-to-noise ratio and detection sensitivity; (ii) inflicts photodamage to living organisms; and (iii) reduces penetration depth in biological tissues due to their strong absorption at low wavelengths (UV-Vis

light).^{34,75–77} Unfortunately, the few pH probes absorbing in the optically transparent window in the far red or near-infrared spectral range have tendency to photobleach or involve complicated, tedious synthesis procedures.^{34,78,79} Photobleaching is especially problematic in sensors because, as an indicator, the dye may need to remain photostable under repeated use for long periods of time. A fluorescent nanoparticle excited at long wavelengths that is straightforward to produce and free of autofluorescence, photobleaching, and photodamage is needed to produce a robust, reliable pH sensor that can be used in tissue.

This thesis proposes that UCNPs are ideal for biological pH sensing due to their NIR excitation spectral range. They have been used for cellular imaging^{80,81} and measurements in complex samples, such as whole blood.^{82,83} UCNPs have this property because of their lanthanide ions, which have unique electronic transitions within the $4f$ electronic shells that enable absorption of multiple low-energy photons and subsequent emission of a high-energy photon. Lanthanide ion emitters have multiple emission peaks,⁸⁴ which make them great candidates for single excitation, multi-emission sensors. Erbium ion (Er^{3+}) mainly emits green and red fluorescence, while thulium ion (Tm^{3+}) emits blue fluorescence strongly and red fluorescence weakly.^{85,86} In addition, UCNPs emit light continuously, unlike QDs, which blink, making them very attractive for bioimaging applications.⁷⁶ Lastly, the synthesis of these UCNPs is quite versatile: the size can be tuned down to 5 nm⁸⁷ and the surface can be modified to target certain types of cells.^{88,89}

1.3 Upconversion nanoparticles

1.3.1 Composition and upconversion mechanisms

During conventional fluorescence, which occurs for organic dyes, one higher-energy photon is absorbed and one lower-energy photon is emitted (Figure 1.6).⁷⁵ In other words, the excitation wavelength is shorter than the emission wavelength. With upconversion, two or more lower-energy photons are absorbed sequentially and one higher-energy photon is emitted, resulting in the so-called anti-Stokes shift (see Figure 1.6).⁹⁰ This is in contrast to two-photon absorption processes that require nearly simultaneous absorption of two coherent photons, resulting in low efficiency.⁸⁸ Upconversion is much more efficient than two-photon absorption because it takes advantage of the long lifetime of the excited energy states, which allows for the aforementioned sequential absorption of photons.⁹¹

Upconversion nanoparticles, which typically have a host matrix made of NaYF_4 , NaLuF_4 , or NaGdF_4 , have this ability because of doped lanthanide ions that can convert NIR light into visible wavelengths.⁹³ Typical ions incorporated in the crystalline matrix include Yb^{3+} ,

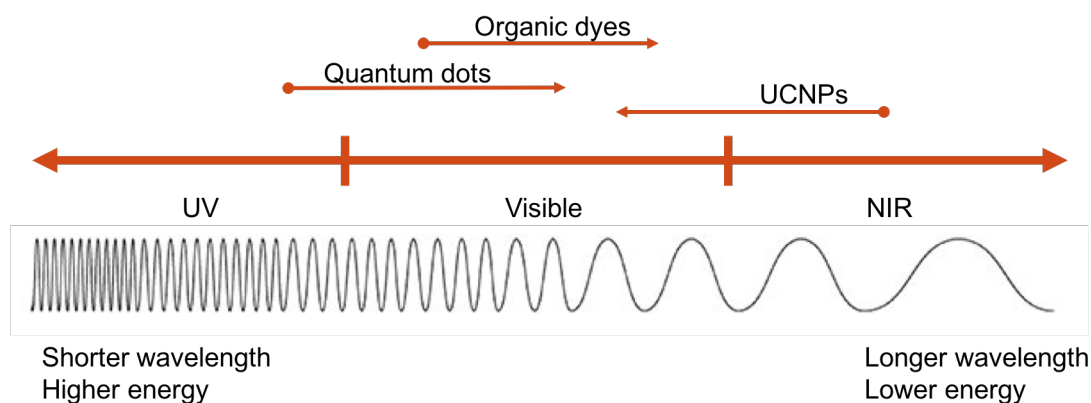


Figure 1.6: Simplified schematic comparing the excitation and emission of organic dyes, quantum dots, and upconversion nanoparticles. The examples represented are fluorescein,⁹² CdSe-ZnS QDs,²³ and NaYF₄: Yb³⁺/Er³⁺,⁹⁰ respectively.

Er³⁺, and Tm³⁺. Yb³⁺ is a sensitizer while Er³⁺ and Tm³⁺ are activators.⁹⁴ There are two crystal phases, cubic (α) and hexagonal (β), of which the latter has higher upconversion efficiency, likely due to lower phonon coupling. The non-harmonic phonon mode is greater in the cubic phase due to the random substitution of Na⁺ and lanthanide cations in the cubic phase compared to the hexagonal lattice, which has a more ordered distribution.⁹⁵ See Appendix A for more details on crystallography. The emission colors and intensities of the nanocrystals can be tuned by changing the sensitizer-activator combination (e.g. Yb³⁺/Er³⁺, Yb³⁺/Tm³⁺) and dopant concentrations, respectively.⁸⁵ Amongst the many sensitizer and activator ions reported in the literature,^{85,91,96} the Yb³⁺/Er³⁺ pair remains the classic combination due to its high efficiency in producing upconversion luminescence in the green and red color region,⁹³ which is very applicable for biosensing applications. The mechanism for this co-doped system will be described in more detail below.

The two main upconversion mechanisms are excited state absorption (ESA) and energy transfer upconversion (ETU). In the case of ESA, only a single activator dopant (e.g. Er³⁺) is needed. First, an incoming photon excites the ion from ground level G to excited metastable level E1 in a process known as ground state absorption (GSA) (Figure 1.7). Then, a second photon promotes the ion from E1 to E2; the transition from E2 back down to G results in upconversion emission.⁹⁷ A ladder-like energy structure with equally spaced energy levels is suitable while using a monochromatic light source, since each absorption step requires the same photon energy.⁹¹ However, this means that cross-relaxation can occur between neighboring ions when doping levels are high, resulting in quenching of excitation energy.⁹⁴ In this self-quenching process, an erbium ion in an upper excited state transfers its energy to an erbium ion in a ground state, bringing both ions to intermediate excited states.^{98,99}

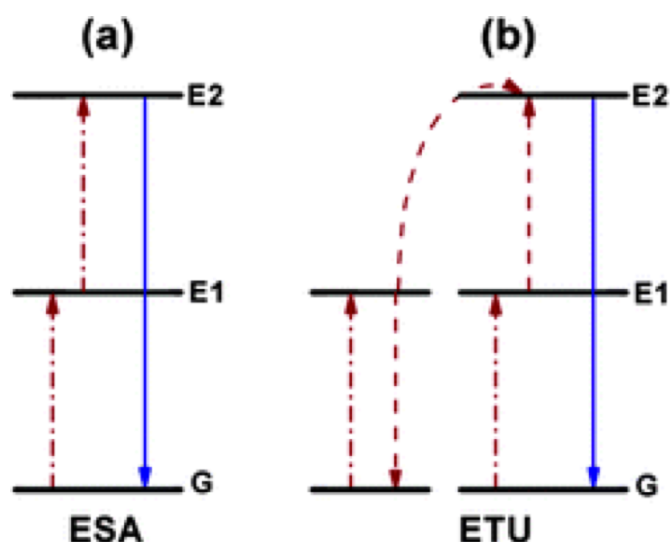


Figure 1.7: Energy diagrams of a) excited state absorption and b) energy transfer upconversion. The dashed/dotted, dashed, and full arrows represent photon excitation, energy transfer, and emission processes, respectively. Adapted from Wang and Liu with permission from The Royal Society of Chemistry.⁹⁴

Although, in principle, increasing the concentration of the lanthanide dopant in the host matrix should improve upconversion emission and increase emission intensity, this is not the actual case.⁹¹ Many research groups have kept the concentration of activator ions low to decrease interionic distance and reduce the probability of cross-relaxation.⁹⁹

Co-doping a sensitizer such as Yb^{3+} , which has a large absorption cross-section, with the activator can enhance upconversion efficiency.⁹⁴ In ETU, both the activator and sensitizer ions are excited to E1 metastable energy states (Figure 1.7). An energy transfer process from the sensitizer to the activator promotes the latter to E2 while the former returns to G in the process. Again, upconversion emission occurs when the activator falls back down to G.⁹⁰ This energy transfer mechanism is shown in more detail in Figure 1.8. The ${}^2\text{F}_{7/2} \rightarrow {}^2\text{F}_{5/2}$ transition of Yb^{3+} is resonant with many f-f transitions of activator ions like Er^{3+} and Tm^{3+} , facilitating energy transfer. For Er^{3+} , the green emissions are the result of transitions from ${}^2\text{H}_{11/2}$ and ${}^4\text{S}_{3/2}$ to ${}^4\text{I}_{15/2}$, while the red emission is attributed to the ${}^4\text{F}_{9/2}$ to ${}^4\text{I}_{15/2}$ transition. The ETU process is much more efficient than ESA.⁹⁴ Because Yb^{3+} has only one excited state, cross-relaxation between two Yb^{3+} does not result in a net loss of energy for upconversion,¹⁰⁰ but it facilitates energy migration through the sensitizer-sensitizer network that eventually reaches the surface quenchers (e.g. ligands, solvents, impurities, defects).^{99,101} Er-Er energy transfer may occur but is less probable at the very low concentrations commonly used for synthesis because of the large distance between two individual activators.¹⁰² At high concentrations of Er^{3+} doping, the common misconception is that

cross-relaxation is the major quenching process, but it is in fact energy migration loss that is mostly responsible for upconversion inefficiency.^{103,104}

Due to the high surface-to-volume ratio stemming from the nanometer dimension, many lanthanide dopants are susceptible to surface-induced deactivation compared to their bulk counterparts.⁸⁴ Johnson et al. found that concentration quenching in nanocrystals is predominantly due to resonance energy transfer from dopant ion to surface, while interionic cross-relaxation is the main reason for concentration quenching in bulk materials.¹⁰³ For a long time, low doping concentration has been an obstacle to engineering small, bright UCNPs as luminescent bioprobes.^{84,99} The use of a core-shell structure can suppress these surface-related quenching effects in nanocrystalline materials.¹⁰⁵ The standard strategy is to use a monolayer that matches the core nanoparticle lattice due to facile formation and photochemical stability, for example, NaYF₄:Yb, Er@NaYF₄:Yb, Er and NaYF₄:Yb, Er@NaYF₄. This removes the risk of nonradiative relaxations that prevail at nonepitaxial core-shell interfaces. Shell precursors can be injected into the solution of growing core nanoparticles (hot-injection strategy), or the shell layer can be grown separately (heat-up strategy).¹⁰⁶

Others including Zhao et al. and Gargas et al. showed that high excitation irradiance ($\sim 10^6$ W cm⁻²) can help overcome concentration quenching at high dopant concentrations.^{107,108} While thulium is usually kept at less than 2 mol% at power densities below 100 W cm⁻², Zhao et al. were able to increase the concentration of the activator to 8 mol% and achieve a 70-fold emission enhancement. Gargas et al. were the first to report ultra bright sub-10-nm UCNPs that were highly doped with Er³⁺ and excited at high power density. When there is high-energy incoming flux from the laser, nearly all the ions are excited and very few are in the ground state. The large distance between ground state ions makes cross-relaxation much less feasible.¹⁰⁹ The downside of this strategy to bypass the concentration quenching effect is that condensed excitation power may not be compatible with applications in living systems.

1.3.2 Synthesis methods

There are many chemical approaches for the synthesis of UCNPs, including coprecipitation, thermal decomposition, hydrothermal/solvothermal, combustion, and sol-gel.¹¹⁰ Among these, the three most widely adopted are the hydrothermal/solvothermal method, the thermal decomposition method, and coprecipitation due to their reported effectiveness in fabricating monodispersed, high-quality crystalline nanoparticles.¹¹¹ These three methods will be the focus of discussion below.

The hydrothermal/solvothermal synthetic method features chemical reactions in aque-

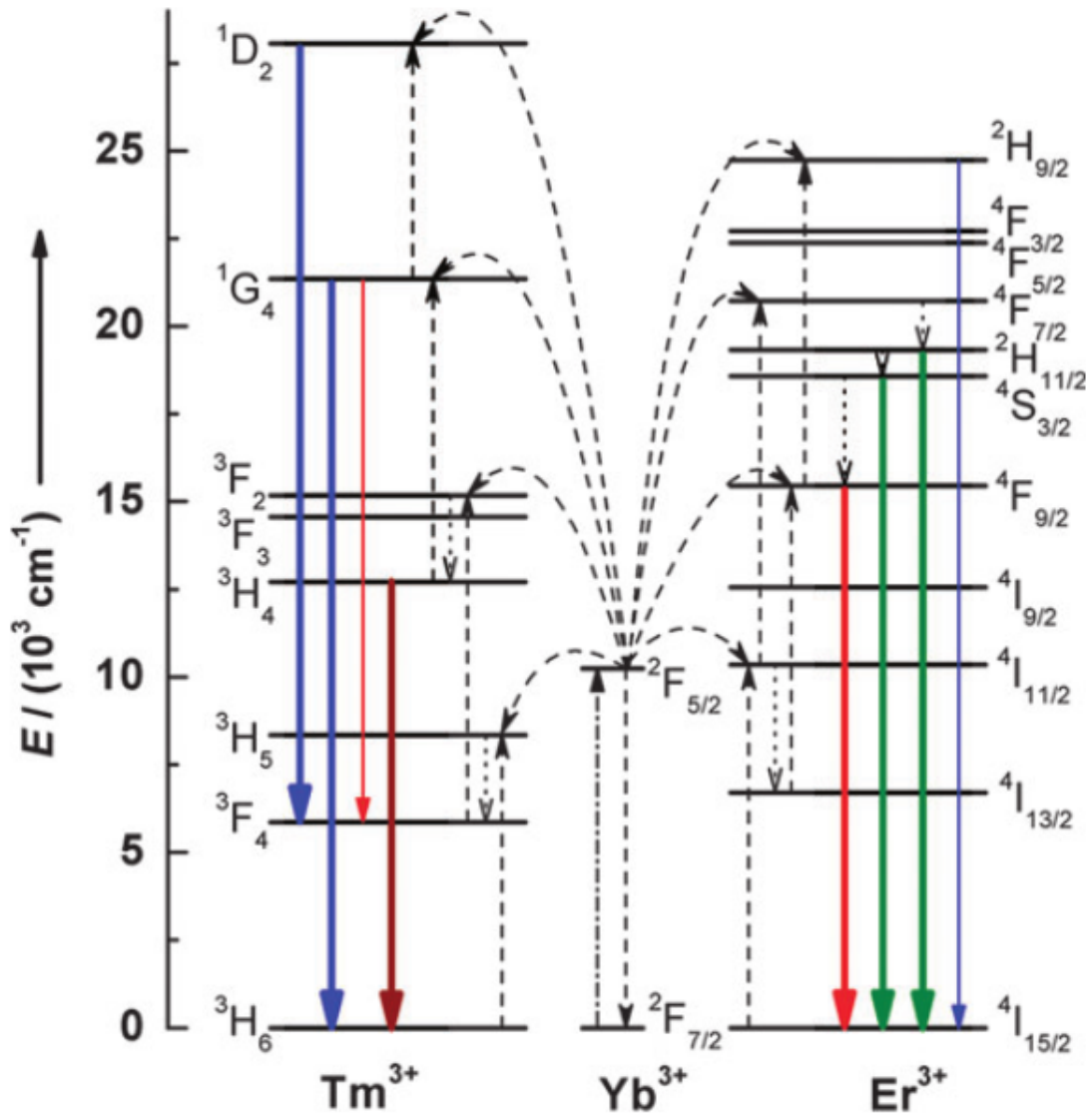


Figure 1.8: Energy transfer mechanisms for upconversion processes in Er^{3+} , Tm^{3+} , and Yb^{3+} doped crystals under 980 nm laser excitation. The dashed-dotted, dashed, dotted, and full arrows represent photon excitation, energy transfer, phonon relaxation, and emission processes, respectively. The colors of the full arrows show the colors of the corresponding visible light emissions. Reproduced from Wang and Liu with permission from The Royal Society of Chemistry.⁹⁴

ous or organic solvent above its critical point.¹¹⁰ Common solvents used in the synthesis of NaYF₄ include ethylene glycol and ethanol.^{112–114} An autoclave is used to achieve the elevated pressure and temperature.¹¹⁰ The process can produce UCNPs with various sizes and shapes (e.g. prisms, disks, and rods).¹¹⁵ In addition, a variety of surfactants such as polyethylenimine (PEI) and polyvinylpyrrolidone (PVP) can be anchored onto the surface of the nanoparticles without the need for an additional modification step.^{112–114} However, the hydrothermal synthetic method still suffers from a couple drawbacks: long reaction times are needed to produce uniform, monodispersed nanoparticles (e.g. 24 hours) and the particles have a tendency to be on the larger side unless strict reaction conditions are followed.¹¹⁰ As a case in point, multiple studies reported in the literature using hydrothermal/solvothermal synthesis were unable to produce uniform, monodisperse, spherical UC-NPs.^{81,82,116}

The thermal decomposition method requires much shorter reaction time while giving well-shaped, small particles.¹¹⁵ UCNPs produced via thermal decomposition can be as small as 8 nm.¹¹⁷ This makes the method suitable for producing UCNPs that are useful for biosensing applications due to the benefit of better cell membrane permeability with smaller size. In addition, it is desirable for intracellular sensors to be small in size so that they do not interfere with the physiological processes of cells and their organelles.⁷⁴ The thermal decomposition method involves dissolving organic precursors (e.g. rare earth trifluoroacetates) in high-boiling-point solvents (e.g. oleic acid, oleylamine, and octadecene) at high temperature under inert gas protection (see Figure 1.9).^{115,118} These surfactants typically have polar capping groups facing the nanocrystal and long hydrocarbon chains dangling in solution. Disadvantages of the thermal decomposition method include production of toxic species (fluorinated and oxy-fluorinated carbon species), rigorous synthesis requirements (anhydrous and oxygen-free), and harsh reaction conditions (high temperature of up to 330 °C).^{97,117,119,120}

Yi et al. prepared NaYF₄:Yb,Er nanoparticles in the presence of ethylenediamine tetraacetic acid (EDTA) using a coprecipitation method.¹²² Fast injection of a rare earth-EDTA complex into a NaF solution at room temperature with vigorous stirring results in the formation of cubic UCNPs through a homogeneous nucleation process.⁹⁷ Annealing them at 400-600 °C transforms them into larger, hexagonal-phase particles with improved upconversion luminescence.⁹¹ This is one of the simplest and most convenient methods for producing UC-NPs due to the mild synthesis conditions, straightforward protocols, short reaction times, and lack of need for costly specialist equipment.⁹⁷

High-temperature coprecipitation is considered to be the most reliable and user-friendly method to produce highly uniform, hexagonal phase nanoparticles with controllable shapes



Figure 1.9: General illustration of UCNP synthesis using oil-based methods. Reproduced from Zhu et al. with permission from The Royal Society of Chemistry.¹²¹

and sizes.¹²³ Li and Zhang developed a protocol for nanocrystals with strong upconversion fluorescence by forming small solid nuclei at room temperature before increasing the temperature for crystal growth/ripening. This avoids the reaction of excess fluoride reactants at high temperature, which can produce HF gas and other fluorinated species. The shape of the NaYF₄:Yb,Er nanocrystals (i.e. nanoplates, nanospheres, nanoellipses) can be controlled by changing the ratio of OA/ODE.¹²⁰

This protocol is a popular choice, but there remain a few disadvantages: it (i) requires careful temperature control at 300 °C for one hour and (ii) is small scale, only producing ~100 mg of UCNPs per batch. This is not ideal for bioanalytical applications because there are slight variations in size, shape, and elemental composition from batch to batch. To address these issues, Wilhelm et al. developed a high-temperature coprecipitation method that does not require stabilization at exactly 300 °C (heating the mixture to reflux instead at ~320 °C) and yields ~2 g of UCNPs in a single batch. After ~22 min of reaction at >300 °C, the upconversion luminescence becomes visible when exciting the reaction vessel with a 980 nm cw diode laser (~10 W cm⁻²). At this stage, some of the UCNPs are larger β -phase ones (~16 nm), while others are smaller α -phase ones (~5 nm). The mixture is cooled to 200 °C to prevent broader particle size distribution, then an additional heating step (>300 °C for ~5 min) is applied to dissolve the remaining α -UCNPs and grow the β -UCNPs. The resulting OA-coated UCNPs are purely hexagonal phase and 22.7±0.7 nm in average core diameter. Possibly due to the fewer number of surface defects, the UCNPs produced from this method achieve a quantum yield (QY) of ~0.35% compared to those synthesized by Boyer et al., which have a QY of ~0.1%.⁷⁶

As described above, the growth of NaREF₄ nanocrystals in OA/ODE solvent is commonly used to obtain monodisperse β -phase particles. It has been shown that this process

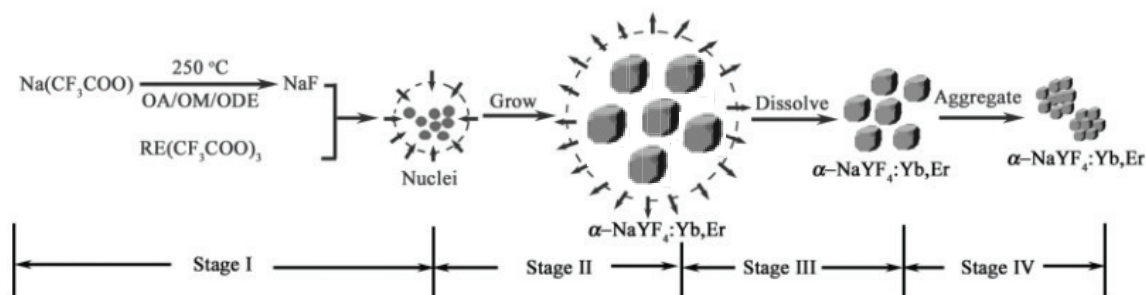


Figure 1.10: Schematic of the growth stages of α - $\text{NaYF}_4:\text{Yb,Er}$ nanocrystals. Reprinted and modified with permission from Mai et al.¹²⁶ Copyright 2007 American Chemical Society.

occurs in two steps. The first product that forms is the metastable α -phase nanocrystals that are then subsequently converted to thermodynamically stable β -phase nanocrystals.^{124,125} The α -phase particles form by nuclei formation, particle growth, dissolution, then aggregation (Figure 1.10).^{115,126} When the reaction mixture is heated for sufficiently long time, small β -phase seeds nucleate in solution.¹²⁷ They then grow via the Ostwald ripening process, in which the monomers from the disintegration of α - NaREF_4 nanocrystals diffuse onto the surface of the β -UCNPs.¹²⁸

1.3.3 Photoluminescence properties

As briefly alluded to beforehand, the unique optical properties of lanthanide ions come from their electronic $[\text{Xe}]4f^N$ configurations ($N=0-14$).¹²⁹ Firstly, the filled $5s^2$ and $5p^6$ subshells shield the $4f$ electrons, resulting in sharp and narrow $f-f$ transition bands due to weak interaction with the local environment (i.e. weak electron-phonon coupling).^{130,131} There are a couple selection rules that govern the transitions between electronic energy levels that these Ln^{3+} ions have to follow. An especially critical one that explains the optical phenomena of upconversion nanoparticles is the Laporte rule, which specifies that the s , p , d , and f orbitals in the same subshell cannot mix for ions in a centro-symmetric environment ($\Delta l = 0$).¹³² In other words, redistributing electrons within a subshell is forbidden so, for example, $4f \rightarrow 4f$ transitions are forbidden.¹³³ This rule is relaxed when there is vibronic coupling, resulting in asymmetry on the timescale of the electronic transition such that weak absorptions can occur, accounting for UCNPs' inefficient absorption of the exciting laser light.^{91,134} This relaxation of the Laporte rule also explains the long luminescence lifetime of UCNPs.¹³⁵ Tetrahedral molecules, which do not have a center of symmetry, are freely allowed to mix orbitals within the same subshell so their $4f \rightarrow 4f$ transitions may appear

stronger.¹³²

In some cases, the absorption of water at 980 nm is a significant cause of concern because of overheating. This drawback, which decreases the power of the excitation light, limits real-world biomedical applications, including photodynamic therapy (PDT) and imaging, of conventional UCNPs that use Yb^{3+} as the light-harvesting lanthanide ion.^{136,137} A few strategies have been established to shift the excitation wavelength from 980 nm to ~800 nm, where there is significantly less absorption of light by water.¹³⁸ Recent progress in the development of dye-sensitized UCNPs overcomes the narrow absorption of lanthanide ions by anchoring organic dyes with broad and intense absorption to the surface of UCNPs. The dyes harvest the excitation light and transfer the energy via FRET and/or Dexter electron transfer to the lanthanides.¹³⁹ For example, IR-806 absorbs NIR light at a maximum of ~800 nm and subsequently transfers the energy to Yb^{3+} ions. The downside is that NIR organic dyes have limited photostability. Because of advances in synthesizing multishell UCNP nanosystems, another strategy of including Nd^{3+} ions in the matrix as cosensitizers was made possible. They absorb the excitation light and then transfer that energy to Yb^{3+} .¹³⁸ The core-shell architectures are essential to prevent back-transfer from the activator to the sensitizer and to ensure $\text{Nd}^{3+} \rightarrow \text{Yb}^{3+} \rightarrow \text{activator}$ energy transfer in that order.^{140,141}

1.3.4 Surface modification

After synthesis by the strategies mentioned in Section 1.3.2 that produce high-quality, β -phase UCNPs, the particles are hydrophobic, coated with organic ligands, and thus not soluble in water.¹¹¹ Especially for bioanalytical applications, surface modification of the as-prepared UCNPs is necessary to convert them into hydrophilic ones that have good dispersibility in aqueous solutions, high colloidal stability, and functional groups that allow for further conjugation with other molecules (e.g. antibodies, oligonucleotides) to bind to target structures or analytes.^{76,142,143} Functional groups such as hydroxyl groups, amines, and carboxylic acids improve the dispersibility of the UCNPs in water. Surface ligands with highly charged groups can especially prevent aggregation by exploiting electrostatic repulsion, which helps with their long-term stability.¹⁴³ Several approaches exist for surface modification, including ligand exchange, ligand oxidation, ligand attraction, layer-by-layer (LbL) assembly, and silica coating.^{111,142,143} These five surface modification methods are summarized in Table 1.1.

In the ligand exchange method, the organic molecules on the surface of the UCNPs are exchanged for hydrophilic ligands, such as polyacrylic acid (PAA), polyethylene glycol (PEG) and PEI.¹⁴⁴ High temperature, an excess of the hydrophilic ligand, and an appropriate solvent can improve the extent of the ligand exchange.¹⁴³ A solvent like DMF or DMSO that

dissolves both polar and nonpolar compounds is suitable.⁸¹ The extent of ligand exchange is also influenced by the number and type of coordination sites in the hydrophobic and new surface ligand. Multidentate ligands with carboxylate groups are more efficient at ligand exchange compared to monodentate ligands with amine groups.¹⁴³

PAA is a commonly used polymer for ligand exchange on UCNPs.¹³⁵ Some carboxylic acid groups attach to the UCNP surface, and the remaining uncoordinated ones enable bio-conjugation. The stability depends on the buffer type, from 24 h in PBS (pH = 7.4) to several weeks in Tris-HCL buffer (pH = 7.4), because salts interfere with the electrostatic repulsion of the negatively charged polymer.¹⁴³ PEI is also applicable for ligand exchange reactions. In fact, Jin et al. found that the cationic UCNP-PEI greatly enhanced cellular uptake when compared to UCNPs covered by neutral (e.g. PVP) or negatively charged (e.g. PAA) polymers.⁸¹ Polyamidoamine (PAMAM) is another ligand with amine functionality. The terminal amines coordinate to the surface of the UCNPs, and the other amines provide multiple binding sites to allow for high loading capacity of probe molecules, which is highly important when the interaction between probe and analyte is weak. Additional benefits of PAMAM include its high hydrophilicity and biocompatibility.¹⁴³

One extremely useful method of ligand exchange relies on nitrosonium tetrafluoroborate (NOBF_4) to remove the oleate. The BF_4^- attaches to the positively charged surface to create nanoparticles that are not dispersible in water but in polar aprotic solvents such as *N,N*-dimethylformamide (DMF) and dimethyl sulfoxide (DMSO). After obtaining BF_4^- stabilization, the UCNPs can be stored for several months in DMF without signs of aggregation.¹⁴³ Furthermore, the BF_4^- ligands can be exchanged for polymers like PAA or small molecules like citrate.⁷⁶ The BF_4^- -stabilized UCNPs can also be subsequently coated with organic dyes like rose bengal (containing carboxyl group) and sulforhodamine B (containing sulfonyl group) by replacing the BF_4^- anions. Direct attachment minimizes the distance between the UCNP and dye and is expected to enhance FRET. Maximum FRET efficiency was found to occur when the diameter of the UCNPs was 21 nm.¹⁴⁵

Alternatively, ligand-free UCNPs can be produced by removing the oleate ligands with acids such as HCl. Oleates are protonated at low pH and thus dissociate from the UCNP surface.¹⁴³ During this time, the surface of the ligand-free UCNP is also protonated to give $[\text{LnOH}_2^+] \cdots \text{Cl}^-$. This positive charge gradually decreases as the pH changes towards the isoelectric point (pH = 5.8) to give LnOH, and at pH ≥ 7 the surface is negatively charged because of further deprotonation to $[\text{LnO}^-] \cdots \text{H}_3\text{O}^+$.¹⁴⁶ Thus, naked UCNPs display good dispersion stability (i.e. absence of agglomeration) at pH ≤ 4 and ≥ 7 .¹⁴³ Afterwards, the UCNPs can remain as is or be attached with new ligands in a separate step.¹⁴⁷

Ligand oxidation reaction can be performed when the organic ligands have unsatu-

rated carbon-carbon bonds. The Lemieux-von Rudloff reagent, comprising permanganate (MnO_4^-) and periodate (IO_4^-), is used to simultaneously cleave the double bond between C_9 and C_{10} of oleic acid (OA) and form carboxyl groups. The procedure essentially coats UCNPs with azelaic acid.^{94,148}

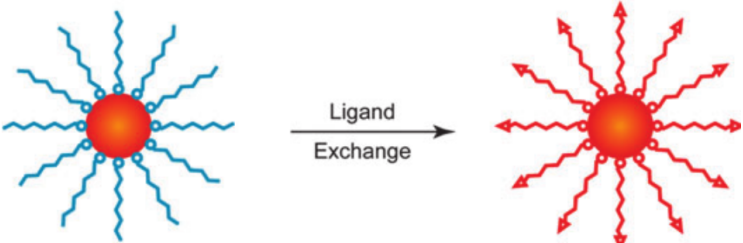
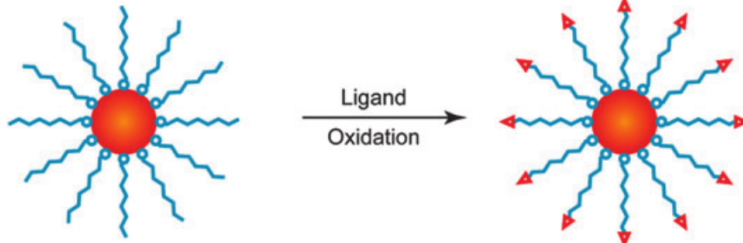
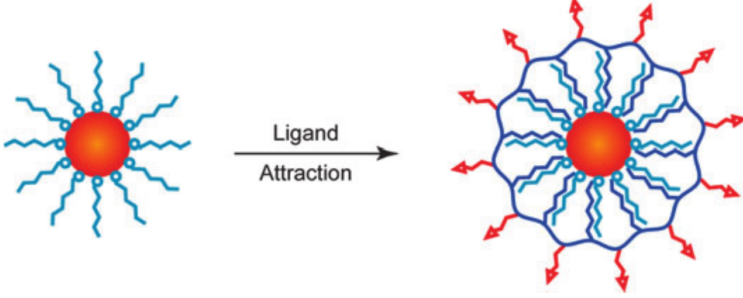
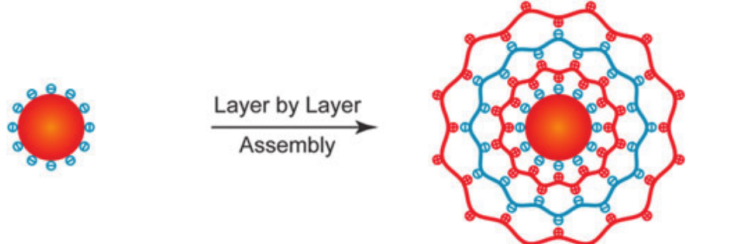
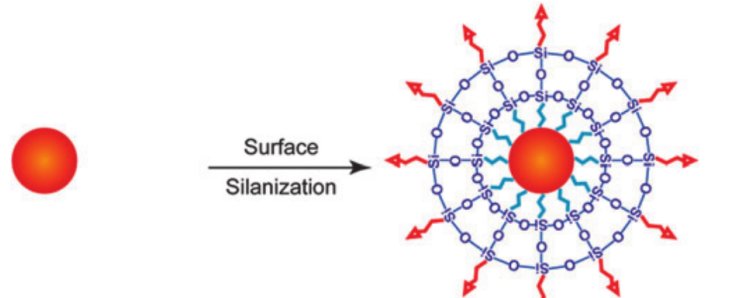
Ligand attraction between the hydrophobic surface ligands on the UCNPs and amphiphilic molecules improves dispersibility in aqueous dispersants without removing the existing coating. Amphiphilic polymers have hydrophobic units like alkyl chains that can interact with the oleate ligands and hydrophilic ends for water dispersibility.¹⁴³ Budijono et al. used Flash NanoPrecipitation to encapsulate hydrophobic UCNPs with block copolymers such as polyethylene glycol-*block*-polycaprolactone (PEG-*b*-PCL).¹⁴⁹

Instead of using block copolymers to add on a hydrophilic layer to the UCNPs, one can also use the LbL method to achieve the same outcome.⁹⁴ Fabrication of multilayers is achieved by adsorption of alternating layers of polyanions and polycations onto the nanoparticles.¹⁵⁰ For example, Wang et al. added a layer of positively charged polyallylamine hydrochloride (PAH) then a layer of negatively charged polystyrene sulfonate (PSS) onto their UCNPs.¹⁵¹ The LbL method is suitable for applications that require fine tuning of coating thickness.⁹⁴

Silica coating is another popular choice because the material is stable, easily functionalized, and nontoxic.⁹³ In the context of PDT, which is an emerging treatment modality for diseases such as cancer, porous silica is especially favored.⁸⁸ The porous matrix traps photosensitizers, yet is permeable enough to allow reactive oxygen species to diffuse out and kill nearby cancer cells.^{93,111} In addition, the encapsulation of photosensitizers protects them from degradation by the outside environment and prevents them from coming into direct contact with the body.⁸⁸ The well-known Stöber process can be used to coat hydrophilic UCNPs with a silica shell in the presence of tetraethyl orthosilicate (TEOS), alcohol, ammonia, and water.¹⁵² Hydrophobic UCNPs are capped with silica using a microemulsion technique. A detergent allows the formation of reverse micelles that act as nanoreactors, small aqueous compartments, where the silica shell is grown during the hydrolysis of TEOS.¹⁴³ The addition of ammonia catalyzes the polymerization.¹⁵³ After the growth of the silica shell, silanization with 3-aminopropyltriethoxysilane (APTES) in the presence of alcohol yields amine-functionalized, silica-coated UCNPs.¹⁵²

Besides the high-energy vibrational modes of hydroxyl groups ($3200\text{-}3600\text{ cm}^{-1}$) in aqueous media, the C-H and O-H vibrational modes of stabilizing ligands can also contribute to quenching.^{76,102} Arppe et al. found that up to 99.9% of UCNP quenching in water could be explained by surface deactivation.¹⁰² The surface dopant ions in incomplete coordination environments are exposed to these quenchers, and the excitation energy of interior

Table 1.1: Summary of surface modification methods. Adapted from Wang and Liu with permission from The Royal Society of Chemistry⁹⁴

Schematic	Description
	<p>Ligand exchange replaces the original organic ligands with other polymeric molecules instead, allowing aqueous dispersion and bioconjugation.</p>
	<p>Ligand oxidation converts the carbon-carbon double bond of the original organic ligands to a carboxylic functional group.</p>
	<p>Ligand attraction relies on adsorption of amphiphilic molecules on the nanoparticle surface. The hydrophobic portion of the copolymer is attracted to the original ligand, and the hydrophilic part faces outward to enable aqueous dispersion.</p>
	<p>Layer-by-layer assembly describes the adsorption of alternately charged polyions on the nanoparticle surface <i>via</i> electrostatic interactions.</p>
	<p>Surface silanization is the addition of organic functional groups onto the nanoparticle surface through hydrolysis and condensation of silanes.</p>

ions can even be transmitted to the surface with the help of adjacent dopant ions for non-radiative dissipation.⁹⁴ As discussed above, smaller nanoparticles have a higher surface-to-volume ratio, and consequently are more susceptible to surface quenching compared to bulk materials.¹²⁹

Thus, selecting the appropriate type of surface modification for the desired application is important because ligands affect the upconversion efficiency / luminescence quenching of UCNPs. To illustrate, particles obtained from ligand exchange are capped by a ligand monolayer and thus have the potential for minimal distance between probe and UCNP, enabling more efficient FRET than those modified by deposition of an amphiphilic or silica coating. Encapsulation strategies like ligand attraction, layer-by-layer assembly, and silica coating add an additional shell on top of the original hydrophobic layer.⁷⁶

1.3.5 UC-IFE sensors

Several UCNP-based sensors have been developed based on the inner filter effect. The first optical pH sensing system based on upconversion luminescence was developed by Sun et al. in 2009.¹⁵⁴ They incorporated upconversion nanorods (NaYF₄:Yb,Er) and bromothymol blue (BTB) in a sensor film made of biocompatible polyurethane hydrogel. The film was responsive from pH 6 to 10, so it could have potentially been used to sense blood pH, which ranges from pH 6.8 to 8.0.¹⁵⁵ In a similar study, Wang et al. mixed NaGdF₄ nanotubes with BTB in buffer solutions to obtain a linear response from pH 6 to 8.¹⁵⁶ The basic form of BTB exerted a much stronger IFE on the red emission of the nanotubes compared to the acidic form, but ratiometric calculations were unable to be performed on the single emission band.

In 2012, Xie et al. successfully measured the pH of buffer solutions and whole blood using thin films embedded with upconversion nanorods and ETH 5418, a chromoionophore.⁸³ The responsive range was pH 6 to 11 for buffer solutions and pH 6 to 9 for blood. The absorption spectra of protonated and deprotonated ETH 5418 overlapped with the UCNP's red and green emission band, respectively. The response curve was derived from the ratio of the red peak (656 nm) to the green peak (542 nm). Addition of ionophores allowed the sensor to measure the concentration of metal ions (Na⁺, Ca²⁺) in solution.

1.3.6 UC-RET sensors

To generate ratiometric pH response curves, UC-RET systems require the close presence of a pH indicator to the UCNP through electrostatic attraction, conjugation, or some other means of immobilization. If the dye is a quencher, the sensing system can rely on the pH-

dependent ratio of the green peak of the UCNP to the red peak of the UCNP (one or both of which are attenuated by the pH indicator). If the dye also fluoresces, the ratiometric analysis can be performed with the sensitized UC-RET emission and one of the UCNP peaks. Time-resolved detection strategies are helpful to confirm the presence of RET in UCNP systems, since the donor luminescence lifetime decreases when the acceptor is present. These types of measurements are particularly appealing because the lifetime is relatively unaffected by experimental parameters (e.g. excitation power density, luminophore concentration).¹⁴⁵ For example, the intensity of UCNPs is nonlinearly dependent on excitation power density as described in the following equation:

$$I \propto P^n \quad (1.12)$$

where I is the intensity of the photoluminescence, P is the power density of the laser, and n is the number of photons needed to produce upconversion.¹⁵⁷ On the other hand, the dependence of luminescence lifetime on excitation power density is much more subtle: when the UCNPs are 30 nm in diameter, the lifetime only increases three-fold when the excitation power density is halved.¹⁵⁸

While there have been many studies on FRET in pH sensing systems where QDs are the donor, UCNP-based FRET systems are still relatively unexplored. Their behavior can differ from other nanoparticle-dye pairs because each UCNP contains many individual Er^{3+} emitters of varying distances from the acceptor,⁵⁶ which is a very different scenario from the 1:1 stoichiometry found in most sensing systems based on QDs, CDs, etc. It is worth noting that particles >15 nm in diameter have a significant fraction of their emitters beyond the allowable distance for efficient FRET.¹⁴⁵ Although only the surface-near lanthanide emitters transfer energy nonradiatively (FRET), these center-near emitters can transfer energy radiatively (photon reabsorption).^{72,159}

Li et al. decorated core-multishell UCNPs with hemicyanine dyes for a RET-based ratiometric pH fluctuation-nanosensor. It linearly senses pH in the 6.0-9.0 range, but it has difficulty entering living cells in acidic conditions, which limits biomedical applications involving cancer and other diseases.¹⁶⁰ Ma et al. developed a probe comprising UCNPs functionalized with xylenol orange that is capable of detecting pH in solution and living cells and shows sensitivity to pH intracellularly from 5 to 8 with image channel ratio ranging from ~1 to ~5.⁷⁸ Both publications assume RET is responsible for the sensing effect based on the overlap between the absorption spectrum of the pH indicator and the emission spectrum of the UCNP, but this is merely a sufficient condition (not a necessary condition) for the non-radiative phenomenon to occur. There is still a shortage of studies on the pairing of UCNPs and organic dyes for upconverting pH nanosensors that go beyond proof of concept

and explore the fundamentals of energy transfer between the two moieties.

The Schäferling group has made progress in characterizing the interaction between UCNP and a rhodamine derivative called pHrodo Red. Arppe et al. designed a pH-sensitive upconverting nanoprobe that linked pHrodo Red to aminosilane-coated UCNPs to qualitatively evaluate pH in HeLa cells, determining whether certain microenvironments experienced lower pHs than others.³⁴ The sensitized red emission of the pHrodo Red was too weak for quantitative analysis, but in a subsequent paper from the same group, Näreoja et al. achieved higher loading by using the abundance of amino groups in polyethylenimine (PEI) to couple the dye. They assigned an upconversion resonance energy transfer (UC-RET) mechanism to the system after observing a decrease in lifetime, although they were not able to exclude photon reabsorption. They were then able to study membrane trafficking and its associated pH changes through confocal microscopy.⁷²

Two recent studies reported UCNP-fluorescein conjugates as pH probes, but each had their limitations. In the earlier publication, Li et al. were able to obtain a change in ratio of 3.63 unit per unit of pH between pH 3.0-7.0 in buffers but failed to show quantitative pH weighted images, only images of how the nanosensors colocalized with a lysosome dye in QBC939 cells.¹⁶¹ In the later report by Du et al., the live cell quantitative imaging was only achievable down to pH 5.0, which is above the pH attained by late endosomes and lysosomes for degrading internalized material.¹⁶²⁻¹⁶⁴ Moreover, they did not calculate and discuss the sensitivity of their nanosensor.

While one study by Jin et al. reported that PEI-coated UCNPs enter mammalian cells through clathrin-mediated endocytosis,⁸¹ no similar study was performed for the UCNPs modified with pH dyes in the above publications. It is possible that modifying the surface of the UCNP with a dye could change the uptake process. The mechanism by which the nanosensor is taken up by the cells is important because it limits the type of drug that can be tracked in drug delivery studies. For example, nanosensors that enter through the clathrin-mediated endocytosis pathway would be unable to sense pH in the endosomes/lysosomes that contain drugs entering through the caveolae-mediated endocytosis pathway.

1.3.7 Toxicity studies

Because nanoparticles used in fluorescence imaging come in contact with cells, toxicity studies are important for understanding their interactions with biological systems. Rare earth elements are known to have lower toxicity than the semiconductor elements used in QDs (LD_{50} is more than one thousand times that of QDs).⁸⁰ Nevertheless, the physical and chemical properties of entire nanoparticles may cause adverse effects in biological systems. The behavior of UCNPs in biological environments is difficult to predict, depending on

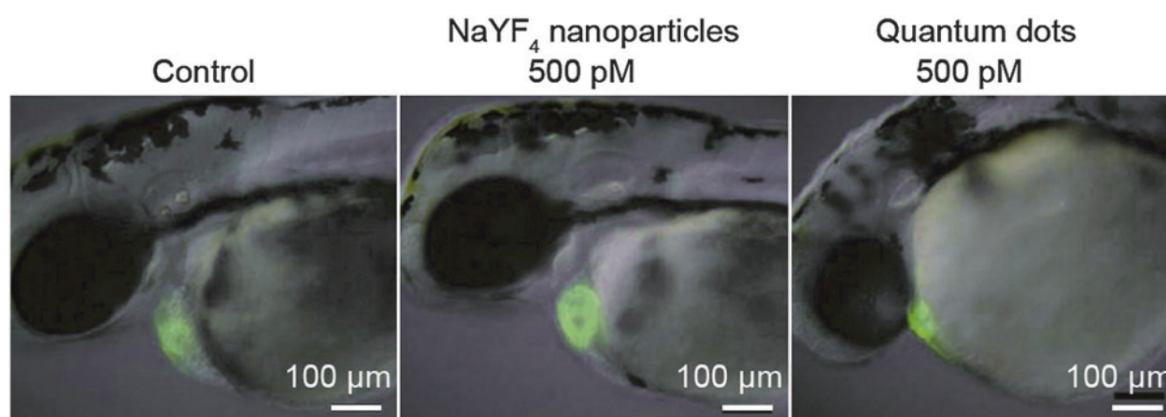


Figure 1.11: Heart function of zebrafish after treatment with upconversion nanoparticles versus quantum dots to visualize toxicity differences. The zebrafish are modified to express GFP in the heart. The hearts of the control and zebrafish treated with NaYF₄ nanoparticles show little difference. The heart of the zebrafish treated with QDs is noticeably smaller and abnormally shaped. Reproduced from Sun et al. with permission from The Royal Society of Chemistry.¹⁶⁸ Original figure from Jang et al., Copyright 2014, with permission from Elsevier.¹⁶⁹

their chemical composition, surface characteristics (e.g. charge, functionality), physical parameters (e.g. size, shape), etc.¹⁶⁵

Even the form which the surface coating is in affects its interaction with organisms. Freestanding PEI is toxic to cells, but it exhibits low toxicity in particulate form.¹⁶⁶ Jin et al. measured the viability of HeLa cells after treating with NaYF₄:Yb/Er-PEI, and at a concentration of 0.25 mg/mL, which is five-fold that used in live-cell imaging, there was no evidence of cytotoxicity.⁸¹ Another MTT assay in HeLa cells but with BaGdF₅:Yb,Er-PEI demonstrated that cell viability remains greater than 95% at a concentration of 1 mg/mL.¹⁶⁷

Jang et al. carried out toxicity assessments of hydrophilic UCNPs in zebrafish (Figure 1.11). When zebrafish were treated with 500 pM of β -NaYF₄:Ce,Tb nanoparticles, the morphology of their hearts were similar to that of the zebrafish in the control group. In comparison, zebrafish that were treated with the same concentration of QDs had hearts that were smaller and without loops. This indicated that QDs delayed development of the heart in embryos.^{168,169}

The results from toxicity studies in murine models vary slightly. One study concluded that silica-coated UCNPs are mostly cleared by seven days after injection in rats.¹⁷⁰ Another study showed that PAA-UCNPs took up to 115 days to be excreted from mice. Within that time frame, UCNPs were imaged in the liver and spleen. The different retention times between the two studies are likely caused by the differences in dosage, size, aggregation, surface coating, and animal type. Nonetheless, even in the second study with longer retention

time, the mice did not experience any adverse effects to their health, and the authors concluded that the upconversion nanophosphors could be used for long-term targeted imaging and therapy studies *in vivo*.¹⁷¹ Recently, Yu et al. studied the biodistribution, excretion, and toxicity of PEI-modified UCNPs in mice using different administration routes (intravenous, intraperitoneal, and intragastric). They found that this surface modification is quite promising for bioprobes due to the particles' low toxicity, minimal accumulation in the liver and spleen, and obvious excretion from the body through feces after intravenous injection.¹⁷²

Most other studies in addition to the ones described above indicate that the UCNPs have little to no toxicity.¹⁷³ However, there is still no guarantee that UCNPs are without health risks when used for biomedical applications. There are currently no reports on long-term toxicity (i.e. several animal generations) nor studies done to observe secondary toxicity effects from UCNP decomposition products.¹⁶⁵ Further studies are necessary to gain a complete picture of the nanotoxicology of UCNPs. Until this is established, the commercial applications of UCNPs may be limited in spite of their advantages compared to traditional approaches.

1.4 Aims and objectives

This thesis aimed to develop and characterize UCNP-based ratiometric probes for sensing and imaging of pH in buffer solutions and cells. So far, studies on UCNPs and pH-sensitive dye combinations focused on their potential use in these media, but the interaction between UCNPs and different pH indicator dyes still requires further review. Here, the pH-dependent effect of CaR and ARS on UCNPs was investigated. Anthraquinones are quite established and well-characterized in the literature, including a prior study in the Cambridge Analytical Biotechnology group that coupled them with QDs,²³ so they were chosen here as model UCNP coupling partners. CaR and ARS are interesting since they are anthraquinones with absorption bands that have strong overlap with the green emission of NaYF₄:Yb, Er particles. After thorough understanding of the sensing mechanisms that govern UCNP-dye combinations, UCNPs were conjugated to a recently commercialized pH sensor dye called pHAb that has strong fluorescence and high enough signal-to-background ratio to be used for confocal microscopy and live cell imaging.¹⁷⁴ The performance of UCNP-pHAb nanoprobe in measuring pH inside SH-SY5Y cells was compared to previously reported ratiometric intracellular pH imaging probes. Colocalization analysis and endocytosis pathway studies were then performed to determine the subcellular location of UCNP-pHAb and deduce the mechanism by which the nanosensor is taken up by the cells. Finally, cytotoxicity studies were conducted to confirm the biocompatibility of the nanosensors.

The following goals were defined to achieve the project:

1. Fabricate and characterize UCNPs using different synthesis methods to identify the one that produces the highest quality UCNPs for biosensing applications (β -phase, monodisperse, uniform shape, <100 nm) while remaining highly reproducible
2. Select shell addition and surface modification strategies that match the pH sensitive dyes and sensing mechanism (inner filter effect, resonance energy transfer)
3. Investigate the interaction mechanism (inner filter effect, resonance energy transfer) between UCNPs and different anthraquinone indicators (CaR, ARS)
4. Measure the pH-dependent effect of the anthraquinones on the UCNPs
5. Evaluate the in vitro performance of UCNP-pHAb for intracellular pH measurements
6. Determine the subcellular localization and endocytosis pathway of UCNP-pHAb in SH-SY5Y cells
7. Assess the cytotoxicity of UCNP-pHAb in SH-SY5Y cells

Chapter 2

Rational design of upconversion nanoparticles for sensing

2.1 Introduction

For bioanalytical applications, UCNPs have to fulfill several conditions that can be accomplished through different synthetic strategies and post-synthetic treatments. One requirement is water dispersibility, so if the chosen synthetic strategy yields hydrophobic UCNPs, hydrophilic ligands have to be introduced. Another requirement is colloidal stability, so it is essential to synthesize nanoparticles that are monodisperse and non-agglomerated. To achieve high signal-to-noise ratio, the UCNPs have to be highly luminescent, which demands pure, hexagonal phase crystals.⁷⁶ The shape and surface chemistry of nanoparticles also affect their interaction with cellular membranes and the resulting uptake efficiency.^{175,176} Depending on whether the sensing scheme relies on inner filter effects or FRET, surface modifications that use a ligand exchange method, add an amphiphilic layer, or coat a layer of silica may be better suited for one application over another.⁷⁶ In particular, shell sizes play a role in FRET efficiency by increasing or decreasing the distance between the lanthanide ion and nearby acceptor molecules.¹⁴⁵

There are various nanochemistry approaches to synthesize lanthanide-doped luminescence nanoparticles that each have their own challenges. The phase and size of UCNPs are difficult to adjust by the solvothermal/hydrothermal route because the PTFE reaction vessels make it impossible to observe the nanocrystal growth during the course of the synthesis.^{177,178} The reaction times can take up to several days, so optimizing the reaction parameters is incredibly time-consuming.¹⁷⁸ Some research groups reported success in synthesizing hexagonal UCNPs,¹¹² while others were only able to synthesize cubic ones.¹⁷⁹

For thermal decomposition, there are a large number of variables that control UCNP morphology, phase, and size and thus make reproducible syntheses exceptionally challenging. These parameters include temperature, reaction time, lanthanide precursor composition, ligand selection, heating rate, cooling rate, and solvent volume ratios.^{180,181} In another study, Yan et al. reported that at the elevated temperatures required for thermal decomposition, the ligand-metal association weakens and can result in polydisperse particles that are irregularly shaped.¹⁸²

These examples highlight a major hurdle that UCNPs face in their road to commercialization. In a recent perspective, Wilhelm emphasized that the next decade of research on this nanomaterial has to evolve from the academic setting into real world applications for it to reach its full translational potential.¹³⁸ A key part of reaching this goal is standardizing protocols and instruments to enable direct comparison of results from different research groups. In order for UCNPs to be used commercially for diagnostics, for instance, every batch of UCNPs made from large scale manufacturing would have to be consistent in size, phase, shape, and coating coverage. It would be impractical to require clinicians to recalibrate an upconverting nanosensor every time it was used in a healthcare setting. A comparative study on UCNPs synthesized from different methods was performed to identify the best one in terms of reproducibility and characteristics for bioanalytical sensing. Surface modification was also performed when the synthesis method yielded hydrophobic materials to enable water dispersibility, which is needed in bioimaging and bioassays.¹⁸³

The coatings discussed in this chapter were selected for the applications described in Chapters 3 and 4. In Chapter 3, where UCNPs are mixed with anthraquinone dyes as pH sensors in buffer solutions, the formation of an additional layer on the surface of the UCNP using amphiphilic reagents was selected because this method results in particles that are highly stable in aqueous solutions. The fact that the thickness of the outer layer increases from ligand addition was not an issue for this application.¹⁸³ The anthraquinone dyes were also attached to the UCNPs through electrostatic attraction. For this type of sensing strategy that may rely on resonance energy transfer, the thickness of the coating must be minimized. In this case, two-step methods relying on complete ligand exchange were ideal because this process attaches new ligands without drastically enlarging the size of the particle.¹⁸³ Chapter 4 relies on a pH-sensitive dye called pHAb that increases in fluorescence as the surrounding environment becomes more acidic. The pHAb has to be conjugated to the UCNP to enable quantitative sensing in cells by way of multiphoton confocal microscopy. pHAb is an amine reactive dye so PEI was an ideal choice for the hydrophilic surface coating of the UCNP due to the presence of primary amines for reaction with the succinimidyl ester group of the dye.¹⁸⁴ PEI also performs well as a coating in cellular imaging applications

because its positive charge enables the particle to traverse the cell membrane without the addition of other molecules to stimulate endocytosis.⁸¹

2.2 Materials and methods

2.2.1 Materials

Sodium chloride (99+%) was obtained from Acros. Ytterbium (III) nitrate pentahydrate (99.9%) was from Aldrich. Yttrium (III) nitrate hexahydrate (99.9%), erbium (III) nitrate pentahydrate (99.9%), ytterbium (III) oxide (99.9%), erbium (III) oxide (99.99%), gadolinium (III) oxide (99.99%), lutetium (III) oxide (99.99%), yttrium (III) oxide (99.99%), sodium fluoride (99.99%), sodium trifluoroacetate (98%), ethylene glycol (99%), and trifluoroacetic acid (99%) were from Alfa. Ethylenediaminetetracetic acid disodium salt dihydrate (ACS reagent, 99.0-101.0%) and ammonium fluoride (ACS reagent, >98.0%) were purchased from Sigma.

Yttrium chloride hexahydrate and ytterbium chloride hexahydrate (both >99.9%) were purchased from Treibacher Industrie AG. Oleic acid and 1-octadecene (both 90%) were obtained from Alfa Aesar. Ammonium fluoride, erbium chloride hexahydrate (99.99%), sodium hydroxide, poly(isobutylene-*alt*-maleic anhydride) (PMA) (average M_w ~6 kDa), dodecylamine (98%), polyethylenimine (PEI) (average M_w ~25 kDa), 4-amino-1,3-dihydroxy-anthraquinone-2-sulfonic acid (calcium red) (CaR), nitrosyl tetrafluoroborate NOBF_4 (95%), citric acid monohydrate, disodium phosphate heptahydrate, and 3,4-dihydroxy-anthraquinone-2-sulfonic acid (alizerin red S) (ARS) were purchased from Sigma-Aldrich. All other chemicals were purchased from Sigma-Aldrich, Merck, or Acros.

2.2.2 Solvothermal synthesis

The synthesis of PEI-modified NaYF_4 : 20% Yb^{3+} , 2% Er^{3+} particles was developed via a modified literature procedure.^{113,185} 2.5 mmol NaCl, 0.4 g PEI, 0.78 mmol $\text{Y}(\text{NO}_3)_3 \cdot 6\text{H}_2\text{O}$, 0.2 mmol $\text{Yb}(\text{NO}_3)_3 \cdot 5\text{H}_2\text{O}$, and 0.02 mmol $\text{Er}(\text{NO}_3)_3 \cdot 5\text{H}_2\text{O}$ were dissolved in ethylene glycol (15 mL) under vigorous stirring with a magnetic stir bar. After the solution became transparent, NH_4F (4 mmol) in ethylene glycol (10 mL) was dropwise added to the solution under vigorous stirring with a magnetic stir bar. After stirring for another 10 min, the whole mixture was transferred into a 45 mL Teflon-lined stainless steel autoclave. The autoclave was sealed and heated under 200 °C for 24 h. After the autoclave cooled down to room temperature naturally, the NaYF_4 : Yb, Er UCNPs were collected by centrifugation and washed with deionized water and ethanol three times.

2.2.3 Thermal decomposition

The synthesis of lanthanide trifluoroacetates was modified from previously reported protocols.^{119,186} 71.6 mg of Lu₂O₃ (0.18 mmol), 98.5 mg of Yb₂O₃ (0.25 mmol), 3.83 mg of Er₂O₃ (0.01 mmol), and 21.7 mg of Gd₂O₃ (0.06 mmol) were added to 10 mL of 50% aqueous trifluoroacetic acid in a round-bottom flask, and the mixture was refluxed at 80 °C until it became clear. The solution was then removed from reflux, and the residual water and acid were slowly evaporated at 60 °C until completely dry. The setup was then cooled to room temperature.

The thermal decomposition method was adapted from previously described procedures.^{117,187} To the reaction flask of Lu(CF₃COO)₃, Yb(CF₃COO)₃, Er(CF₃COO)₃, and Gd(CF₃COO)₃ at room temperature were added given amounts of NaCF₃COO (2.0 mmol, 0.2720 g), 8.47 g oleic acid (90%, 30 mmol), and 8.42 g 1-octadecene (90%, 30 mmol). The mixture was heated to 140 °C under vacuum and maintained for several hours under vigorous stirring to completely remove water and oxygen from the flask. The pellucid solution was heated to 320 °C or 340 °C under nitrogen protection and maintained at this temperature for 1.5 h. After cooling to room temperature, the produced nanoparticles were washed with 50 mL ethanol and cyclohexane (1:1 v/v) three times, collected by centrifugation, and then dispersed in chloroform.

2.2.4 Low-temperature coprecipitation

The low-temperature coprecipitation method was modified from one described by Yi et al.¹²² Rare earth nitrate stock solutions of 0.2 M were prepared by mixing 0.766 g of Y(NO₃)₃·6H₂O in 10 mL deionized water, 0.180 g of Yb(NO₃)₃·5H₂O in 2 mL deionized water, and 0.044 g Er(NO₃)₃·5H₂O in 0.5 mL deionized water. The final solutions were adjusted to pH 2 with hydrochloric acid to avoid hydrolysis. A stock solution of 0.2 M EDTA was prepared by dissolving 0.744 g EDTA in 10 mL deionized water.

0.21 g of NaF was dissolved in 6 mL of deionized water. Another solution was prepared by mixing together 1.6 mL of 0.2 M Y(NO₃)₃, 0.34 mL of 0.2 M Yb(NO₃)₃, 0.06 mL of 0.2 M Er(NO₃)₃, and 2 mL of 0.2 M EDTA stock solutions to form the metal-EDTA complex. The complex solution was injected into the NaF solution quickly using a needle and syringe, and the mixture was stirred for 1 h at room temperature. Precipitates from the reaction were centrifuged, washed three times using deionized water, and washed once with ethanol. The precipitates were then dried under vacuum, and a white powder was obtained.

The nanoparticles were then annealed under a nitrogen atmosphere by heating them to 400 °C at a rate of 7 °C per min, and this temperature was maintained for 30 min or 5 h. The

particles were then naturally cooled down to room temperature under the same atmospheric environment.

2.2.5 High-temperature coprecipitation

This high-temperature coprecipitation method was based on a procedure by Li and Zhang and optimized by Wilhelm et al.^{76,120} Oleate-capped NaYF₄: 20% Yb, 2% Er@NaYF₄ nanocrystals were synthesized. The molar doping ratio of 20% Yb and 2% Er was selected due to its well-established usage in literature.^{119,188} To synthesize core-shell UCNPs, the core material (β -NaYF₄: Yb, Er particles) and shell precursor (α -NaYF₄) were synthesized separately. An additional reaction step added the shell precursor to the core material to produce core-shell particles.

The following describes the synthesis of 1 mmol of β -NaYF₄: 20% Yb, 2% Er particles, but the protocol can be scaled up to 20 mmol batches. The corresponding molar ratios of the lanthanide chloride hexahydrates were dissolved in 5 mL of methanol and transferred into a three-neck round bottom flask. Oleic acid (8 mL) and 1-octadecene (15 mL) were added under nitrogen flow. The mixture was heated to 160 °C then a vacuum was applied for 30 min, after which a clear solution formed. After the solution was cooled to room temperature, ammonium fluoride (4.0 mmol) and sodium hydroxide (2.5 mmol) were dissolved in methanol and added to the flask. The solution was maintained at 120 °C for 30 min then heated to 325 °C. A 980 nm cw laser module (200 mW, 130 W cm⁻²) was used to monitor the reaction progress. The reaction was maintained for an additional 8 minutes after upconversion luminescence could be observed by the naked eye. The reaction mixture was cooled to room temperature using a heating gun. The particles were precipitated by adding ethanol and collecting by centrifugation at 1,000 g for 5 min. The precipitate was washed twice with chloroform/ethanol (1:10 v/v) and three times with cyclohexane/ethanol (1:10 v/v) by repeated redispersion-precipitation-centrifugation cycles. The particles were dispersed in cyclohexane (10 mL), centrifuged at 1,000 g for 3 min to remove remaining aggregates, and the clear supernatant was collected.

The synthesis procedure for α -NaYF₄ was identical to that for β -NaYF₄: Yb, Er (described above), except for the last heating step. Here, the mixture was heated to 240 °C for 30 min. The core material (β -NaYF₄: Yb, Er particles) and shell precursor (α -NaYF₄ particles) dispersed in cyclohexane were transferred into separate three-neck round bottom flasks under nitrogen flow. Oleic acid (5 mL) and 1-octadecene (5 mL) were added. Both flasks were heated to 100 °C, and a vacuum was applied for 30 min to remove the cyclohexane. Next, the hexagonal particles were heated to 325 °C and the cubic particles were kept at 100 °C under nitrogen flow. Small volumes (<3 mL) of the shell precursor were injected into the

other flask every 10 min, making sure to prevent the temperature dropping below 300 °C. The suspension was cooled to room temperature using a heating gun 10 min after the last injection. The same redispersion-precipitation-centrifugation steps as described above were performed to precipitate and purify the core-shell nanoparticles.

2.2.6 Surface modification for uncapped UCNPs

Hydrophobic, oleate-coated upconversion nanoparticles were rendered water dispersible by a two-step ligand exchange. In the first step, the oleic acid was removed via NOBF_4 . Thereafter, the nanoparticles were dispersed in a two-phase system (equivalent volumes of cyclohexane and DMF), NOBF_4 (1 mg per 1 mg UCNPs) was added, and the mixture was stirred vigorously for 20 min at 30 °C.

Afterwards, the nanoparticles were transferred from the cyclohexane phase to the DMF phase, whereas the free oleic acid stayed in the cyclohexane phase. The cyclohexane phase was rejected, and the BF_4^- stabilized particles were precipitated with an excess of chloroform and separated by centrifugation (1000 g, 5 min). The resulting gel-like pellet was redispersed in DMF and washed one time with chloroform/DMF. Finally, the pellet was dispersed in the desired volume of DMF and centrifuged (1000 g, 3 min) to remove aggregates. The supernatant was collected and stored in the dark at 4 °C.

2.2.7 Surface modification with PEI

100 mg PEI (high molecular weight) was dissolved in 8 mL double distilled water and heated up to 50 °C under magnetic stirring. 40 mg of the uncapped UCNPs dispersed in 2 mL DMF were added dropwise. The dispersion was heated to 80 °C and stirred for 90 min under reflux. The particles were centrifuged at 21,000 g, washed with double distilled water, and redispersed by sonication. The washing step was repeated three times. The particles were filtered with a 220 nm PES filter. The concentration of the particles was determined by ICP-OES.

2.2.8 Surface modification with PMA

Poly(isobutylene-*alt*-maleic anhydride) (M_w 6000) was modified with dodecylamine side chains as reported in the literature.¹⁸⁹ 75 mg of the oleate-capped, core-shell nanoparticles were dispersed in 2 mL chloroform and 560 μL of the polymer solution (cM = 0.5 M) was added. The dispersion was stirred for 30 min for room temperature. Chloroform was removed with a rotary evaporator. The particles were dispersed in 15 mL NaOH solution

(0.2 M), assisted by sonication. Afterwards, they were centrifuged at 21,000 *g*, washed with double distilled water, and redispersed by sonication again. This washing step was repeated three times. The particles were filtered with a 220 nm PES filter. The concentration of the particles was determined by ICP-OES.

2.2.9 Photoluminescence spectroscopy

The UCNPs were excited at 980 nm with a Spectra-Physics Mai Tai Ti:Sapphire NIR/IR laser (Newport). The laser power was set to 500 mW. The emission spectra were measured with a USB spectrometer (Ocean Optics). A 750 nm shortpass filter (Thorlabs) was used to protect the spectrometer from being flooded with light from the laser. The UCNP samples were diluted to a concentration of 1 wt% in cyclohexane in a UV fused quartz cuvette (Thorlabs). Analyses of the spectra were performed with PlotDigitizer (SourceForge). The UCNPs were also excited with the tunable setting of the laser from 900-1020 nm using a step size of 1 nm. The heat map showing emission intensity as a function of excitation was created with Igor Pro software (WaveMetrics).

Luminescence spectra were also obtained with an AMINCO-Bowman Series 2 luminescence spectrometer (formerly from Thermo Fisher) in which an external cw 980 nm laser module (focusable, power ranging from 200 mW) (Picotronic) was installed. All spectra were recorded at room temperature.

2.2.10 X-ray diffraction

Powder XRD patterns were collected on a Bruker D8 diffractometer at a scanning rate of 1.5°/min in the 2θ range from 10 to 80° (Cu $K\alpha$ radiation, $\lambda = 1.5406 \text{ \AA}$) or a STADI P diffractometer (STOE) equipped with a Mythen 1K detector (Dectris) with a resolution of 0.005° (2θ) and a monochromatized Cu $K\alpha 1$ radiation ($\lambda = 1.54056 \text{ \AA}$).

2.2.11 Transmission electron microscopy

Images of the UCNPs were taken with a Tecnai G2 80-200 kV TEM (FEI) set at 200 kV or 120 kV Philips CM12 transmission electron microscope (FEI). The sizes were calculated from TEM images by measuring and averaging the diameters of particles with ImageJ software (National Institutes of Health). The exception was the hexagonal NaLuF₄ particles, whose images were taken with a Tecnai 20 TEM (FEI). The microscope was also set at 200 kV. The size of these particles was calculated from TEM images by measuring and averaging the diameters of 50 particles with ImageJ software, version 1.50i (National Institutes of Health).

Health). In all cases, samples were prepared by placing a drop of cyclohexane solution with UCNPs on the surface of a copper grid. Energy-dispersive X-ray (EDX) analysis and EDX elemental map of the hexagonal NaLuF₄ particles were also performed during the TEM measurements with the Tecnai 20.

2.2.12 Scanning electron microscopy

Images of the hexagonal NaLuF₄ particles were taken with a Verios 460L (FEI). The sample was prepared by placing a drop of cyclohexane solution with UCNPs on the surface of 400 mesh holey carbon support films (EM Resolutions). The thickness of these particles was calculated from SEM images by measuring and averaging the thicknesses of 20 particles with ImageJ software (National Institutes of Health).

2.2.13 Zeta, DLS, and ICP measurements

Dynamic light scattering and ζ -potential measurements were performed with a Zetasizer Nano ZS (Malvern) at a constant temperature of 20 °C. Samples and standards (Y³⁺, Er³⁺, Yb³⁺) of known volume were analyzed with an inductively coupled plasma optical emission spectrometer (ICP-OES) (Spectro) to determine the rare-earth ion content of the UCNPs and concentration of the UCNPs in solution. Electrons take up high energy from the plasma, and light is emitted when the electrons drop back down to ground level. Each element has a distinct emission spectrum. The intensity can be measured and, with the calibration, used to calculate the composition (%) then concentration (mmol/L) of ions in solution. The concentration of UCNPs in solution can then be calculated from the concentration of ions and molar mass of the UCNPs.

2.3 Results and discussion

2.3.1 UCNPs from solvothermal synthesis

Water-soluble, PEI-coated UCNPs were first synthesized using the solvothermal method due to its one-pot technique that requires only one preparatory step. In other words, this synthesis method is simpler compared to the others because a separate surface modification step is not needed. The solvothermal technique requires lower temperatures than other synthetic methods like thermal decomposition because it depends on a sealed autoclave that prompts crystallization by bringing the solvent to temperatures and pressures above the critical point.^{112,180}

The luminescence spectrum of the UCNPs produced with this method is shown in Figure 2.1a. The emission bands were not sharp, and on top of this, the emission was not visible to the naked eye, unlike those of UCNPs reported in the literature.^{117,142,188,190,191} Further investigation by XRD (Figure 2.1b) revealed that the particles were purely in the cubic phase, which has significantly lower upconversion efficiency than β -UCNPs. See Appendix A for additional information on XRD. In fact, it has been found that the green emission of β -NaYF₄: Yb, Er is 10 times stronger than that of its α -phase counterpart.⁹⁷ Moreover, the bimodal size distribution from the DLS measurement revealed the presence of aggregates (Figure 2.1c). Aggregates of nanoparticles show up as a second peak because they are several times the size of the individual particles.¹⁹² The first peak indicates one group of particles that avoided agglomeration, but the second peak suggests a second group that formed clusters several hundred nanometers in size. Chen et al. also reported water-soluble UCNPs with broad size distribution and poor shape from one-pot synthesis.¹¹⁵

The mixture was reacted for 24 h at 200 °C, yet the phase of the resulting UCNPs was still the same as that of the UCNPs produced from autoclaving for 2 h by Cong et al.¹⁷⁹ Shang et al. reported that the phase transformation process ($\alpha \rightarrow \beta$) occurs gradually when reaction time goes from 3 h (mixture of cubic and hexagonal phase) to 24 h (pure hexagonal phase),¹⁹³ but that was not observed here. Furthermore, the ratio of F⁻/Ln³⁺, which has been shown to be an important factor in obtaining uniform nanocrystals,¹⁹⁴ was kept the same as that used in solvothermal procedures that had produced monodisperse particles,^{113,185} but polydisperse UCNPs were still produced here. Even if hexagonal particles had been produced, they likely would have been bigger size microcrystals.¹⁹³ From these results, it appears that UCNPs synthesized under a solvothermal condition may have issues of reproducibility that are important to consider for adoption outside the research environment. It is concluded that another synthesis method is preferable to produce UCNPs that meet the size and phase criteria for applications in pH sensing.

2.3.2 UCNPs from thermal decomposition

UCNPs were next synthesized using thermal decomposition, which produces hydrophobic particles capped with OA. With this method, Liu et al. fabricated sub-10 nm β -NaLuF₄ nanocrystals with Gd³⁺ doping for inducing phase transition and reducing average crystallite size. They found that their nanocrystals outperformed β -NaYF₄ nanocrystals on emission intensity at the same concentration in cyclohexane.¹¹⁷ Thus, NaLuF₄ was chosen as the host material here due to its superior upconversion efficiency.

The upconversion luminescence spectrum of the synthesized NaLuF₄: 12% Gd, 50% Yb, 2% Er nanocrystals is shown in Figure 2.2a. They displayed the characteristic green

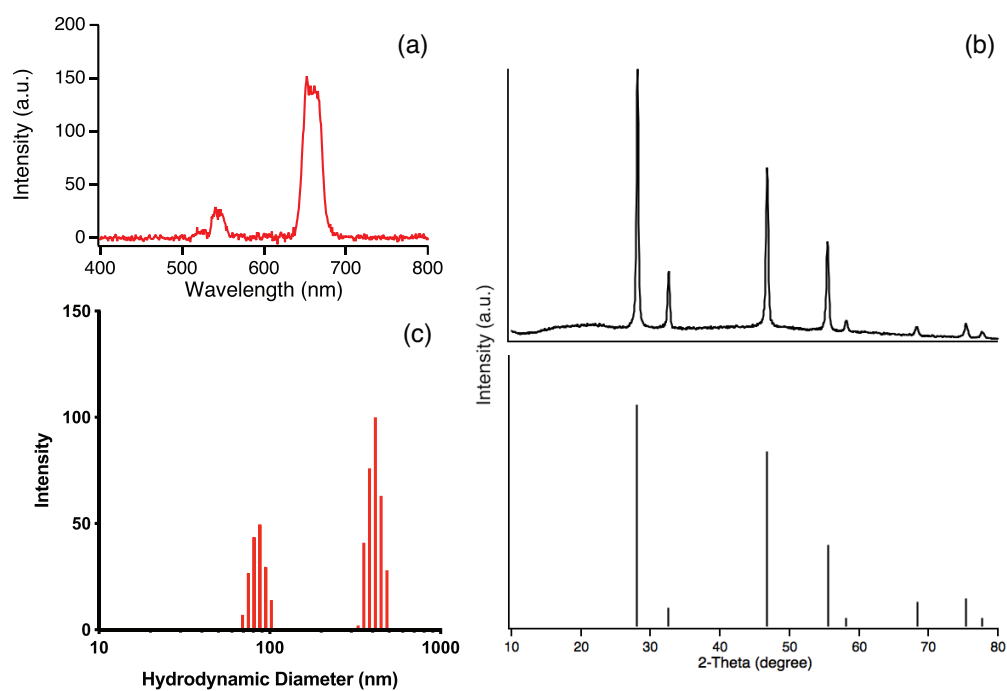


Figure 2.1: (a) Luminescence spectrum of PEI-coated UCNPs synthesized via solvothermal synthesis. The 1 wt% colloidal solution in water was excited by a 980 nm laser. (b) Experimental powder XRD data from solvothermal synthesis (upper part) and standard XRD pattern (lower part) for α -NaYF₄. The calculated line pattern for the α -NaYF₄ structure was taken from Heer et al.¹⁹⁵ (c) Intensity-weighted histogram of particle diameters obtained from DLS.

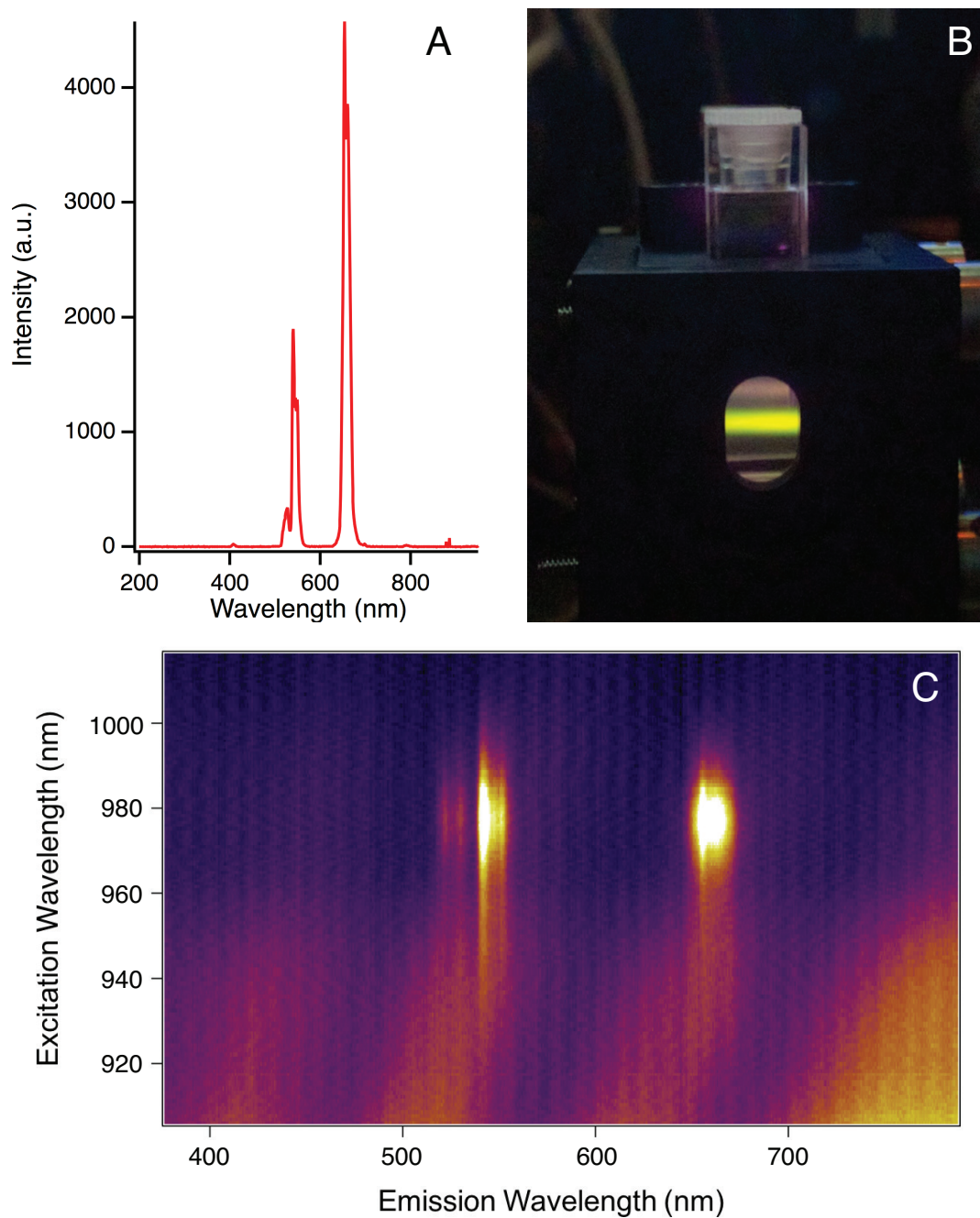


Figure 2.2: (a) shows the luminescence spectrum of OA-coated UCNPs synthesized via thermal decomposition. The 1 wt% colloidal solution in cyclohexane was excited by a 980 nm laser. (b) shows that the luminescence intensity of the nanoparticles is strong enough to be seen by the naked eye. (c) shows a heat map of α -NaLuF₄ nanoparticles synthesized via thermal decomposition at 320 °C. The purple to yellow gradient represents low to high emission intensity.

and red emission bands corresponding to the transitions from the emitting energy levels of the Er^{3+} ions.¹⁸⁷ Unlike the particles described in Section 2.3.1, the particles here had sharply defined luminescence emission bands. The green emissions at 514-534 and 534-560 nm result from the ${}^2\text{H}_{11/2}$ and ${}^4\text{S}_{3/2}$ to ${}^4\text{I}_{15/2}$ transitions, respectively, and the red emission at 635-680 nm originates from the ${}^4\text{F}_{9/2}$ to ${}^4\text{I}_{15/2}$ transition (Figure 1.8). The luminescence appears yellow in color to the naked eye due to the combination of green and red emissions (Figure 2.2b). The λ_{max} of the green peak was 540 nm, while the λ_{max} of the red peak was 650 nm. The Gd^{3+} ions do not participate in the energy transfer mechanisms but were introduced to help reduce the average crystallite size.¹¹⁷

A heat map was also produced to verify that 980 nm is the optimal excitation wavelength for UCNPs. In order to determine the excitation wavelength that results in the best upconversion efficiency, the laser was scanned in the 900-1020 nm NIR range while the upconversion emission was simultaneously captured. Figure 2.2c confirms that the most intense green and red emissions result when the UCNPs are excited at wavelengths near 980 nm, which supports the excitation wavelength used in the vast majority of previous publications on UCNPs.^{91,115,118,135} The upconversion efficiency dropped off significantly below 972 nm or above 983 nm, indicating that excitation wavelength should be kept within this narrow range. The heat map also suggests that exciting UCNPs at lower wavelength (e.g. 920 nm) results in blueshift. The emission in the bottom right corner of Figure 2.2c resulted from laser leakage through the shortpass filter.

Figure 2.3 shows a TEM image of the UCNPs. The particles showed some polydispersity in shape and size, which can be explained by imperfect crystal growth during synthesis. They exhibited approximately spherical morphology with an average diameter of 30 nm (calculated from TEM images). The diameter distribution ranged from 15 to 45 nm. At 37 ± 6 nm, the effective diameter measured using DLS was slightly larger than the average diameter calculated from TEM. This was expected because DLS calculations account for the coating material (i.e. OA) and solvent layer, while TEM measurements capture only the inorganic core.¹⁹⁶

The sharp diffraction peaks of the experimental XRD pattern (Figure 2.4a) demonstrate the nanoparticles' crystallinity. However, the Gd^{3+} doping did not appear to induce phase transition as intended. The XRD pattern indicates that thermal decomposition at 320 °C resulted in cubic-phase nanocrystals since their peak positions and intensities correlate very well with the ones calculated for the cubic NaLuF_4 phase in the literature (JCPDS no. 27-0725).¹⁹⁸ The α - NaLuF_4 particles formed because as physical dimensions reduce, the resulting higher surface tension favors isotropic particles (i.e. 0D structures, spherical nanoparticles, nanopolyhedra).¹⁹⁹

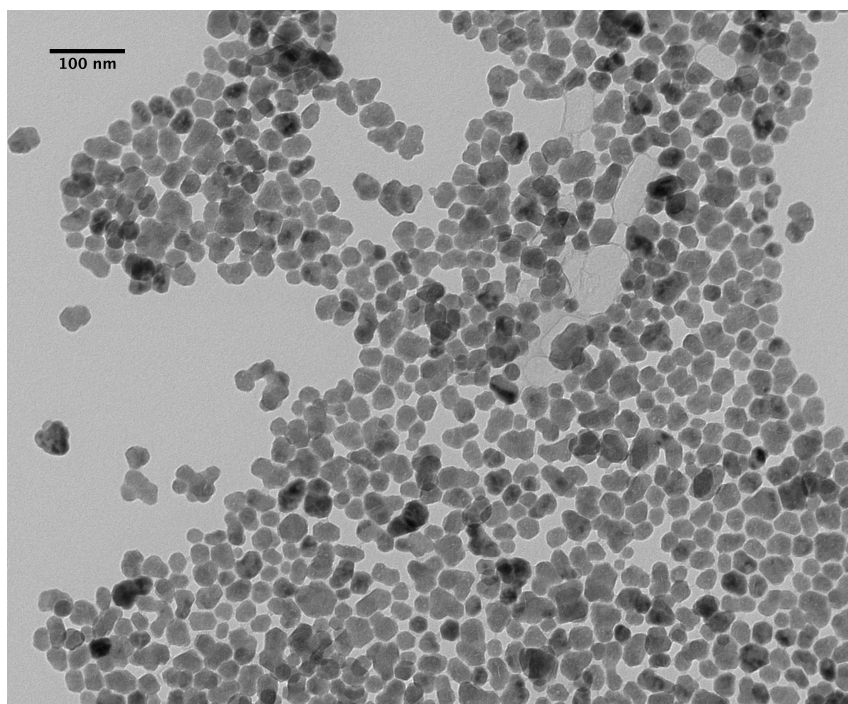


Figure 2.3: TEM image of UCNPs synthesized via thermal decomposition at 320 °C.

Drastic conditions such as high reaction temperature (>330 °C) can encourage the pure hexagonal form of NaLuF_4 to materialize.²⁰⁰ Thus, when the temperature of the reaction was increased to 340 °C, there was a transition to hexagonal-phase nanocrystals (Figure 2.4b); the peak positions and intensities from the experimental XRD pattern agree well with the standard spectrum for hexagonal NaLuF_4 (JCPDS no. 27-0726).¹⁸⁷ No diffraction peaks corresponding to α -phase compounds or other impurities were observed, indicating the success in the synthesis of pure hexagonal-phase NaLuF_4 nanocrystals.

These nanocrystals were much larger in size than the UCNPs synthesized at 20 °C lower temperature. Figure 2.5 presents a representative TEM image and SEM image of the as-prepared β - NaLuF_4 particles. They were hexagonal prisms with a mean diameter of 690 ± 160 nm (calculated from TEM images) and mean height of 120 ± 10 nm (calculated from SEM images). The size of these β -phase particles was not measured using DLS because the characterization of plate-shaped nanoparticles with this method is difficult due to high spatial asymmetry.²⁰¹ The hydrodynamic size calculated with DLS is the diameter of a hypothetical hard sphere that diffuses comparably to the particle of interest, so the number would not be representative of the β - NaLuF_4 particles here.

The four axes of the hexagonal structure consist of three assistant axes crossing each other at 60° angles (all three parallel to both hexagonal faces) and a principle one that is perpendicular to the hexagonal faces. The morphology of the final crystal depends on the

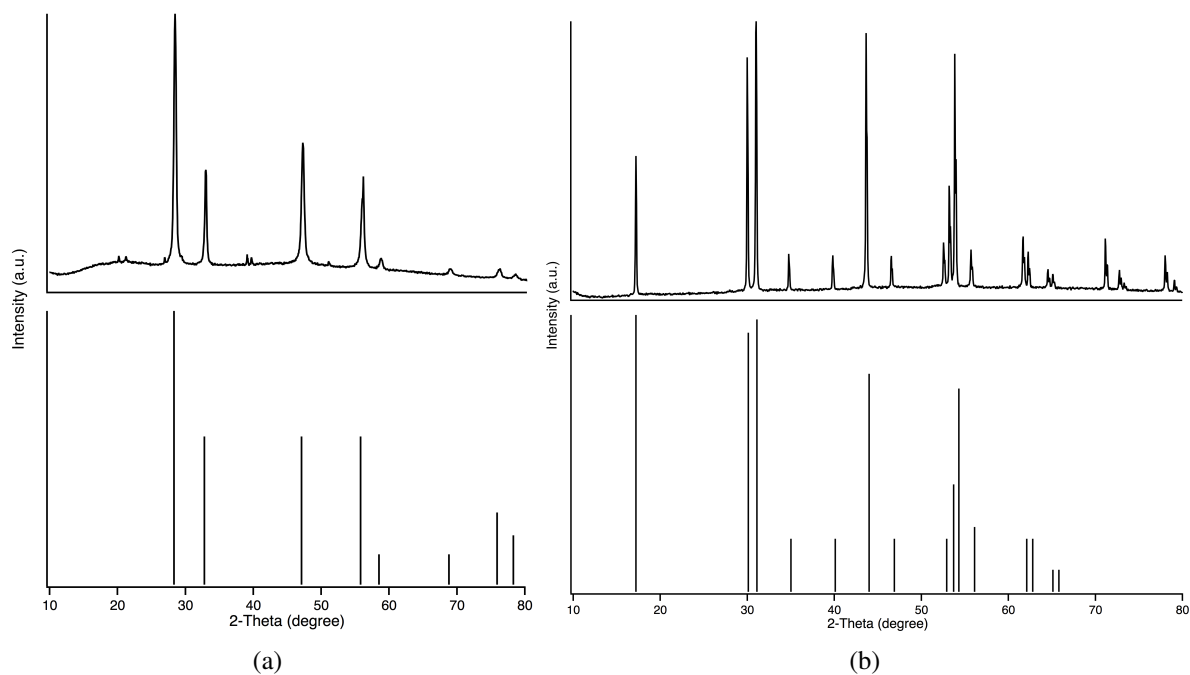


Figure 2.4: (a) shows the experimental powder XRD data from thermal decomposition at 320 °C (upper part) and standard XRD pattern (lower part) for α -NaLuF₄. The calculated line pattern for the α -NaLuF₄ structure was taken from Zhu et al.¹⁹⁷ (b) shows the experimental powder XRD data from thermal decomposition at 340 °C (upper part) and standard XRD pattern (lower part) for β -NaLuF₄. The calculated line pattern for the β -NaLuF₄ structure was taken from Zhu et al.¹⁹⁷

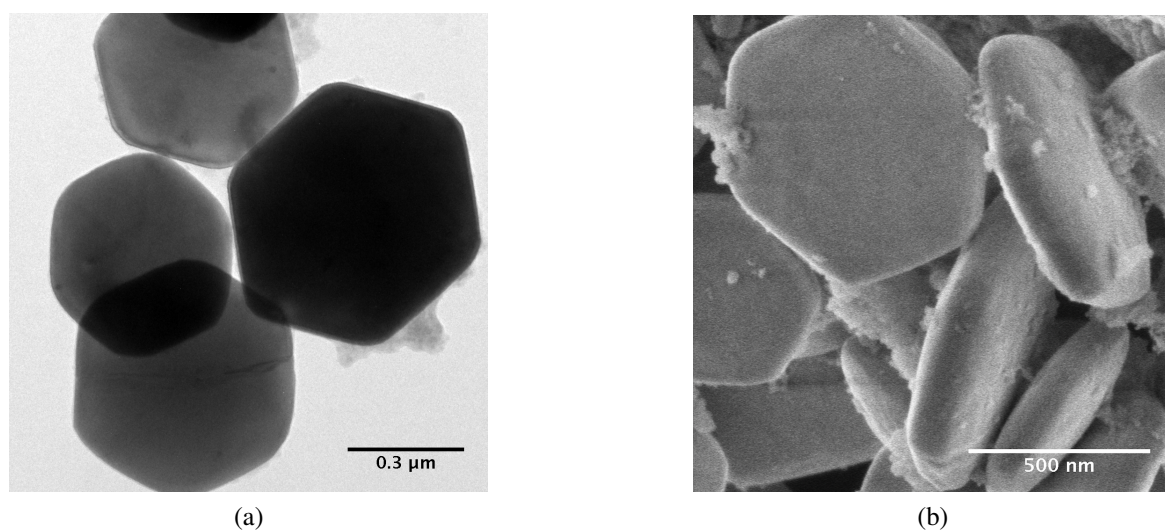


Figure 2.5: (a) shows a TEM image and (b) shows an SEM image of UCNPs synthesized via thermal decomposition at 340 °C.

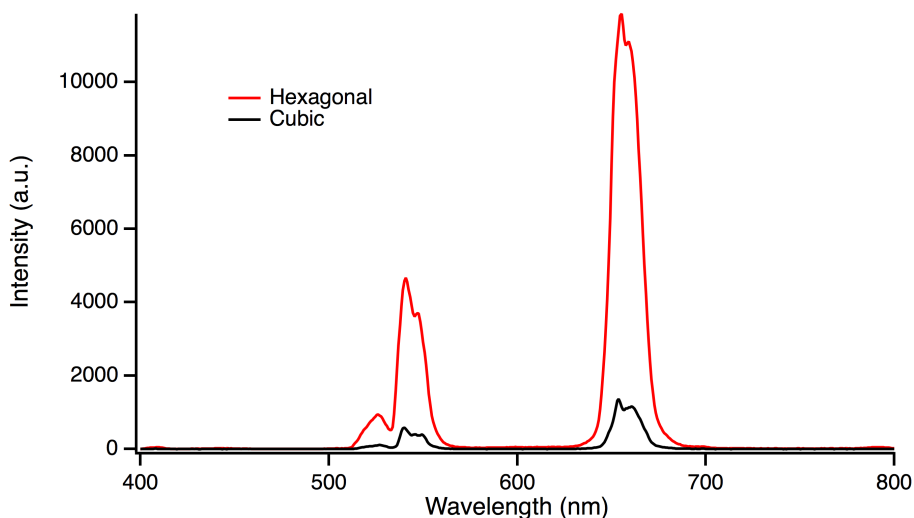


Figure 2.6: Comparison of luminescence spectra of UCNPs synthesized via thermal decomposition at 320 °C (black) and 340 °C (red). Both spectra came from 1 wt% colloidal solutions in cyclohexane that were excited by a 980 nm laser at 500 mW.

growth rates along the different axes.²⁰² The top and bottom hexagonal faces are (001) planes. The six rectangular side planes, which have (100) orientation, are equivalent in energy. When OA chelates more strongly with (001) facets, hexagonal nanoplates take shape due to predominant growth in the [100] direction.²⁰³ Appendix A covers additional information on XRD and crystallography.

These hexagonal-phase nanoplatelets had significantly greater emission than their cubic counterparts due to the difference in phase (Figure 2.6). The difference was almost 10-fold. While a previous study found that gadolinium helps to reduce average crystallite size,¹¹⁷ this does not always appear to be the case. The results from EDXA and elemental mapping (Figures 2.7 and 2.8) show that the NaLuF₄-based nanocrystals were evenly doped with Gd³⁺, but their dimensions remained characteristic of those of large hexagonal phase particles. EDXA of the β -NaLuF₄ nanocrystals was performed during SEM measurements to confirm the presence and composition of Na, Lu, Yb, Gd, F and C in the sample (Figure 2.7 and Table 2.1). This indicates that Yb and Gd were successfully doped into the host matrix. The amount of Er was below the limit of detection, which was consistent with previous EDXA results.¹¹⁷ The additional Cu peak can be explained by the presence of the copper grid. The atomic composition ratios did not correspond exactly to the theoretical ratios, but they follow the same decreasing trend in which F has the largest atomic percentage and Gd has the least (Table 2.1). Figure 2.8 combines SEM with X-ray chemical imaging, verifying that the elements were homogeneously spread out in each nanoplate. Carbon was present because of the OA molecules on the surface of the UCNPs.

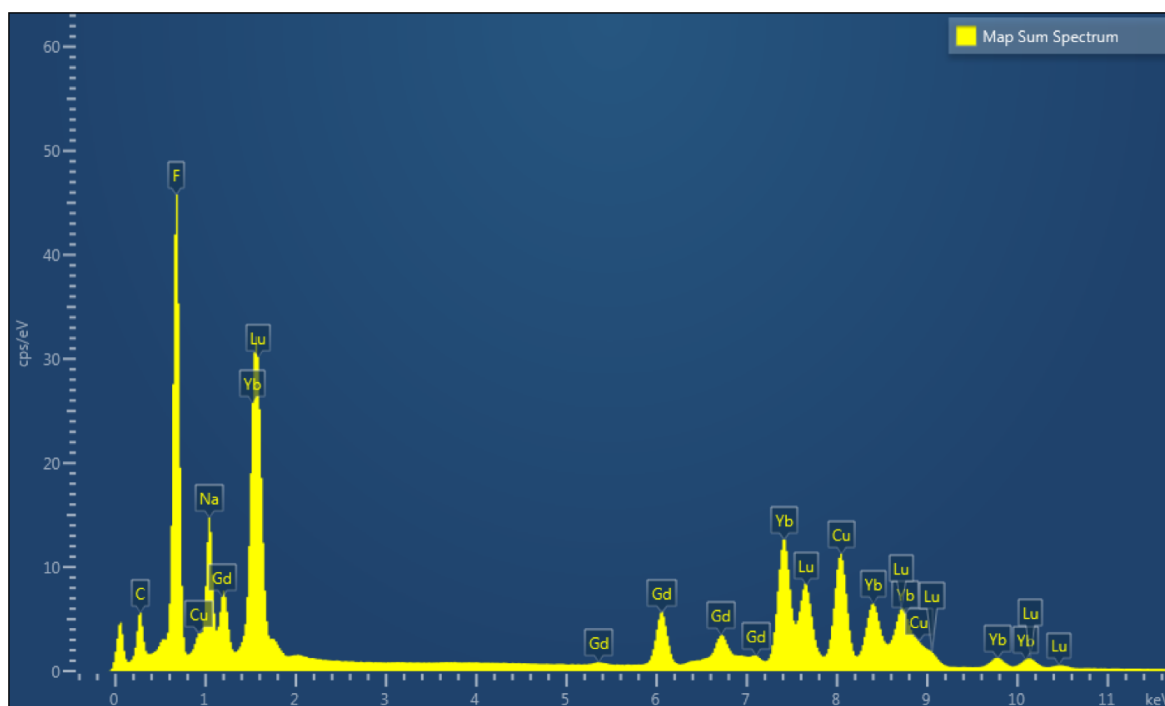


Figure 2.7: EDXA spectrum of β -NaLuF₄ nanoplates synthesized via thermal decomposition at 340 °C.

The enlarged crystal size and platelike nanocrystals were not atypical; similar hexagonal-phase UCNPs produced from co-thermolysis of NaCF₃COO and RE(CF₃COO)₃ precursors without Gd³⁺ doping in OA and ODE had been seen in prior studies.^{199,200} These disparities show that there is still difficulty in controlling the size and shape of the UCNPs produced from thermal decomposition. Moreover, the micrometer dimensions of the β -NaLuF₄ nanocrystals make them ill-suited for cellular applications that rely on uptake.^{204–206} Thus, the coprecipitation method was the next synthesis method of interest.

Table 2.1: Compositional analysis by EDXA of β -NaLuF₄ nanoplates synthesized via thermal decomposition at 340 °C. The Er atomic composition was left out of these calculations

	At% (theoretical)	At% (actual)
F	66.9	62.5
Na	16.7	12.7
Yb	8.4	12.2
Lu	6.0	7.8
Gd	2.0	4.7

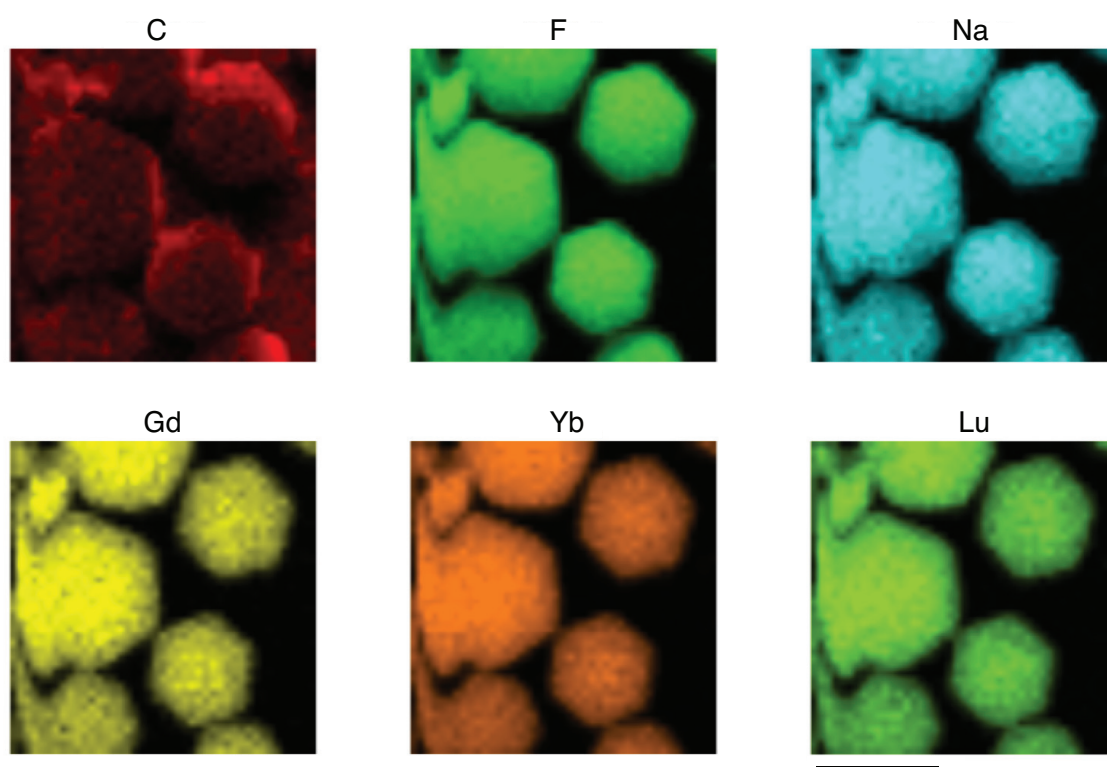


Figure 2.8: SEM image of β -NaLuF₄ nanoplates synthesized via thermal decomposition at 340 °C overlaid with chemical mapping from EDXA to show the distribution of the different elements. Scale bar is 500 nm.

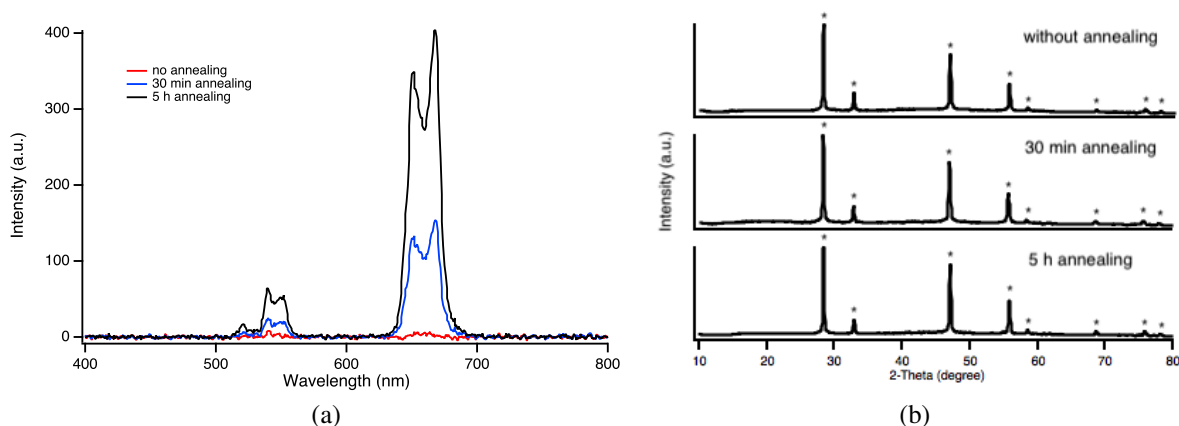


Figure 2.9: (a) presents the luminescence spectrum of UCNPs synthesized via low-temperature coprecipitation method. The 1 wt% colloidal solution in water was excited by a 980 nm laser. (b) presents the experimental powder XRD data of UCNPs synthesized from the low-temperature coprecipitation method. The peaks marked with an asterisk refer to cubic-phase NaYF_4 .

2.3.3 UCNPs from low-temperature coprecipitation

Coprecipitation of UCNPs can take place at low temperature or high temperature, resulting in UCNPs of differing size, quality, and shape depending on which reaction temperature is chosen. Typically for low-temperature coprecipitation, solutions of lanthanide nitrates or chlorides are quickly injected into a solution of sodium fluoride to spontaneously form precipitation in the presence of a chelating agent like EDTA. Annealing/calcination is performed afterwards to obtain UCNPs with higher upconversion efficiency.²⁰⁷ Publications exploring the low-temperature synthesis route reported drawbacks of broad size distribution, irregular shapes, and low upconversion efficiency.¹²³ This is confirmed by Figures 2.9 and 2.10. The spectrum of the UCNPs without annealing was practically nonexistent. Annealing for 30 min or 5 h increased the intensity of the UCNP luminescence as shown in Figure 2.9a, but the emission bands were still broad and indistinct. In addition, the luminescence was not visible to the naked eye. From Figure 2.9b, it is clear that the UCNPs were purely cubic; annealing did not seem to change the phase of the UCNPs from cubic to hexagonal, although another study reported being able to do so.¹²²

The TEM images indicate the physical effects of the annealing: the thin EDTA layer was burned off at the high temperature and the UCNPs appeared to be more porous after the treatment (compare Figure 2.10a to 2.10b and Figure 2.10a to 2.10c). The images also show that the UCNPs varied widely in shape and size. The high resolution of the TEM images enabled analysis of the crystal structure of $\alpha\text{-NaYF}_4$, which is discussed in Appendix

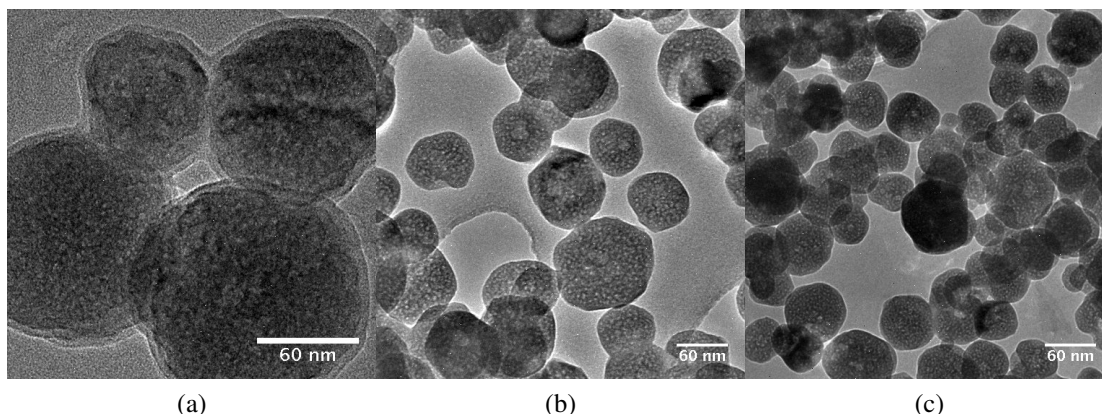


Figure 2.10: TEM images of UCNPs synthesized via low-temperature coprecipitation with three different durations of annealing: (a) none, (b) 30 min, and (c) 5 h.

A. High-quality products (pure β -phase, well-shaped, monodisperse) are important for the sensitivity, route of internalization, and intracellular fate of biosensors.^{200,208,209} Because the low-temperature coprecipitation method attempted here did not achieve UCNPs with those three qualities, the high-temperature coprecipitation procedure was carried out next.

2.3.4 UCNPs from high-temperature coprecipitation

Coprecipitation at high temperature requires different reagents and synthesis setup from its low-temperature counterpart. The method can be thought of as thermal decomposition that has been modified to have milder/safer reaction conditions and simpler protocols,¹²³ but it derives its coprecipitation name from the fact that the reactive fluoride reactants are consumed at room temperature to form NaYF_4 nuclei before increasing the temperature to improve the quality of the nanocrystals.¹²⁰

Core-only β - NaYF_4 : Yb, Er UCNPs have very low QY (<1%), so an inactive shell layer of undoped NaYF_4 is typically added to increase the QY by reducing surface quenching.^{145,210} When the core and shell have the same host material, the interface between the core and shell is more homogeneous to effectively suppress deactivation at the surface of the core nanoparticle.²¹¹ The shell formation was undertaken here because it has been well-documented for high-temperature coprecipitation.^{145,212,213} Successful deposition of the shell layer can be deduced from observing an increase of particle size and enhancement of the luminescence efficiency rather than visually comparing before and after TEM images because the core and shell have identical contrast.^{91,211}

Two shell thicknesses were grown: ‘thin’ (<1 nm) and ‘thick’ (3 nm). It is clear from the TEM images (Figure 2.11) that a largely monodisperse population was produced in each

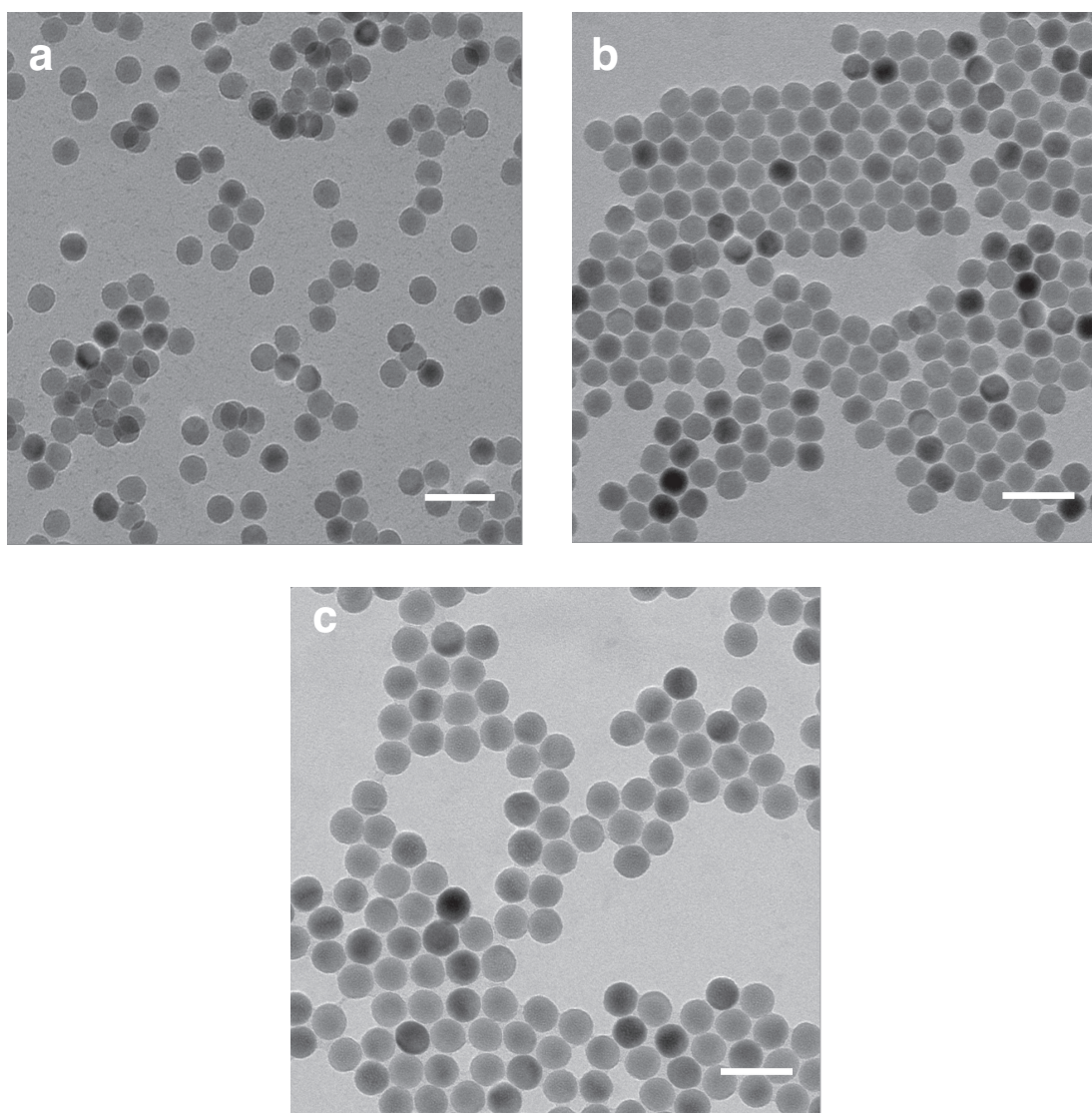


Figure 2.11: TEM images of (a) core NaYF₄: Yb, Er particles, (b) core particles with a ‘thin’ shell of NaYF₄, and (c) core particles with a ‘thick’ shell of NaYF₄ from high-temperature coprecipitation. The scale bars are 60 nm.

case, with mean diameter increasing from 23.8 nm for the core to 24.6 nm for the ‘thin’ shell product and 29.7 nm for the ‘thick’ shell product, with a standard deviation of 1.2 nm, 0.9 nm, and 1.2 nm, respectively (Figure 2.12). The core-only UCNPs were also characterized by XRD (Figure 2.13a) and can be indexed to β -NaYF₄ (ICDD PDF #16-0334), confirming that the synthesis yielded a high purity hexagonal phase product.

The emission spectra for these UCNPs, excited at 980 nm, showed sets of emission peaks with maxima at 540 nm and 650 nm (Figure 2.13b). Both types of core-shell UCNPs displayed greater luminescence than the core-only UCNPs because the shells reduce nonradiative vibrational deactivation processes. The thick-shell UCNPs were even brighter than the thin-shell UCNPs because the thicker shell further lengthens the distance between the luminescent centers and surface-related vibrational modes.²¹⁴ The emission lines were sharp; a Lorentzian fit was used to obtain the full width at half maximum (FWHM) of ~10 nm (core), ~11 nm (thin shell), and ~13 nm (thick shell) at 540 nm.^{215,216} These values were similar to those reported in previous publications.^{80,173}

Thus, in this work, the thin-shell UCNPs were used when the pH-sensitive dyes were electrostatically or covalently attached and the thick-shell UCNPs were selected for the sensing studies that directly mixed UCNPs and indicators. The upconversion photoluminescence of UCNPs is almost independent of pH,³⁴ but inclusion of pH-sensitive probes enables one to explore the feasibility of developing a pH sensor based on UCNPs.

UCNPs synthesized from high-temperature coprecipitation meet the requirements (monodisperse, hexagonal phase, highly crystalline, strong luminescence) outlined above for biosensing. In addition, this method can be monitored with the naked eye, is relatively simple to control, does not require stabilization at an exact temperature, and is highly reproducible.⁷⁶ Therefore, this synthesis method was used to fabricate the UCNPs used in Chapters 3 and 4.

2.3.5 Surface modification for biological applications

Chapter 3 studies the interaction between UCNPs and anthraquinone dyes by adding different amounts of CaR and ARS into a fixed concentration of UCNP in solution. The thick-shell UCNPs were modified with the amphiphilic polymer PMA to avoid direct electrostatic attraction between particle and dye. The ζ -potential measurement of -33 mV indicated the success of the surface modification with the polymer (Figure 2.14a). The colloidal stability, including the absence of particle aggregation, was confirmed by unimodal size distribution from DLS (Figure 2.14b). The two polymer-coated UCNPs were measured in different solvents (cyclohexane and water), so a direct comparison to deduce PMA coating thickness was not considered here.

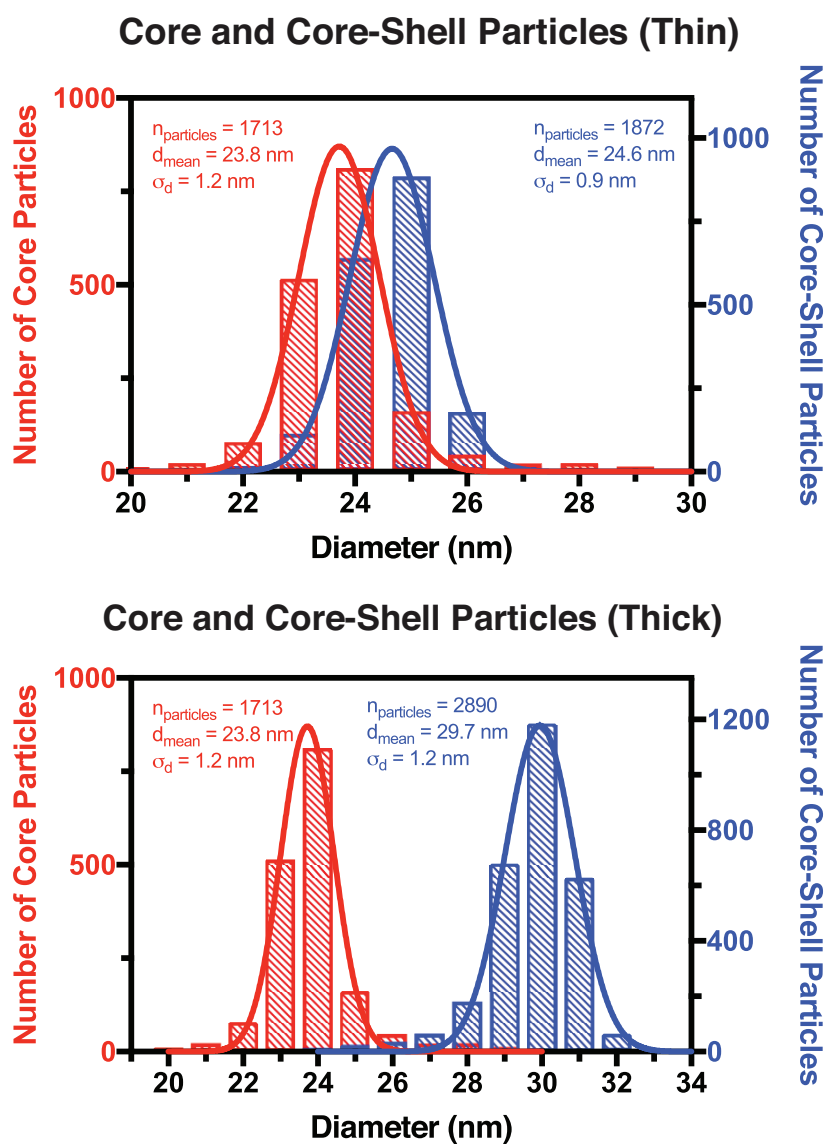


Figure 2.12: Size distribution of hexagonal-phase, oleate-capped NaYF_4 : 20% Yb, 2% Er UCNPs calculated from the transmission electron micrographs in Figure 2.11.

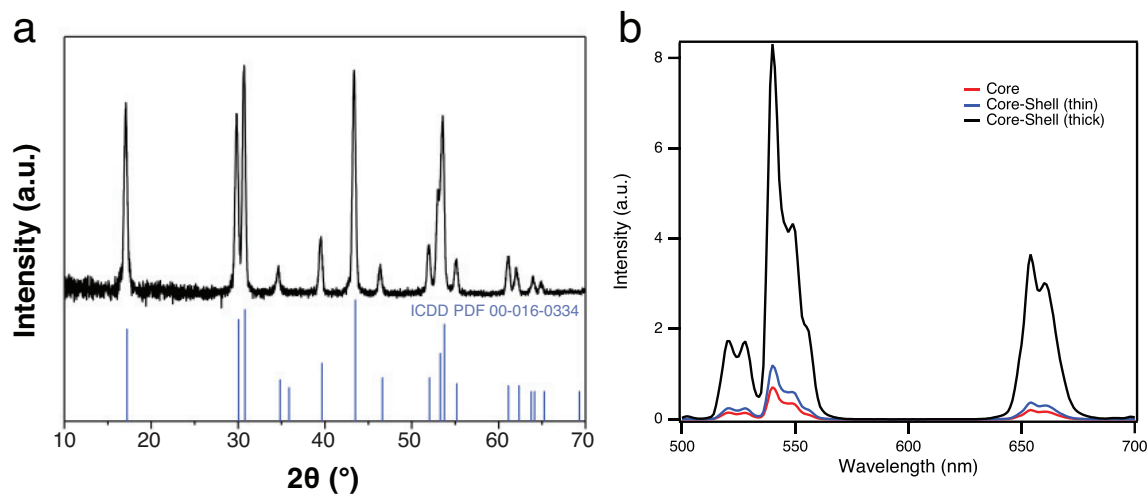


Figure 2.13: (a) XRD pattern of the UCNPs from Figure 2.11a in black and the reference XRD pattern of β -NaYF₄ in blue. (b) Emission spectra of core, core-shell (thin), and core-shell (thick) UCNPs at 1 wt%.

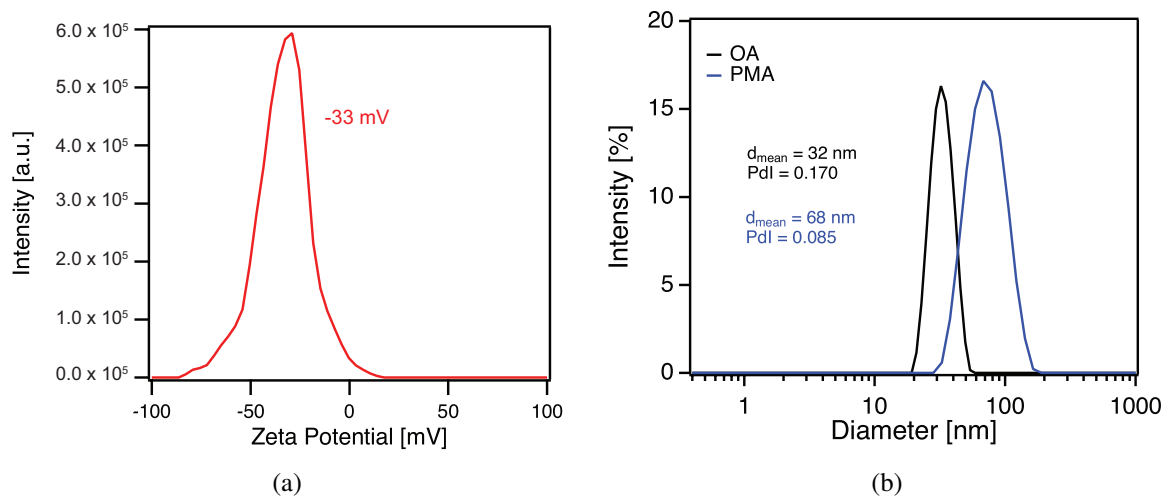


Figure 2.14: (a) Zeta potential measurement of UCNPs coated with PMA after a two-step ligand exchange process and (b) intensity-weighted DLS measurements in backscatter mode of UCNPs coated with OA in cyclohexane and PMA in water.

Table 2.2: Average hydrodynamic diameters of thin-shell UCNPs coated with high molecular weight PEI and their respective PDI from pH 5.0-7.0

	pH 5.0	pH 5.5	pH 6.0	pH 6.5	pH 7.0
Average hydrodynamic diameter (nm)	81.04	88.35	90.07	89.80	88.52
PDI	0.172	0.185	0.179	0.181	0.181

Chapter 3 also looks at integrating UCNPs and anthraquinones together for a versatile assay that can potentially be employed in cellular samples. Since the CaR and ARS dyes used in this work are anthraquinone derivatives with a negatively charged sulfonate group, they can be expected to form UCNP-CaR and UCNP-ARS conjugates through electrostatic interaction with a positively charged UCNP. A two-step ligand-exchange protocol was used to modify the surface of the thin-shell nanoparticles with PEI, a polymer which is abundant in amino groups.¹⁴⁵ First, the UCNPs were stabilized with BF_4^- to prevent particle aggregation and improve stability during the exchange process.¹⁸³ Next, the PEI was added to replace BF_4^- .

TEM images of the PEI-coated particles are shown in Figure 2.15. The thickness of the coating, which was calculated by measuring the edges with a different contrast in Figure 2.15b, was 2.1 ± 0.3 nm. The ligand exchange process did not affect the shape of the UCNPs and many of the particles were visibly separated, which suggests that there was not much aggregation in solution.¹⁹² However, some of the UCNPs were clustered in Figure 2.15a. Higher magnification of the cluster shows that the UCNPs were loosely next to each other rather than forming an entire solid mass that would be indicative of aggregation (Figure 2.15b).^{192,217} It is likelier to be an artefact of the drying process when the solvent evaporates off the copper grid and forces the UCNPs to cluster.¹⁹²

To confirm that the UCNPs were successfully coated with PEI, zeta potential measurements were carried out. Figure 2.16a shows that the UCNPs were positively charged (+36 mV), consistent with PEI surface modification. Figure 2.16b confirms that stable colloids without apparent aggregation resulted from the surface modification even at different pHs. Across two units of pH, the hydrodynamic diameter did not vary by more than 10 nm and every measured PDI was less than 0.190, which indicates highly uniform particles. The hydrodynamic diameter values in Table 2.2 were >80 nm, but they include the surrounding hydration layers. The hydrodynamic diameter is the size of a hypothetical sphere that diffuses in the same fashion as that of the measured particle. This sphere would account for the hydration layers that travel with the charged particles in the solution. The high surface charge of the UCNP-PEI allows the particles to overcome aggregation in solution by inducing a large layer of water molecules to surround the particle, causing the bigger size

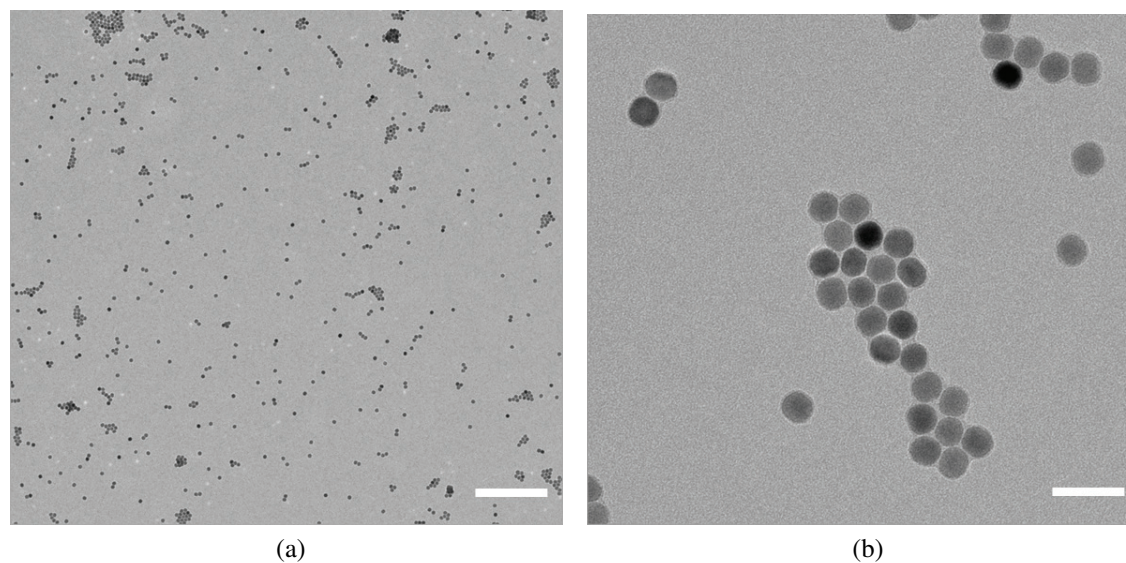


Figure 2.15: (a) TEM images of NaYF₄:Yb, Er nanoparticles with high molecular weight PEI (scale bar = 500 nm) and (b) the same particles at higher magnification (scale bar = 60 nm).

measured by DLS compared to TEM.¹⁹²

Chapter 4, which explores the use of upconverting pH nanoprobes to measure pH intracellularly, also uses thin-shell UCNP-PEI to conjugate to pHAb amine reactive dye. The positive charge and narrow size distribution (<30 nm from TEM) help to encourage cellular uptake.²¹⁸ While the UCNP-PEI surface could theoretically be covered with additional polymer coatings to reduce cytotoxicity, there exists a trade-off in the brightness of the particles.²¹⁹ Extra external polymer coatings were not added in this thesis to maximize the brightness of the photoluminescence signal for sensing, and the cytotoxicity studies in Chapter 4 show that PEI did not display extremely toxic behavior for the duration of the experiments when it was immobilized on particles.

2.4 Conclusions

This chapter explored various synthetic strategies (solvothermal, thermal decomposition, low-temperature coprecipitation, high-temperature coprecipitation) to identify the method that has ideal qualities (reproducible, yielding high-quality particles) for biosensing applications. The UCNPs were characterized using methods such as XRD for phase analysis, TEM for size distribution, DLS for aggregation, and photoluminescence spectroscopy for upconversion efficiency. High-temperature coprecipitation was successfully identified as

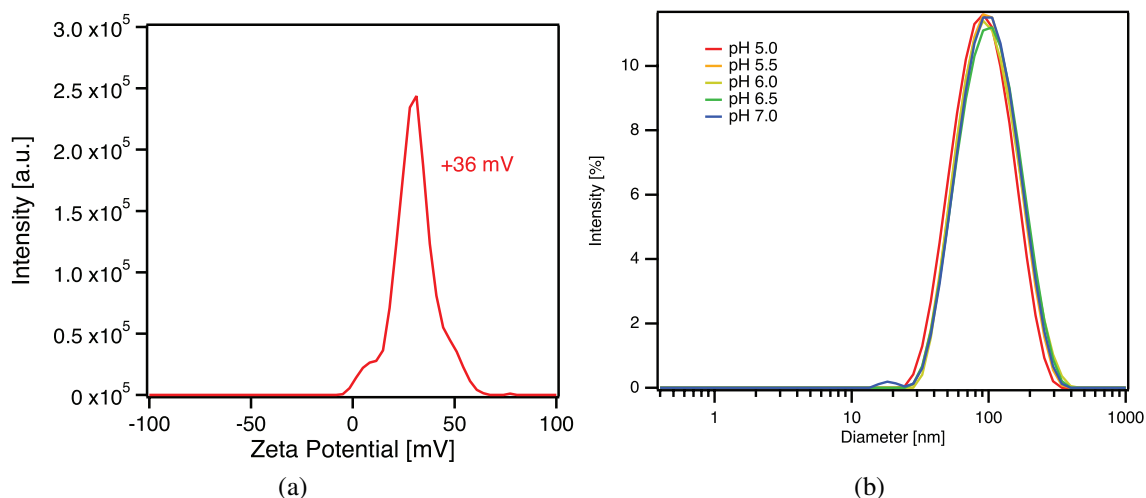


Figure 2.16: (a) Zeta potential measurement of UCNPs coated with PEI after a two-step ligand exchange process and (b) DLS measurements of UCNPs coated with PEI at different pHs.

the best synthesis route because it produced UCNPs that were β -phase, uniform (core-only particles had diameter of 23.8 ± 1.2 nm), monodisperse (DLS measurements showed PDI = 0.170 in cyclohexane), and bright (fluorescence can be observed with the naked eye). The other three synthetic techniques encountered various problems. The solvothermal method produced α -phase particles that were partly aggregated. Thermal decomposition yielded α -phase UCNPs when the mixture was heated to 320 °C and micrometer-sized, β -UCNPs when the solution was reacted at 340 °C. Finally, low-temperature coprecipitation yielded α -NaYF₄ with nonuniform shape and size even after annealing.

After core UCNPs were produced from high-temperature coprecipitation, ‘thin’ (<1 nm) and ‘thick’ (3 nm) shells made of inactive NaYF₄ were grown to increase the QY by minimizing surface deactivation. The thin-shell UCNPs are highly useful for sensing applications that rely on distance-dependent interactions like FRET. These UCNPs were coated with PEI to (i) electrostatically attract the anthraquinone dyes used in Chapter 3 for pH sensing in buffers or (ii) conjugate with the pHAb dye used in Chapter 4 for ratiometric intracellular imaging. The thick-shell UCNPs are suitable for sensing applications that rely on IFE. These UCNPs were coated with PMA, which leads to colloidal stable particles in water, before being mixed with anthraquinones to enable pH responses in buffer solutions in Chapter 3.

These results also highlight that the high-temperature coprecipitation method is a strong contender for the large-scale syntheses that will be required when UCNPs are eventually used commercially for diagnostics and sensing research. So far, the procedure has been

scaled to yield up to 2 g in a single batch.⁷⁶ The synthetic technique has also showed reliability in terms of producing high-quality UCNPs consistently here and in previous studies.^{76,120,220}

Chapter 3

Energy transfer mechanisms from UCNPs to pH dyes

3.1 Introduction

UCNPs have been widely used for various biosensing applications in recent years. However, the effect of pH dyes on UCNPs has not been well studied. The work so far on UCNPs and pH-sensitive dye combinations have focused on their potential use in buffer solution and for intracellular measurement, but the interaction between UCNPs and different pH indicator dyes still requires further characterization. Many studies claim UC-RET to be the main or sole process of energy transfer but do not investigate lifetimes or determine FRET parameters.^{78,160} Photon reabsorption (IFE) could potentially be a contributor to the energy transfer, as was the case in a 2011 study that examined the nature of the energy transfer mechanism between UCNP and three acceptors (B-phycoerythrin, ATTO565, DY556).²²¹ The authors found a significant decrease in one lifetime component (64-72% reduction), supporting their hypothesis that RET was the primary mechanism while photon reabsorption was secondary, but pH effects were not discussed.

A class of dyes that is known to retain its high pH sensitivity when coupled with nanoparticles is anthraquinones.²³ The effect of two anthraquinone dyes, Calcium Red and Alizarin Red S, was measured by spectroscopic techniques at various pHs. The pH-dependent effect of CaR and ARS on UCNPs was investigated next. CaR and ARS are interesting since they are anthraquinones with absorption bands that have strong overlap with the green emission of NaYF₄: Yb, Er particles. When the UCNPs and dyes were mixed directly, the green emission band of the UCNPs was quenched by a pH-dependent inner filter effect while the red emission band remained unchanged and acted as the reference signal for ratiometric pH

measurements. When the anthraquinones were attached onto the UCNPs through electrostatic attraction, inner filter effect remained the dominant quenching mechanism compared to resonance energy transfer. This work offers a new opportunity to improve pH measurement through UCNP coupling partners and investigate the presence of IFE and RET mechanisms.

3.2 Materials and methods

3.2.1 Materials

4-amino-1,3-dihydroxy-anthraquinone-2-sulfonic acid (calcium red) (CaR), 3,4-dihydroxy-anthraquinone-2-sulfonic acid (alizarin red S) (ARS), citric acid monohydrate, and disodium phosphate heptahydrate were purchased from Sigma-Aldrich. UCNPs were synthesized and modified using the protocols described in Section 2.2.

3.2.2 Anthraquinone attachment

A dispersion of PEI-modified UCNPs was added to a solution containing excess dye (0.05 mg per mg UCNP) and stirred for 15 min at room temperature. The particles were separated from the rest of the solution by centrifugation (21,000 *g*, 3 min) and washed with double distilled water until the supernatant was colorless.

3.2.3 Characterization methods

An inductively coupled plasma optical emission spectrometer (ICP-OES) (Spectro) was used for the concentration determination of the nanoparticles. Absorption measurements were performed at room temperature with a Lambda 14P UV/VIS spectrometer (PerkinElmer) or Synergy HT (BioTek). Luminescence spectra for the quenching experiments were obtained with an AMINCO-Bowman Series 2 luminescence spectrometer (formerly from Thermo Fisher) in which an external cw 980 nm laser module (focusable, power ranging from 200 mW) (Picotronic) was installed. Luminescence spectra for the pH titration experiments were obtained with a USB4000-FL spectrometer (Ocean Optics) excited at 980 nm with a Spectra-Physics Mai Tai Ti:Sapphire NIR/IR laser (Newport) and protected with a 750 nm shortpass filter (Thorlabs). All spectra were recorded at room temperature.

For lifetime measurements, a setup consisting of a 980 nm cw laser module (200 mW) (Picotronic) and an optical chopper (MC2000 with two slot chopper blade MC1F2) (Thorlabs) was used. The signal was amplified by a photomultiplier tube (PreSens) and analyzed

with a digital storage oscilloscope (DSO 8204) (Voltcraft). Optical bandpass filters (FF01-535/150-25 and FF01-665/150-25) (Semrock) were used for measuring luminescence decays of the green and red upconversion emission bands. For the UCNP-only measurements, the concentration of particles in water was 1 mg/mL. For the UCNP-dye mixture measurements, the concentration of particles in solution was maintained at 1 mg/mL, while the concentration of CaR was 0.03 mM and the concentration of ARS was 0.07 mM. For the UCNP-dye conjugates, the above anthraquinone attachment procedure was followed before measuring the lifetime of the solution with UCNP concentration of 1 mg/mL. The average lifetime values ($\bar{\tau}$) were calculated by averaging the lifetimes obtained from three monoexponential fits of the solution of interest. The Curve Fitting Toolbox in MATLAB (MathWorks) was used to calculate the monoexponential fits from the decay data.

3.2.4 Spectroscopic measurements of CaR solutions

Solutions of CaR buffered with 0.2 M phosphate/citrate buffers at different pHs were scanned between 300 and 600 nm using a BioTek Synergy HT to measure absorption. Samples were prepared by adding 70 μ l of phosphate/citrate buffer at different pHs into 70 μ l of a 0.02 wt% CaR solution. The pH response curve was obtained by fitting the data to a sigmoidal equation using Igor Pro software (Wavemetrics). The pK_a was calculated by finding the inflection point of the pH response curve with Mathematica (Wolfram Research).

Fluorescence emission spectra were measured with a Cary-Eclipse Fluorescence Spectrophotometer (Varian). Instrument excitation and emission slits were both set at 10 nm, and the scan rate was 30 nm/min. All samples were excited at 533 nm, and the emission was scanned from 550 to 650 nm. The photomultiplier tube detector voltage was set at 800 V. Samples were prepared by adding 70 μ l of 0.2 M phosphate/citrate buffer at different pHs into 70 μ l of a 0.1 wt% CaR solution. Again, the pH response curve was obtained by fitting the data to a sigmoidal equation using Igor Pro software (Wavemetrics), and the pK_a was calculated by using Mathematica to find the inflection point (Wolfram Research).

3.2.5 Spectroscopic measurements of ARS solutions

Solutions of ARS buffered with 0.2 M phosphate/citrate buffers at different pHs were scanned between 300 and 700 nm using a BioTek Synergy HT to measure absorption. Samples were prepared by adding 70 μ l of phosphate/citrate buffer at different pHs into 70 μ l of a 0.04 wt% ARS solution. The pH response curve was obtained by fitting the data to a sigmoidal equation using Igor Pro software (Wavemetrics). The pK_a was calculated by finding the inflection point of the pH response curve with Mathematica (Wolfram Research).

Fluorescence emission spectra were measured with a Cary-Eclipse Fluorescence Spectrophotometer (Varian). Instrument excitation and emission slits were both set at 10 nm, and the scan rate was 600 nm/min. All samples were excited at 520 nm and the emission was scanned from 540 to 700 nm. The photomultiplier tube detector voltage was set at 800 V. Samples were prepared by adding 70 μl of 0.2 M phosphate/citrate buffer at different pHs into 70 μl of a 0.2 wt% ARS solution. Again, the pH response curve was obtained by fitting the data to a sigmoidal equation using Igor Pro software (Wavemetrics), and the $\text{p}K_a$ was calculated by using Mathematica to find the inflection point (Wolfram Research).

3.2.6 Spectroscopic measurements of UCNP-anthraquinone mixtures

Different concentrations of CaR or ARS in 0.2 M phosphate/citrate buffers of different pHs were added to PMA-modified UCNP (3 nm shell) solutions in water. The final concentration of UCNPs was 1 mg/mL. The pH response curve from the ratiometric measurements was obtained by fitting the data to a sigmoidal equation using Prism 8 software (GraphPad). The ratio of UCNP to dye was kept at 2.5:1 (on a mass basis) for these pH titration experiments. The concentration of CaR was 0.4 mM, and the concentration of ARS was 2 mM. UCNP-ARS mixture required a higher dye concentration to produce a measurable pH response due to the lower quenching efficiency of ARS.

3.2.7 Spectroscopic measurements of UCNP-anthraquinone nanoconjugates

Phosphate/citrate buffers of different pHs (0.2 M) were added to UCNP-CaR or UCNP-ARS (PEI-modified, <1 nm shell) solutions in water. The pH response curve from the ratiometric measurements was obtained by fitting the data to a sigmoidal equation using Prism 8 software (GraphPad). The spectral overlap integrals of the UC-RET pairs were calculated with ale software (FluorTools).

3.2.8 Dye loading calculations

The following equations were used to estimate the UCNP/dye ratio.

$$n_{dye} = c_{dye} V_{sample}$$

where n = number of moles, c = concentration, and V = volume. C_{dye} was obtained from absorbance spectroscopy. A calibration curve was first obtained from dilutions of a standard with known concentration to determine the linear range of the dye for the instrument. Given

this relationship, the concentration of dye in a sample could then be calculated from the absorbance measurement.

$$N_{dye} = n_{dye}N_A$$

where N = number of molecules and N_A = Avogadro's number.

$$V_{UCNP} = \frac{4}{3}\pi r_{UCNP}^3$$

where r = radius (obtained from TEM images).

$$m_{UCNP} = V_{UCNP}\rho_{UCNP}$$

where m = the mass of one particle and ρ = density.

$$M_{UCNP} = V_{sample}C_{UCNP}$$

where M = total mass in the sample. C_{UCNP} was obtained from ICP measurements.

$$N_{UCNP} = M_{UCNP}/m_{UCNP}$$

The number of dye molecules on each UCNP particle was calculated from N_{dye}/N_{UCNP} .

3.3 Results and discussions

3.3.1 Shell thickness selection

An important requirement of UC-RET is a close-enough distance between the donor (Er^{3+}) and acceptor (dye). Theoretical calculations of RET efficiency can provide information about the feasibility of the process given a system of interest (Figure 3.1). Using Equations 1.6 and 1.7, the Förster distance values for the UCNP/CaR and UCNP/ARS UC-RET pair combinations were estimated to be 1.78 nm and 1.52 nm, respectively, assuming a Q_D of 0.01, κ^2 of 2/3 (due to the long lifetime of UCNPs),²²² and n of 1.48 (for NaYF_4).²²³ Calculations yielded a J of $2.6 \times 10^{14} \text{ nm}^4 \text{ M}^{-1} \text{ cm}^{-1}$ for the UCNP/CaR pair and $1.0 \times 10^{14} \text{ nm}^4 \text{ M}^{-1} \text{ cm}^{-1}$ for the UCNP/ARS pair. The estimated value for Q_D was based on the estimation range provided by Muhr et al.¹⁴⁵ due to the same choice of synthesis strategy used to produce the UCNPs in this thesis. Q_D is different from the overall quantum yield of the UCNP, which is much lower due to multiple possible transitions between the various lanthanide energy levels and surface quenching.²²²

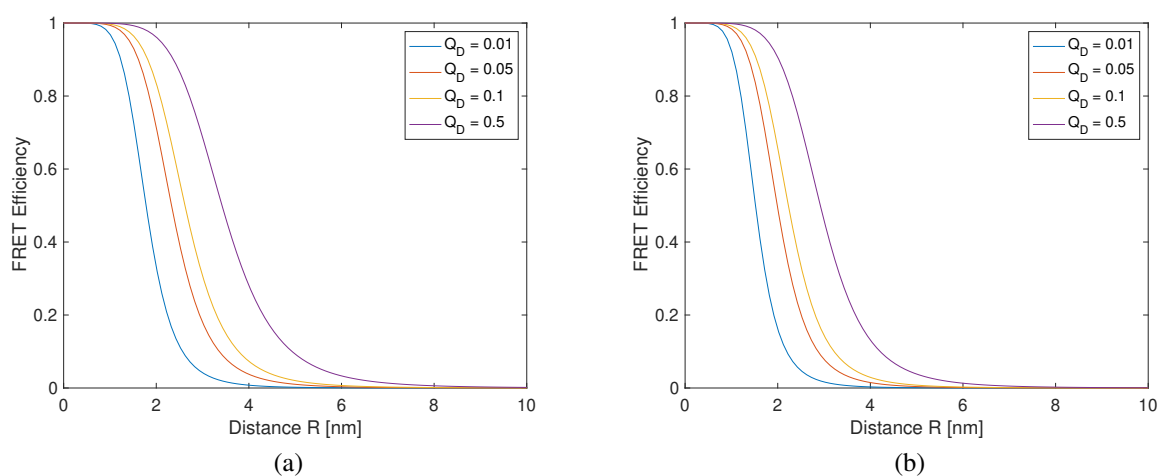


Figure 3.1: Theoretical calculations of Förster distances between donor (Er^{3+}) and acceptor (dye) for (a) CaR and (b) ARS at pH 8. Typical Förster distances ($E = 50\%$) for these four Q_D values are 1.8-3.4 nm for CaR and 1.5-2.9 nm for ARS. A higher Q_D results in a longer R_0 .

For UCNP/CaR, the efficiency goes from 99+% to 4% when distance between UCNP and dye is 0.4 nm and 3 nm, respectively. Similarly for UCNP/ARS, the efficiency decreases from 99+% to 2% when distance is 0.4 nm versus 3 nm, respectively. Thus, potential RET mechanisms, as previously reported,^{72,145} would only be expected to be suitable for the less bright thin-shell UCNPs in Figure 2.11b because distance between the donor (lanthanide ions) and acceptors (analyte-responsive dyes) is minimized. In contrast, the UCNPs in Figure 2.11c would be better matched to sensing schemes that rely on IFE due to lower anticipated energy deactivation provided by a thicker shell.²²⁴⁻²²⁶

The upconversion photoluminescence of UCNPs alone is almost independent of pH, which can be seen in Figure 3.2 where the ratio of the green peak at 540 nm to the red peak at 650 nm ($I_{g/r}$) is 2.7 ± 0.2 across the 6 different pHs. However, by inclusion of pH-sensitive probes the feasibility of developing a pH sensor based on UCNPs can be explored.

3.3.2 UCNP mixed with CaR and ARS in solution

CaR and ARS are anthraquinone dyes with similar absorbance maxima in the visible light region at pH 7 ($\lambda_{max} = 535$ nm and 520 nm, respectively, Figure 3.3) overlapping with the emission wavelength for the UCNPs, but different response at low pH where the ARS develops a new non-overlapping absorption maximum at 420 nm. Furthermore, the fluorescence of CaR and ARS are pH dependent. The fluorescence of CaR ($\lambda_{ex} = 535$ nm, $\lambda_{em} = 585$

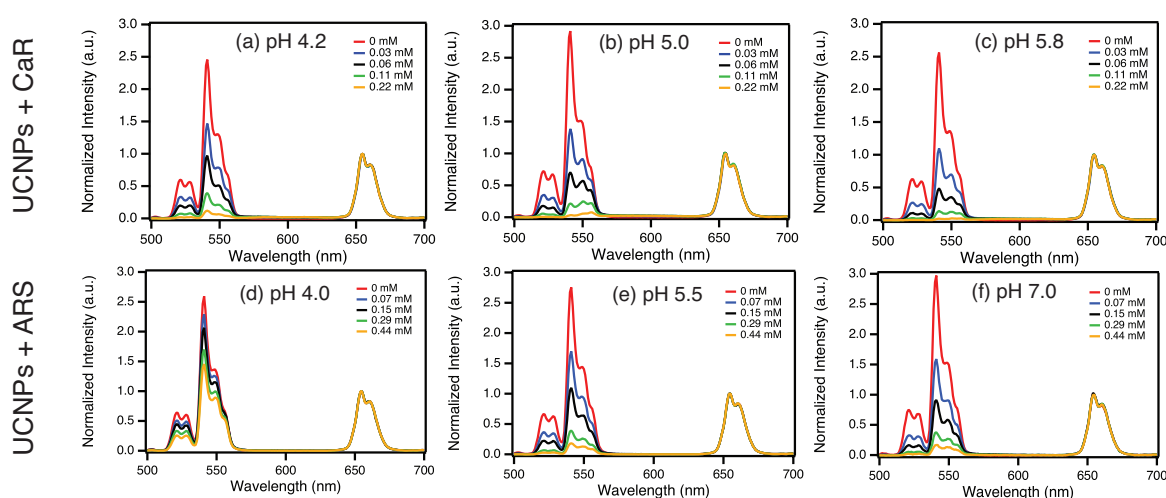


Figure 3.2: Effect of different amounts of CaR on the luminescence spectra of UCNP in phosphate/citrate buffer of different pH values: (a) 4.2, (b) 5.0, and (c) 5.8. The concentration of UCNP was fixed at 1 mg/mL, and the concentrations of CaR were 0, 0.03, 0.06, 0.11, and 0.22 mM separately. Effect of different amounts of ARS on the luminescence spectra of UCNP in phosphate/citrate buffer of different pH values: (d) 4.0, (e) 5.5, and (f) 7.0. The concentration of UCNP was fixed at 1 mg/mL, and the concentrations of ARS were 0, 0.07, 0.15, 0.29, and 0.44 mM separately. Excitation was at 980 nm with a 200 mW cw laser.

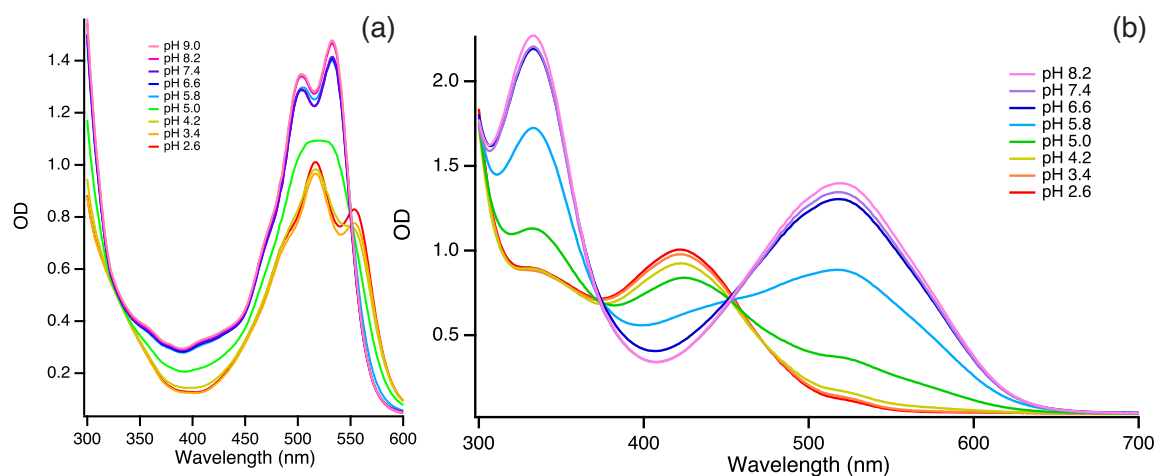


Figure 3.3: Absorption spectra of (a) CaR and (b) ARS in solution buffered with 0.2 M phosphate/citrate at different pHs.

nm) increases when pH is changed from 4-6 (Figure 3.4a). The fluorescence of ARS is also pH dependent, but due to the absorbance wavelength shift from 420 nm (low pH) to 520 nm (high pH), the dye is almost not fluorescent at acidic pH and the intensity only increases dramatically when $\text{pH} > 7$ ($\lambda_{ex} = 520$ nm, $\lambda_{em} = 555$ nm, Figure 3.4b).

To study the interaction between UCNPs and these anthraquinone dyes, different amounts of CaR and ARS were added into a fixed concentration of UCNP in solution. The UCNPs were modified with the amphiphilic polymer PMA to avoid direct electrostatic attraction between particle and dye. UCNPs that are functionalized with an amphiphilic coating on top of the original oleate capping are known to exhibit higher $I_{g/r}$ compared to those that are surface modified through ligand exchange. This is highly beneficial for sensing applications that use the green luminescence as the analyte-dependent signal.⁷⁶ Figure 3.2a-c displays the normalized emission spectra of the UCNP-CaR mixtures, and a $\text{p}K_a$ of ~ 5.0 is estimated from the change in absorbance at 533 nm (Figure 3.5a). Without taking into account any shift in the apparent $\text{p}K_a$ due to interactions with the PMA on the UCNP, the dye is predominantly in its protonated form at pH 4.2 and mostly unprotonated at pH 5.8.²²⁷ In this pH range, it is clear that CaR plays a role in quenching the green emission of the UCNP, with intensity decreasing relative to the red intensity as the concentration of dye increases.

In contrast, Figure 3.2d-f shows the normalized emission spectra of the UCNP-ARS mixtures. Figure 3.5b suggests a $\text{p}K_a$ of ~ 5.5 for ARS in solution at 520 nm, so the dye is mostly protonated at pH 4.0 and primarily unprotonated at pH 7.0. Like CaR, higher concentration of ARS increases quenching of the green peak of the UCNP relative to the red peak, but this is less pronounced at pH 4.0. In this case, there is a clearer pH response

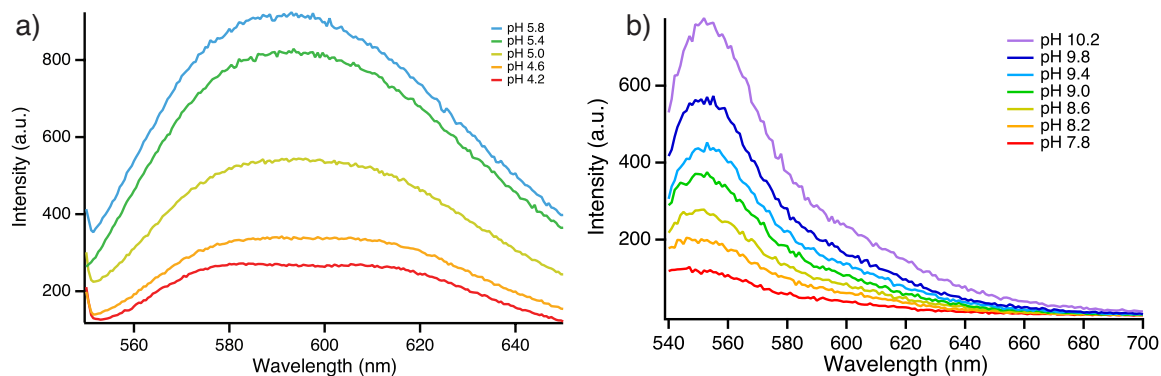


Figure 3.4: Fluorescence emission spectra of (a) CaR and (b) ARS in solution buffered with 0.2 M phosphate/citrate at different pHs. At acidic pHs, the change in fluorescence of ARS could not be detected by the spectrofluorimeter.

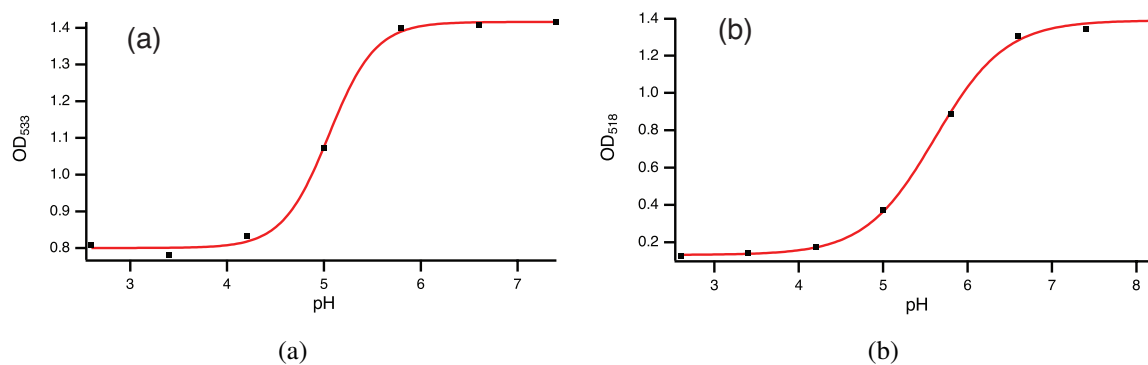


Figure 3.5: pH response curve in 0.2 M phosphate/citrate buffer of (a) CaR solution at an absorbance of 533 nm and (b) ARS solution at an absorbance of 518 nm.

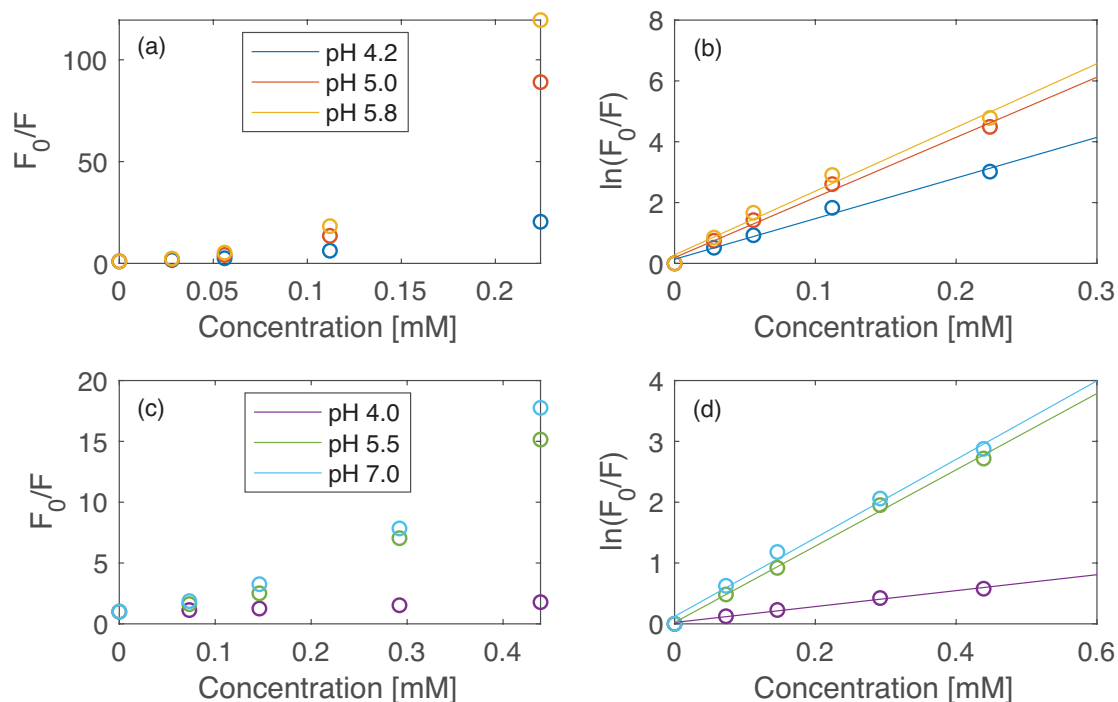


Figure 3.6: Plots showing (a) Stern-Volmer quenching for UCNP-CaR, (b) Perrin model sphere of action quenching for UCNP-CaR, (c) Stern-Volmer quenching for UCNP-ARS, and (d) Perrin model sphere of action quenching for UCNP-ARS. The open circles show the quenching data, and the lines show the Perrin model fits.

for a given dye concentration.

The Stern-Volmer equation is frequently used to describe fluorescence quenching:

$$\frac{F_0}{F} = 1 + K_{SV}[Q] \quad (3.1)$$

where, in this setting, F_0 and F are the fluorescence intensities of UCNPs in the absence and presence of anthraquinone dye, K_{SV} is the Stern-Volmer quenching constant, and $[Q]$ is the concentration of CaR or ARS.^{19,228}

The linear Stern-Volmer plots expected from Equation 3.1 are not obtained here (Figure 3.6a,c); instead, positive deviations are observed. Upward-curving Stern-Volmer plots can result from: static and dynamic quenching occurring simultaneously and/or "static-like" quenching due to the fluorophore's adjacency to the quencher at high concentrations.^{19,228,229}

The most definitive method of distinguishing between the two mechanisms is to carry out fluorescence lifetime measurements.²³⁰ Fluorescence lifetimes were measured for UCNPs at 540 nm in the absence and presence of CaR (Table 3.1) and ARS (Table 3.2). The average

Table 3.1: Fluorescence lifetimes at 540 nm of thick-shell UCNPs, UCNP-CaR mixtures, thin-shell UCNPs, and UCNP-CaR conjugates in phosphate/citrate buffer solution of different pH values

pH	$\bar{\tau}$ (thick UCNPs, μs)	$\bar{\tau}$ (mixtures, μs)	$\bar{\tau}$ (thin UCNPs, μs)	$\bar{\tau}$ (conjugates, μs)
4.2	270 ± 15	272 ± 1	243 ± 2	228 ± 9
5.0	274 ± 3	275 ± 8	247 ± 2	229 ± 10
5.8	274 ± 5	279 ± 7	247 ± 1	224 ± 3

Table 3.2: Fluorescence lifetimes at 540 nm of thick-shell UCNPs, UCNP-ARS mixtures, thin-shell UCNPs, and UCNP-ARS conjugates in phosphate/citrate buffer solution of different pH values. Different batches of UCNPs were used for the lifetime studies with the dyes in Tables 3.1 and 3.2, resulting in different lifetimes due to batch-to-batch variation

pH	$\bar{\tau}$ (thick UCNPs, μs)	$\bar{\tau}$ (mixtures, μs)	$\bar{\tau}$ (thin UCNPs, μs)	$\bar{\tau}$ (conjugates, μs)
4.0	161 ± 3	160 ± 6	129 ± 2	120 ± 4
5.5	157 ± 2	156 ± 17	127 ± 3	118 ± 1
7.0	162 ± 3	158 ± 8	128 ± 6	116 ± 1

fluorescence lifetime at this wavelength is almost unchanged after addition of CaR or ARS in solution. For example, the lifetime of UCNP-CaR mixture is $272 \mu s$ compared to $270 \mu s$ for thick-shell UCNPs in pH 4.2 buffer solution. The overlap of the decay curves (Figure 3.7a-c) also confirms this. As validation, the lifetime at 650 nm was also measured and found to be independent of the presence or absence of dye (Table 3.3). Additionally, there is no significant lifetime variation of the UCNP green emission across different pHs, indicating that the UCNPs are relatively stable towards pH change in this range.

These data could point to a static quenching mechanism, with a non-fluorescent ground-state complex forming between the fluorophore and quencher. Examination of the absorption spectra can determine whether such a complex exists between the UCNP and anthraquinone dye after mixing. Dynamic quenching only affects the excited state of the

Table 3.3: Fluorescence lifetimes at 650 nm of thick-shell UCNPs, UCNP-CaR mixtures, thin-shell UCNPs, and UCNP-CaR conjugates in phosphate/citrate buffer solution of different pH values. UCNP-ARS mixture and UCNP-ARS conjugate had similar trends in their lifetime data.

pH	$\bar{\tau}$ (thick UCNPs, μs)	$\bar{\tau}$ (mixtures, μs)	$\bar{\tau}$ (thin UCNPs, μs)	$\bar{\tau}$ (conjugates, μs)
4.0	561 ± 2	561 ± 3	523 ± 1	522 ± 5
5.5	562 ± 7	561 ± 5	525 ± 6	528 ± 14
7.0	567 ± 4	565 ± 6	519 ± 3	523 ± 9

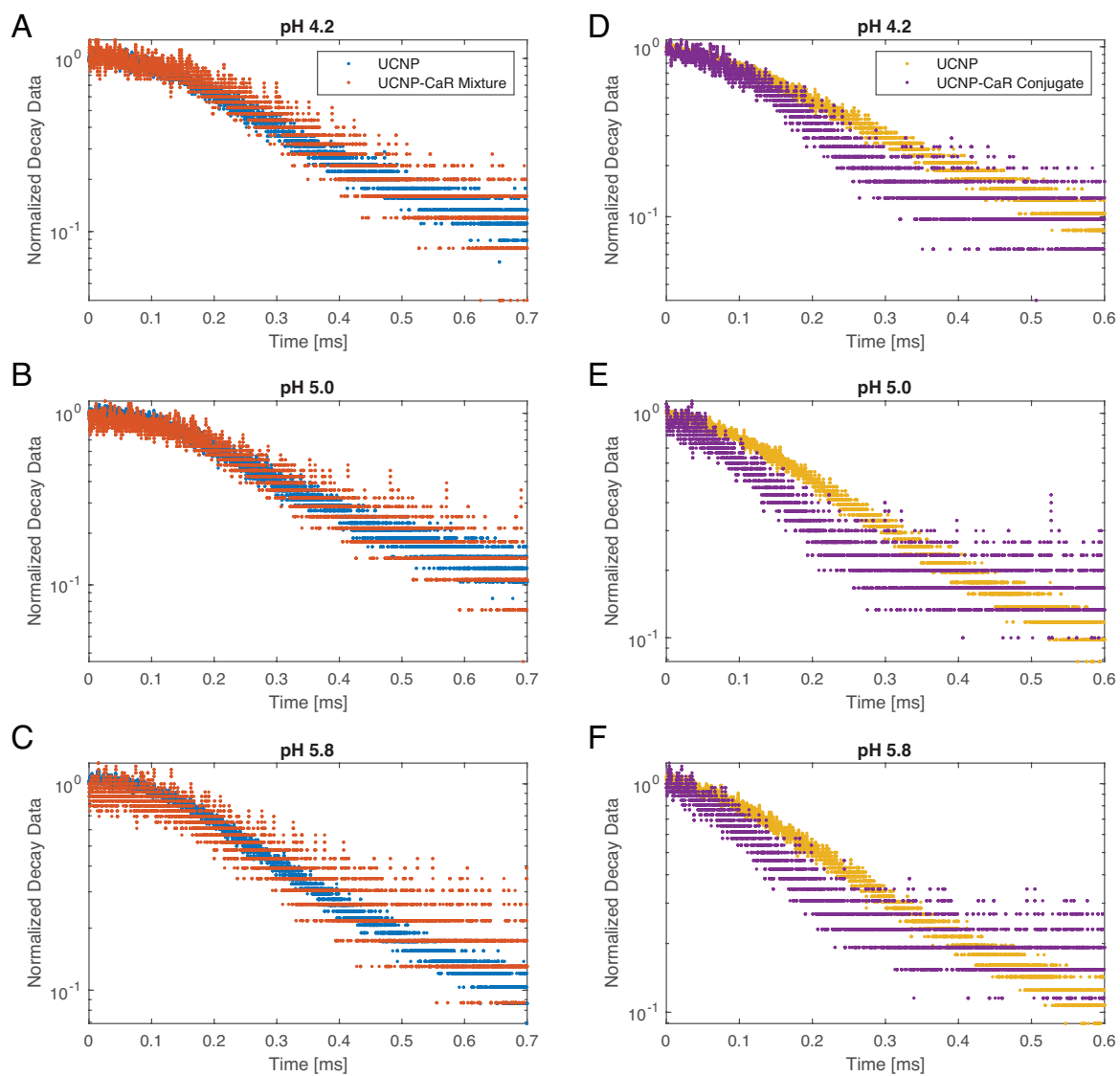


Figure 3.7: Cut and normalized decay data of the 540 nm emission of UCNPs-CaR mixture (A-C) and UCNPs-CaR conjugate (D-F) in phosphate/citrate buffer solution of different pH values. Each average lifetime was calculated from monoexponential fits of three decay curves. UCNPs-ARS mixture and UCNPs-ARS conjugate had similar trends in their decay data.

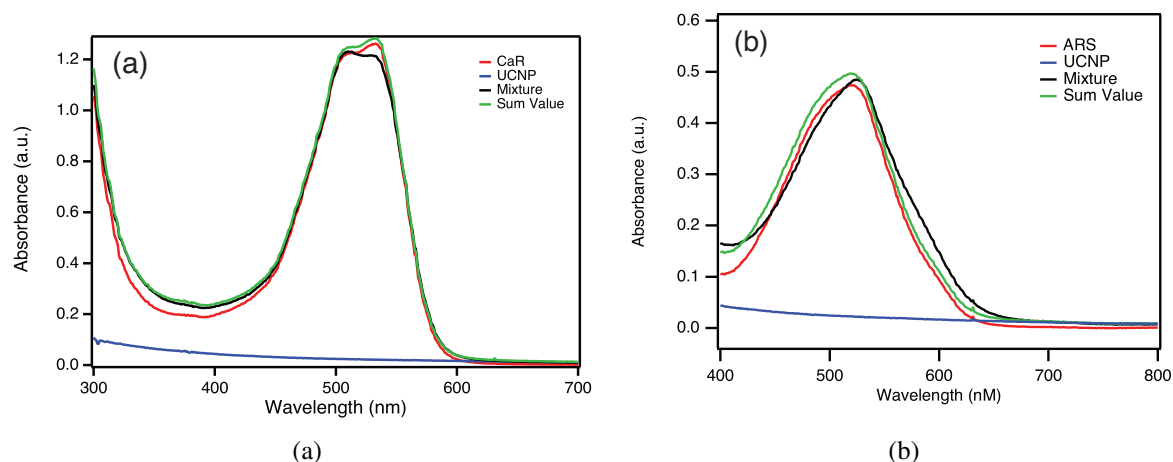


Figure 3.8: (a) Absorption spectra of CaR, UCNP, UCNP-CaR mixture, and the sum value of the absorbance of UCNP and CaR. (b) Absorption spectra of ARS, UCNP, UCNP-ARS mixture, and the sum value of the absorbance of UCNP and ARS.

UCNP so its absorption spectrum is not expected to change, while ground-state complex formation results in a new, unique absorption spectrum.¹⁹ Because there is no significant difference (e.g. emergence of a new peak or shoulder) between the absorption spectrum of UCNP-CaR mixture and that of the sum value of UCNP and CaR individually (Figure 3.8a), we can infer that no ground-state complex formed.^{52,231}

The same principle applies for UCNP-ARS mixtures (Figure 3.8b). However, although the formation of a ground-state complex is ruled out, Figure 3.2 indicates that some sort of non-diffusional quenching is responsible for the decrease in the green luminescence intensity of the UCNP when anthraquinone dye is present. Perrin's model of static quenching does not assume complex formation; rather, there is apparent static quenching because of the proximity between the fluorophore and quencher during excitation, which results in immediate quenching that makes the pair act like a dark complex.^{19,232} At high concentrations, any quencher molecule found within a sphere-of-action is deactivated instantaneously with probability of unity, and those outside the volume do not participate in quenching.^{232,233} Because of this, $\tau = 0$ inside V and $\tau = \tau_0$ outside V , which is consistent with the lack of change in lifetime for non-diffusional quenching.²³³ There have been multiple reports of using the Perrin model to fit the upward curvature in Stern-Volmer plots, including systems involving small molecules as the quencher.^{231,234,235}

The Perrin model without diffusional contribution has the following relationship:

$$\frac{F_0}{F} = \exp(\alpha[Q]) \quad (3.2)$$

Table 3.4: Radii of the quenching spheres for UCNP-CaR mixtures and UCNP-ARS mixtures

pH	r (UCNP-CaR, nm)	pH	r (UCNP-ARS, nm)
4.2	1.74	4.0	0.80
5.0	1.99	5.5	1.35
5.8	2.02	7.0	1.37

where $\alpha = N_A V$. N_A is Avogadro's number and V is the volume of the sphere of action.^{23,231,232}

Figure 3.6b,d shows the fitting of the quenching data. Based on the Perrin analysis, the sphere of action, obtained from the slope of the lines, shows an increase with pH (Table 3.4). Larger sphere volumes represent higher efficiency of quenching.²³⁶ This trend matches what we find in Figure 3.2, where quenching is greatest and the sphere of action is largest at the highest pH (for a given concentration of CaR or ARS). From this analysis, we can also see that CaR, which has larger sphere volumes, is a more efficient quencher than ARS. This is also confirmed by a higher concentration of ARS being required to obtain the same quenching effect as CaR (Figure 3.2).

The spectral overlap between the green band of the luminescence spectrum of UCNP and absorption spectra of CaR at different pH values explain these different pH-dependent effects (Figure 3.9a). The pH-independent red emission band (650 nm) of the UCNP can act as a reference signal for quantitative ratiometric measurement of pH, linked with the CaR/CaRH⁺-dependent green luminescence of the UCNP (Figure 3.9b).

For ARS, the red emission band can also be used as the reference signal for quantitative measurements of pH, but only the absorption spectra of the deprotonated ARS overlaps with the green emission band of the UCNP (Figure 3.10a). The spectral overlap of ARS with UCNP increases with pH, causing the UCNP intensity at 540 nm to decrease relative to the intensity at 650 nm (Figure 3.10b).

Thus, depending on whether the anthraquinones are in their acidic form or basic form, the dyes exert an inner filter effect on the green emission of the UCNP. The absorption coefficient for the dye at the wavelength of spectral overlap increases with pH for both CaR and ARS so the IFE efficiency is higher at higher pH, resulting in a sigmoidal response curve of the relative quenching for both CaR and ARS (Figure 3.11a,c). The experimental pK_a calculated from the sigmoidal fit is 5.0 ± 0.2 for the UCNP-CaR mixture, which is the same as that of the dye alone. The experimental pK_a of the UCNP-ARS mixture calculated from the sigmoidal fit is 5.4 ± 0.1 , which is a little lower than that of the dye alone.

For real-life applications of pH measurement, the concentration of UCNP to dye should

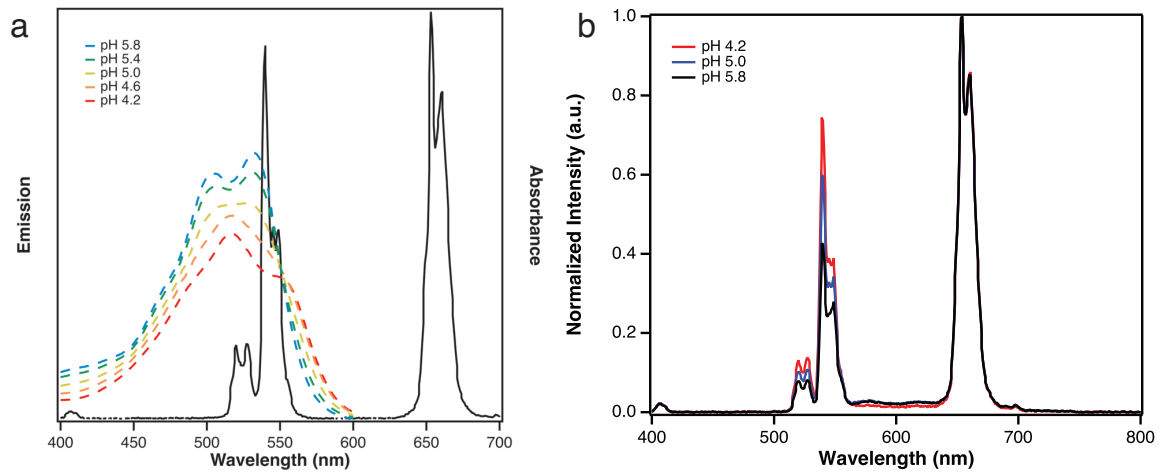


Figure 3.9: (a) Absorption spectra (dashed lines in color, right y-axis) of CaR in aqueous solutions of different pHs overlaid with the emission spectrum of the UCNP in water upon 980 nm excitation (solid black line, left y-axis). (b) Normalized emission spectra of UCNP-CaR mixtures at pH 4.2, 5.0, and 5.8 upon 980 nm excitation.

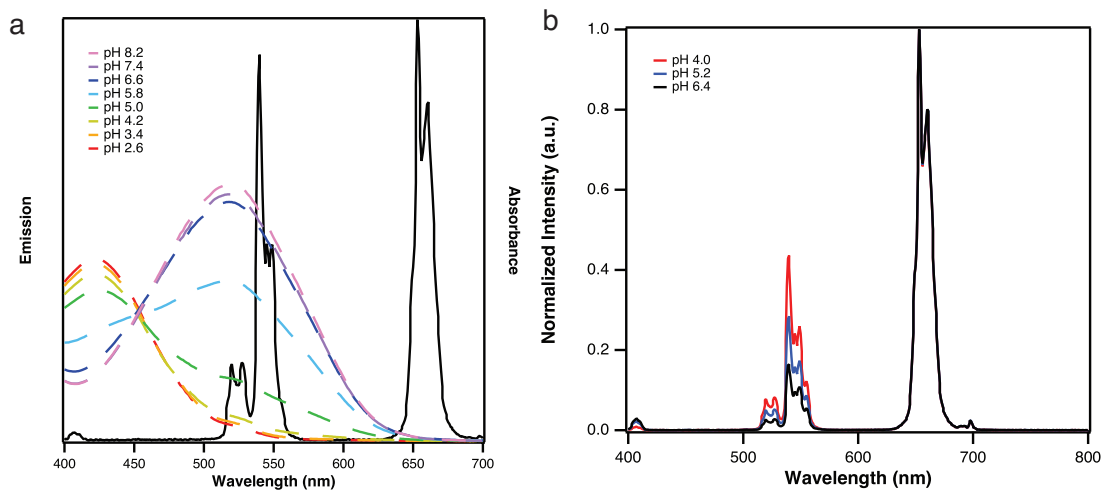


Figure 3.10: (a) Absorption spectra (dashed lines in color, right y-axis) of ARS in aqueous solutions of different pHs overlaid with the emission spectrum of the UCNP in water upon 980 nm excitation (solid black line, left y-axis). (b) Normalized emission spectra of UCNP-ARS mixtures at pH 4.0, 5.2, and 6.4 upon 980 nm excitation.

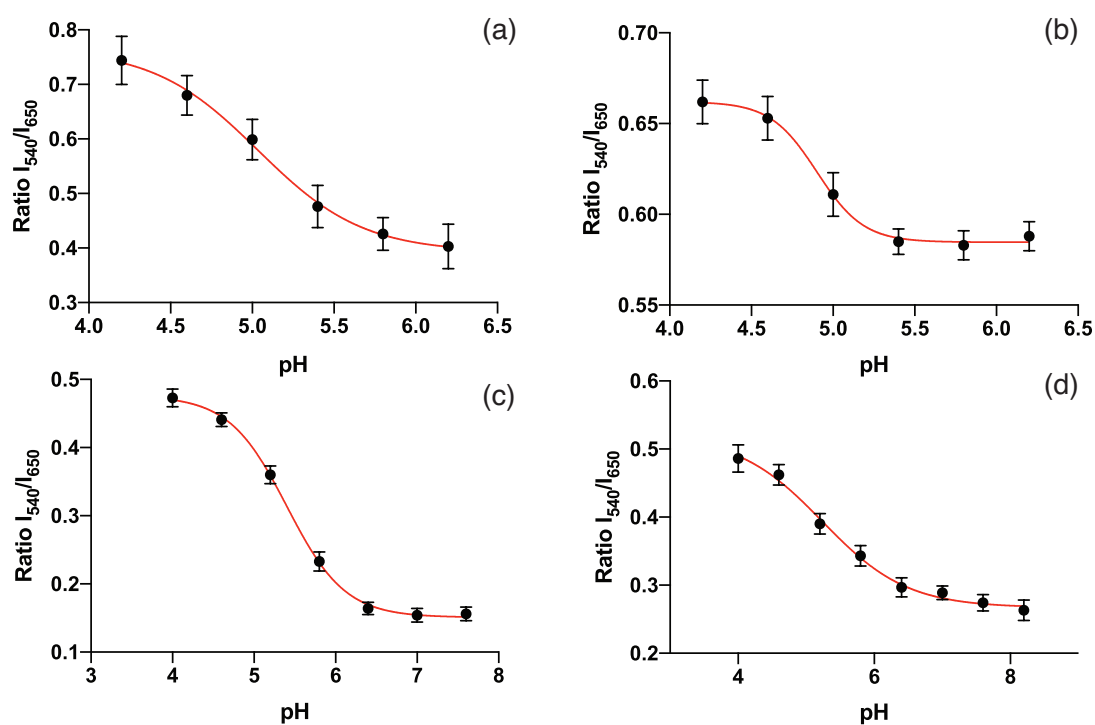


Figure 3.11: Ratiometric pH-titration data measured at 540 nm and 650 nm of (a) UCNP-CaR mixture, (b) UCNP-CaR conjugate, (c) UCNP-ARS mixture, and (d) UCNP-ARS conjugate. The red lines represent the sigmoidal interpolation curves.

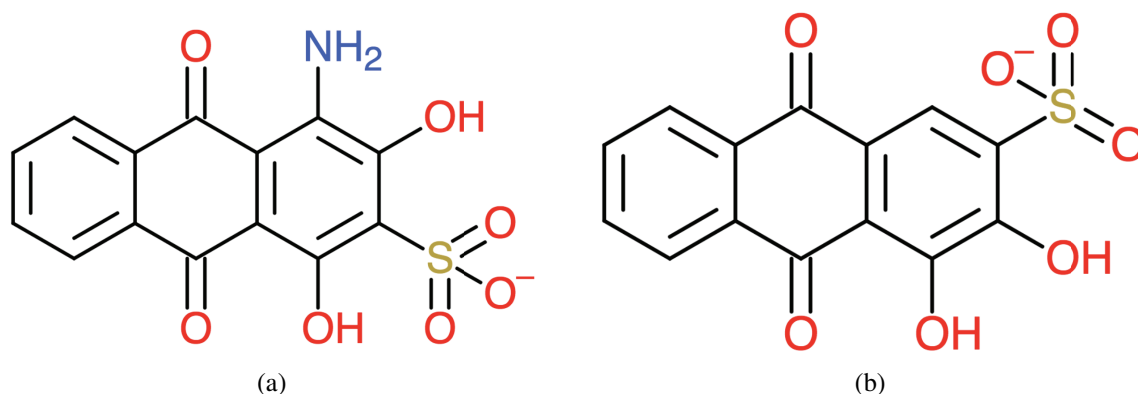


Figure 3.12: Structures of the (a) CaR and (b) ARS anthraquinone derivatives used in this work. Drawings were created with ChemDoodle.

remain as constant as possible given that the green/red photoluminescence ratio of the pH sensor experiences both a concentration-induced and pH-induced response (Figure 3.2). This can be accomplished with incorporation of both UCNP and dye in a support material to prevent leakage that would affect the ratio between the two components.¹⁵⁴

3.3.3 UCNP-CaR and UCNP-ARS nanoconjugates

Although these data support an IFE rather than the RET mechanism proposed previously for UCNP-dye combinations, the shell thickness of 3 nm would be expected to limit RET. In contrast, the 0.4 nm shell UCNPs are less efficient emitters, but their UCNP to dye distance could potentially support RET. The CaR and ARS dyes used in this study are anthraquinone derivatives with a negatively charged sulfonate group (Figure 3.12), so they can be expected to form UCNP-CaR and UCNP-ARS conjugates through electrostatic interaction with a positively charged UCNP (Figure 3.13).

CaR attachment onto PEI-modified UCNP was easily confirmed by the pink color on the surface of the particles, after purification by redispersion-precipitation-centrifugation cycles to remove excess, non-attached dye. In the case of ARS, the color observed was purple. Although the dyes are attached to the UCNP through electrostatic attraction, which is a weaker interaction than covalent bonding, the conjugates are still quite stable and do not exhibit major leakage of the dye. Tables 3.5 and 3.6 show that the fraction of CaR and ARS remaining on the UCNP remains ~90% after each wash step.

The dye loading of CaR and ARS can be calculated from a combination of ICP and absorbance spectroscopy (see Section 3.2 for more details). For the same excess dye concentration (0.05 mg per mg UCNP) the UCNP-CaR conjugates have approximately 120 dye

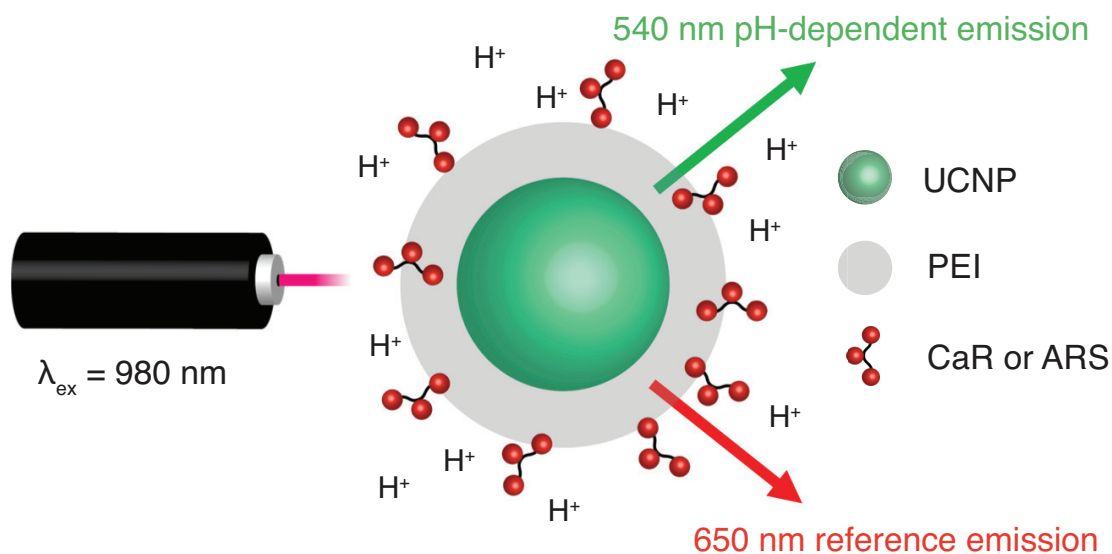


Figure 3.13: Schematic of the UCNP-anthraquinone conjugate sensor. The CaR or ARS dye is attached to the UCNP through electrostatic attraction between the positively charged amino groups of the PEI and the negatively charged sulfonate group of the CaR. The sensitized emission is the 540 nm emission, whose intensity changes depending on pH. The pH-independent 650 nm emission acts as the reference signal.

Table 3.5: Fraction of excess starting CaR dye on UCNPs after wash steps. S =supernatant and c_s =concentration of supernatant.

				CaR on UCNPs (mg)	Fraction on UCNPs
	OD_{520}	c_s (mM)	Start	0.357	
$S1$	0.183	0.028	Wash 1	0.328	0.92
$S2$	0.079	0.0073	Wash 2	0.320	0.90
$S3$	0.064	0.0044	Wash 3	0.315	0.88

Table 3.6: Fraction of excess starting ARS dye on UCNPs after wash steps. S =supernatant and c_s =concentration of supernatant.

				ARS on UCNPs (mg)	Fraction on UCNPs
	OD_{421}	c_s (mM)	Start	0.342	
$S1$	0.063	0.019	Wash 1	0.322	0.94
$S2$	0.047	0.008	Wash 2	0.314	0.92
$S3$	0.048	0.008	Wash 3	0.305	0.89

Table 3.7: Förster distances and donor quantum yields for different Er^{3+} (donor) and anthraquinone (acceptor) distances, given a UC-RET efficiency of 0.09 calculated from the lifetime data. 4.8 nm is the distance at which Q_D would be 100% for UCNP-CaR. 5.7 nm is the distance at which Q_D would be 100% for UCNP-ARS

r (nm)	R_0 (nm)	Q_D (UCNP-CaR)	Q_D (UCNP-ARS)
0.4	0.27	1.3×10^{-7}	3.3×10^{-7}
1	0.68	3.1×10^{-5}	8.0×10^{-5}
2	1.4	0.0020	0.0051
4	2.7	0.13	0.33
4.8	3.3	...	1.0
5.7	3.8	1.0	...

molecules per UCNP particle and the UCNP-ARS conjugates have around 1600 molecules per particle. It is anticipated that the protonated amino group of the CaR will reduce electrostatic binding to the protonated amino groups of the PEI covering the surface of the UCNPs, so the attachment is not as strong compared to that of ARS.

$$E = 1 - \frac{\tau(\text{UCNP} - \text{dye})}{\tau(\text{UCNP})} \quad (3.3)$$

Lifetime experiments were performed before and after dye attachment to determine whether the anthraquinones are close enough to the UCNP in this conjugate design for UC-RET to take place between the donor (UCNP) and acceptor (CaR or ARS). There is a decrease of 10-30 μs in the lifetime of the green emission band at 540 nm after CaR attachment (Table 3.1, Figure 3.7d-f). There is an even more modest decrease in lifetime of the green upconversion band after ARS attachment, from 127-129 μs to 116-120 μs (Table 3.2). Equation 3.3 relates UC-RET efficiency to lifetime of the UCNP in the presence and absence of dye. From the lifetime data, UC-RET efficiencies of 4-9% for UCNP-CaR and 7-9% for UCNP-ARS are obtained. Thus, the quenching mechanism in this conjugate system can be attributed to a combination of UC-RET and emission-reabsorption, with the latter being the primary pH responsive process.

These UC-RET efficiencies allow the estimation of distances between donor and acceptor using Equations 1.6 and 1.7 (Table 3.7), the reverse of the theoretical calculations of RET efficiencies performed at the start of this section. Since Q_D cannot be greater than 100%, the maximum distance between UCNP and anthraquinone is 5.7 nm for the UCNP-CaR combination and 4.8 nm for the UCNP-ARS combination, given a UC-RET efficiency of 0.09. Based on acceptable boundary values for Q_D (on the order of 0.1% to 5%),^{222,237} the distance between UCNP and anthraquinone molecule cannot be less than 1 nm. Thus, the

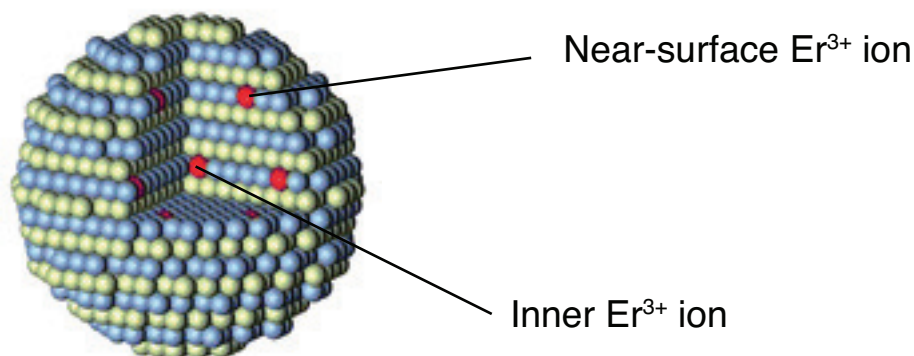


Figure 3.14: Schematic of UCNP crystal structure to illustrate the distribution of Er^{3+} ions in the host lattice. An Er^{3+} ion near the surface of the particle is closer to electrostatically attached dyes, enabling UC-RET. The majority of the emitting ions are too far away from the dyes for UC-RET but can still participate in radiative energy transfer (photon reabsorption). Adapted from Wang et al. with permission from The Royal Society of Chemistry.¹³⁵

actual UCNP-anthraquinone distances were estimated to be 1-3 nm, with the same UC-RET efficiency. Because the polymer does not form a densely packed layer due to charge repulsion from the positive amino groups on PEI,²³⁸⁻²⁴⁰ the dyes may be able to penetrate the PEI layer and become attached by electrostatic forces within the polymer layer and not just at the surface. This porosity would also infer that protons diffusing into a dye-PEI matrix are in equilibrium with a PEI buffered environment. Yet, only a small fraction of the dye is within the Förster distance while the majority is too far away to accept energy through non-radiative energy transfer (Figure 3.14). UC-RET occurs mostly between the Er^{3+} ions near the surface of the UCNPs and the closest attached dyes, while the inner Er^{3+} ions contribute to radiative energy transfer to the dyes through reabsorption.²⁴¹

Figure 3.15a shows the normalized emission spectra of UCNP-CaR conjugates at different pHs after excitation with a 980 nm laser. In this instance, the green UCNP emission coincides well with the excitation wavelength for CaR ($\lambda_{max} = 535$ nm); there is a small decrease in the emission intensity at 540 nm but no clear evidence of UC-RET acceptor emission at 585 nm. The small change in UC-RET efficiency (4-9%) while varying pH from 4.2 to 5.8 suggests that IFE plays a more significant role in the decrease in green emission of the UCNP.

Figure 3.15b shows the normalized emission spectra of UCNP-ARS conjugates at various pHs with the same laser. In this case, the green peak of the UCNP shows a more significant decrease relative to the red peak as pH increases, likely due to the higher dye loading compared to the CaR system. However, varying pH from 4.0 to 7.0 does not significantly

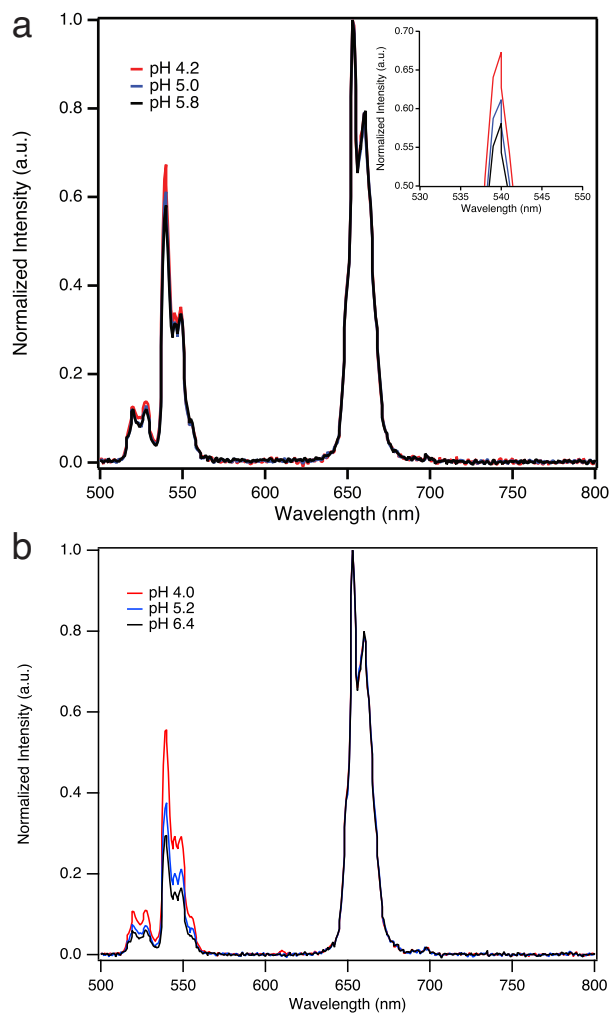


Figure 3.15: (a) Normalized emission spectra of UCNP-CaR conjugates in phosphate/citrate buffer solutions of pH 4.2, 5.0, and 5.8 and (b) normalized emission spectra of UCNP-ARS conjugates in phosphate/citrate buffer solutions of pH 4.0, 5.2, and 6.4 upon 980 nm excitation.

impact the UC-RET efficiency (7-9%), so again, reabsorption appears to be the primary reason for the pH-dependent quenching of the UCNP. The fact that the UCNP-ARS conjugate has more dye molecules per particle than the UCNP-CaR conjugate may explain why the former experiences greater quenching and hence sharper decrease in green:red emission compared to the latter.

The UCNP-CaR nanosensor exhibits dynamic range between pH ~4.6 and ~5.2. From the sigmoidal fit (Figure 3.11b), the experimental pK_a is 4.9 ± 0.1 , which is equivalent to the UCNP-CaR mixture and prior studies involving the dye.^{23,242} The pH range is ideal for tracking pH in endosomes and lysosomes.^{21,243} The UCNP-ARS nanoconjugate shows a wider range of pH responsiveness (Figure 3.11d), between pH ~4.4 and ~6.4, with pK_a of 5.4 ± 0.4 and a similar pH sensitivity of ~0.1 ratio difference per pH unit.

3.4 Conclusions

In this work, the effect of two anthraquinone dyes, CaR and ARS, on UCNPs was studied in two different types of systems: mixture and conjugate. When thick-shell UCNPs and anthraquinones were mixed directly, the decrease in the green intensity of the UCNPs was due to IFE. However, when thin-shell UCNPs and anthraquinones were conjugated through electrostatic attraction with PEI coated on the particle, UC-RET could occur between the UCNPs and dye, but the main quenching mechanism was still emission-reabsorption.

The potential of UCNP-anthraquinone coupling was demonstrated for pH measurement. The UCNP-ARS nanosensor displayed a broader range of pH response compared to the UCNP-CaR nanosensor. The range studied has potential application for intracellular pH determination. ARS is better suited for neutral pH, while the lower CaR pK_a is better tuned to measurement of pH in endosomes and lysosomes. However, CaR loading on the PEI coating of the UCNP is low, probably due to the amine group of the dye. This suggests that other anthraquinones with appropriate spectral overlap could be selected to increase sensitivity and extend the measurable pH range.

The integration between the UCNP and dye through electrostatic binding has the potential for continuous sensing of pH in cells. It is worth noting here that these quantitative titration measurements were performed using a simple spectrometer without a photomultiplier tube. A plate reader with a more sensitive detector can capture >100,000 counts for the UCNP signals at a hundredth of the concentration,³⁴ which would add significantly to the sensitivity of pH that is reported here.

This study provides the framework for creating pH sensing systems using UCNPs and charged dyes based on their spectral overlap. It is critical to examine the interplay between

static and dynamic energy transfer when optimizing pH sensing nanoplatfoms.²⁴⁴ This work shows that energy transfer mechanisms other than UC-RET may dominate even when the distance between UCNP and pH dye is close.²⁴⁵ As strategies to enhance the brightness of UCNPs improve, their use as probes in biosensing and other applications will increase.²⁴⁶ With the adaptability of the surface chemistry of UCNPs,¹⁴³ the method introduced here can be extended to a wide range of pH-sensitive molecules.

Chapter 4

Ratiometric sensing of pH in live cells

4.1 Introduction

Intracellular sensing of pH is of interest due to the impact of pH on cellular function and health, but it is particularly important in studies of endocytosis when outside material is moved into and around the cell. The endocytic pathway relies on vacuolar compartments that can degrade inside contents upon increasing acidification. Endocytic pathways can also be used for delivery of drugs and gene therapies as long as the cargo escapes into the cytosol before it is degraded.^{72,247} Observing the pH of these compartments is therefore critical for drug development studies.

Different ratiometric pH nanosensors using QDs,^{23,73,248} CDs,^{74,249} and PDs^{59,250,251} have been developed and tested, but these studies utilize short wavelength excitation, which encounters problems of autofluorescence, photodamage, and limited penetration depth. The NIR window is optically transparent for biological tissue, so it is a much better option as the wavelength range for excitation. Recently, upconversion-based nanoprobe that measure intracellular pH have been described in the literature,^{34,72,161,162} but they fall short on mapping pH quantitatively at the subcellular level or their range does not cover the lower end of pH found in lysosomes. In addition, UC-based pH sensing studies so far have not quantified colocalization with endosomes/lysosomes nor studied the endocytic method of uptake.

One of the issues is that some of the current equipment that is required for these studies is not set up for NIR excitation so, in this chapter, a new ratiometric imaging probe that is capable of sensing pH at the subcellular level was designed and developed. It can be excited directly or via the UCNP, which provides an intermediate proof of principle to stimulate future equipment development. The probe uses UCNPs conjugated to pHAb, a pH-sensitive dye that increases in fluorescence as the environment becomes more acidic (Figure 4.1). The absorption of pHAb coincides well with the green emission band of the UCNP, and the dye's

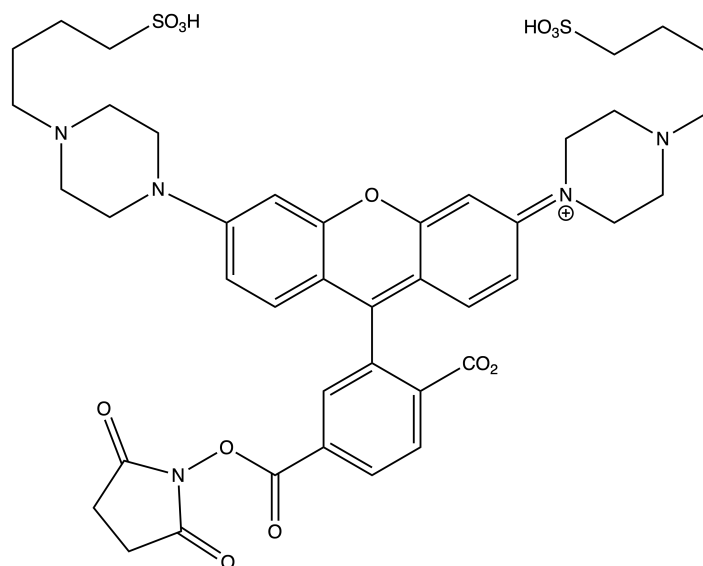


Figure 4.1: Molecular structure of pHAb amine reactive dye. The succinimidyl ester group here can react with primary amines to form an amide bond. Structure created with Chem-Draw.

emission varies from pH 4.0 to 6.0. This makes it ideal for sensing in acidic compartments like endosomes and lysosomes that are involved in endocytosis. After an evaluation of the pH response of the probes in buffer solution, the focus turned to their capability for ratiometric imaging. Colocalization studies were conducted to determine the subcellular location of the UCNP-pHAb nanoconjugates and pharmacological inhibitor studies helped determine the mechanism by which the nanosensors are taken up by the cells. Finally, cytotoxicity experiments were completed to ensure cell viability during the duration of the experiments.

4.2 Materials and methods

4.2.1 Materials

The pHAb amine reactive dye was purchased from Promega. DMSO (99+%) was from Alfa Aesar. Potassium chloride (99+%) and sodium bicarbonate (99+%) were from Acros Organics. Amine conjugation buffer was made by dissolving 0.084 g sodium bicarbonate in water, adjusting the pH to 8.5 using HCl/NaOH (100 mM), then adjusting the final volume to 100 mL with water. Citric acid monohydrate, disodium phosphate heptahydrate, and chlorpromazine hydrochloride ($\geq 98\%$) were purchased from Sigma-Aldrich. All cell culture media were purchased from Thermo Fisher Scientific. Nigericin sodium salt was from Cayman

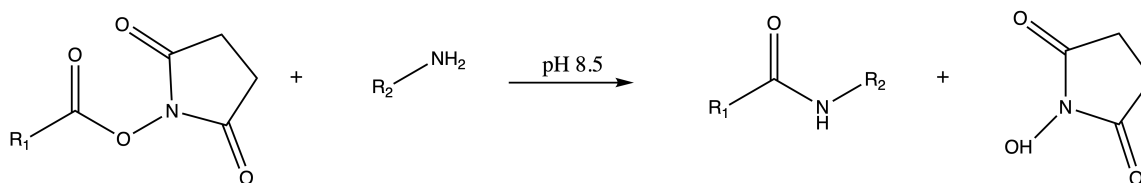


Figure 4.2: Succinimidyl ester and primary amine crosslinker chemistry. Diagram created with ChemDraw.

Chemical. Cell Navigator green fluorescence with 405 nm excitation lysosome staining kit was purchased from AAT Bioquest. Nystatin was obtained from BioVision. The resazurin-based alamarBlue cell viability reagent and Trypan blue solution (0.4%) were purchased from Thermo Fisher Scientific. SH-SY5Y cells were obtained from the MRC Stem Cell Institute (University of Cambridge).

4.2.2 Synthesis of UCNP-PEI-pHAb conjugate

The oleate-capped UCNPs were synthesized according to the high-temperature coprecipitation method and modified with PEI as described in Section 2.2. The pHAb amine reactive dye was quickly centrifuged (i.e., 14000x g using a tabletop centrifuge for 5-10 seconds) and dissolved at 10 mg/mL by adding 25 μ L of 1:1 DMSO-water mix. It was mixed by vortexing until the dye was dissolved completely (1-3 minutes). 5 mg of the PEI-coated UCNPs in amine conjugation buffer was mixed with the pHAb amine reactive dye in DMSO-water. The mixture underwent stirring for 60 min while protected from light. During this time, the succinimidyl ester on the pHAb dye reacts with the primary amine groups of the PEI to form a stable amide bond (Figure 4.2), and the basic environment minimizes any hydrolysis side reaction of the succinimidyl ester. The UCNP-PEI-pHAb conjugate was washed three times with water. Finally, it was suspended in water and stored at 4 °C.

4.2.3 Characterization of the pH nanoprobes

TEM images of the oleate-capped UCNPs were obtained with a 120 kV Philips CM12 transmission electron microscope (FEI). The images of the UCNPs were analyzed with ImageJ software (NIH) to obtain size distribution. Phosphate/citrate buffers of different pHs (0.2 M) were added to UCNP-pHAb solution (~1 mg/mL) in a 1:1 volume ratio. A Cary-Eclipse Fluorescence Spectrophotometer (Varian) was used to collect the emission spectra of UCNP-pHAb when the dye was directly excited. Instrument excitation and emission slits were both set at 5 nm, and the scan rate was 120 nm/min. All samples were excited at 532 nm, and the emission was scanned from 540 to 650 nm. The photomultiplier tube detector

voltage was set at 800 V. A QE65000 spectrometer (Ocean Optics) was used to obtain the luminescence spectra for the pH titration experiment wherein the UCNP was directly excited at 980 nm with a Spectra-Physics Mai Tai Ti:Sapphire NIR/IR laser (Newport). A 750 nm shortpass filter (Thorlabs) protected the detector from the laser. All spectra were recorded at room temperature. Binomial filtering with Igor Pro software (Wavemetrics) was used to smooth the spectra because it reduces noise while maintaining peak position.²⁵² The hydrodynamic diameter and zeta potential of the UCNP-pHAb were measured with a ZetaPALS (Brookhaven Instruments) at room temperature.

The lifetime measurements used the same setup as described in Section 3.2. A standard UV/VIS lamp (Type NU-4; 254 nm and 366 nm, 2 x 4 W) (Konrad Benda Laborgeräte) was used to illuminate the samples for 300 min for the photobleaching experiments. The samples for the original and photobleaching experiments were prepared by adding the UCNP-pHAb solution to phosphate/citrate buffer (1:1 volume ratio). The samples for the dilution experiments were diluted by one, five, and ten times. The decay fits were obtained with Prism 8 (GraphPad).

4.2.4 Multiphoton imaging of the pH nanoprobe

200 μL of agarose gel in phosphate-buffered saline (PBS) (2.5%) was mixed with 100 μL of UCNP-pHAb in water (1 mg/mL) at 90 °C. 100 μL of the resulting mixture was pipetted into an 8-well ibiTreat μ -Slide (Ibidi), placed in a refrigerator until solidified, then imaged with a TCS SP5 Confocal (Leica) equipped with a pulsed Chameleon Ultra II IR laser (Coherent). Three color channels were captured using HyD hybrid detectors (Leica): 500-550 nm (UCNP green emission), 565-630 nm (pHAb yellow emission), and 640-680 nm (UCNP red emission).

4.2.5 Multiphoton imaging of cells

SH-SY5Y cells were cultured at 37 °C in 5% CO₂ in Dulbecco's Modified Eagle Medium (DMEM) supplemented with 10% fetal bovine serum (FBS) and 1% penicillin/streptomycin in a 4-well ibiTreat Ph+ μ -Slide (Ibidi). 50k cells were plated in each well (700 μL) ~36 h before imaging then UCNP-PEI-pHAb conjugates in clear DMEM/F-12 (0.01 mg/mL) were added ~12 h before imaging. For in situ pH calibration, the intracellular pH was adjusted to that of the extracellular environment according to previously described protocols.^{72,253,254} Briefly, the cells were treated with citric acid/phosphate buffer of certain pH supplemented with 140 mM KCl and 10 μM nigericin then returned to incubation for 10 min. Multiphoton imaging was performed on a TCS SP5 Confocal (Leica) equipped with a

pulsed Chameleon Ultra II IR laser (Coherent). A CO₂ and temperature control incubator was placed on the microscope stage for live cell imaging. Three color channels were captured using HyD hybrid detectors (Leica): 500-550 nm (UCNP green emission), 565-630 nm (pHAb yellow emission), and 640-680 nm (UCNP red emission). Cell outlines were visualized with transmission detection. Control cells were imaged after ~12 h of incubation with UCNP-PEI-pHAb conjugates but were not exposed to pH buffer supplemented with KCl and nigericin.

MATLAB (Mathworks) was used for image processing and analysis, which were based on previously reported methods.²⁵³⁻²⁵⁶ After median filtering, a mask was created using a threshold obtained from Otsu's method. Using this mask, the pHAb (yellow channel) to UCNP (red channel) intensity ratio was calculated at each pixel. The average ratios were plotted as a function of pH to obtain a calibration curve. The ratiometric images were generated after the described masking had been applied. The intensity value of each pixel in the pHAb channel (yellow) was divided by that of the corresponding pixel in the UCNP channel (red). The image pseudocolors were rescaled according to the calibration curve, and a colorbar was applied to the image.

4.2.6 Confocal laser scanning imaging of cells

SH-SY5Y cells were cultured at 37 °C in 5% CO₂ in Dulbecco's Modified Eagle Medium (DMEM) (Thermo Fisher Scientific) supplemented with 10% fetal bovine serum (FBS) and 1% penicillin/streptomycin in a 4-well glass bottom μ -Slide (Ibidi) coated with poly-D-lysine. 50k cells were plated in each well (700 μ L) ~60 h before imaging then UCNP-PEI-pHAb conjugates in clear DMEM/F-12 (0.01 mg/mL) were added ~12 h before imaging. The lysosomal-staining solution was prepared by diluting the LysoBrite dye in the live cell staining buffer provided in the Cell Navigator kit (20 μ L:10 mL). 350 μ L of medium was taken out and replaced by 350 μ L of dye working solution then placed in the incubator for 30 min. Confocal laser scanning microscopy was performed on a TCS SP8 (Leica) equipped with a white light laser source and 405 nm diode laser. The LysoBrite dye was excited at 405 nm, and the pHAb dye was excited at 532 nm. Photomultiplier tubes (Leica) collected emission from 480-520 nm (cyan channel) and 565-630 nm (yellow channel). The imaging system was enclosed to maintain temperature at 37 °C and CO₂ at 5% for live cell imaging.

Fiji, an open-source image processing package, and Coloc 2, a plugin, were used for colocalization analysis.²⁵⁷ Using the image preprocessing and analysis methods outlined by Dunn et al.,²⁵⁸ background images were created for both channels in which the value of each pixel from the original image was replaced with the median intensity of a surrounding 26 \times 26 (yellow channel) or 32 \times 32 (cyan channel) pixel region. These background images

were then subtracted pixel-by-pixel from the original image to generate a median-subtracted image. To analyze intracellular vesicles, the region of interest (ROI) was defined as the cytoplasm, excluding the extracellular space and nucleus. The two probes, LysoBrite and pHAb, were designated C and Y , respectively. Manders' colocalization coefficients (MCCs) were then calculated for the ROI with the following equations:

$$MCC_1 = \frac{\sum_i C_{i,colocal}}{\sum_i C_i} \quad (4.1)$$

$$MCC_2 = \frac{\sum_i Y_{i,colocal}}{\sum_i Y_i} \quad (4.2)$$

where MCC_1 is the fraction of C in compartments containing Y and MCC_2 is the fraction of Y in compartments containing C . C_i and Y_i are the intensities of C and Y , respectively, at pixel i . $C_{i,colocal} = C_i$ if $Y_i > 0$ and $C_{i,colocal} = 0$ if $Y_i = 0$. $Y_{i,colocal} = Y_i$ if $C_i > 0$ and $Y_{i,colocal} = 0$ if $C_i = 0$.

Statistical tests were performed with Prism 8 (GraphPad) based on the significance tests of MCC measurements of colocalization described by McDonald et al.²⁵⁹ The expected MCC was the proportion of pixels above background. This value was subtracted from the observed MCC to obtain MCC_{diff} . The mean MCC_{diff} was compared to 0 using a Student's one-tailed, one-sample t-test, with the significance level set to 0.05.

4.2.7 Endocytosis experiments

The protocol for the endocytosis experiments was adapted from a method developed by Teplensky et al.²⁶⁰ The concentrations of chlorpromazine and nystatin were based on the ones that Qu et al. used with SH-SY5Y cells.²⁶¹

SH-SY5Y cells were cultured before being seeded on a 24-well plate at a density of 100,000 cells/well. After approximately 24 h, the cells were washed with PBS before a pretreatment 30 min incubation with different inhibitors in DMEM/F-12 without phenol red at 37 °C: untreated (200 μ L), chlorpromazine (200 μ L, 10 μ g/mL), nystatin (200 μ L, 25 μ g/mL). Afterwards, the medium was aspirated and replaced with a solution of UCNP-pHAb (0.1 mg/mL, DMEM/F-12 without phenol red) in each set of conditions: untreated (200 μ L), chlorpromazine (200 μ L, 10 μ g/mL), nystatin (200 μ L, 25 μ g/mL). The plate was incubated for 1.5 h at 37 °C. After incubation, the well contents were removed and washed three times with PBS. The cells were then incubated with trypsin for 5 min at 37 °C. Medium was added to the wells to stop the trypsinization, and the contents were transferred to tubes and centrifuged at 1300 rpm for 5 min. The cells were resuspended in 300 μ L of flow buffer (PBS with BSA). Samples were kept on ice until measurement with a CyAn

ADP flow cytometer (Beckman Coulter). The data were analyzed with FlowJo and Prism 8 (GraphPad) software. A longer incubation time of 3 h induced a cytotoxic response for the cells treated with chlorpromazine.

4.2.8 Linearity of alamarBlue

To determine the plating density and incubation time such that the alamarBlue cell viability assay is in the linear range, a serial dilution of SH-SY5Y cells was performed in a clear-bottom 96-well plate. The volume of cells plus medium was 100 μL . After the cells were incubated at 37 °C and in 5% CO_2 for 24 h, they were treated with alamarBlue reagent (10 μL of 10x solution) and placed back in the incubator. The fluorescence was measured 4 h later with a SpectraMax M2 (Molecular Devices) (λ_{ex} =560 nm, λ_{em} =590 nm). To minimize experimental errors, measurements were made from 6 replicates of experimental and no-cell control samples. The alamarBlue mechanism diagram was created with ChemDoodle (iChemLabs).

4.2.9 Cell viability assay with alamarBlue

SH-SY5Y cells (10,000 cells in 50 μL per well) were plated in a clear-bottom 96-well plate. After the cells were incubated at 37 °C and in 5% CO_2 for 6 h, they were treated with 50 μL of UCNP-pHAb solution (0.01 mg/mL or 0.001 mg/mL in DMEM/F-12, no phenol red) and incubated for another 18 h. The cells were then treated with alamarBlue reagent (10 μL of 10x solution) and placed back in the incubator for 4 h. The fluorescence was measured with a SpectraMax M2 (Molecular Devices) (λ_{ex} =560 nm, λ_{em} =590 nm). To minimize experimental errors, measurements were made from 6 replicates of experimental and no-cell control samples.

4.2.10 Cell viability assay with trypan blue exclusion assay

SH-SY5Y cells were plated in two wells of a 6-well plate. After the cells were incubated at 37 °C and in 5% CO_2 for 24 h, one well was treated with 2 mL of UCNP-pHAb solution (0.01 mg/mL in DMEM/F-12, no phenol red) and the other well was treated with 2 mL of DMEM/F-12 medium without phenol red. The cells were then incubated for another 24 h. The adherent cells were suspended using 2 mL of trypsin and gently triturated with a pipette to break up clumps. 0.1 mL of cell suspension was mixed with 0.1 mL of trypan blue solution. A hemocytometer chamber was filled with 15 μL of the mixture and viewed

under a light microscope. The number of viable (bright cells) and non-viable cells (stained blue) were counted, and the cell viability was calculated using the following formula:

$$\text{Percentage viability} = \text{Number of viable cells} / \text{Total number of cells} \times 100 \quad (4.3)$$

4.3 Results and discussions

4.3.1 Preparation and characterization of UCNP-pHAb sensor

UCNPs are an ideal candidate for reproducible, background-free, and self-ratiometric pH sensing in cells.¹⁶² As shown in the previous chapter, the multiple emissions of the UCNPs at different wavelengths allow ratiometric sensing via surface modification with pH indicators. The objective here is to use one band of the UCNP (green emission) to excite a pH sensitive moiety through energy transfer and the other band (red emission) to act as a reference for quantitative ratiometric measurements. While the anthraquinone dyes in Chapter 3 were superb quenchers, their pH-dependent fluorescence was poorly resolved when coupled to UCNPs. Ratiometric imaging could theoretically rely on the turn-off of the green UCNP emission band relative to the red reference UCNP emission band, but the turn-on of a separate analyte-dependent peak relative to a reference UCNP emission band could be much more sensitive for pH sensing in cells due to less background fluorescence. It also gives the opportunity for either the green or red band to be used as a reference (or both) and, for the study here, for the pH sensing dye to be excited directly or via the UCNP.

pHAb is a dye that strongly increases in fluorescence as the pH of the solution becomes more acidic. It was selected as the pH indicator because its absorption band overlaps well with the luminescence of Er^{3+} at 540 nm across intracellular pHs (Figure 4.3). Moreover, the pH-sensitive emission band of pHAb largely avoids the Er^{3+} luminescence at 650 nm, which functions as the reference signal. Thus, the strategy is to use the pHAb emission and red UCNP emission together in a sensing system for ratiometric intracellular pH imaging. Despite there being some overlap between the green UCNP and the dye emission in this particular configuration, the ability to reference to the red band provides a good analytical option. By examining Figure 4.3, it can be seen that a single wavelength intensity measurement at around 575 nm or an integration from circa 565-630 nm could be selected to largely avoid cross-talk.

A shell layer of inactive NaYF_4 was grown around the $\text{NaYF}_4: \text{Yb}^{3+}, \text{Er}^{3+}$ core to minimize the quenching effects of surface defects and solvent. The thickness of the shell

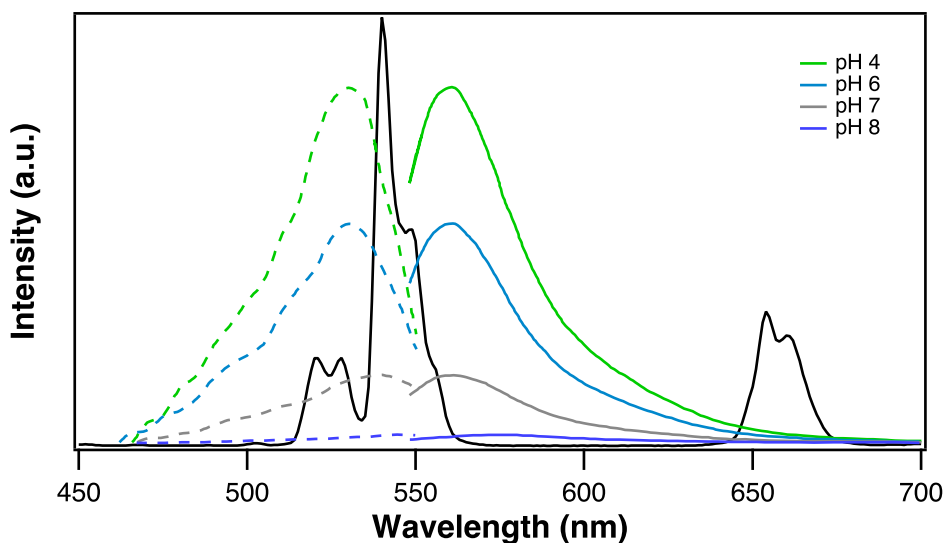


Figure 4.3: Overlaid excitation/emission spectra of UCNP and pHAb. The absorption (dashed) and emission (solid) spectra of pHAb (in color) are overlaid with the emission spectrum of thin-shell, PEI-coated UCNP (in black). The pHAb spectra were obtained from Promega.

was 1 nm (calculated from the TEM images in Figure 4.4) to balance between the thinness required for RET and the thickness that promotes bright luminescence. Branched, high molecular weight PEI was selected as the coating for its high dye loading capacity and ability to facilitate cellular uptake.^{34,72} PEI also provides the amine groups that can conjugate to the succinimidyl ester group of pHAb. Covalent attachment of pHAb to the surface of UCNPs minimizes dye leaching and also prevents the dye and UCNPs from localizing in different parts of the cells.¹⁶² Successful conjugation of pHAb to the UCNP was confirmed by the red color on the surface. From absorbance and ICP-OES measurements, this reaction was estimated to yield ~400 dye molecules per UCNP.

Even after conjugation to the UCNP, the pHAb dye retains its fluorescence response to pH change when directly excited (Figure 4.5). Moreover, there is no noticeable shift in the emission band. Figure 4.6 shows the emission spectra of UCNP-pHAb nanoconjugate in 0.2 M citrate/phosphate buffer from pH 4.0-6.0 under 980 excitation. Unlike the UCNP-CaR and UCNP-ARS combinations in Chapter 3, the UCNP-pHAb conjugate did not display a noticeable pH-dependent decrease in the 540 nm emission intensity. The sensitized emission of the pHAb dye is hardly observable in Figure 4.6a because the intensities of the UCNP luminescence are over 100-fold greater, but a zoom-in to the relevant wavelengths confirms a pH dependence of the dye both before and after binomial smoothing (Figure 4.6c,d). Due to the low signal-to-noise (SNR) ratio of the pHAb emission from the spectrometer detector,

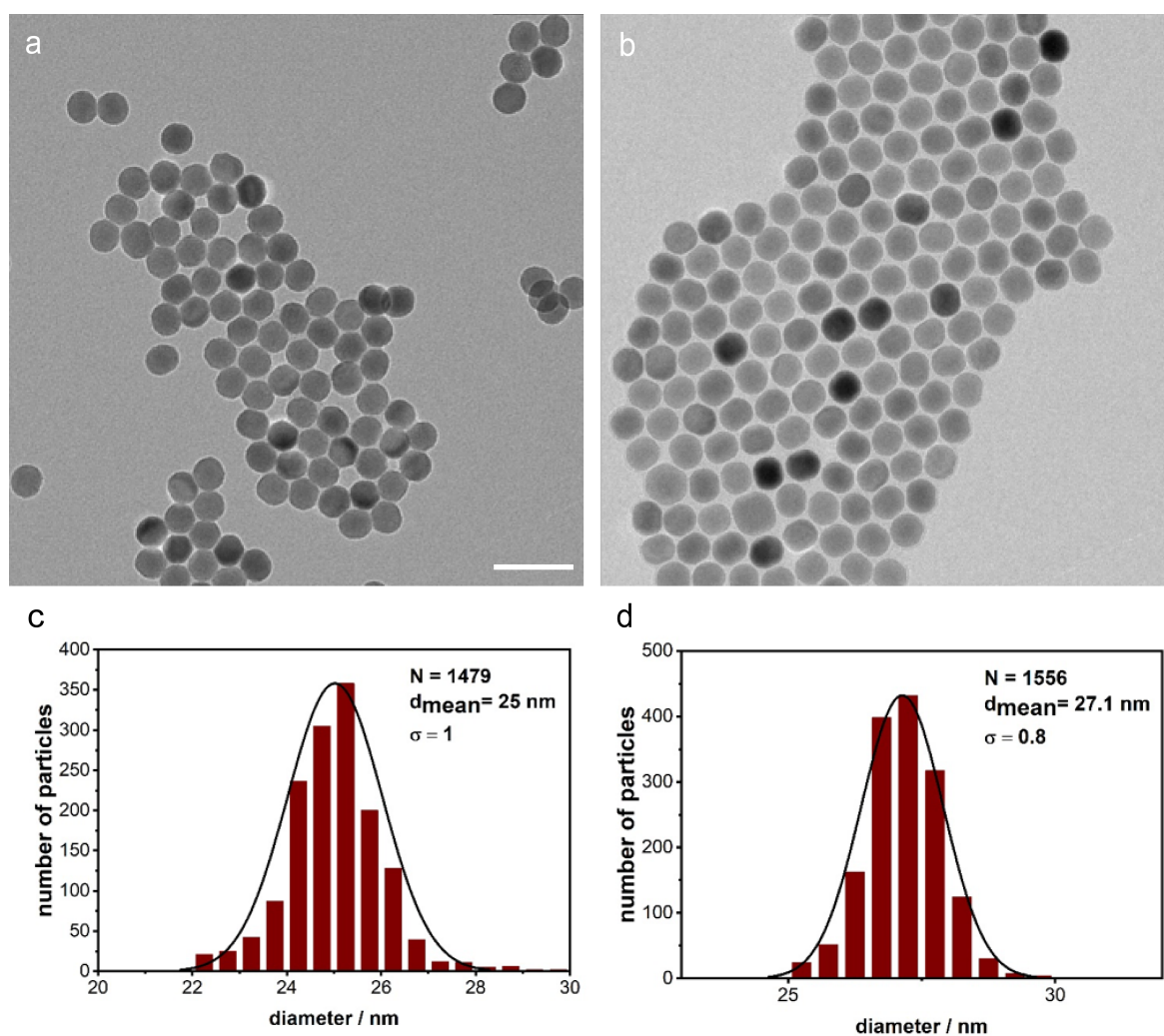


Figure 4.4: TEM images of monodisperse, oleate-capped (a) core NaYF_4 : 20% Yb, 2% Er and (b) core-shell NaYF_4 : 20% Yb, 2% Er@ NaYF_4 . The scale bars are 60 nm. Histograms of the size distribution from the TEM images are shown in (c) and (d) for the core and core-shell particles, respectively.

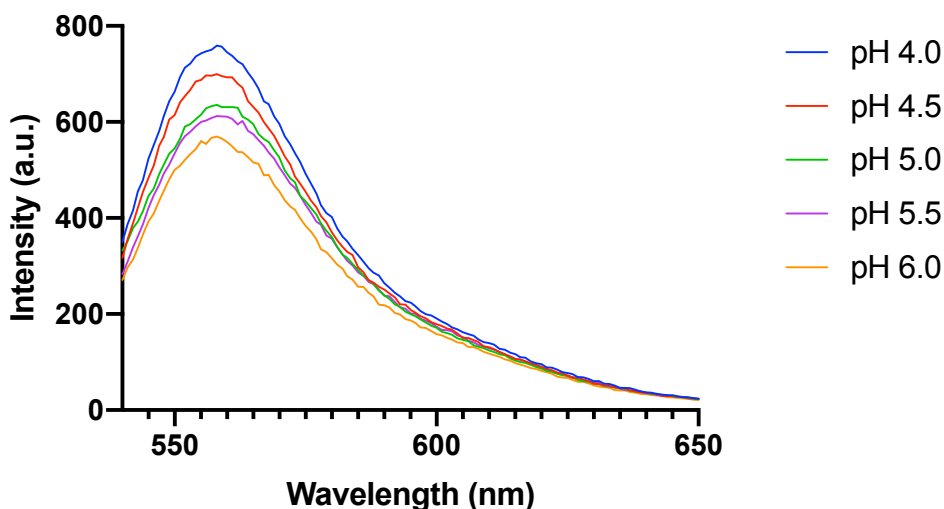


Figure 4.5: Emission spectra at various pHs when UCNP-pHAb in phosphate/citrate buffer is excited at 532 nm (direct excitation of the dye).

Table 4.1: Lifetimes of 540 nm green emission of UCNPs, diluted UCNP-pHAb, and photobleached UCNP-pHAb

	pH 4	pH 5	pH 6
UCNPs	$356 \pm 9 \mu s$	$329 \pm 5 \mu s$	$359 \pm 13 \mu s$
UCNP-pHAb (diluted)	$254 \pm 44 \mu s$	$248 \pm 9 \mu s$	$251 \pm 45 \mu s$
UCNP-pHAb (photobleached)	$282 \pm 11 \mu s$	$269 \pm 9 \mu s$	$250 \pm 26 \mu s$

a smoothing procedure was applied to more clearly illustrate the underlying pH-dependent trends. Binomial filtering was selected over other spectral smoothing methods like Savitzky-Golay because it has the property of negligible phase shift.²⁵² Figure 4.6b demonstrates similar peak positions to Figure 4.6a even after 50 passes. The UCNP-pHAb nanosensor showed a decreasing ratiometric response between pH 4.0 and 6.0 when titrated with buffer solution (Figure 4.7). The reference was the 650 nm emission of the UCNP because it does not participate in any energy transfer (Figure 4.3).

Lifetimes from the fluorescence decays of the 540 nm emission of the PEI-coated UCNPs and the pHAb-conjugated UCNPs were compared to determine whether a UC-RET mechanism occurred (Table 4.1). The green emission of the UCNPs had lifetimes that varied from 330-360 μs and did not show pH dependence between pH 4 and 6. Due to the high dye loading, it was not possible to measure the lifetime of the green luminescence of the UCNP-pHAb particles in a cuvette at the same concentration as that of UCNPs alone. Because only a small fraction of the cuvette was illuminated by the laser ($2 \times 1.5 \times 10$ mm) and the green light was only collected from the middle of the cuvette, the light had to pass

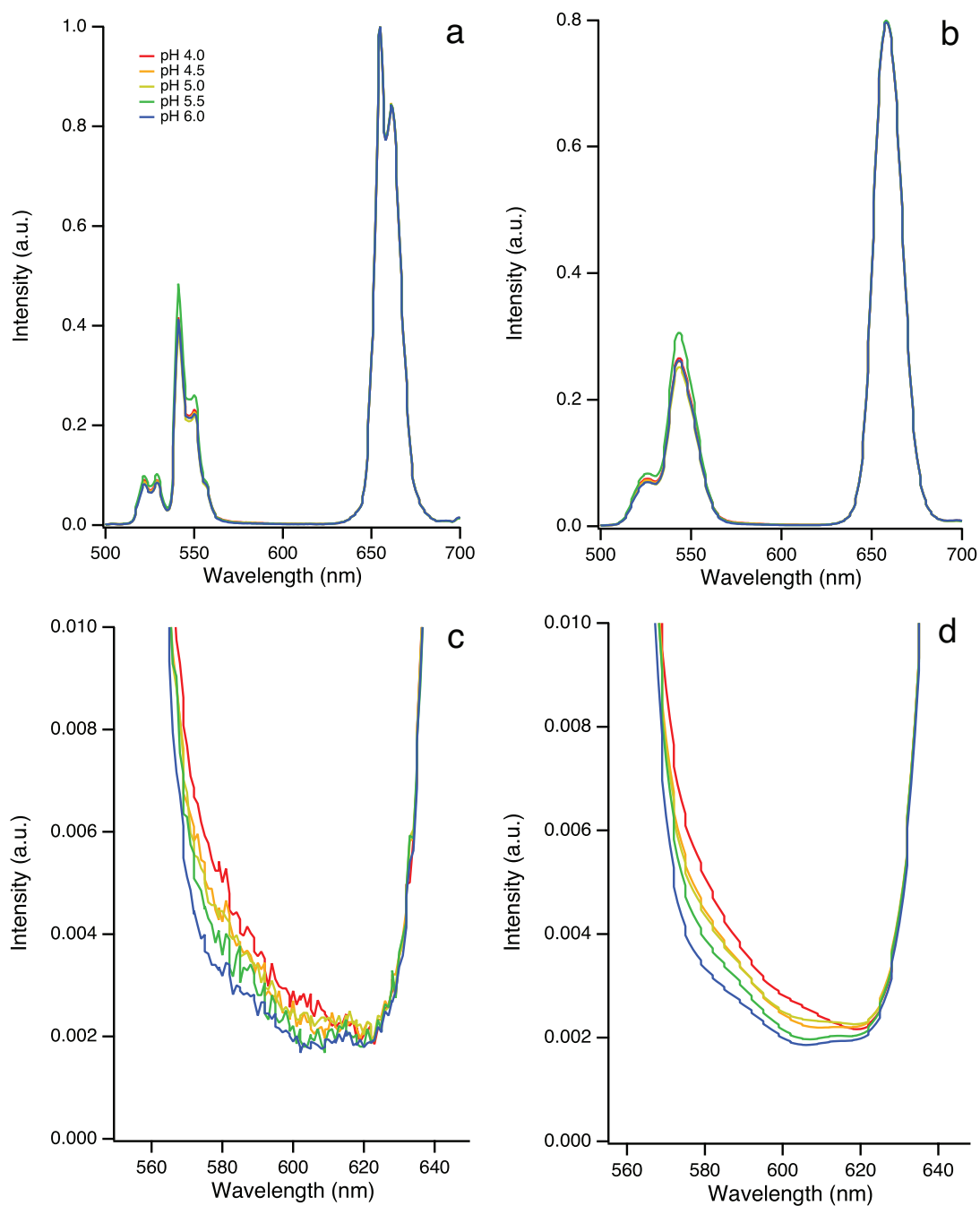


Figure 4.6: (a) Raw data of UCNP-pHAb spectra in 0.2 M phosphate/citrate buffer at pH 4.0, 4.5, 5.0, 5.5, and 6.0. (b) shows that 50 passes of binomial smoothing do not shift the positions of the peaks. (c) and (d) are the zoom-ins of the sensitized pHAb emission spectra from (a) and (b), respectively.

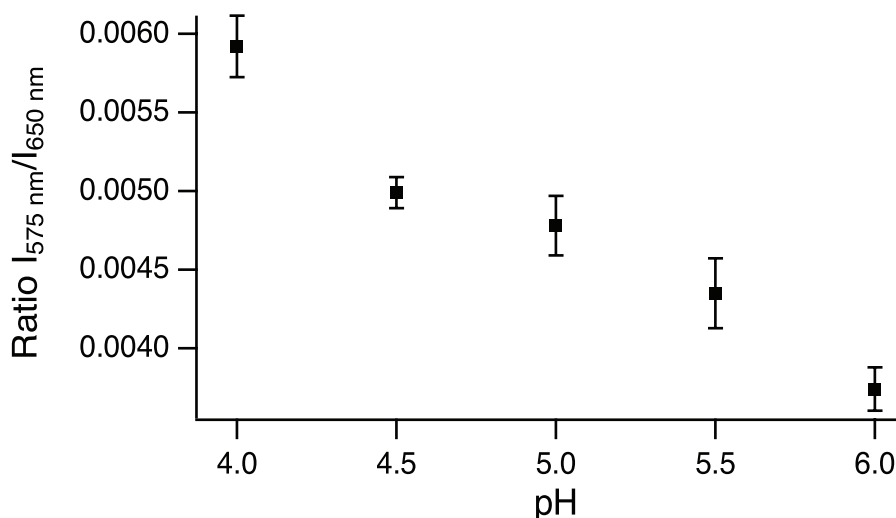


Figure 4.7: Ratiometric pH titration curves of UCNP-pHAb in 0.2 M phosphate/citrate buffer. The ratio of the intensities of the sensitized emission of pHAb at 575 nm and the reference emission of UCNP at 650 nm was calculated at each pH.

an additional 2.3 mm of solvent containing particles modified with dye. Too much of the green light was reabsorbed by the dye to obtain a sufficiently high photon count on the PMT. The lifetimes of the 540 nm green emission could be measured after the UCNP-pHAb in buffer solution was diluted ($\sim 250 \mu\text{s}$ from pH 4-6), yet the confidence intervals were wide because the fits were not unique (i.e. curves generated from other values of variables would fit almost as well) due to the low signal from the small concentration of sample. To further confirm that there was indeed a decrease in lifetime in the presence of the dye, the samples at the original concentration were photobleached with a UV-lamp to reduce the number of dye molecules available for reabsorption. The lifetimes of the 540 nm green emission ranged from 250-280 μs , indicating that there was still UC-RET with the lower acceptor to donor ratio and only a small fraction of the dyes was photobleached after 300 min of lamp illumination. The UC-RET efficiencies at different pHs were calculated with the UCNP and UCNP-pHAb (diluted) lifetimes using Equation 3.3. They ranged from 25-30% (Figure 4.8), which were significantly higher than the RET efficiencies of the UCNP-anthraquinone combinations studied in Chapter 3. The higher RET efficiency of UCNP-pHAb was likely due to the larger extinction coefficient of pHAb ($75,000 \text{ M}^{-1}\text{cm}^{-1}$) compared to CaR and ARS.

The colloidal stability of nanoparticles is important when they are dispersed in aqueous media for cellular applications. As described in Chapter 2, the highly positively charged PEI coating provided the particles with a zeta potential of +36 mV. Generally, nanoparticles with

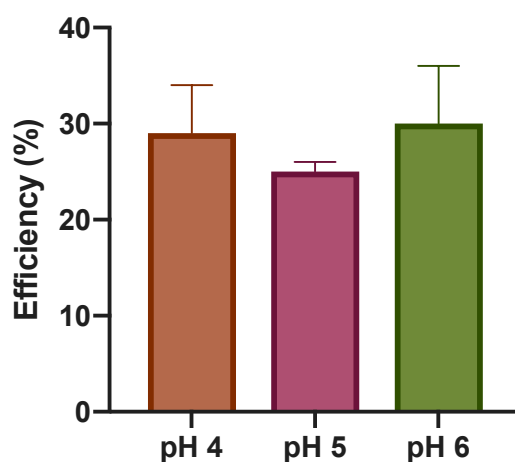


Figure 4.8: UC-RET efficiency values for UCNP-pHAb at pH 4, 5, and 6. The bars represent the mean values from three independent measurements, and the error bars correspond to ± 1 standard deviation.

a zeta potential below -30 mV or above $+30$ mV have sufficient electrostatic stabilization such that they do not aggregate quickly.⁷² The DLS measurements confirmed this in Chapter 2. UCNP-PEI had a hydrodynamic diameter of ~ 90 nm with PdI < 0.190 , indicating high monodispersity. After pHAb conjugation, the particles had two size distribution peaks of 141 ± 10 (s.d.) nm and 481 ± 33 (s.d.) nm, of which the latter suggested some aggregation (Figure 4.9). This slight decrease in colloidal stability is due to the lower zeta potential of $+22$ mV, which indicates less stabilization by electrostatic repulsion. The decrease in zeta potential is expected because the primary amine groups of PEI convert to amide linkages after reacting with the succinimidyl ester group of the pHAb dye.²⁶²

Endocytosis describes the internalization of extracellular material whereby a portion of plasma membrane surrounds the material, then a vesicle with the ingested content buds off inside the cell.²⁶³ Most nanomaterials are ingested this way.²⁶⁴ In general, particles that are $< 5 \mu\text{m}$ in size can be internalized by cells through endocytosis.²⁶⁵ The nanoparticle needs to be small enough to diffuse easily through the cell matrix yet large enough to ensure sufficient interaction with cell membrane surface receptors.²⁶⁶ In any case, most adherent cell lines should spontaneously take up the UCNP-pHAb by endocytosis because it still has an excess of free amines to give the particles a net positive charge and it has suitable size distribution,^{267,268} so alternative approaches of introducing the nanosensors into cells, such as microinjection²⁶⁹ or particle bombardment,^{270–272} were not considered here.

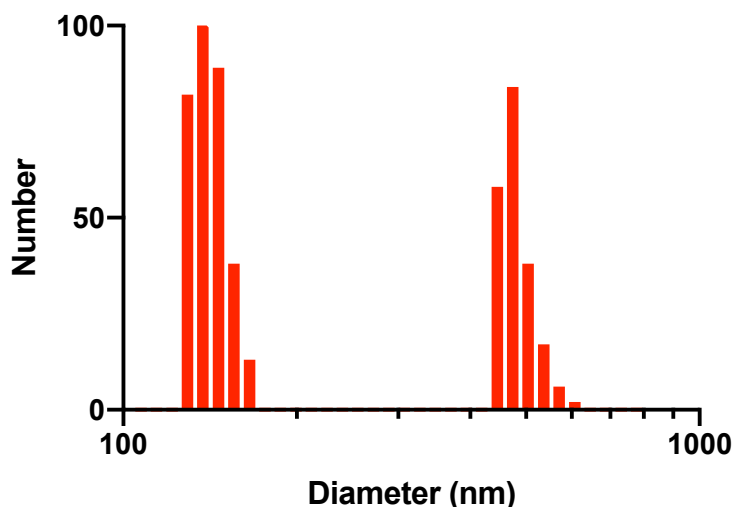


Figure 4.9: Number-weighted histogram of particle diameters obtained from DLS.

4.3.2 Calibration of the UCNP-pHAb nanoprobe

Before proceeding with the in situ calibration and in vitro validation of the pH nanosensor, the UCNP-pHAb conjugate was imaged on its own. The aim was to confirm the feasibility of using the probe for optical imaging with a Leica SP5 confocal fluorescence microscope. Green (500-550 nm), yellow (565-630 nm), and red (640-680 nm) emission channels were acquired upon 980 nm excitation of UCNP-pHAb conjugate in agarose gel. These channel ranges were selected to minimize cross-talk: even though the emission maximum for pHAb is at 560 nm, there is still ~4% signal intensity of the UCNP green emission peak at that wavelength compared to ~0.3% at 565 nm (Figure 4.3).

Single particles could not be resolved under these conditions, yet the largest nanosensor aggregates in agarose gel could be viewed under the microscope (Figure 4.10). The green channel is the 540 nm emission of the UCNP, the yellow channel is the 560 nm emission of the pHAb, and the red channel is the 650 nm emission of the UCNP. The pHAb dye was not directly excited at 532 nm, indicating that the UCNP transferred energy to the dye as a result of the overlap between the absorption spectra of the pHAb dye and the emission spectrum of the UCNP.

Proper calibration of pH nanosensors for quantitative intracellular sensing is not a trivial task. Many instances of prior work on upconversion pH nanoprobe calibrate by measuring the luminescence spectra of the probes in cells with a spectrofluorometer,¹⁶¹ directly applying the calibration curve from pH titration of the nanosensor alone in buffer to fluorescent imaging in cells,²⁷³ or limiting their calibration to buffers only,³⁴ but these all have downsides. Although spectrofluorometer measurements are highly reliable, they do

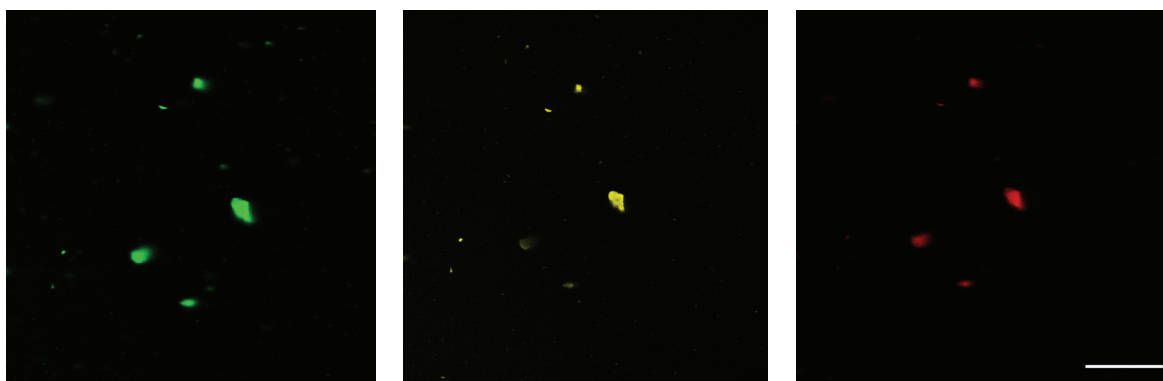


Figure 4.10: Confocal fluorescence microscope images of the green, yellow, and red emission of UCNP-pHAb conjugate in agarose gel. The brightness was increased with Photo-shop. Scale bar is 50 μm .

not show spatial resolution.²⁷⁴ Applying the calibration curve obtained from one system to measure samples in another does not always translate well; performing in situ calibrations that match the conditions to be used for each experiment is recommended instead.^{29,275} Lastly, the nanosensor should be tested in cellular environments that resemble where the actual experimental measurements will take place because of the possibility that its performance is diminished by the presence of ions or macromolecules inside the cells. For these in situ calibrations, an ionophore such as nigericin is introduced after the nanosensor has been taken up by the cells, then live-cell images are taken with a confocal microscope.²⁶⁷

Nigericin is impermeable to the membrane in its anionic form but becomes permeable as a neutral complex when its carboxyl group is bounded to a K^+ cation or H^+ proton.²⁷⁶ For example, an electroneutral K^+ efflux cycle leads to acidification of the cytosol. Nigericin binds to H^+ on the extracellular side, passes through the cell membrane as nigericin-H, and releases the proton inside the cell. The ionophore then binds to K^+ , goes back across the membrane as nigericin-K, and releases the cation outside of the cell.²⁷⁷ The KCl concentration of phosphate/citrate buffer matches that inside the cells so the difference between extracellular and intracellular proton levels drives the equilibration of pH across the cell membranes (i.e. $[\text{K}^+]_e / [\text{K}^+]_i = [\text{H}^+]_e / [\text{H}^+]_i$).^{267,278}

Figures 4.11-4.15 display the 500-550 nm (UCNP green), 565-630 nm (pHAb yellow), and 640-680 nm (UCNP red) channels of UCNP-pHAb conjugates in SH-SY5Y cells equilibrated to pH 4.0, 4.5, 5.0, 5.5, and 6.0 in separate wells. It is clear that the UCNP-pHAb conjugates were taken up by the cells since signals from the nanoparticle (green and red fluorescence) and dye (yellow fluorescence) can be seen at all five pHs. In addition, no signals were observed outside the cells after the three PBS washes, indicating that the probes do not leach from the cells during the time it takes to perform the experiments. The transmission

images in Figures 4.11-4.15d indicate healthy, adherent SH-SY5Y cells characteristically extending their neurites and spreading.^{279–281}

When the extracellular pH increases, the fluorescence images acquired suggest the consequent changes of pH inside the cells: the ratio of the intensity collected from the yellow channel to that from the red channel decreases until there is nearly no signal intensity in the yellow channel at pH 6.0 (Figure 4.15c). The respective green and red channels (Figure 4.11-4.15a,c) remain roughly the same intensity across the different pHs, with minor variations and drifts caused by variations in probe concentration and differences in imaging conditions (e.g. focus shift) that can be canceled out by ratiometric methods.^{282,283}

These fluorescence images were collected with 2-fold frame accumulation to increase overall brightness to more easily compare the similarities and differences at the various pHs, but the actual ratiometric analysis and pH calibration curve generation were performed on images without frame accumulation (Figure B.2, Appendix B) to avoid saturation, which causes loss of information in the brightest areas of the sample. The image lookup table (LUT) in the Leica confocal laser scanning microscope software, which shows pixels of zero intensity in one color and saturated pixels in another color, was used during imaging to verify that the intensity data were collected in a quantitative manner.²⁸⁴

The average yellow/red signal was calculated at the different pHs. These values were then fitted to a linear equation, producing the calibration curve shown in Figure 4.16. The ratiometric images of the cells equilibrated to the various pHs (Figure 4.17) show a clear decrease of intracellular pH as the pH of the external environment decreases. This lanthanide-based upconverting pH imaging probe is unique in its acidic sensing range down to pH 4.0; more commonly, probes have been designed and validated at higher pH ranges.¹⁶²

The UCNP-pHAb conjugates were next used to measure the pH values of various intracellular compartments in SH-SY5Y cells (Figure 4.18). The nanoprobe was taken up by the cells without requiring the addition of other compounds or other means of stimulating uptake, which is likely due to the PEI coating.¹⁶² After overnight incubation, the nanosensors were mostly in acidic compartments (pH ~4.0). However, different signal ratios still appeared in different spaces of the cells; yellow (pH ~4.0) points are next to those that are turquoise (pH ~5.0) and violet (pH ~6.0). These results indicate that the intracellular pH is not homogeneous and the UCNP-pHAb conjugates possess high spatial resolution.

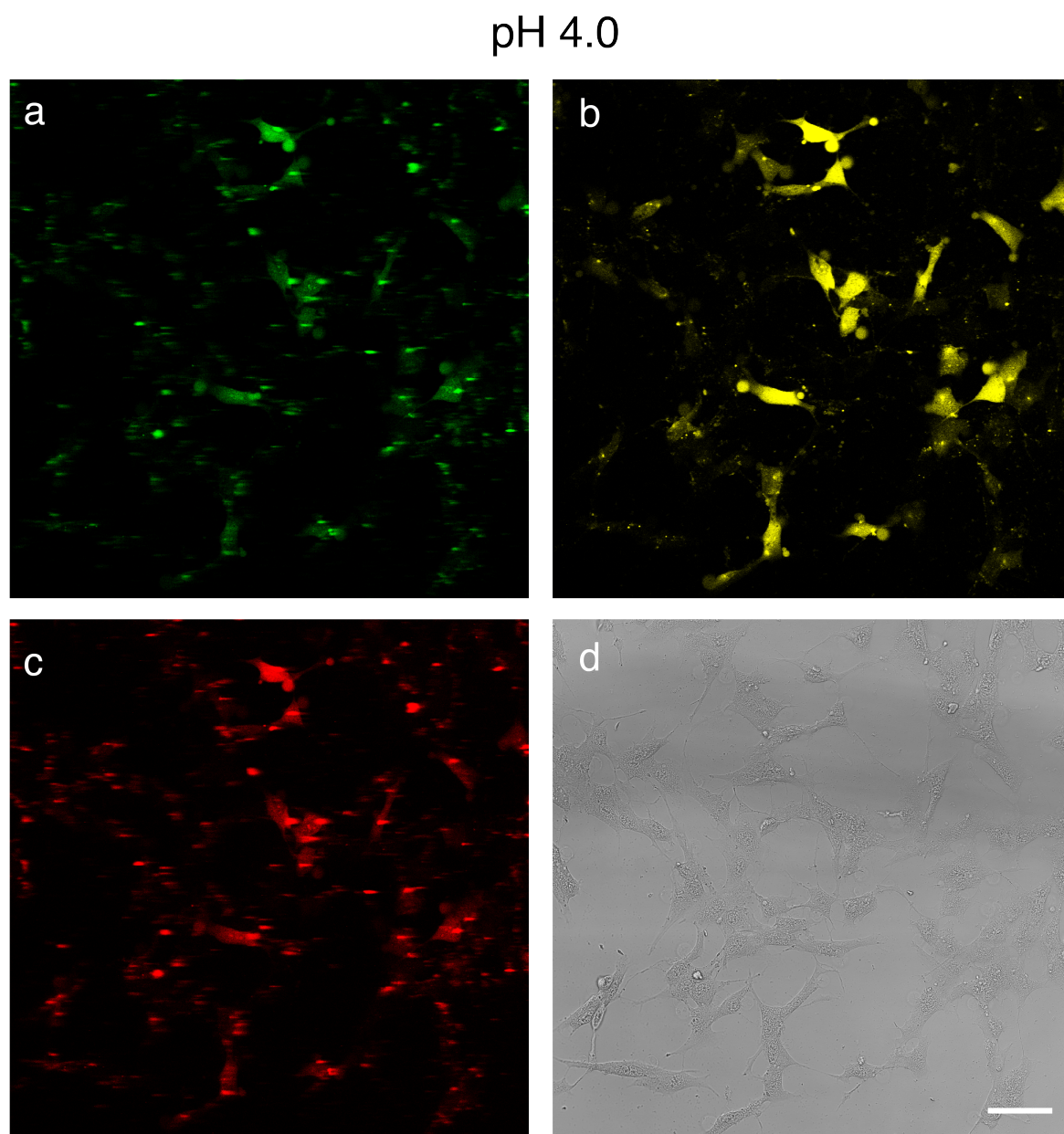


Figure 4.11: Multiphoton confocal microscopy images of UCNP-pHAb in nigericin-treated SH-SY5Y cells exposed to citric acid/phosphate buffer with KCl at pH 4.0. The excitation wavelength was 980 nm, and the images were collected with 2x frame accumulation in the ranges of 500-550 nm (UCNP green), 565-630 nm (pHAb yellow), and 640-680 nm (UCNP red). The corresponding transmission image is also shown. Using Photoshop (Adobe), the green, yellow, and red images were enhanced to +50 brightness and the transmission image was adjusted to +100 contrast. Original images are shown in Figure B.1 (Appendix B). Scale bar = 50 μm .

pH 4.5

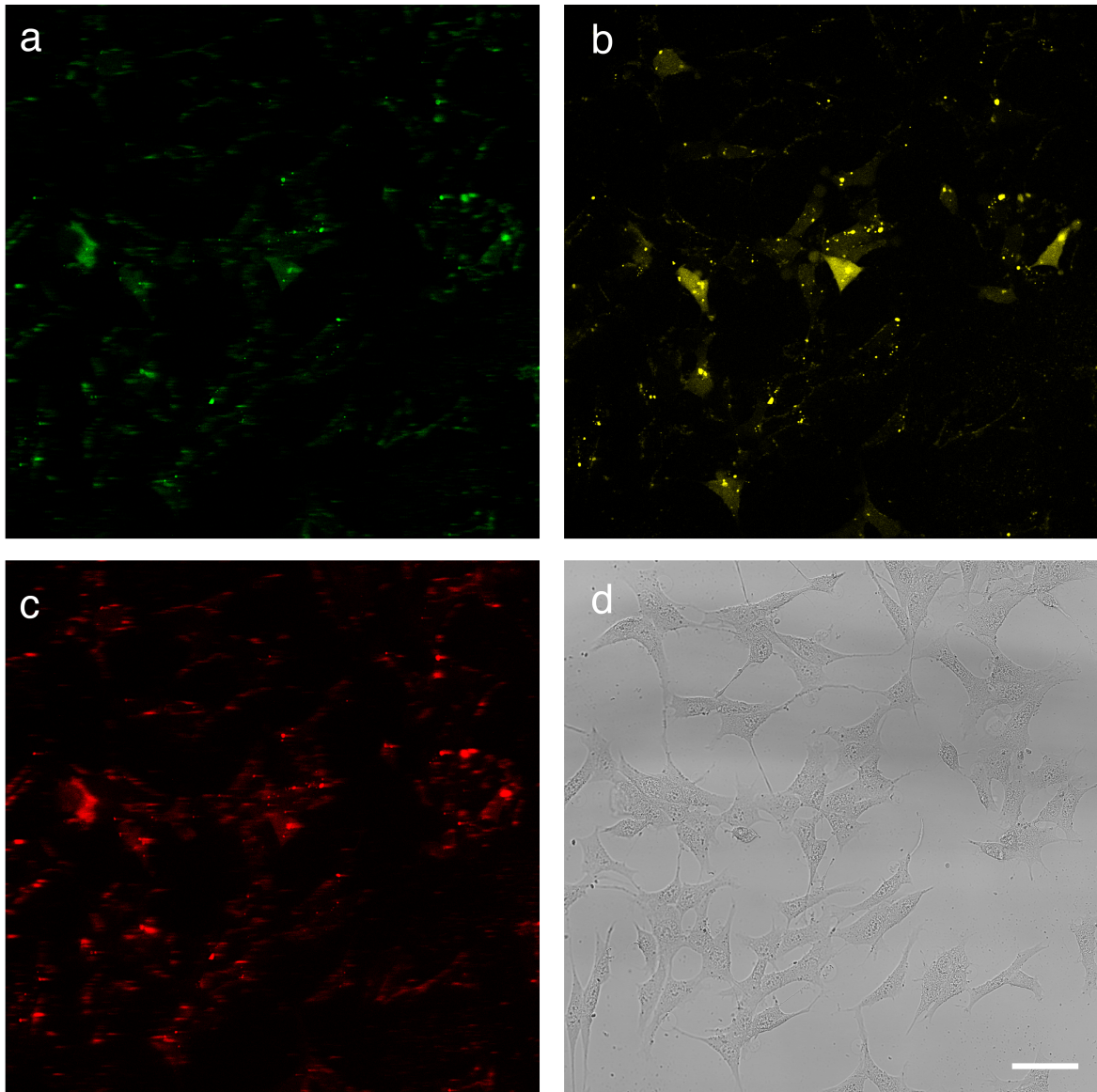


Figure 4.12: Multiphoton confocal microscopy images of UCNP-pHAb in nigericin-treated SH-SY5Y cells exposed to citric acid/phosphate buffer with KCl at pH 4.5. The excitation wavelength was 980 nm, and the images were collected with 2x frame accumulation in the ranges of 500-550 nm (UCNP green), 565-630 nm (pHAb yellow), and 640-680 nm (UCNP red). The corresponding transmission image is also shown. Using Photoshop (Adobe), the green, yellow, and red images were enhanced to +50 brightness and the transmission image was adjusted to +100 contrast. Original images are shown in Figure B.1 (Appendix B). Scale bar = 50 μm .

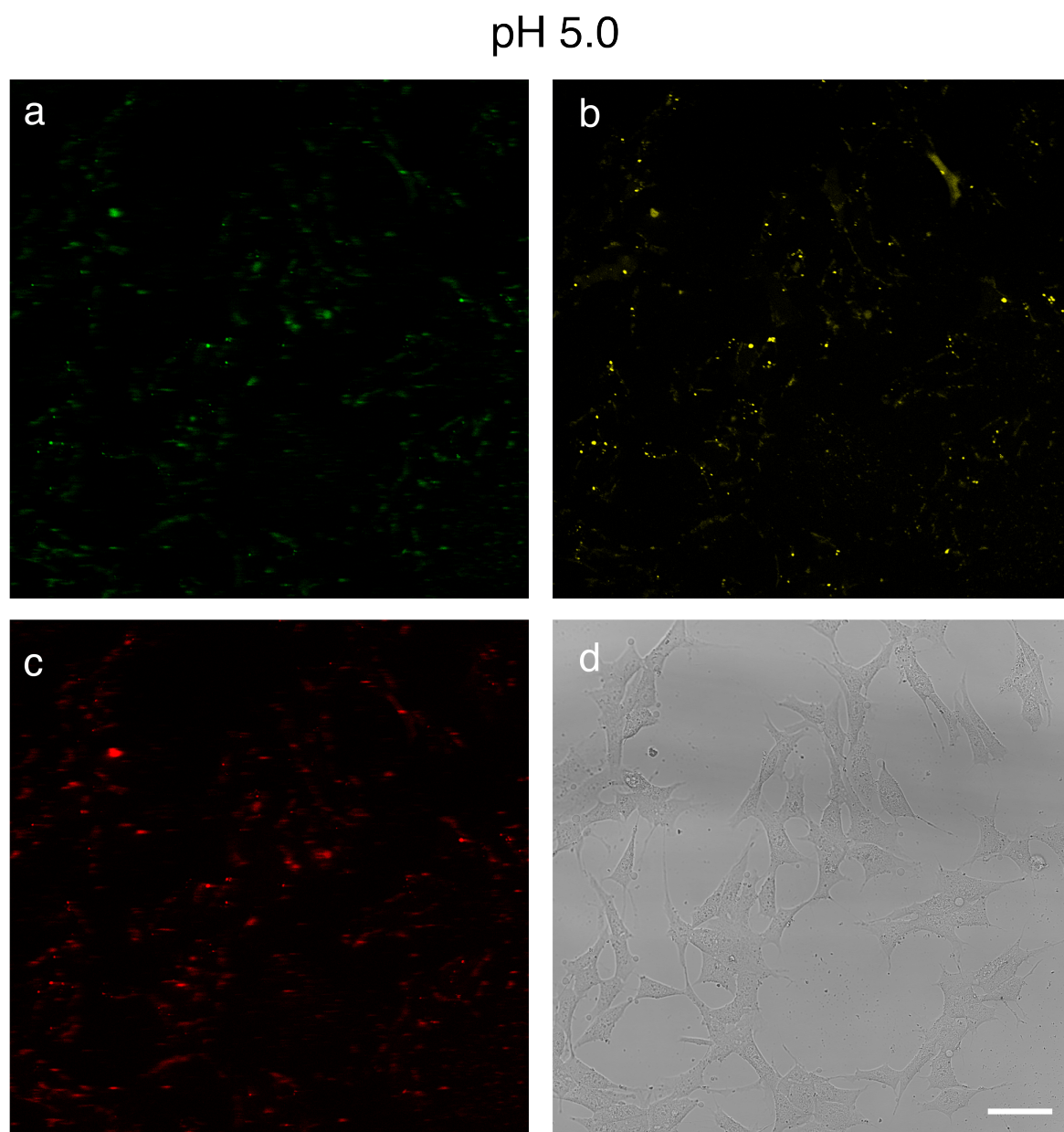


Figure 4.13: Multiphoton confocal microscopy images of UCNP-pHAb in nigericin-treated SH-SY5Y cells exposed to citric acid/phosphate buffer with KCl at pH 5.0. The excitation wavelength was 980 nm, and the images were collected with 2x frame accumulation in the ranges of 500-550 nm (UCNP green), 565-630 nm (pHAb yellow), and 640-680 nm (UCNP red). The corresponding transmission image is also shown. Using Photoshop (Adobe), the green, yellow, and red images were enhanced to +50 brightness and the transmission image was adjusted to +100 contrast. Original images are shown in Figure B.1 (Appendix B). Scale bar = 50 μm .

pH 5.5

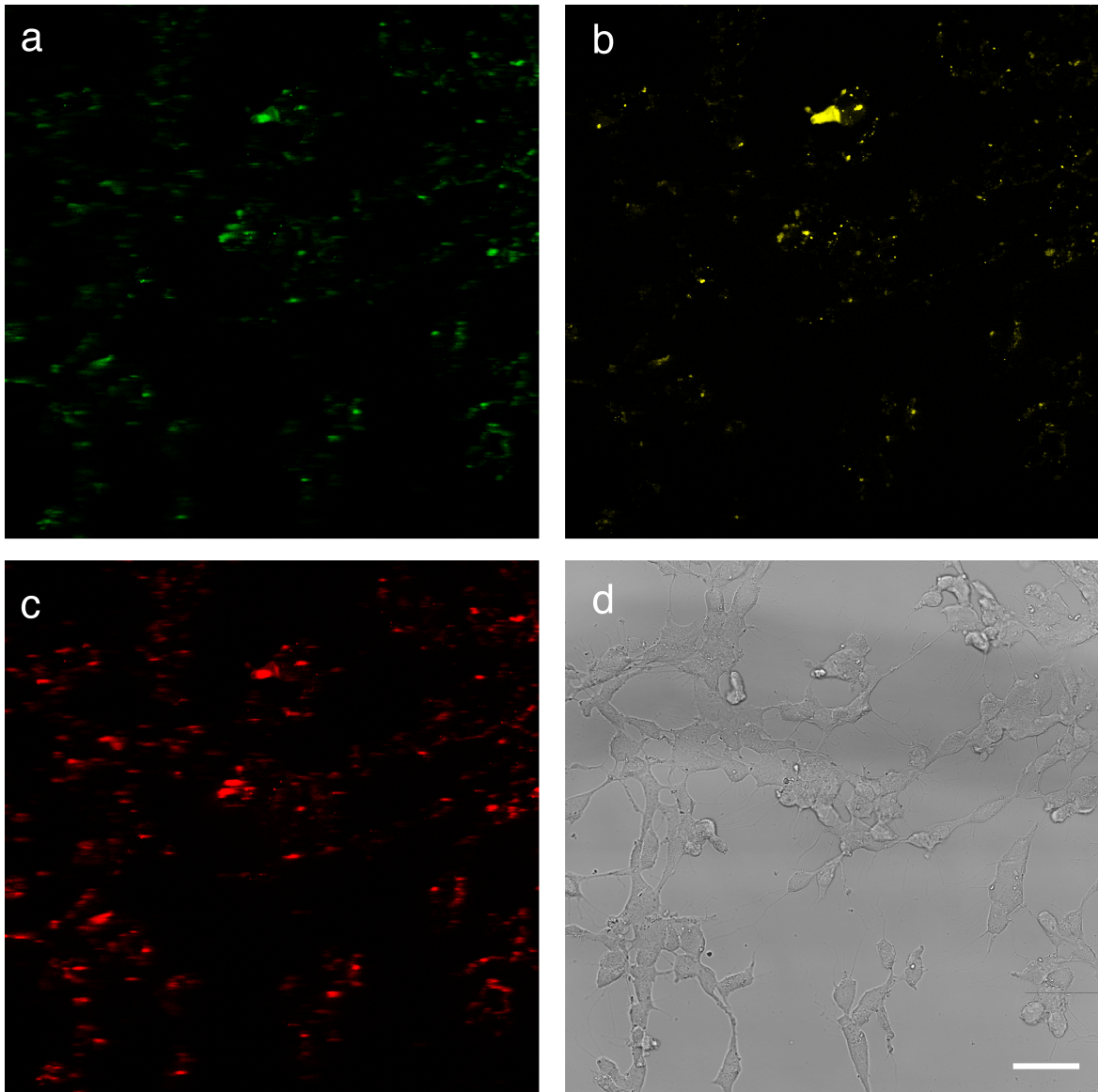


Figure 4.14: Multiphoton confocal microscopy images of UCNP-pHAb in nigericin-treated SH-SY5Y cells exposed to citric acid/phosphate buffer with KCl at pH 5.5. The excitation wavelength was 980 nm, and the images were collected with 2x frame accumulation in the ranges of 500-550 nm (UCNP green), 565-630 nm (pHAb yellow), and 640-680 nm (UCNP red). The corresponding transmission image is also shown. Using Photoshop (Adobe), the green, yellow, and red images were enhanced to +50 brightness and the transmission image was adjusted to +100 contrast. Original images are shown in Figure B.1 (Appendix B). Scale bar = 50 μm .

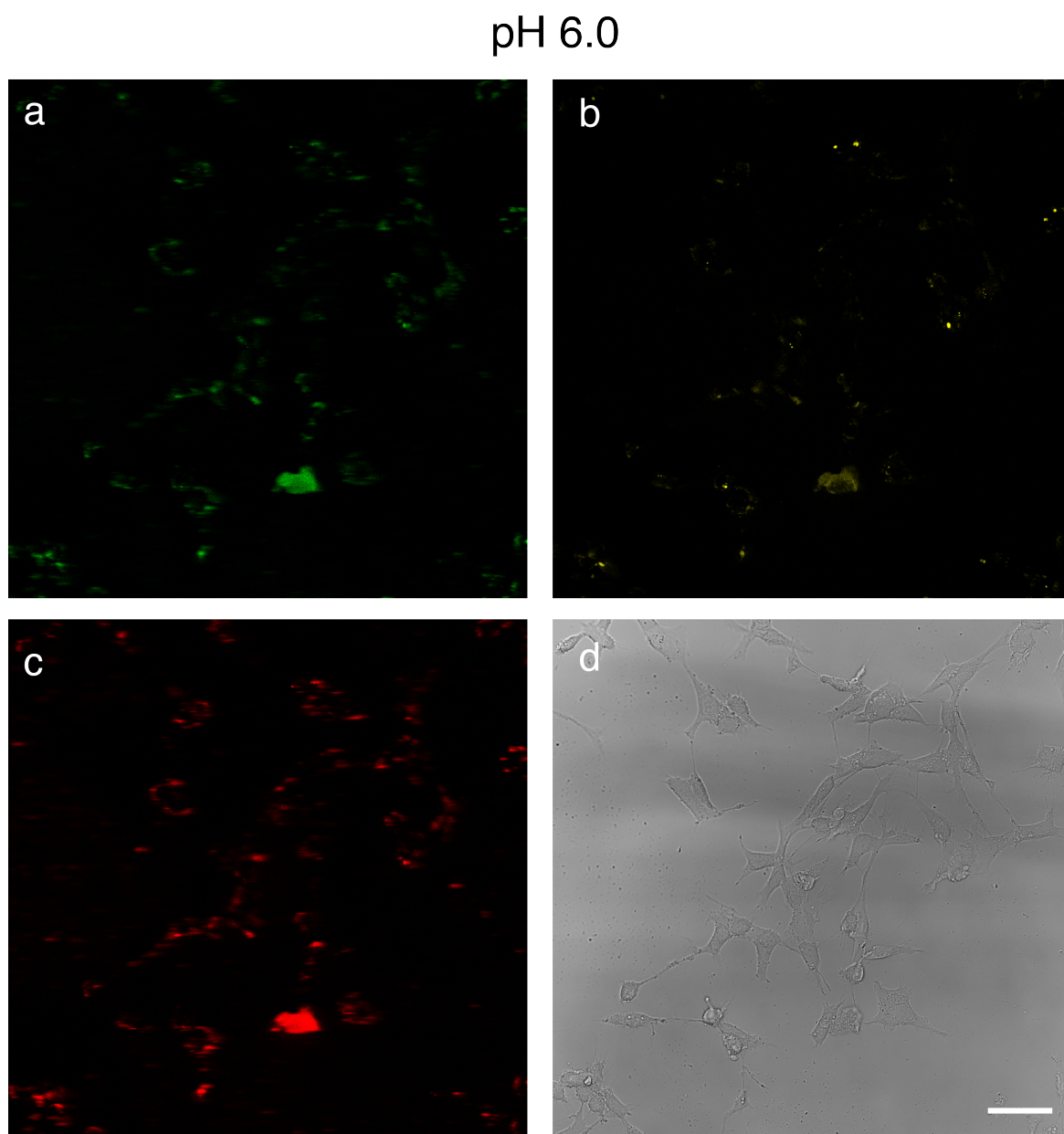


Figure 4.15: Multiphoton confocal microscopy images of UCNP-pHAb in nigericin-treated SH-SY5Y cells exposed to citric acid/phosphate buffer with KCl at pH 6.0. The excitation wavelength was 980 nm, and the images were collected with 2x frame accumulation in the ranges of 500-550 nm (UCNP green), 565-630 nm (pHAb yellow), and 640-680 nm (UCNP red). The corresponding transmission image is also shown. Using Photoshop (Adobe), the green, yellow, and red images were enhanced to +50 brightness and the transmission image was adjusted to +100 contrast. Original images are shown in Figure B.1 (Appendix B). Scale bar = 50 μm .

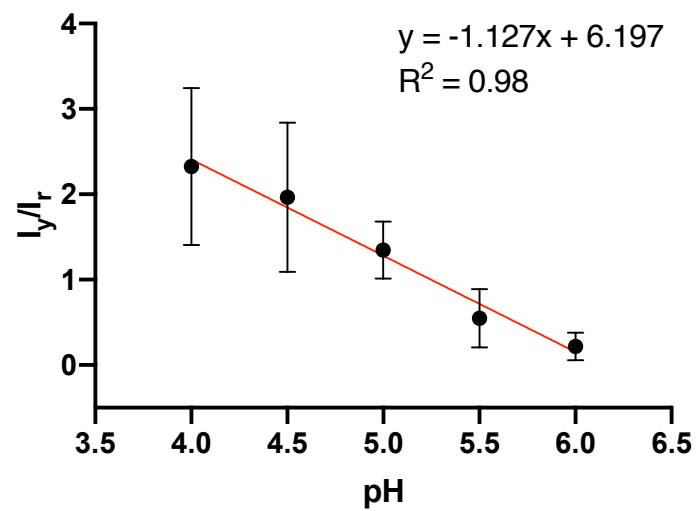


Figure 4.16: pH calibration curve of UCNP-pHAb in SH-SY5Y cells, based on the average of the ratio of yellow (I_y) to red (I_r) fluorescence intensity at each pixel of interest.

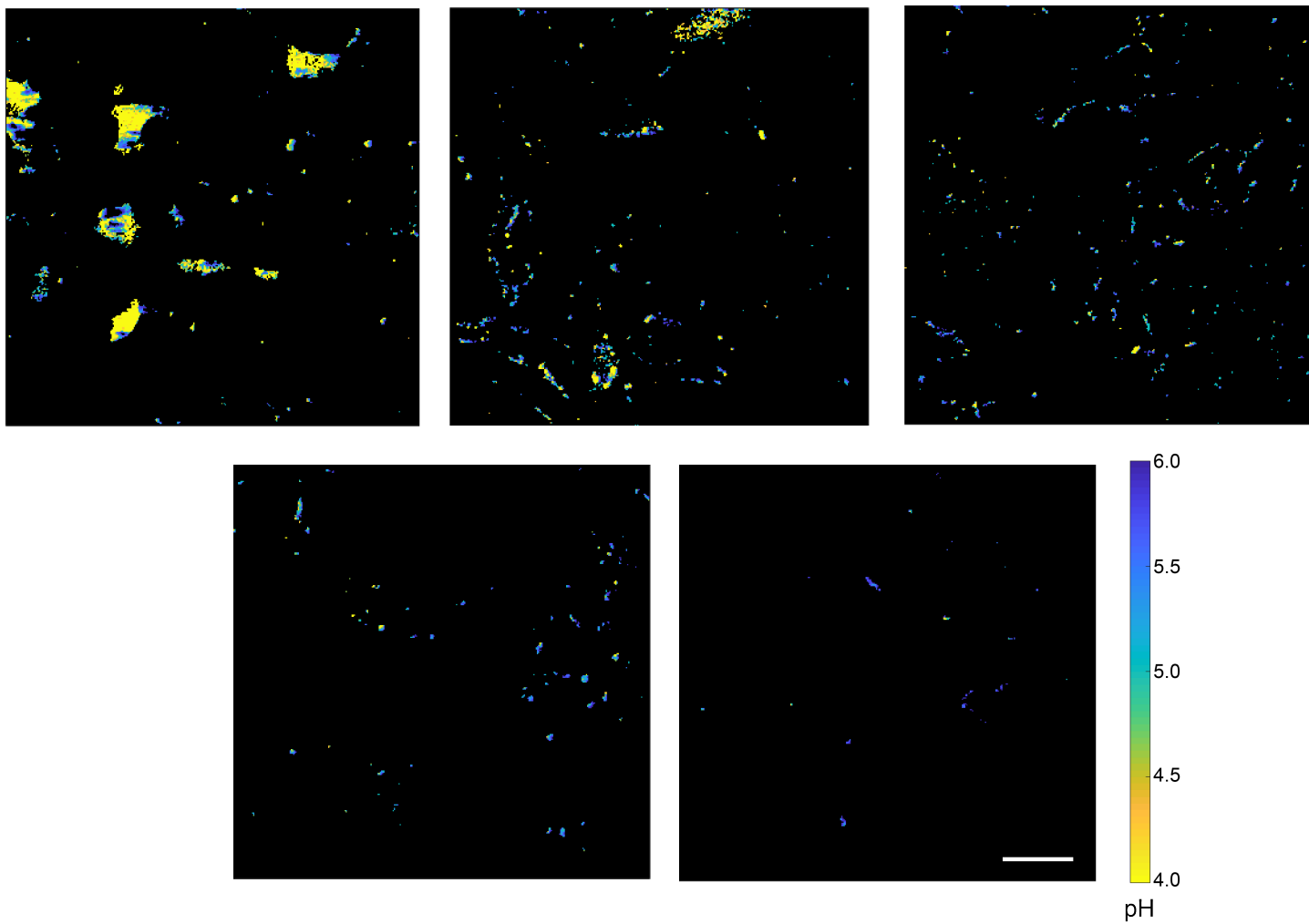


Figure 4.17: Ratiometric images of UCNP-pHAb in SH-SY5Y cells at pH 4.0, 4.5, 5.0, 5.5, and 6.0. The colorbar shows the pseudocolor change with pH. Scale bar = 30 μm .

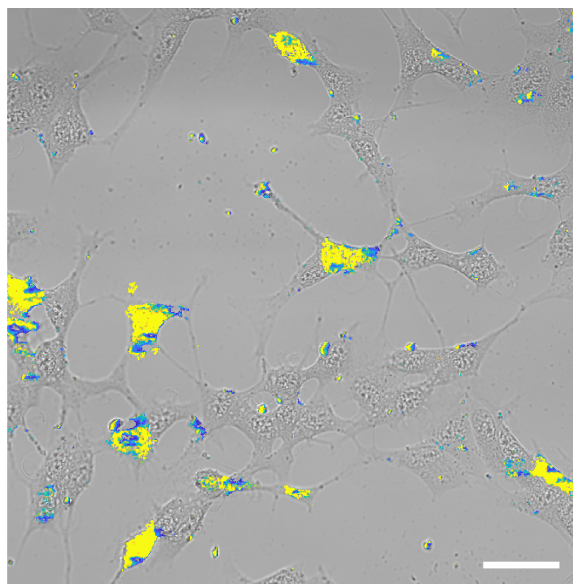


Figure 4.18: Pseudocolor ratiometric images of UCNP-pHAb in various intracellular compartments of SH-SY5Y cells overlaid with transmission images obtained through multiphoton confocal microscopy. The color scale is the same as that used in Figure 4.17. Scale bar = 30 μm .

The sensitivity of the nanosensor was 1.1/unit pH (defined as the slope of the linear calibration curve), which was an improvement over the sensitivity of 0.65/unit pH obtained in a recently reported intracellular pH imaging probe by Du et al. that used lanthanide-doped upconverting nanoparticles conjugated to fluorescein.¹⁶² While their nanoprobe was responsive from pH 5.0 to 7.4 in live cells, the nanosensor described here performs well from pH 4.0 to 6.0, covering the range of pHs encountered in the endosomal/lysosomal cycle that would be important for drug degradation studies. The error bars in Figure 4.16 are admittedly still large at the lower end of the pH range. This appears to be a common problem that previously reported ratiometric pH biosensors also encountered.²⁵³ Other times, error bars were not reported when the average ratiometric signal calculated from images of cells incubated with the nanosensors was plotted against pH.^{78,162} Resolution is an important characteristic of a sensing system that is influenced by the standard deviations of measurements. Based on the calculations performed by Sedlmeier et al.,²⁸⁵ the resolution was defined as the ratio between the standard deviation at a specific pH and the slope of the fit. The averaged resolution here was 0.5 unit pH, which was comparable to the 0.7 unit pH resolution obtained by a recent ratiometric pH biosensor from Richardson et al. that fitted \log_{10} ratio values to a linear equation.²⁵³

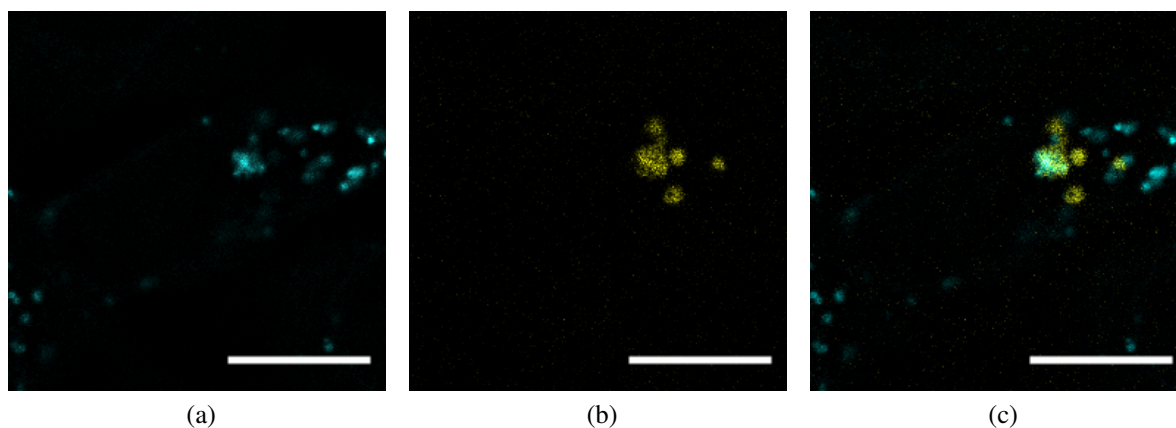


Figure 4.19: Images of SH-SY5Y cells incubated with UCNP-pHAb and LysoBrite. (a) shows the LysoBrite channel under 405 nm excitation and (b) shows the pHAb channel under 532 nm excitation. (c) is the merged image of (a) and (b). Scale bar = 10 μm .

4.3.3 Colocalization with lysosome indicator

The cellular fate of the UCNP-pHAb probe was determined by staining with LysoBrite dye. A lysosome marker was chosen because the vast majority of nanosensors were located in acidic compartments (pH \sim 4.0) after >12 h of incubation (Figure 4.18). Previous studies evaluating whether the pH probe and lysosome marker codistributed with one another treated the colocalization experiment data subjectively,^{161,286,287} solely observing whether there was color present that reflected the combined contributions of both probes when the microscopy images were superimposed.²⁵⁸ For example, Li et al. concluded that their fluorescein-based upconversion nanoprobe (blue emission) and LysoTracker Red colocalized after observing violet areas in the merged images of the cells.¹⁶¹ This is not particularly rigorous analysis because the intermediate color is only obtained when the fluorescence intensities of both probes are similar.²⁵⁸ If one dimmer probe spatially overlapped with another brighter probe, the combined image would lead one to incorrectly believe that the two probes localized in different compartments.

Colocalization actually has two components: co-occurrence (spatial overlap of two probes) and correlation (proportional codistribution within and between structures).²⁵⁸ In this case, the UCNP-pHAb would be expected to overlap with LysoBrite if the probe localized in lysosomes (co-occurrence), but the UCNP-pHAb would not be expected to enter every lysosome in the cell (correlation). It would not be unusual to see some lysosomes with UCNP-pHAb and others without, so the colocalization component of interest here is co-occurrence.

Visual evaluation of colocalization suggests that the UCNP-pHAb and LysoBrite as-

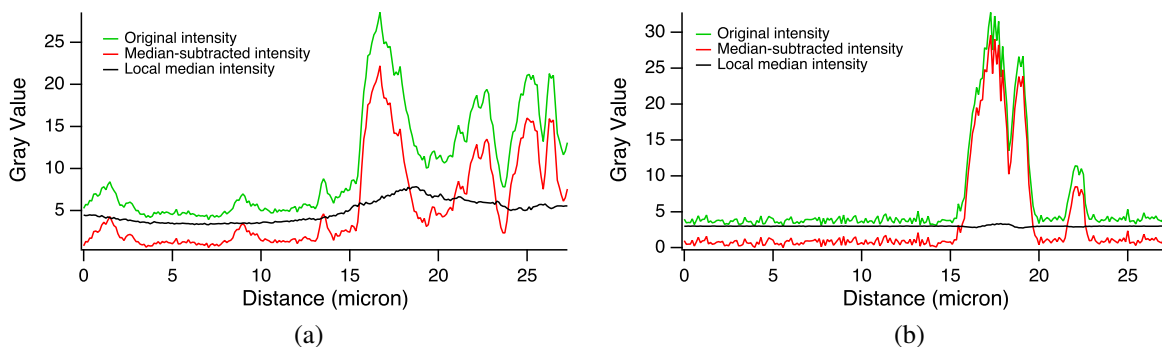


Figure 4.20: Pixel intensities along a line drawn through the cell in Figure 4.19. (a) is the LysoBrite channel and (b) is the pHAb channel.

sociate with the same structure (Figure 4.19). The green color in parts of the combined image also implies that the two probes have similar intensities, which was the intent when conducting image collection. It also appears that some of the lysosomes in the cell do not contain UCNP-pHAb. Quantitative colocalization analysis can calculate the relative distribution of the two probes and determine whether the degree of colocalization exceeds random chance.^{258,259}

Pearson's correlation coefficient (PCC) is a commonly used statistic to quantify colocalization because it is simple to calculate. PCC is independent of background noise, so no preprocessing step is required.²⁵⁸ A scatter plot is constructed with the intensity of a given pixel in one channel as the x-axis and the intensity of the same pixel in the second channel as the y-axis. Possible numbers for PCC range from 1 (perfect positive correlation) to -1 (perfect negative correlation). A PCC close to 1 would have a thin cloud of pixels distributed along the regression line of the scatter plot.²⁸⁸ However, the biology of the system must be carefully considered to determine the suitability of a correlation coefficient in describing the colocalization event. PCC is a poor measure of colocalization when the fluorophores co-occur in varying proportions in different cellular compartments,²⁵⁸ so another approach is needed here.

Manders' colocalization coefficient (MCC) measures co-occurrence independent of correlation, so it is an appropriate measure when one probe localizes in more compartments relative to another probe. For example, this scenario occurs when all of probe A is found in regions with probe B, but probe B is found in additional regions missing probe A.²⁵⁸ When used here, MCC calculates the fraction of pHAb with LysoBrite and the fraction of LysoBrite with pHAb. MCC is very sensitive to background because the calculation does not subtract out the channel mean intensity (unlike PCC), so the background values need to be identified and subtracted from the images before any calculations are performed. The

Table 4.2: MCC values for pHAb and LysoBrite in cells after median subtraction

MCC_1 (fraction of cyan with yellow)	MCC_2 (fraction of yellow with cyan)
0.18	0.96
0.39	0.87
0.10	0.75
0.31	0.92
0.19	0.68

Costes thresholding method is widely used to eliminate background, but it fails when there are significant differences in the number of compartments labeled with each fluorophore. Median subtraction does not encounter this problem and has been shown to work for dispersed objects like endosomes,²⁵⁸ so it is applied here.

To obtain the median-subtracted intensity (Figure 4.20), the local median intensity was subtracted from the original intensity at each pixel along a line drawn through one cell. Figure 4.20 shows that median subtraction is quite effective at removing the background noise in Figure 4.19. The original pixel intensities (indicated by the green lines) do not reach a gray value of zero, even in places where the images appear black in Figure 4.19. The local median intensity of a square pixel region captures the low background variation (black lines). Subtracting the median intensities from the original intensities gives intensity profiles (red lines) that match the trend of the original image profiles while successfully isolating the signal from the background. These median-subtracted intensities were then used to calculate MCC values that quantify the fractional overlap between the LysoBrite and pHAb dyes.

The resulting MCC values after median subtraction are shown in Table 4.2. The MCC_1 values suggest that not all lysosomes contain UCNP-pHAb, while the MCC_2 values indicate that the vast majority of the UCNP-pHAb probes are in lysosomes. Significance testing is performed next to determine whether UCNP-pHAb colocalizes with LysoBrite dye more than what would be expected by chance. Because every cell has a different proportion of cyan pixels to begin with, each $MCC_{expected}$ will also be different under the null hypothesis of no colocalization. The t-test needs to be done on the difference (MCC_{diff}) between $MCC_{observed}$ and $MCC_{expected}$ (Table 4.3).²⁵⁹ Student's one-sample, one-tailed test to compare the mean MCC_{diff} to 0 gives $p < 0.0001$ ($t = 14.5$, d.f. = 4, $\alpha = 0.05$), confirming that the UCNP-pHAb localizes in lysosomes. The small fraction of UCNP-pHAb not in these compartments (complement of fractions in second column, Table 4.2) may be in early endosomes or late endosomes instead, which matches the pHs shown in the ratiometric image (turquoise and violet areas in Figure 4.18).

Table 4.3: MCC values for one-tailed, one-sample t-test

$MCC_{expected}$	$MCC_{observed}$	MCC_{diff}
0.118	0.957	0.839
0.172	0.868	0.696
0.071	0.748	0.677
0.105	0.917	0.812
0.113	0.679	0.566

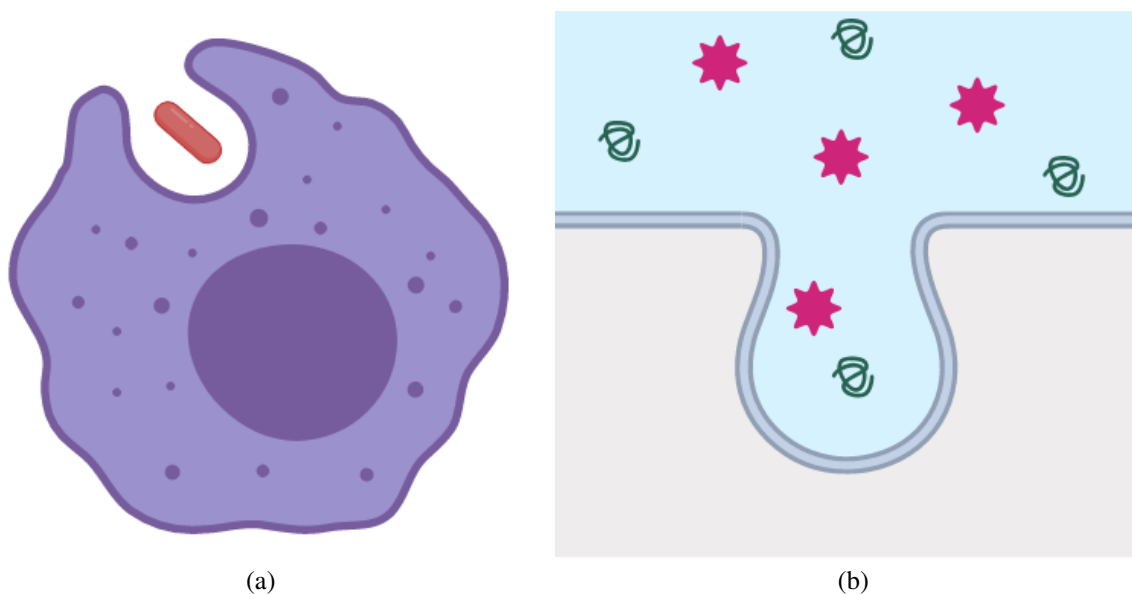


Figure 4.21: Schematics of (a) phagocytosis and (b) pinocytosis. In (a), a macrophage engulfs a pathogen. In (b), a cell takes in extracellular fluid to sample whatever molecules and nutrients happen to be nearby. Created with BioRender.

4.3.4 Endocytosis pathway studies

Phagocytosis and pinocytosis are the two categories of endocytic pathways that enable cells to internalize particles (Figure 4.21). Phagocytosis is largely limited to immunogenic cells, but the latter includes macropinocytosis, caveolae-mediated endocytosis, and clathrin-mediated endocytosis, which differ with respect to the protein coat, size, and fate of the vesicles.²⁶⁴ Although it is still a challenge to predict the uptake mechanism based on a given nanoparticle property, size is considered to be the major factor.^{218,264,289} Macropinocytosis involves particles $>1 \mu\text{m}$, caveolae-mediated endocytosis is limited to particles $<100 \text{ nm}$, and materials $<200 \text{ nm}$ can participate in clathrin-mediated endocytosis to enter the endosomal/lysosomal trafficking route.^{264,290} Given the distribution of particle sizes from DLS (Figure 4.9), clathrin-mediated endocytosis appears to be the most likely uptake mechanism

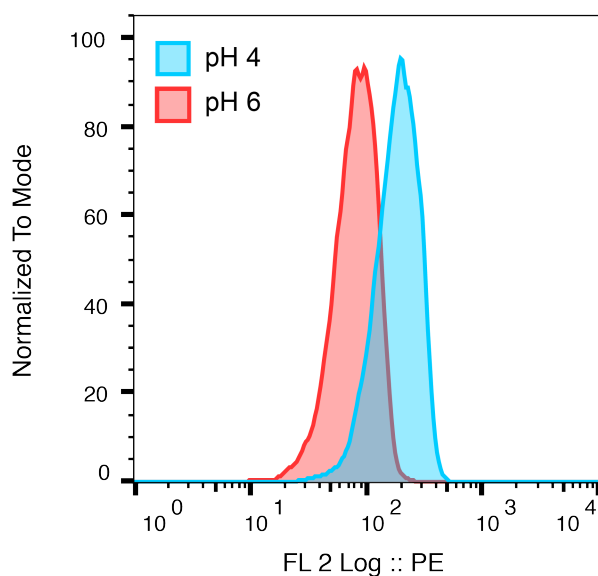


Figure 4.22: Fluorescence histogram of UCNP-pHAb at pH 4 and 6 from flow cytometry. Excitation was at 488 nm to directly excite the dye, and a PE filter was chosen because it overlapped well with the emission of the dye.

for the nanosensor.

Figure 4.23 shows the different internalization mechanisms of cargo between (a) clathrin-mediated endocytosis and (b) caveolae-mediated endocytosis. Both are categorized as receptor-mediated endocytosis, wherein the receptor proteins on the cell surface target specific molecules. Coat proteins (clathrin and caveolin) are clustered on the cytoplasmic side. When the target molecules bind to the receptors, a vesicle is formed with those contents inside and stabilized by the coat proteins.²⁹¹

Drug inhibitor studies were performed with flow cytometry to confirm the mechanism(s) by which the UCNP-pHAb nanosensor is taken up by the SH-SY5Y cells. To first confirm that the flow cytometer was able to detect the fluorescent response of pHAb with a PE filter, the dye was directly excited with a 488 nm laser in citrate/phosphate buffer of two different pHs. At pH 4, the flow cytometer detected higher fluorescence from the UCNP-pHAb compared to the particles at pH 6 (Figure 4.22). This matched the expected pH-dependent emissive response of pHAb from Figures 4.3 and 4.5.

Chlorpromazine (CPZ) and nystatin (NYS) were selected as drug inhibitors because they interfere with clathrin-mediated endocytosis and caveolae-mediated endocytosis, respectively, and have been used previously in endocytosis studies with SH-SY5Y cells. CPZ stops AP2 adapter protein from binding to clathrin-coated vesicles,²⁹² and NYS binds to the cholesterol that is needed to maintain the structural integrity of the caveolae coat.²⁹³ If

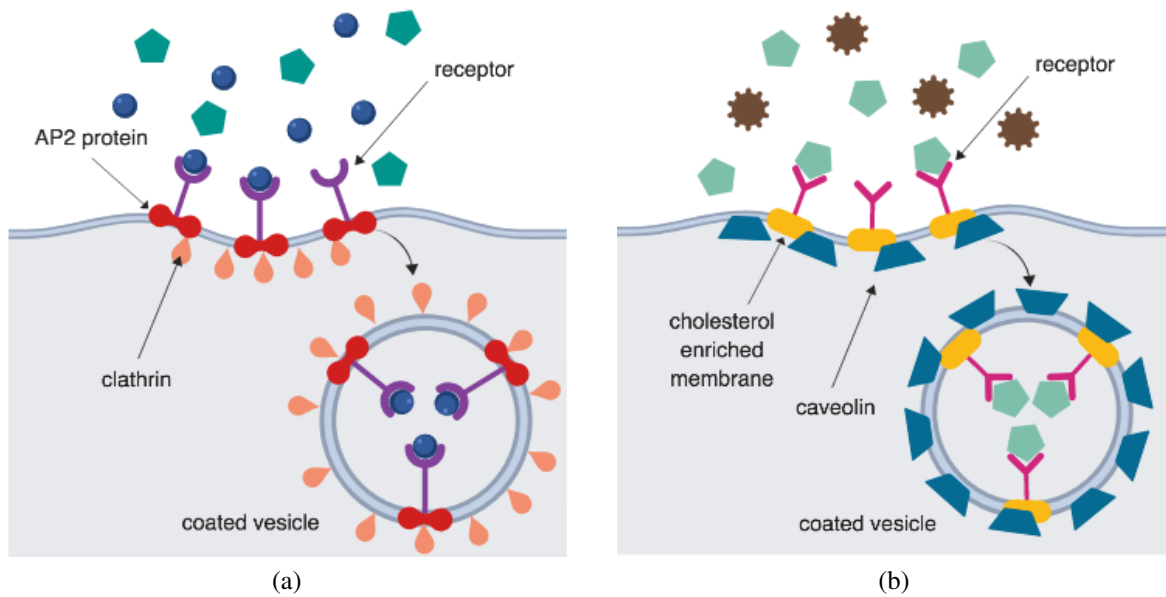


Figure 4.23: Illustrations of (a) clathrin-mediated endocytosis and (b) caveolae-mediated endocytosis. Created with BioRender.

the drug induces a significant decrease in intracellular pHAb fluorescence, that is an indication that the corresponding endocytic mechanism plays a significant role in uptake of the nanosensor. The pHAb fluorescence was quantified after introducing a series of gates to remove cell debris, doublets, and low fluorescence (Figures 4.24 and 4.25).

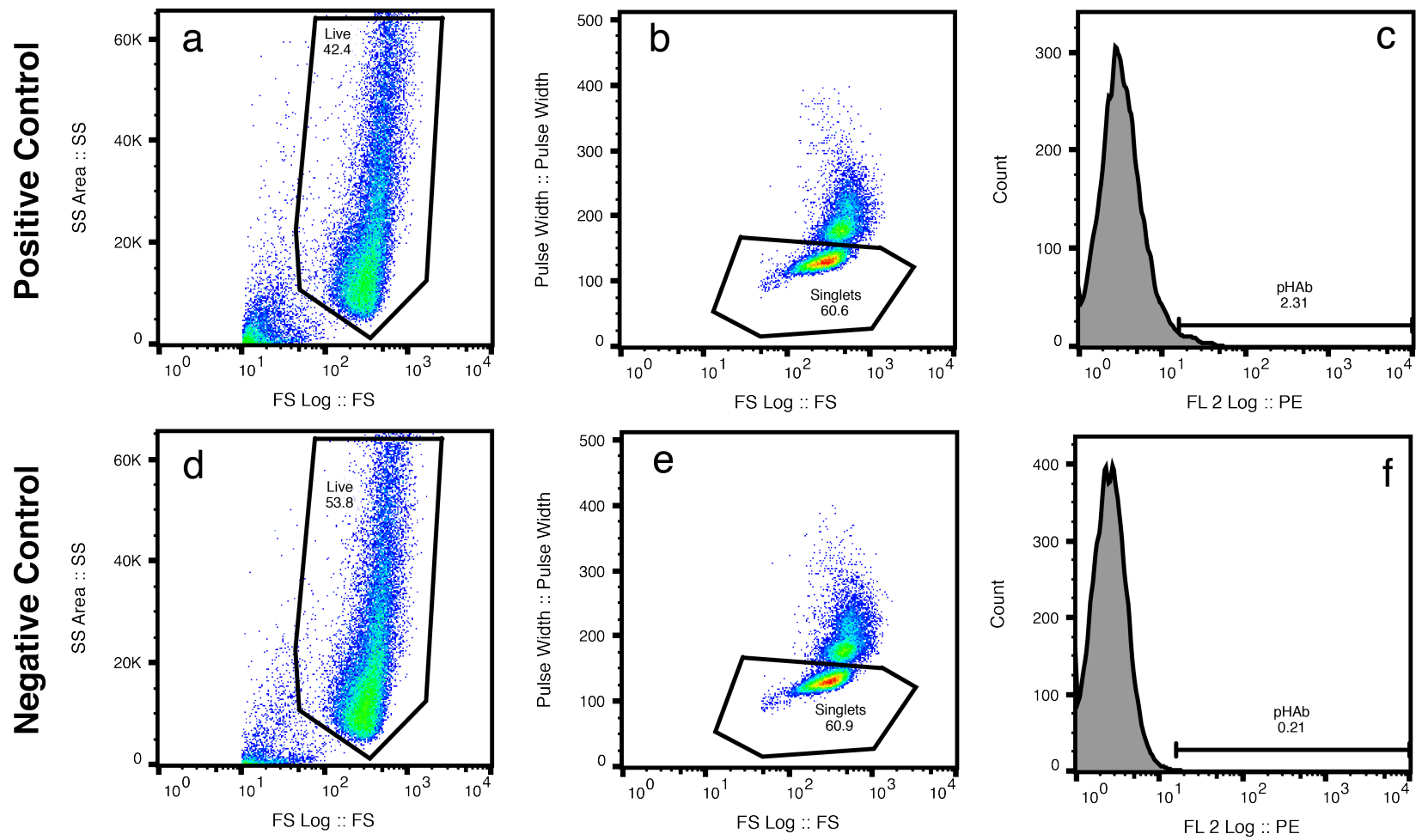


Figure 4.24: Gating strategy for the endocytosis pathway studies (positive and negative control). Cell debris was minimized using the side scatter and forward scatter plots (a,d). Doublets were excluded using the pulse width and forward scatter plots (b,e). Cells with low fluorescence were excluded using the PE filter histogram (c,f). The numbers next to the gates represent the percentage of events from the parent population contained within the child gate.

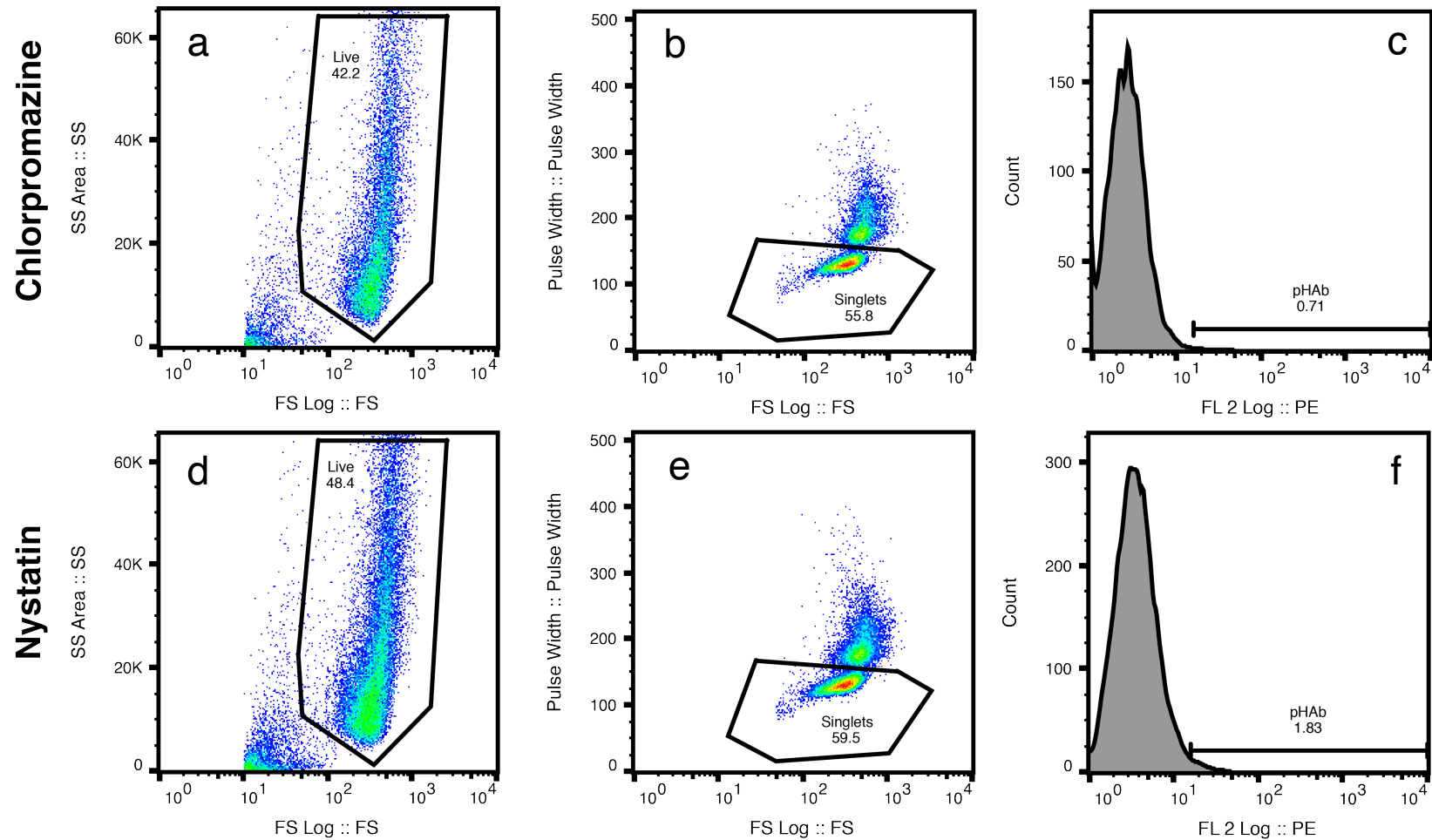


Figure 4.25: Gating strategy for the endocytosis pathway studies (chlorpromazine and nystatin). Cell debris was minimized using the side scatter and forward scatter plots (a,d). Doublets were excluded using the pulse width and forward scatter plots (b,e). Cells with low fluorescence were excluded using the PE filter histogram (c,f). The numbers next to the gates represent the percentage of events from the parent population contained within the child gate.

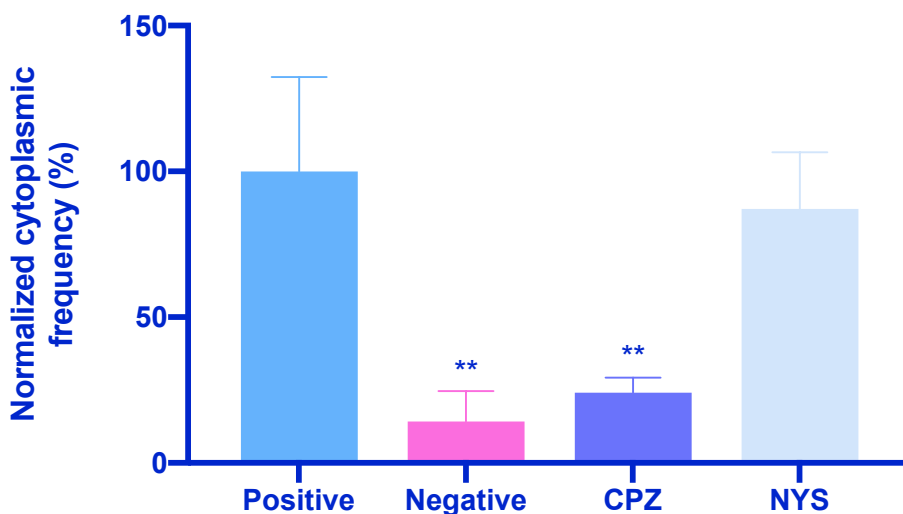


Figure 4.26: Effects of pharmacological inhibitors on UCNP-pHAb uptake after 1.5 h of incubation. The samples were measured with flow cytometry, and each experiment was repeated three times. Statistical significance was calculated with one-way analysis of variance (ANOVA) and Dunnett's Multiple Comparison Test compared to the positive control. ** means $P \leq 0.01$.

The negative control (media only), CPZ, and NYS groups were normalized to the positive control of UCNP-pHAb (Figure 4.26). The intrinsic fluorescence of the SH-SY5Y cells was negligibly low; any higher measurement of fluorescence could be assumed to come from the internalized pHAb. Incubation with CPZ showed a ~75% decrease in fluorescence, indicating the importance of clathrin-mediated endocytosis in the uptake of these nanosensors. Incubation with NYS showed ~10% decrease in fluorescence, which was not statistically significant and suggested that caveolae-mediated endocytosis was not an essential method of uptake (Figure 4.27). This information suggests that the UCNP-pHAb nanosensor can be used to track the pH of drugs that participate in clathrin-mediated endocytosis.

4.3.5 Cell viability assays

Cell viability can be quantitatively measured through various methods that examine cell health indicators such as membrane integrity, nucleic acid content, and metabolism.^{294,295} The alamarBlue reagent relies on the reducing power of the cytosol in living cells. Resazurin, the active component of alamarBlue, is cell permeable and virtually non-fluorescent. After entering the cells, resazurin is reduced to resorufin, which is red and strongly fluorescent (see Figure 4.28).²⁹⁵

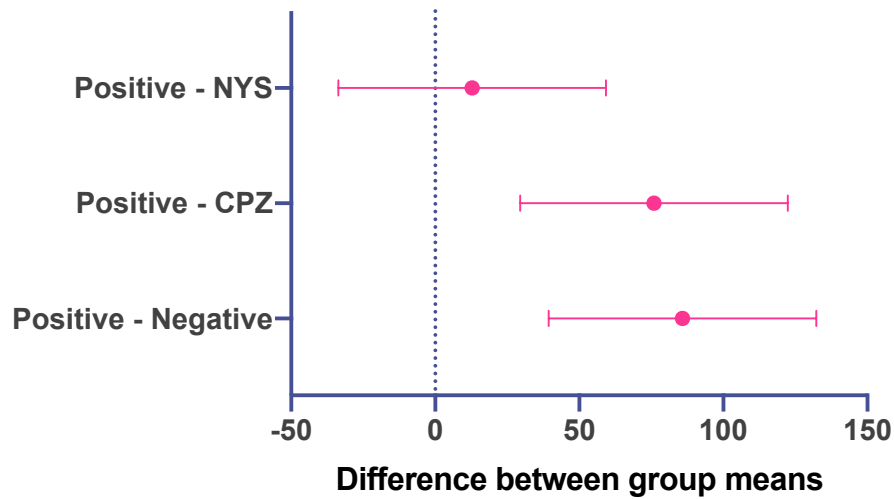


Figure 4.27: 95% confidence intervals for Dunnett's multiple comparison test. The group means of NYS, CPZ, and the negative control were compared to the group mean of the positive control. The 95% confidence band had to be greater than zero to be considered statistically significant.



Figure 4.28: alamarBlue mechanism. Resazurin (left) is converted to resorufin (right) inside the reducing environment of metabolically active cells.

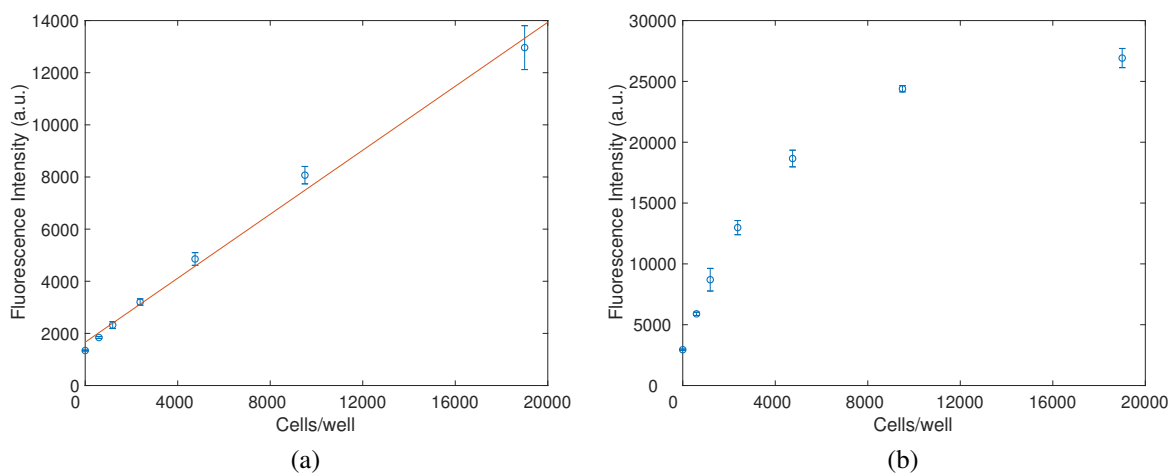


Figure 4.29: (a) Linearity of alamarBlue. The fluorescence of alamarBlue was linear from ~500 to 20,000 cells/well after 28 hours of incubation of which the last 4 hours was with the reagent. (b) Nonlinearity of alamarBlue. The fluorescence of alamarBlue was no longer linear from ~500 to 20,000 cells/well after 48 hours of incubation of which the last 24 hours was with the reagent.

Appropriate plating density and incubation time have to be determined first to ensure that the amount of fluorescence produced is proportional to the number of viable cells. Figure 4.29a shows that the fluorescence intensity is linear from ~500 to 20,000 cells/well after 24 hours for adhesion and growth and another 4 hours of incubation with alamarBlue. With 20 hours of further incubation of the same 96-well plate, the same range of cells per well becomes nonlinear (Figure 4.29b).

To accurately determine cell viability within this linear range, 10k cells were plated per well, incubated for several hours to allow adhesion and growth, and then treated with UCNP-pHAb at 0.01 mg/mL and 0.001 mg/mL. Even after the false-positive effect due to the interference of UCNP-pHAb luminescence was subtracted from the resulting data (see Figure 4.30),^{296,297} the cells still showed viability beyond the control at both concentrations of nanoparticles. Because the alamarBlue assay does not measure true viability but cellular metabolism, it is possible that the increase in resorufin is real due to the fact that the cells are becoming more metabolically active in the presence of the UCNPs. Another possibility is that the uptake of UCNPs inadvertently stimulates uptake of resazurin by the cells, causing more turnover compared to the control. Cell viability studies involving nanoparticles have been known to generate false negatives and false positives so performing independent assays to complement observations can help avoid errors.^{296,298}

A second cell viability test is performed with trypan blue exclusion assay, which relies

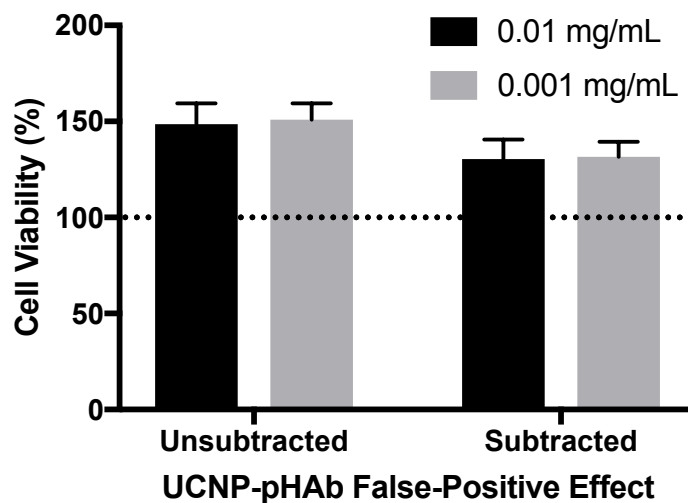


Figure 4.30: Cell viability with alamarBlue assay. Subtracted has taken into account the false-positive effect from the interference of UCNP-pHAb luminescence. Because alamarBlue and pHAb both exhibit absorbance at $\lambda_{ex}=560$ nm, the fluorescence from the latter needs to be excluded. The dotted line is the control reference (UCNP-free cells). $N = 6$ for all measurements.

on the cell membrane as another health indicator. The blue dye stains dead cells due to their permeability,²⁹⁹ so a hemocytometer can be used to count the number of viable and non-viable cells to calculate cell viability. Figure 4.31 displays the cell viabilities obtained from the trypan blue exclusion assay. The control had 98% cell viability, while the cells incubated with 0.01 mg/mL UCNP-pHAB for 24 h showed 97% viability. While free PEI has been found to be cytotoxic, the effect is significantly reduced when the polymer is bound to a surface.⁷² Long-term in vivo toxicity studies to understand the distribution and excretion of the nanosensors are needed before they are used for biological applications with animals or humans, but for the purpose of the in vitro cell imaging studies here, the trypan blue exclusion assay shows that the nanoconjugates essentially have no effect on the SH-SY5Y cell line after 24 h of incubation.

4.4 Conclusions

This chapter examined the design and application of a novel ratiometric intracellular pH imaging probe based on UCNP and pHAb dye. The dual wavelength nanosensor was based on the ratio of the sensitized yellow emission from pHAb and the reference red emission from UCNP. Intracellular calibration of the probe was performed after treatment with nigericin, which equilibrated the internal pH to that of the extracellular environment. After

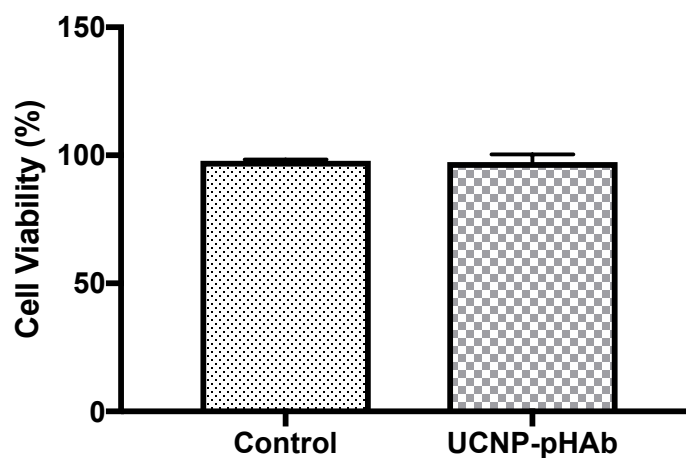


Figure 4.31: Cell viability with trypan blue exclusion assay. The control had $98 \pm 1\%$ cell viability and the cells incubated with UCNP-pHAb (0.01 mg/mL) had $97 \pm 3\%$ cell viability. The SH-SY5Y cells did not show significant decrease in cell viability after 24 h of incubation with 0.01 mg/mL UCNP-pHAb.

this calibration, the pH sensors were used to measure the pH of compartments inside the cell. The nanosensor exhibited comparable or higher sensitivity, resolution, and range for ratiometric imaging compared to previous upconversion nanosensors in the literature.

The UCNP-pHAb sensor was non-toxic to cells for the duration of the experiments. Colocalization and endocytosis pathway studies also confirmed that the nanosensor was taken up mostly by clathrin-mediated endocytosis and localized in lysosomes, making them ideal probes to study compartmentalization of drugs and vesicle acidification. These probes work well for detecting pH changes in *in vitro* biological systems due to their strong fluorescence and may also prove useful in more complex 3D models such as organoids. These results were promising, suggesting that upconversion-based pH nanosensors can be used to study live cells when they are exposed to different stimuli that induce pH change.

As research on upconversion nanomaterials matures, it will be useful to develop commercial instrumentation beyond custom built setups because the latter ones typically are not well characterized, leading to challenges when comparing results from different research groups.¹³⁸ It will also be of great value to equip conventional microscopes and flow cytometers with NIR excitation sources. Direct excitation of the dye provided a proof of concept for the colocalization and endocytosis pathway studies in this chapter, but indirect excitation through energy transfer would provide an even more comprehensive study of UCNP-pHAb in the cell.

Chapter 5

Conclusions and future work

In this thesis, UCNPs together with pH-sensitive dyes were investigated to examine their combined potential for sensing pH in different environments (buffer solutions, cellular compartments). The findings and discussions presented here show that anthraquinones quenched the green emission of UCNPs in solution, and a pH-dependent quenching response could be measured when the two moieties were mixed or conjugated together. When coupled to UC-NPs, pHAb dye exhibited a pH-sensitive emission upon excitation at 980 nm that enabled ratiometric imaging in SH-SY5Y cells.

A summary of the major findings and conclusions based on the thesis objectives in Section 1.4 are discussed below. The limitations are considered alongside suggestions for future work that can broaden the scope of this project. Taking these factors into account, the thesis concludes with a final evaluation of UCNPs for pH sensing.

5.1 Summary of findings

Due to their unique optical properties, upconversion nanomaterials can overcome limitations of common optical probes used in bioanalytical applications, such as limited tissue penetration by light in the visible wavelength range and high autofluorescence background. The UCNPs need to be small enough to pass through the cell membrane for in vitro applications. There is also a demand for high brightness and monodispersity to increase sensor performance and reproducibility, so β -phase particles, which are known to be brighter than their α -phase counterparts, of uniform shape and size are required. Out of four different synthesis strategies, high-temperature coprecipitation was found to be the most reproducible for synthesizing β -NaYF₄:Yb, Er particles that are highly uniform in shape (nanospheres) and size (<30 nm). Cellular uptake has been shown to be more efficient for spherical nanoparticles compared to rod-like ones. In this instance, the hexagonal packing shape approaches

a spherical particle more than an elongated rod shape. This synthesis method is attractive because the experimental setup and strong luminescence of the UCNPs allow the process to be monitored and the reaction time to be properly controlled.

Because surface defects, ligands, and solvent molecules can quench upconversion luminescence, surface passivation can enhance the brightness of UCNPs. Inert shells of different thicknesses were added to reduce surface quenching. ‘Thin’ (≤ 1 nm) and ‘thick’ (3 nm) shells were coated around core NaYF₄:Yb, Er particles (24 nm in diameter) and used to test for resonance energy transfer and inner filter effect sensing mechanisms. Both types of core-shell UCNPs were brighter than core-only UCNPs. This is associated with protection of the UCNP from quenching so the thick-shell UCNPs had higher emission than the thin-shell ones. The distance dependence of FRET means that the energy transfer efficiency drops drastically for UCNPs with thicker shell, so thin-shell UCNPs were explored for applications that relied on UC-RET.

A two-step ligand exchange process assisted by NOBF₄ coated the UCNPs with PMA or PEI to enable water dispersibility. In Chapter 3, PMA-coated particles were selected to study quenching by inner filter effect. The negative charge of PMA prevented direct electrostatic attraction between UCNP and anthraquinone. PEI-coated particles were chosen to study excitation of the anthraquinone when it was attached to the UCNP, because the positive amino groups electrostatically interacted with the negatively charged sulfonate group of the anthraquinone derivatives, decreasing the distance between donor (exciter) and acceptor (fluorophore) and making it more likely for RET to compete with IFE. For the conjugation of UCNP and pHAb in Chapter 4, the amines of the PEI coating reacted with the succinimidyl ester group of the dye. Covalent immobilization also minimizes leaching of the dye from the particle, which is critical for sensing in cells.

Mixtures and conjugates of UCNPs and anthraquinones were studied to examine the quenching effect. Anthraquinones were chosen with excitation coincident with the green emission peak for the UCNP. The decrease in the green peak of the thick-shell UCNPs could be attributed to IFE when mixed directly with the dyes. However, UC-RET was at least partially responsible for the phenomenon when thin-shell UCNPs and anthraquinones were conjugated, although photon reabsorption was still the more dominant component.

The UCNP-anthraquinone coupling via mixture and conjugation was then applied to pH measurement. The ratio of the green intensity to the red intensity was calibrated to phosphate/citrate buffer solutions of varying pH. Ratios were lower in basic environments because of the higher spectral overlap between the UCNP green emission and deprotonated anthraquinone absorption band. The UCNP-ARS nanosensor exhibited a broader pH response (pH ~4.4 to ~6.4) than the UCNP-CaR nanosensor (pH ~4.6 to ~5.2), with pK_a of

5.4 and 4.9, respectively. The range studied in this work fits within the intracellular pH encountered in live cells. Both nanosensors had a sensitivity of ~ 0.1 ratio difference per unit of pH.

For ratiometric imaging of pH in cells, it is advantageous to choose a dye whose sensitized pH-dependent emission can be referenced to a pH-insensitive upconversion emission band. Turn-on ratiometric sensors that rely on the emergence of a new analyte-dependent peak have higher sensitivity than turn-off ones that rely on the quenching of one peak relative to another due to background fluorescence in the latter,³⁰⁰ which is critical for imaging analysis. To take advantage of the benefits of NIR excitation, the pH-dependent absorption band of the dye should overlap with one of the emission bands of the UCNP to accept energy from the particle rather than from direct excitation by a laser. A dye called pHAb fit these criteria; studies of the pH response of UCNP-pHAb nanoconjugate in buffer solution revealed that the UCNP-pHAb had higher UC-RET efficiencies (25-30%) compared to the UCNP-anthraquinone combinations, while the green UCNP emission hardly changed at all at different pHs. Thus, UC-RET efficiencies and quenching efficiencies are quite dependent on the choice of pH dye and the thickness of the shell should be tuned accordingly. In the case of UCNP-pHAb, a shell thickness of ~ 1 nm was selected to accommodate UC-RET while maintaining UCNP brightness.

The nanosensor's applicability for ratiometric pH imaging was demonstrated by imaging the two emissions of the probe (pHAb 560 nm sensitized emission, UCNP 650 nm reference emission) in SH-SY5Y cells with a confocal microscope upon 980 nm excitation. Nigericin, which equilibrates the pH inside and outside cells, was used for the in situ pH calibration before the nanoprobe was used to measure the pH of endosomes and lysosomes after ~ 12 hours of incubation with the cells. The positive charge of PEI is known to induce passive cellular uptake of nanoparticles through endocytosis. Colocalization analysis confirmed that the UCNP-pHAb localized in these compartments, and endocytosis pathway studies revealed that these nanoprobe mostly entered the cell through clathrin-mediated endocytosis. Cytotoxicity studies concluded that the nanoprobe did not affect cell viability even after 24 h of incubation. The nanosensor introduced in this work had comparable or higher sensitivity, resolution, and range for measuring the pH range of interest versus previously published NIR excitable nanosensors.

5.2 Limitations and future work

In order to amplify the sensitized emission of the pHAb dye to improve the performance metrics of the pH nanosensor, a highly amino-functionalized polymer coating (PEI) was

used for high coverage of dye molecules. Yet, while the number of conjugated indicators was beneficial for the quantitative measurement of pH in cells, it led to the pHAb-conjugated nanosensor in Chapter 4 experiencing some aggregation because the zeta potential (+22 mV) was not high enough to repel particles from each other. Before conjugation, the PEI-coated UCNPs were colloidally stable with a zeta potential of +36 mV, so the dye modification decreased colloidal stability. In general, nanoparticles with a zeta potential between -30 mV and +30 mV will aggregate because the like-charge repulsion is overpowered by the stronger hydrophobic effect. Optimizing the surface coating will require finding the right number of dye molecules per particle that balances high sensitivity and reduced aggregation. This can be achieved by using polymer coatings with higher amino functionalization, which will increase the amount of pHAb indicators that can be conjugated while maintaining high zeta potential.

Intensity-based measurements have been popular for spectroscopy and imaging because the instruments they rely on are relatively cheaper and straightforward to use compared to those used in lifetime-based measurements. Ratiometric sensing and imaging have largely overcome challenges associated with measuring single emission changes, but ratiometric sensors still require multi-channel detection in microscopy. This can be a critical problem when working with live cells, since they may move in the time frame between the scans of the different channels. As a result, fluorescence lifetime imaging microscopy (FLIM) can be a good alternative for intracellular sensing. UCNPs have significantly longer lifetimes (μs) than the autofluorescence decay of cells (2-3 ns)³⁰¹, so background noise will be removed with time-resolved detection.³⁰² There are still very few examples of FLIM with UCNPs, likely due to the need for more complex instruments and analysis. In order to generate a temporally-resolved image, an exponential decay has to be fit at each pixel to calculate lifetime. Yet, the upsides of FLIM, such as enhanced sensitivity and selectivity, make it of interest. A study by Orte et al. applied QDs capped with mercaptopropionic acid to measure intracellular pH with high sensitivity and selectivity in two different cell lines.³⁰³

The PEI coating alone was sufficient to enable passive uptake of the nanosensors through endocytosis, which sequestered them into endosomes/lysosomes and led to scattered fluorescence throughout the cytoplasm. No additional modifications were made to the surface coating, making this passive delivery method simple to implement. However, the sequestration prevented the nanosensors from labeling other intracellular structures.³⁰¹ The surface of the UCNPs could be modified with ligands such as peptide localization sequences to direct entry into organelles other than endocytic vesicles. The PEI-coated nanosensors in this work are also nonspecific to cells. Targeting molecules and antibodies can enable the probes to go after specific types of cells. For example, nanoparticles conjugated with folic acid will

specifically target cells that express high levels of folate receptors, which is common for cancer cells.⁹⁷ Those complexed with epidermal growth factor (EGF) will target cells with EGF receptor due to the specificity of antibody-antigen interaction. Modifying the surface of the nanosensors increases their versatility and can be considered alongside more active delivery methods such as microinjection and electroporation.³⁰¹

In looking to apply the pH nanosensors to drug delivery/degradation studies, the first area of investigation should be their ability to track pH temporally upon introduction of drugs with known behavior of changing pH. For example, chloroquine is an antimalarial medication that has been shown to increase lysosomal pH in live cells.²⁵⁵ If the nanoprobe can sense an increase in pH after the cells are exposed to this stimulus, they are good candidates for further studies that track the pH of endosomal/lysosomal compartments in combination with degradation studies of drugs. For pharmaceuticals to pass the preclinical research and development phase, they have to escape from the acidity of the lysosome and reach their cellular target before they degrade.

Research on organoids, which are 3D cellular structures derived from stem cells that mimic the structure and function of organs,³⁰⁴ has flourished over the last ten years due to their usefulness in drug screens and preclinical drug development.³⁰⁵ They are more realistic and efficient in comparison to current model systems like cell lines and patient-derived xenograft models, respectively. Flat cells attached to the hard plastic of cell culture plates are hardly representative of the complexity and dimensionality of in vivo tissue,³⁰⁶ and organoids can test the drug response of specific patients in as little as 12 weeks.³⁰⁴ In an editorial naming organoids as the 2017 Method of the Year, *Nature Methods* stated that “one of the most powerful aspects of organoids as research tools is just how well they synergize with other cutting-edge methods. Imaging, for example, has been advancing tremendously within the past decade, particularly in its ability to image deeper into tissue in ways both fast enough to capture living biology and gentle enough not to damage the sample much.”³⁰⁶ With their capacity for deep tissue imaging, UC nanosensors are ideal candidates for tracking the evolution of pH in the endosomes and lysosomes of organoids upon introduction of drugs. Volume imaging of the nanosensors would make it possible to visualize drug distribution in early endosomes, late endosomes, and lysosomes within the overall tissue architecture,³⁰⁷ which is more representative of how drugs interact with in vivo systems.

5.3 Conclusions

Overall, the findings from this thesis demonstrate the potential of upconversion-based pH nanosensors for optical sensing and bioanalytical applications. A thorough search of the

relevant literature suggested that this was the first work that investigated the interaction between UCNPs and different pH indicator dyes beyond measurement in buffer solution and cells. The type of system (mixture or conjugate) influenced the energy transfer mechanism between UCNP and anthraquinone dye. When the two entities were close enough via conjugation, UC-RET was partly responsible for the decrease in the green emission of the UCNP. The change in ratio of the green peak to red peak of the UCNP with pH was used to construct sigmoidal response curves. This study provided the framework for creating a new sensing system based on UCNP and pHAb dye that could measure pH in endosomes and lysosomes through ratiometric imaging. The nanoconjugate was shown to enter the cell through clathrin-mediated endocytosis and localize in endosomes and lysosomes. Moreover, the nanosensor was not toxic to the cells in the timescale associated with the studies performed here.

Future work should focus on upconversion enhancement strategies to improve the nanosensor's performance characteristics as well as surface chemistry to reduce particle aggregation. FLIM can be explored as an option if intensity-based ratiometric imaging still suffers from low sensitivity and resolution after improving the brightness of UCNPs. Adding targeting ligands to the particle can further increase the ability of these nanoprobe to selectively sense pH in different environments. Improvements in these areas will accelerate the development of UCNPs towards commercial use, starting with measurements of pH changes from known stimuli as proof-of-concept before proceeding to their use in delivery/degradation studies of drugs in more complex preclinical models like organoids.

Appendix A

Crystal structure of NaYF₄

Crystals are highly ordered structures of atoms, ions, or molecules that extend in all three dimensions in an endless, repetitive fashion. By assigning the atoms positions in a unit cell, one can essentially describe the structural information of the entire crystal because the unit cells repeat in space. The simplest crystal structure is the cubic (α) one, of which there are three types as shown in Figure A.1: simple cubic (SC), face-centered cubic (FCC), and body-centered cubic (BCC). The latter two are much more commonly observed in nature. The cube edge, also known as the lattice parameter, distinguishes substances from one another. For example, if Fe atoms are placed at each lattice point in a BCC structure with a lattice parameter of 0.287 nm, metallic iron forms.³⁰⁸

Crystals form diffraction patterns when x-ray beams hit them. The patterns depend on the wavelength of the incident light, the angle of diffraction, and the d-spacing. The wavelength depends on the element for the x-ray source, which is commonly copper with an emission wavelength of 1.539 Å. The diffractometer used for XRD analysis measures double this angle, which is why XRD patterns often display data in terms of 2θ . The d-spacing is the distance between adjacent planes in a family of parallel planes. Thus, according to Bragg's law, one can calculate the interplanar spacing. The equation is:

$$n\lambda = 2d \sin \theta$$

where n is an integer (1, 2, 3, ...), λ is the wavelength, d is the interplanar spacing, and θ is the diffraction angle. Because λ and θ are known, the interplanar spacing can be determined.³⁰⁹ Each d-spacing represents a family of similar atomic planes. With combined knowledge of these d-spacings, one can come up with the crystal structure of an unknown material.³¹⁰ Because of the phase problem of crystallography, only the axes and angles of the unit cell can be determined but not the exact atom location in the unit cell.³¹¹

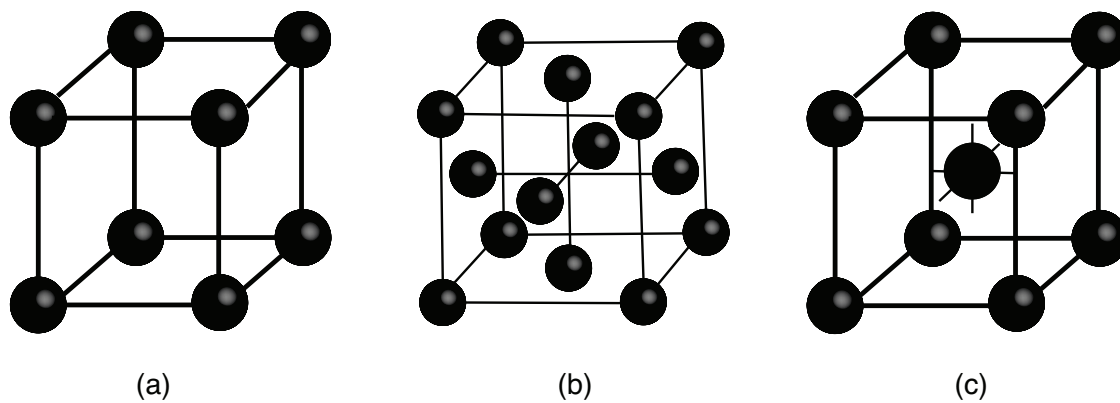


Figure A.1: The three types of unit cells for the cubic crystal: (a) simple cubic, (b) face-centered cubic, and (c) body-centered cubic.

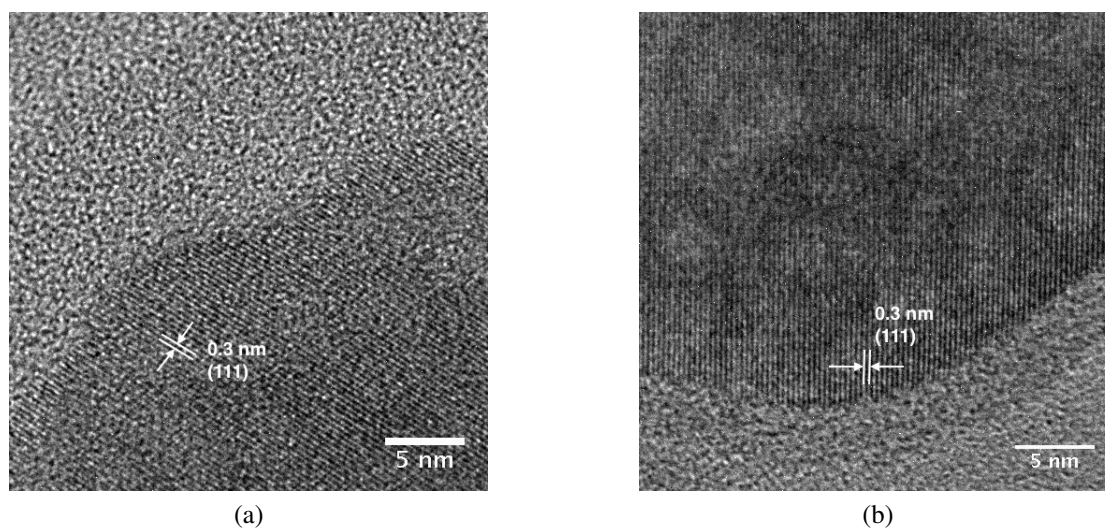


Figure A.2: HR-TEM images of UCNPs synthesized via low-temperature coprecipitation. (a) shows the UCNPs without annealing and (b) shows the UCNPs with 30 min of annealing.

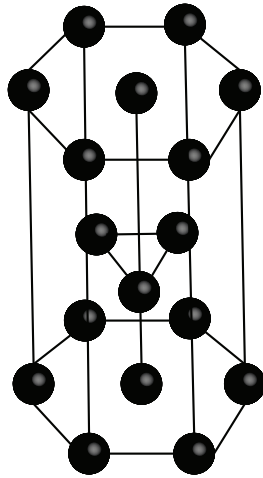


Figure A.3: The unit cell of the hexagonal close-packed structure.

High-resolution TEM (HR-TEM) images (Figure A.2) can confirm the high crystallinity of materials to further support XRD results. The d-spacing can also be determined from these HR-TEM images. The distance of 0.3 nm between adjacent lattice fringes, seen in Figure A.2, agrees with the d_{111} spacing of the cubic structure of NaYF_4 .^{312,313} The atoms that make up NaYF_4 can also be arranged in another structure, i.e. hexagonal (β), with different interplanar spacings, atomic locations, and lattice parameters (Figure A.3).³¹⁴ For example, the hexagonal structure of NaYF_4 has d_{100} spacing of 0.5 nm.³¹⁵

Appendix B

Supplemental microscopy images of UCNP-pHAb in cells

Frame accumulation takes a specified number of scans and adds up the pixel values, displaying the sum in the final image. Accumulation is useful for amplifying weak signals, but it can result in saturation of the highest intensity pixels. Accurate quantitative analysis of images requires pixel values to remain unsaturated; otherwise, intensity differentiation is lost at the upper end of the image pixels. Thus, frame accumulation is ideal for improving specimen visibility for visualization purposes but should be scrutinized before images are collected this way for ratiometric analysis.

Figure B.2 shows the 500-550 nm (first row, UCNP green), 565-630 nm (second row, pHAb yellow), and 640-680 nm (third row, UCNP red) channels of optimized UCNP-pHAb in SH-SY5Y cells calibrated to different pHs using citrate/phosphate buffer supplemented with nigericin and KCl. Because these fluorescence images were collected without frame accumulation and the microscope parameters were adjusted to avoid image saturation, they were used to produce the calibration represented by the pseudocolor change with pH shown in the colorbar and the ratiometric images in the fifth row. The transmission images (fourth row) show the cell outlines, confirming that the UCNP-pHAb conjugates go inside the cells after overnight incubation.

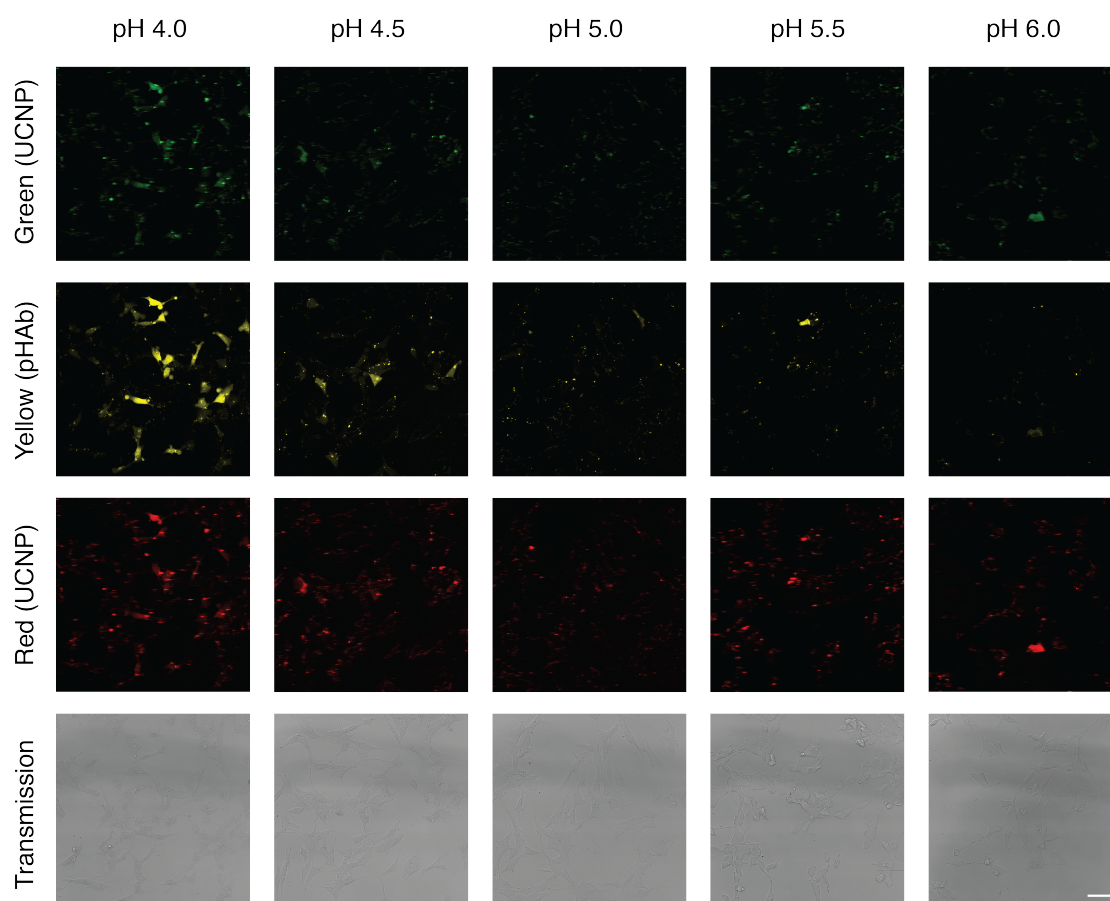


Figure B.1: Raw multiphoton confocal microscopy images of optimized UCNP-pHAb in nigericin-treated SH-SY5Y cells exposed to citric acid/phosphate buffer with KCl at pH 4.0, 4.5, 5.0, 5.5, and 6.0. The excitation wavelength was 980 nm, and the images were collected with 2x frame accumulation in the ranges of 500-550 nm (first row, UCNP green), 565-630 nm (second row, pHAb yellow), and 640-680 nm (third row, UCNP red). The corresponding transmission images (fourth row) are also shown. Scale bar = 50 μm .

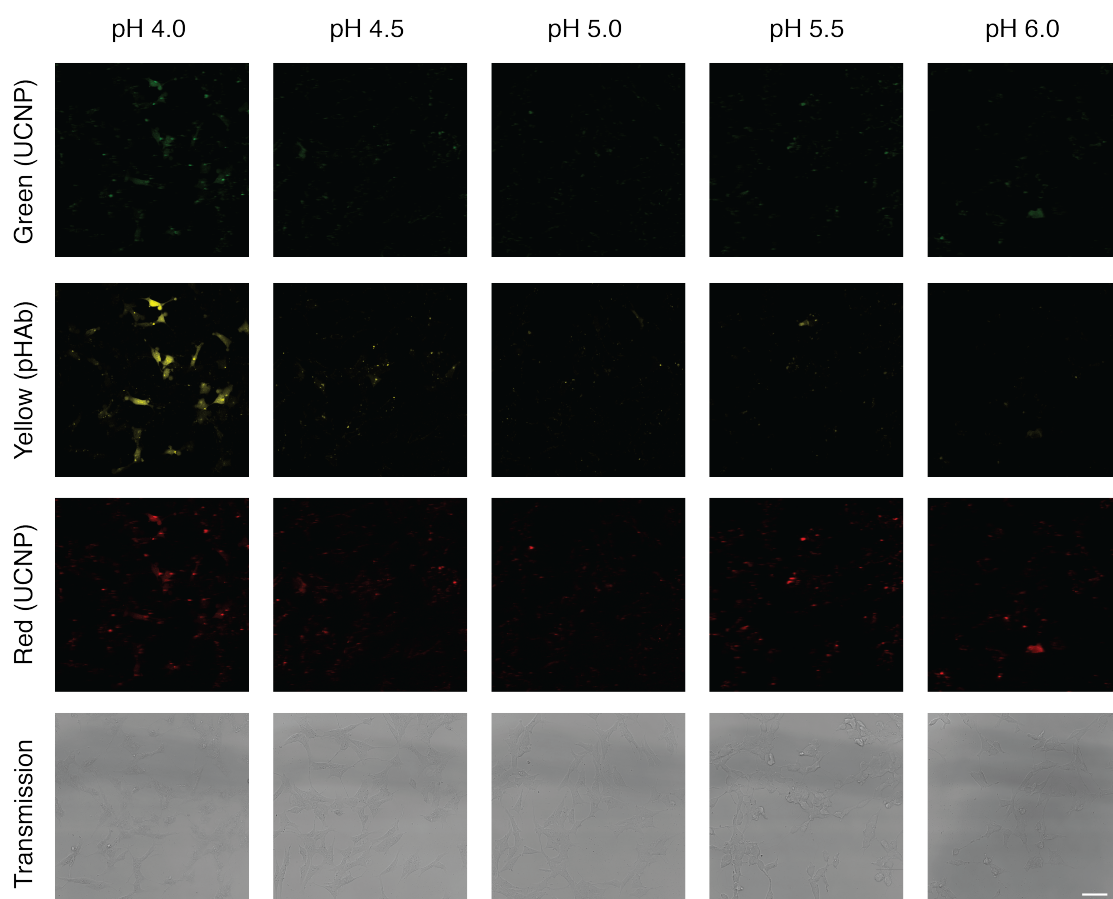


Figure B.2: Raw multiphoton confocal microscopy images of optimized UCNP-pHAb in nigericin-treated SH-SY5Y cells exposed to citric acid/phosphate buffer with KCl at pH 4.0, 4.5, 5.0, 5.5, and 6.0. The excitation wavelength was 980 nm, and the images were collected with 1x frame accumulation in the ranges of 500-550 nm (first row, UCNP green), 565-630 nm (second row, pHAb yellow), and 640-680 nm (third row, UCNP red). The corresponding transmission images (fourth row) are also shown. Scale bar = 50 μ m.

Appendix C

Copyright permissions



Title: Size- and Phase-Controlled Synthesis of Monodisperse NaYF₄:Yb,Er Nanocrystals from a Unique Delayed Nucleation Pathway Monitored with Upconversion Spectroscopy

Author: Hao-Xin Mai, Ya-Wen Zhang, Ling-Dong Sun, et al

Publication: The Journal of Physical Chemistry C

Publisher: American Chemical Society

Date: Sep 1, 2007

Copyright © 2007, American Chemical Society

Logged in as:
Evaline Tsai
University of Cambridge
Account # :
3001404003

[LOGOUT](#)

PERMISSION/LICENSE IS GRANTED FOR YOUR ORDER AT NO CHARGE

This type of permission/license, instead of the standard Terms & Conditions, is sent to you because no fee is being charged for your order. Please note the following:

- Permission is granted for your request in both print and electronic formats, and translations.
- If figures and/or tables were requested, they may be adapted or used in part.
- Please print this page for your records and send a copy of it to your publisher/graduate school.
- Appropriate credit for the requested material should be given as follows: "Reprinted (adapted) with permission from (COMPLETE REFERENCE CITATION). Copyright (YEAR) American Chemical Society." Insert appropriate information in place of the capitalized words.
- One-time permission is granted only for the use specified in your request. No additional uses are granted (such as derivative works or other editions). For any other uses, please submit a new request.

**Royal Society of Chemistry LICENSE
TERMS AND CONDITIONS**

Mar 09, 2019

This is a License Agreement between University of Cambridge -- Evaline Tsai ("You") and Royal Society of Chemistry ("Royal Society of Chemistry") provided by Copyright Clearance Center ("CCC"). The license consists of your order details, the terms and conditions provided by Royal Society of Chemistry, and the payment terms and conditions.

All payments must be made in full to CCC. For payment instructions, please see information listed at the bottom of this form.

License Number	4524350562466
License date	Feb 08, 2019
Licensed content publisher	Royal Society of Chemistry
Licensed content title	Chemical Society reviews
Licensed content date	Jan 1, 1972
Type of Use	Thesis/Dissertation
Requestor type	Academic institution
Format	Print, Electronic
Portion	chart/graph/table/figure
Number of charts/graphs/tables/figures	3
The requesting person/organization is:	Evaline Tsai
Title or numeric reference of the portion(s)	Figure 1, Figure 3, Table 2
Title of the article or chapter the portion is from	Recent advances in the chemistry of lanthanide-doped upconversion nanocrystals
Editor of portion(s)	N/A
Author of portion(s)	Feng Wang and Xiaogang Liu
Volume of serial or monograph.	38
Issue, if republishing an article from a serial	4
Page range of the portion	976-989
Publication date of portion	12 Feb 2009
Rights for	Main product
Duration of use	Life of current edition
Creation of copies for the disabled	no
With minor editing privileges	yes
For distribution to	Worldwide
In the following language(s)	Original language of publication
With incidental promotional use	no
The lifetime unit quantity of new product	Up to 499
Title	Upconversion Nanoparticles for pH Sensing and Imaging
Institution name	University of Cambridge
Expected presentation date	Feb 2019

**Royal Society of Chemistry LICENSE
TERMS AND CONDITIONS**

Mar 09, 2019

This is a License Agreement between University of Cambridge -- Evaline Tsai ("You") and Royal Society of Chemistry ("Royal Society of Chemistry") provided by Copyright Clearance Center ("CCC"). The license consists of your order details, the terms and conditions provided by Royal Society of Chemistry, and the payment terms and conditions.

All payments must be made in full to CCC. For payment instructions, please see information listed at the bottom of this form.

License Number	4524360801106
License date	Feb 08, 2019
Licensed content publisher	Royal Society of Chemistry
Licensed content title	Chemical Society reviews
Licensed content date	Jan 1, 1972
Type of Use	Thesis/Dissertation
Requestor type	Academic institution
Format	Print, Electronic
Portion	chart/graph/table/figure
Number of charts/graphs/tables/figures	1
The requesting person/organization is:	Evaline Tsai
Title or numeric reference of the portion(s)	Figure 3
Title of the article or chapter the portion is from	Anti-Stokes shift luminescent materials for bio-applications
Editor of portion(s)	N/A
Author of portion(s)	Xingjun Zhu, Qianqian Su, Wei Feng and Fuyou Li
Volume of serial or monograph.	46
Issue, if republishing an article from a serial	4
Page range of the portion	1025-1039
Publication date of portion	14 Dec 2016
Rights for	Main product
Duration of use	Life of current edition
Creation of copies for the disabled	no
With minor editing privileges	yes
For distribution to	Worldwide
In the following language(s)	Original language of publication
With incidental promotional use	no
The lifetime unit quantity of new product	Up to 499
Title	Upconversion Nanoparticles for pH Sensing and Imaging
Institution name	University of Cambridge
Expected presentation date	Feb 2019

**ELSEVIER LICENSE
TERMS AND CONDITIONS**

Mar 09, 2019

This Agreement between University of Cambridge -- Evaline Tsai ("You") and Elsevier ("Elsevier") consists of your license details and the terms and conditions provided by Elsevier and Copyright Clearance Center.

License Number	4524370891430
License date	Feb 08, 2019
Licensed Content Publisher	Elsevier
Licensed Content Publication	Biomaterials
Licensed Content Title	A systematic in-vivo toxicity evaluation of nanophosphor particles via zebrafish models
Licensed Content Author	Gun Hyuk Jang, Mintai P. Hwang, Su Yeon Kim, Ho Seong Jang, Kwan Hyi Lee
Licensed Content Date	Jan 1, 2014
Licensed Content Volume	35
Licensed Content Issue	1
Licensed Content Pages	10
Start Page	440
End Page	449
Type of Use	reuse in a thesis/dissertation
Intended publisher of new work	other
Portion	figures/tables/illustrations
Number of figures/tables/illustrations	1
Format	both print and electronic
Are you the author of this Elsevier article?	No
Will you be translating?	No
Original figure numbers	Figure 7
Title of your thesis/dissertation	Upconversion Nanoparticles for pH Sensing and Imaging
Publisher of new work	University of Cambridge
Expected completion date	Feb 2019
Estimated size (number of pages)	1
Requestor Location	University of Cambridge Department of Chemical Engineering and Biotechnology Philippa Fawcett Drive Cambridge, other CB3 0AS United Kingdom Attn: University of Cambridge
Publisher Tax ID	GB 494 6272 12

**Royal Society of Chemistry LICENSE
TERMS AND CONDITIONS**

Mar 09, 2019

This is a License Agreement between University of Cambridge -- Evaline Tsai ("You") and Royal Society of Chemistry ("Royal Society of Chemistry") provided by Copyright Clearance Center ("CCC"). The license consists of your order details, the terms and conditions provided by Royal Society of Chemistry, and the payment terms and conditions.

All payments must be made in full to CCC. For payment instructions, please see information listed at the bottom of this form.

License Number	4524371439905
License date	Feb 08, 2019
Licensed content publisher	Royal Society of Chemistry
Licensed content title	Chemical Society reviews
Licensed content date	Jan 1, 1972
Type of Use	Thesis/Dissertation
Requestor type	Academic institution
Format	Print, Electronic
Portion	chart/graph/table/figure
Number of charts/graphs/tables/figures	1
The requesting person/organization is:	Evaline Tsai
Title or numeric reference of the portion(s)	Figure 14
Title of the article or chapter the portion is from	The biosafety of lanthanide upconversion nanomaterials
Editor of portion(s)	N/A
Author of portion(s)	Yun Sun, Wei Feng, Pengyuan Yang, Chunhui Huang and Fuyou Li
Volume of serial or monograph.	44
Issue, if republishing an article from a serial	6
Page range of the portion	1509-1525
Publication date of portion	12 Aug 2014
Rights for	Main product
Duration of use	Life of current edition
Creation of copies for the disabled	no
With minor editing privileges	yes
For distribution to	Worldwide
In the following language(s)	Original language of publication
With incidental promotional use	no
The lifetime unit quantity of new product	Up to 499
Title	Upconversion Nanoparticles for pH Sensing and Imaging
Institution name	University of Cambridge
Expected presentation date	Feb 2019

**Royal Society of Chemistry LICENSE
TERMS AND CONDITIONS**

Mar 09, 2019

This is a License Agreement between University of Cambridge -- Evaline Tsai ("You") and Royal Society of Chemistry ("Royal Society of Chemistry") provided by Copyright Clearance Center ("CCC"). The license consists of your order details, the terms and conditions provided by Royal Society of Chemistry, and the payment terms and conditions.

All payments must be made in full to CCC. For payment instructions, please see information listed at the bottom of this form.

License Number	4527080005787
License date	Feb 13, 2019
Licensed content publisher	Royal Society of Chemistry
Licensed content title	The analyst online
Licensed content date	Jan 1, 1876
Type of Use	Thesis/Dissertation
Requestor type	Academic institution
Format	Print, Electronic
Portion	chart/graph/table/figure
Number of charts/graphs/tables/figures	1
The requesting person/organization is:	Evaline Tsai
Title or numeric reference of the portion(s)	Figure 2
Title of the article or chapter the portion is from	Upconversion nanoparticles in biological labeling, imaging, and therapy
Editor of portion(s)	N/A
Author of portion(s)	Feng Wang, Debapriya Banerjee, Yongsheng Liu, Xueyuan Chen and Xiaogang Liu
Volume of serial or monograph.	135
Issue, if republishing an article from a serial	8
Page range of the portion	1839-1854
Publication date of portion	18 May 2010
Rights for	Main product
Duration of use	Life of current edition
Creation of copies for the disabled	no
With minor editing privileges	yes
For distribution to	Worldwide
In the following language(s)	Original language of publication
With incidental promotional use	no
The lifetime unit quantity of new product	Up to 499
Title	Upconversion Nanoparticles for pH Sensing and Imaging
Institution name	University of Cambridge
Expected presentation date	Feb 2019

Bibliography

- [1] C. Pelejero, E. Calvo, M. T. McCulloch, J. F. Marshall, M. K. Gagan, J. M. Lough and B. N. Opdyke, *Science*, 2005, **309**, 2204–2207.
- [2] K. Caldeira and M. E. Wickett, *Nature*, 2003, **425**, 365.
- [3] C. Edwards and P. Bohlen, *Biology and Ecology of Earthworms*, Chapman & Hall, London, 3rd edn., 1996.
- [4] R. W. Putnam, in *Cell Physiology: Source Book*, ed. N. Sperelakis, Academic Press, San Diego, 1995, ch. 16, pp. 212–229.
- [5] D. Wencel, T. Abel and C. McDonagh, *Anal. Chem.*, 2014, **86**, 15–29.
- [6] W. Tan, Z.-Y. Shi, S. Smith, D. Birnbaum and R. Kopelman, *Science*, 1992, **258**, 778–781.
- [7] H. Xu, S. M. Buck, R. Kopelman, M. A. Philbert, M. Brasuel, E. Monson, C. Behrend, B. Ross, A. Rehemtulla and Y.-E. L. Koo, in *Topics in Fluorescence Spectroscopy*, ed. C. D. Geddes and J. R. Lakowicz, Springer, New York, 2005, vol. 10, ch. 4, pp. 69–126.
- [8] A. Schulz and C. McDonagh, *Soft Matter*, 2012, **8**, 2579–2585.
- [9] A. Burns, P. Sengupta, T. Zedayko, B. Baird and U. Wiesner, *Small*, 2006, **2**, 723–726.
- [10] S. Modi, S. M. G., D. Goswami, G. D. Gupta, S. Mayor and Y. Krishnan, *Nat. Nanotechnol.*, 2009, **4**, 325–330.
- [11] H. Pan and J. Kopecek, in *Multifunctional Water-Soluble Polymers for Drug Delivery*, ed. V. Torchilin, Springer, New York, 1st edn., 2008, ch. 4, pp. 81–142.

- [12] R. Chen, in *Drug Delivery Systems: Advanced Technologies Potentially Applicable in Personalised Treatment*, ed. J. Coelho, Springer, Dordrecht, 1st edn., 2013, ch. 1, pp. 1–34.
- [13] N. F. Sheppard, Jr. and A. Guiseppi-Elie, in *The Measurement, Instrumentation, and Sensors Handbook*, ed. J. G. Webster, CRC Press, Boca Raton, 1999, ch. 71, pp. 1–16.
- [14] L. Rovati, P. Fabbri, L. Ferrari and F. Pilati, in *Fiber Optic Sensors*, ed. M. Yasin, InTech, 2012.
- [15] V. Shukla, G. Kandeepan, M. R. Vishnuraj and A. Soni, *Agric. Res.*, 2016, **5**, 205–209.
- [16] R. J. Anderson, D. J. Bendell and P. W. Groundwater, *Organic Spectroscopic Analysis*, Royal Society of Chemistry, Cambridge, 2004.
- [17] P. F. Gordon, *Organic Chemistry in Colour*, Springer-Verlag, Berlin, 1983.
- [18] R. L. Mahaffey, in *Handbook of Detergents, Part A: Properties*, ed. G. Broze, Marcel Dekker, New York, 1999, ch. 20, pp. 721–742.
- [19] J. R. Lakowicz, *Principles of Fluorescence Spectroscopy*, Springer, New York, 3rd edn., 2006.
- [20] S. Murray, in *Paper Chemistry*, ed. J. Roberts, Blackie & Son, London, 1991, ch. 9, pp. 132–161.
- [21] J. Han and K. Burgess, *Chem. Rev.*, 2010, **110**, 2709–2728.
- [22] A. N. Diaz, *J. Photochem. Photobiol. A*, 1990, **53**, 141–167.
- [23] M. J. Ruedas-Rama and E. A. H. Hall, *Nanotechnology*, 2014, **25**, 195501.
- [24] H. Sun, A. M. Scharff-Poulsen, H. Gu and K. Almdal, *Chem. Mater.*, 2006, **18**, 3381–3384.
- [25] W. Shi, X. Li and H. Ma, *Angew. Chem.*, 2012, **124**, 6538–6541.
- [26] H. Ogawa and J. P. Miller, in *Methods in Neuroethological Research*, ed. H. Ogawa and K. Oka, Springer, Tokyo, 2013, ch. 5, pp. 71–88.
- [27] C. S. Owen, *Anal. Biochem.*, 1992, **204**, 65–71.

- [28] J. Louisse, Y. Bai, M. Verwei, J. J. van de Sandt, B. J. Blaauboer and I. M. Rietjens, *Toxicol. Appl. Pharmacol.*, 2010, **245**, 236–243.
- [29] Z. Diwu, C.-S. Chen, C. Zhang, D. H. Klaubert and R. P. Haugland, *Chem. Biol.*, 1999, **6**, 411–418.
- [30] K. Shimizu, Y. D. Amo, M. A. Brzezinski, G. D. Stucky and D. E. Morse, *Chem. Biol.*, 2001, **8**, 1051–1060.
- [31] H. A. Clark, M. Hoyer, M. A. Philbert and R. Kopelman, *Anal. Chem.*, 1999, **71**, 4831–4836.
- [32] H. A. Clark, R. Kopelman, R. Tjalkens and M. A. Philbert, *Anal. Chem.*, 1999, **71**, 4837–4843.
- [33] O. Wolfbeis, *J. Mater. Chem.*, 2005, **15**, 2657–2669.
- [34] R. Arppe, T. Nareoja, S. Nylund, L. Mattsson, S. Koho, J. M. Rosenholm, T. Soukka and M. Schaferling, *Nanoscale*, 2014, **6**, 6837–6843.
- [35] B. M. Weidgans, C. Krause, I. Klimant and O. S. Wolfbeis, *Analyst*, 2004, **129**, 645–650.
- [36] M. Strobl, T. Rappitsch, S. M. Borisov, T. Mayr and I. Klimant, *Analyst*, 2015, **140**, 7150–7153.
- [37] H.-S. Peng, J. A. Stolwijk, L.-N. Sun, J. Wegener and O. S. Wolfbeis, *Angew. Chem.*, 2010, **122**, 4342–4345.
- [38] G. Chen, F. Song, X. Xiong and X. Peng, *Ind. Eng. Chem. Res.*, 2013, **52**, 11228–11245.
- [39] A. Elasersawi, *World of Nanobioengineering*, AuthorHouse, Bloomington, 2010.
- [40] S. Zhu, Y. Song, X. Zhao, J. Shao, J. Zhang and B. Yang, *Nano Res.*, 2015, **8**, 355–381.
- [41] P. Elvati, E. Baumeister and A. Violi, *RSC Adv.*, 2017, **7**, 17704–17710.
- [42] L. Bao, C. Liu, Z.-L. Zhang and D.-W. Pang, *Adv. Mater.*, 2015, **27**, 1663–1667.
- [43] D. Tong, W. Li, Y. Zhao, L. Zhang, J. Zheng, T. Cai and S. Liu, *RSC Adv.*, 2016, **6**, 97137–97141.

- [44] J. Kim and T. S. Lee, *Small*, 2018, **14**, 1702758.
- [45] S. Chen, Y.-L. Yu and J.-H. Wang, *Anal. Chim. Acta*, 2018, **999**, 13–26.
- [46] C. A. Parker and W. J. Barnes, *Analyst*, 1957, **82**, 606–618.
- [47] M. L. Mertens and J. H. R. Kagi, *Anal. Biochem.*, 1979, **96**, 448–455.
- [48] N. K. Subbarao and R. C. MacDonald, *Analyst*, 1993, **118**, 913–916.
- [49] M. Kubista, R. Sjoback, S. Eriksson and B. Albinsson, *Analyst*, 1994, **119**, 417–419.
- [50] EU Pat., EP0304248B1, 1992.
- [51] M. Lin, H. Y. Zou, T. Yang, Z. X. Liu, H. Liu and C. Z. Huang, *Nanoscale*, 2016, **8**, 2999–3007.
- [52] H. Liu, C. Xu, Y. Bai, L. Liu, D. Liao, J. Liang, L. Liu and H. Han, *Spectrochim. Acta A*, 2017, **171**, 311–316.
- [53] Y. Hiruta, N. Yoshizawa, D. Citterio and K. Suzuki, *Anal. Chem.*, 2012, **84**, 10650–10656.
- [54] J. Shi, F. Tian, J. Lyu and M. Yang, *J. Mater. Chem. B*, 2015, **3**, 6989–7005.
- [55] S. C. Warren, A. Margineanu, D. Alibhai, D. J. Kelly, C. Talbot, Y. Alexandrov, I. Munro, M. Katan, C. Dunsby and P. M. W. French, *PLoS ONE*, 2013, **8**, e70687.
- [56] S. Melle, O. G. Calderon, M. Laurenti, D. Mendez-Gonzalez, A. Egatz-Gomez, E. Lopez-Cabarcos, E. Cabrera-Granado, E. Diaz and J. Rubio-Retama, *J. Phys. Chem. C*, 2018, **122**, 18751–18758.
- [57] B. Corry, D. Jayatilaka, B. Martinac and P. Rigby, *Biophys. J.*, 2006, **91**, 1032–1045.
- [58] S. Terjung and Y. Belyaev, in *Optical Probes in Biology*, ed. J. Zhang, S. Mehta and C. Schultz, CRC Press, Boca Raton, 2015, ch. 2, pp. 33–72.
- [59] Y.-H. Chan, C. Wu, F. Ye, Y. Jin, P. B. Smith and D. T. Chiu, *Anal. Chem.*, 2011, **83**, 1448–1455.
- [60] A. J. Lam, F. St.-Pierre, Y. Gong, J. D. Marshall, P. J. Cranfill, M. A. Baird, M. R. McKeown, J. Wiedenmann, M. W. Davidson, M. J. Schnitzer, R. Y. Tsien and M. Z. Lin, *Nat. Methods*, 2012, **9**, 1005–1012.

- [61] G. N. M. van der Krogt, J. Ogink, B. Ponsioen and K. Jalink, *PLoS ONE*, 2008, **3**, e1916.
- [62] S. Doughan, U. Uddayasankar and U. J. Krull, *Anal. Chim. Acta*, 2015, **878**, 1–8.
- [63] L. Haarbosch, J. Goedhart, M. A. Hink, L. van Weeren, D. S. Bindels and T. W. J. Gadella, in *Optical Probes in Biology*, ed. J. Zhang, S. Mehta and C. Schultz, CRC Press, Boca Raton, 2015, ch. 1, pp. 3–32.
- [64] P. Didier, K. K. Sharma and Y. Mely, in *Biophysical Approaches Determining Ligand and Binding to Biomolecular Targets: Detection, Measurement and Modelling*, ed. A. Podjarny, A. P. Dejaegere and B. Kieffer, Royal Society of Chemistry, Cambridge, 2011, ch. 5, pp. 156–199.
- [65] M. C. Leake, *Biophysics: Tools and Techniques*, CRC Press, Boca Raton, 2016.
- [66] C. Biskup and T. Gensch, in *Fluorescence Lifetime Spectroscopy and Imaging: Principles and Applications in Biomedical Diagnostics*, ed. L. Marcu, P. M. W. French and D. S. Elson, CRC Press, Boca Raton, 2015, ch. 24, pp. 497–534.
- [67] G. Keiser, *Biophotonics: Concepts to Applications*, Springer, Singapore, 2016.
- [68] M. I. Rowley, A. C. C. Coolen, B. Vojnovic and P. R. Barber, *PLoS ONE*, 2016, **11**, e0158404.
- [69] S. M. Muller, H. Galliardt, J. Schneider, B. G. Barisas and T. Seidel, *Front. Plant Sci.*, 2013, **4**, 8–27.
- [70] Y. Ueda, S. Kwok and Y. Hayashi, *Front. Neural Circuits*, 2013, **7**, 1–19.
- [71] D. S. Elson, L. Marcu and P. M. W. French, in *Fluorescence Lifetime Spectroscopy and Imaging: Principles and Applications in Biomedical Diagnostics*, ed. L. Marcu, P. M. W. French and D. S. Elson, CRC Press, Boca Raton, 2015, ch. 1, pp. 3–22.
- [72] T. Nareoja, T. Deguchi, S. Christ, R. Peltomaa, N. Prabhakar, E. Fazeli, N. Perala, J. M. Rosenholm, R. Arppe, T. Soukka and M. Schaferling, *Anal. Chem.*, 2017, **89**, 1501–1508.
- [73] K. Susumu, L. D. Field, E. Oh, M. Hunt, J. B. Delehanty, V. Palomo, P. E. Dawson and A. L. H. an Igor L. Medintz, *Chem. Mater.*, 2017, **29**, 7330–7344.
- [74] F. Du, Y. Ming, F. Zeng, C. Yu and S. Wu, *Nanotechnology*, 2013, **24**, 365101.

- [75] H. S. Qian, H. C. Guo, P. C.-L. Ho, R. Mahendran and Y. Zhang, *Small*, 2009, **5**, 2285–2290.
- [76] S. Wilhelm, M. Kaiser, C. Wurth, J. Heiland, C. Carrillo-Carrion, V. Muhr, O. S. Wolfbeis, W. J. Parak, U. Resch-Genger and T. Hirsch, *Nanoscale*, 2015, **7**, 1403–1410.
- [77] E. Werkmeister, H. Kerdjoudj, L. Marchal, J. F. Stoltz and D. Dumas, *Clin. Hemorheol. Micro.*, 2007, **37**, 77–88.
- [78] T. Ma, Y. Ma, S. Liu, L. Zhang, T. Yang, H.-R. Yang, W. Lv, Q. Yu, W. Xu, Q. Zhao and W. Huang, *J. Mater. Chem. C*, 2015, **3**, 6616–6620.
- [79] Y. Zhang, S. Xia, M. Fang, W. Mazi, Y. Zeng, T. Johnston, A. Pap, R. L. Luck and H. Liu, *Chem. Commun.*, 2018, **54**, 7625–7628.
- [80] D. K. Chatterjee, A. J. Rufaihah and Y. Zhang, *Biomaterials*, 2008, **29**, 937–943.
- [81] J. Jin, Y.-J. Gu, C. W.-Y. Man, J. Cheng, Z. Xu, Y. Zhang, H. Wang, V. H.-Y. Lee, S. H. Cheng and W.-T. Wong, *ACS Nano*, 2011, **5**, 7838–7847.
- [82] Y. Wang, P. Shen, C. Li, Y. Wang and Z. Liu, *Anal. Chem.*, 2012, **84**, 1466–1473.
- [83] L. Xie, Y. Qin and H.-Y. Chen, *Anal. Chem.*, 2012, **84**, 1969–1974.
- [84] S. Wen, J. Zhou, K. Zheng, A. Bednarkiewicz, X. Liu and D. Jin, *Nat. Commun.*, 2018, **9**, 1–12.
- [85] F. Wang and X. Liu, *J. Am. Chem. Soc.*, 2008, **130**, 5642–5643.
- [86] Z. Li, Y. Zhang and S. Jiang, *Adv. Mater.*, 2008, **20**, 4765–4769.
- [87] Y. Hu, B. Wu, Q. Jin, X. Wang, Y. Li, Y. Sun, J. Huo and X. Zhao, *Talanta*, 2016, **152**, 504–512.
- [88] N. M. Idris, M. K. Gnanasammandhan, J. Zhang, P. C. Ho, R. Mahendran and Y. Zhang, *Nat. Med.*, 2012, **18**, 1580–1585.
- [89] A. B. Chinen, C. M. Guan, J. R. Ferrer, S. N. Barnaby, T. J. Merkel and C. A. Mirkin, *Chem. Rev.*, 2015, **115**, 10530–10574.
- [90] D. K. Chatterjee and Z. Yong, *Nanomedicine*, 2008, **3**, 73–82.
- [91] M. Haase and H. Schafer, *Angew. Chem. Int. Ed.*, 2011, **50**, 5808–5829.

- [92] A. Keppler, H. Pick, C. Arrivoli, H. Vogel and K. Johnsson, *PNAS*, 2004, **101**, 9955–9959.
- [93] N. M. Idris, M. K. G. Jayakumar, A. Bansal and Y. Zhang, *Chem. Soc. Rev.*, 2015, **44**, 1449–1478.
- [94] F. Wang and X. Liu, *Chem. Soc. Rev.*, 2009, **38**, 976–989.
- [95] M. W. Pin, E. J. Park, S. Choi, Y. I. Kim, C. H. Jeon, T. H. Ha and Y. H. Kim, *Sci. Rep.*, 2018, **8**, 2199.
- [96] X. Chen, W. Zhang and Q. Zhang, *Physica B*, 2011, **406**, 1248–1252.
- [97] M. Wang, G. Abbineni, A. Clevenger, C. Mao and S. Xu, *Nanomedicine: NBM*, 2011, **7**, 710–729.
- [98] P. Villanueva-Delgado, K. W. Kramer and R. Valiente, *J. Phys. Chem. C*, 2015, **119**, 23648–23657.
- [99] Y. Zhang and X. Liu, *Nat. Nanotechnol.*, 2013, **8**, 702–703.
- [100] D. S. Funk and J. G. Eden, in *Rare-Earth-Doped Fiber Lasers and Amplifiers*, ed. M. J. Digonnet, Marcel Dekker, New York, 2nd edn., 2001, ch. 4, pp. 195–282.
- [101] F. Wang, J. Wang and X. Liu, *Angew. Chem. Int. Ed.*, 2010, **49**, 7456–7460.
- [102] R. Arppe, I. Hyppanen, N. Perala, R. Peltomaa, M. Kaiser, C. Wurth, S. Christ, U. Resch-Genger, M. Schaferling and T. Soukka, *Nanoscale*, 2015, **7**, 11746–11757.
- [103] N. J. J. Johnson, S. He, S. Diao, E. M. Chan, H. Dai and A. Almutairi, *J. Am. Chem. Soc.*, 2017, **139**, 3275–3282.
- [104] Y. Shang, S. Hao, W. Lv, T. Chen, L. Tian, Z. Lei and C. Yang, *J. Mater. Chem. C*, 2018, **6**, 3869–3875.
- [105] G. Chen, H. Agren, T. Y. Ohulchanskyy and P. N. Prasad, *Chem. Soc. Rev.*, 2015, **44**, 1680–1713.
- [106] X. Chen, D. Peng, Q. Ju and F. Wang, *Chem. Soc. Rev.*, 2015, **44**, 1318–1330.
- [107] J. Zhao, D. Jin, E. P. Schartner, Y. Lu, Y. Liu, A. V. Zvyagin, L. Zhang, J. M. Dawes, P. Xi, J. A. Piper, E. M. Goldys and T. M. Monroe, *Nat. Nanotechnol.*, 2013, **8**, 729–734.

- [108] D. J. Gargas, E. M. Chan, A. D. Ostrowski, S. Aloni, M. V. P. Altoe, E. S. Barnard, B. Sani, J. J. Urban, D. J. Milliron, B. E. Cohen and P. J. Schuck, *Nat. Nanotechnol.*, 2014, **9**, 300–305.
- [109] F. Benz and H. P. Strunk, *AIP Adv.*, 2012, **2**, 042115.
- [110] S. Hao, G. Chen and C. Yang, *Theranostics*, 2013, **3**, 331–345.
- [111] L. Cheng, C. Wang and Z. Liu, *Nanoscale*, 2013, **5**, 23–27.
- [112] Q. Wang, M. C. Tan, R. Zhuo, G. Kumar and R. E. Riman, *J. Nanosci. Nanotechnol.*, 2010, **10**, 1685–1692.
- [113] S. Xu, B. Dong, D. Zhou, Z. Yin, S. Cui, W. Xu, B. Chen and H. Song, *Sci. Rep.*, 2016, **6**, 1–9.
- [114] J.-C. Zhou, Z.-L. Yang, W. Dong, R.-J. Tang, L.-D. Sun and C.-H. Yan, *Biomaterials*, 2011, **32**, 9059–9067.
- [115] J. Chen and J. X. Zhao, *Sensors*, 2012, **12**, 2414–2435.
- [116] M. Wang, C. Mi, Y. Zhang, J. Liu, F. Li, C. Mao and S. Xu, *J. Phys. Chem. C*, 2009, **113**, 19021–19027.
- [117] Q. Liu, Y. Sun, T. Yang, W. Feng, C. Li and F. Li, *J. Am. Chem. Soc.*, 2011, **133**, 17122–17125.
- [118] M. Lin, Y. Zhao, S. Wang, M. Liu, Z. Duan, Y. Chen, F. Li, F. Xu and T. Lu, *Biotechnol. Adv.*, 2012, **30**, 1551–1561.
- [119] J.-C. Boyer, F. Vetrone, L. A. Cuccia and J. A. Capobianco, *J. Am. Chem. Soc.*, 2006, **128**, 7444–7445.
- [120] Z. Li and Y. Zhang, *Nanotechnology*, 2008, **19**, 1–5.
- [121] X. Zhu, Q. Su, W. Feng and F. Li, *Chem. Soc. Rev.*, 2017, **46**, 1025–1039.
- [122] G. Yi, H. Lu, S. Zhao, Y. Ge, W. Yang, D. Chen and L.-H. Guo, *Nano Lett.*, 2004, **4**, 2191–2196.
- [123] Y. Liu, D. Tu, H. Zhu and X. Chen, *Chem. Soc. Rev.*, 2013, **42**, 6924–6958.
- [124] T. Rinkel, J. Nordmann, A. N. Raj and M. Haase, *Nanoscale*, 2014, **6**, 14523–14530.

- [125] W. Huang, M. Ding, H. Huang, C. Jiang, Y. Song, Y. Ni, C. Lu and Z. Xu, *Mater. Res. Bull.*, 2013, **48**, 300–304.
- [126] H.-X. Mai, Y.-W. Zhang, L.-D. Sun and C.-H. Yan, *J. Phys. Chem. C*, 2007, **111**, 13730–13739.
- [127] J. Nordmann, B. Voss, R. Kompan, K. Kompe, A. N. Raj, T. Rinkel, S. Duhnen and M. Haase, *Z. Phys. Chem.*, 2015, **229**, 247–262.
- [128] B. Voss, J. Nordmann, A. Uhl, R. Kompan and M. Haase, *Nanoscale*, 2013, **5**, 806–812.
- [129] W. Zheng, P. Huang, D. Tu, E. Ma, H. Zhu and X. Chen, *Chem. Soc. Rev.*, 2015, **44**, 1379–1415.
- [130] F. Zhang, *Photon Upconversion Nanomaterials*, Springer, Heidelberg, 2015.
- [131] K. M. Murdoch and J. C. Wright, in *Shpol'skii Spectroscopy and Other Site-Selection Methods: Applications in Environmental Analysis, Bioanalytical Chemistry, and Chemical Physics*, ed. C. Gooijer, F. Ariese and J. W. Hofstraat, John Wiley & Sons, New York, 1st edn., 2000, ch. 17, pp. 503–542.
- [132] *Why are d-d electronic transitions forbidden and weakly absorbing? Why do they occur at all?*, <https://chemistry.stackexchange.com/questions/16091/why-are-d-d-electronic-transitions-forbidden-and-weakly-absorbing-why-do-they-o>, accessed Dec 2017.
- [133] *Selection Rules for Electronic Spectra of Transition Metal Complexes*, <http://wwwchem.uwimona.edu.jm/courses/selrules.html>, accessed Dec 2017.
- [134] C. Jones and J. Thornback, *Medicinal Applications of Coordination Chemistry*, Royal Society of Chemistry, Cambridge, 2007.
- [135] F. Wang, D. Banerjee, Y. Liu, X. Chen and X. Liu, *Analyst*, 2010, **135**, 1839–1854.
- [136] F. Ai, Q. Ju, X. Zhang, X. Chen, F. Wang and G. Zhu, *Sci. Rep.*, 2015, **5**, 1–11.
- [137] D. Wang, B. Xue, X. Kong, L. Tu, X. Liu, Y. Zhang, Y. Chang, Y. Luo, H. Zhao and H. Zhang, *Nanoscale*, 2015, **7**, 190–197.
- [138] S. Wilhelm, *ACS Nano*, 2017, **11**, 10644–10653.

- [139] X. Wang, R. R. Valiev, T. Y. Ohulchanskyy, H. Agren, C. Yang and G. Chen, *Chem. Soc. Rev.*, 2017, **46**, 4150–4167.
- [140] Y. Zhong, G. Tian, Z. Gu, Y. Yang, L. Gu, Y. Zhao, Y. Ma and J. Yao, *Adv. Mater.*, 2013, **26**, 2831–2837.
- [141] Y.-F. Wang, G.-Y. Liu, L.-D. Sun, J.-W. Xiao, J.-C. Zhou and C.-H. Yan, *ACS Nano*, 2013, **7**, 7200–7206.
- [142] C. Liu, H. Wang, X. Li and D. Chen, *J. Mater. Chem.*, 2009, **19**, 3546–3553.
- [143] A. Sedlmeier and H. H. Gorris, *Chem. Soc. Rev.*, 2015, **44**, 1526–1560.
- [144] M. Liras, M. Gonzalez-Bejar, E. Peinado, L. Frances-Soriano, J. Perez-Prieto, I. Quijada-Garrido and O. Garcia, *Chem. Mater.*, 2014, **26**, 4014–4022.
- [145] V. Muhr, C. Wurth, M. Kraft, M. Buchner, A. J. Baeumner, U. Resch-Genger and T. Hirsch, *Anal. Chem.*, 2017, **89**, 4868–4874.
- [146] N. Bogdan, F. Vetrone, G. A. Ozin and J. A. Capobianco, *Nano Lett.*, 2011, **11**, 835–840.
- [147] W. Kong, T. Sun, B. Chen, X. Chen, F. Ai, X. Zhu, M. Li, W. Zhang, G. Zhu and F. Wang, *Inorg. Chem.*, 2017, **56**, 872–877.
- [148] E. A. Grebenik, A. B. Kostyuk and S. M. Deyev, *Russ. Chem. Rev.*, 2016, **85**, 1277–1296.
- [149] S. J. Budijono, J. Shan, N. Yao, Y. Miura, T. Hoye, R. H. Austin, Y. Ju and R. K. Prud'homme, *Chem. Mater.*, 2010, **22**, 311–318.
- [150] G. Decher, *Science*, 1997, **277**, 1232–1237.
- [151] L. Wang, R. Yan, Z. Huo, L. Wang, J. Zeng, J. Bao, X. Wang, Q. Peng and Y. Li, *Angew. Chem.*, 2005, **44**, 6054–6057.
- [152] S. Wu, N. Duan, Z. Wang and H. Wang, *Analyst*, 2011, **136**, 2306–2314.
- [153] A. Shao, X. Wu and W. Zhu, in *Near-Infrared Nanomaterials: Preparation, Bioimaging and Therapy Applications*, ed. F. Zhang, Royal Society of Chemistry, Cambridge, 2016, ch. 5, pp. 125–157.

- [154] L.-N. Sun, H. Peng, M. I. J. Stich, D. Achatz and O. S. Wolfbeis, *Chem. Commun.*, 2009, **0**, 5000–5002.
- [155] H. S. Stoker, *General, Organic, and Biological Chemistry*, Brooks/Cole, Belmont, 6th edn., 2013.
- [156] S. Wang, J. Feng, S. Song and H. Zhang, *RSC Adv.*, 2014, **4**, 55897–55899.
- [157] R. Arppe, *Ph.D. thesis*, University of Turku, 2015.
- [158] D. J. Gargas, E. M. Chan, A. D. Ostrowski, S. Aloni, M. V. P. Altoe, E. S. Barnard, B. Sani, J. J. Urban, D. J. Milliron, B. E. Cohen and P. J. Schuck, *Nat. Nanotechnol.*, 2014, **9**, 300–305.
- [159] Q. Su, W. Feng, D. Yang and F. Li, *Acc. Chem. Res.*, 2017, **50**, 32–40.
- [160] H. Li, H. Dong, M. Yu, C. Liu, Z. Li, L. Wei, L.-D. Sun and H. Zhang, *Anal. Chem.*, 2017, **89**, 8863–8869.
- [161] C. Li, J. Zuo, L. Zhang, Y. Chang, Y. Zhang, L. Tu, X. Liu, B. Xue, Q. Li, H. Zhao, H. Zhang and X. Kong, *Sci. Rep.*, 2016, **6**, 38617.
- [162] S. Du, J. Hernandez-Gil, H. Dong, X. Zheng, G. Lyu, M. Banobre-Lopez, J. Gallo, L.-D. Sun, C.-H. Yan and N. J. Long, *Dalton Trans.*, 2017, **46**, 13957–13965.
- [163] A. Sorkin and M. von Zastrow, *Nat. Rev. Mol. Cell Biol.*, 2002, **3**, 600–614.
- [164] B. Chu, B. Song, X. Ji, Y. Su, H. Wang and Y. He, *Anal. Chem.*, 2017, **89**, 12152–12159.
- [165] A. Gnach, T. Lipinski, A. Bednarkiewicz, J. Rybka and J. A. Capobianco, *Chem. Soc. Rev.*, 2015, **44**, 1561–1584.
- [166] F. Wang, D. K. Chatterjee, Z. Li, Y. Zhang, X. Fan and M. Wang, *Nanotechnology*, 2006, **17**, 5786–5791.
- [167] S. Zeng, M.-K. Tsang, C.-F. Chan, K.-L. Wong, B. Fei and J. Hao, *Nanoscale*, 2012, **4**, 5118–5124.
- [168] Y. Sun, W. Feng, P. Yang, C. Huang and F. Li, *Chem. Soc. Rev.*, 2015, **44**, 1509–1525.
- [169] G. H. Jang, M. P. Hwang, S. Y. Kim, H. S. Jang and K. H. Lee, *Biomaterials*, 2014, **35**, 440–449.

- [170] R. A. Jalil and Y. Zhang, *Biomaterials*, 2008, **29**, 4122–4128.
- [171] L. Xiong, T. Yang, Y. Yang, C. Xu and F. Li, *Biomaterials*, 2010, **31**, 7078–7085.
- [172] J. Yu, W. Yin, T. Peng, Y.-N. Chang, Y. Zu, J. Li, X. He, X. Ma, Z. Gu and Y. Zhao, *Nanoscale*, 2017, **9**, 4497–4507.
- [173] J. Zhou, Z. Liu and F. Li, *Chem. Soc. Rev.*, 2012, **41**, 1323–1349.
- [174] N. Nath, B. Godat, C. Zimprich, S. J. Dwight, C. Corona, M. McDougall and M. Urh, *J. Immunol. Methods*, 2016, **431**, 11–21.
- [175] N. Oh and J.-H. Park, *Int. J. Nanomedicine*, 2014, **9**, 51–63.
- [176] S. Dasgupta, T. Auth and G. Gompper, *Nano Lett.*, 2014, **14**, 687–693.
- [177] N. Kang, C.-C. Ai, Y.-M. Zhou, Z. Wang and L. Ren, *Nanotechnology*, 2018, **29**, 075601.
- [178] S. Wilhelm, *Ph.D. thesis*, University of Regensburg, 2014.
- [179] T. Cong, Y. Ding, S. Xin, X. Hong, H. Zhang and Y. Liu, *Langmuir*, 2016, **32**, 13200–13206.
- [180] C. F. Gainer and M. Romanowski, *J. Innov. Opt. Heal. Sci.*, 2014, **7**, 1330007.
- [181] J. Shan and Y. Ju, *Nanotechnology*, 2009, **20**, 275603.
- [182] C. Yan, H. Zhao, D. F. Perepichka and F. Rosei, *Small*, 2016, **12**, 3888–3907.
- [183] V. Muhr, S. Wilhelm, T. Hirsch and O. S. Wolfbeis, *Acc. Chem. Res.*, 2014, **47**, 3481–3493.
- [184] A. von Harpe, H. Petersen, Y. Li and T. Kissel, *J. Control. Release*, 2000, **69**, 309–322.
- [185] H. Zhu, F. Lu, X.-C. Wu and J.-J. Zhu, *Analyst*, 2015, **140**, 7622–7628.
- [186] J.-C. Boyer, L. A. Cuccia and J. A. Capobianco, *Nano Lett.*, 2007, **7**, 847–852.
- [187] Q. Yuan, Y. Wu, J. Wang, D. Lu, Z. Zhao, T. Liu, X. Zhang and W. Tan, *Angew. Chem. Int. Ed.*, 2013, **52**, 13965–13969.
- [188] G. S. Yi and G. M. Chow, *Adv. Funct. Mater.*, 2006, **16**, 2324–2329.

- [189] C.-A. J. Lin, R. A. Sperling, J. K. Li, T.-Y. Yang, P.-Y. Li, M. Zanella, W. H. Chang and W. J. Parak, *Small*, 2008, **4**, 334–341.
- [190] M. K. Gnanasammandhan, N. M. Idris, A. Bansal, K. Huang and Y. Zhang, *Nature Protocols*, 2016, **11**, 688–713.
- [191] Q. Liu, W. Feng, T. Yang, T. Yi and F. Li, *Nature Protocols*, 2013, **8**, 2033–2044.
- [192] D. K. Chatterjee, *Ph.D. thesis*, National University of Singapore, 2007.
- [193] Y. Shang, S. Hao, J. Liu, M. Tan, N. Wang, C. Yang and G. Chen, *Nanomaterials*, 2015, **5**, 218–232.
- [194] C. Liu, H. Wang, X. Zhang and D. Chen, *J. Mater. Chem.*, 2009, **19**, 489–496.
- [195] S. Heer, K. Kompe, H.-U. Gudel and M. Haase, *Adv. Mater.*, 2004, **16**, 2102–2105.
- [196] *Hydrodynamics Size of Nanoparticles*, https://www.researchgate.net/post/Hydrodynamics_size_of_n accessed Jan 2018.
- [197] X. Zhu, J. Zhou, M. Chen, M. Shi, W. Feng and F. Li, *Biomaterials*, 2012, **33**, 4618–4627.
- [198] Y. Yang, Y. Sun, T. Cao, J. Peng, Y. Liu, Y. Wu, W. Feng, Y. Zhang and F. Li, *Biomaterials*, 2013, **34**, 774–783.
- [199] F. Wang, Y. Han, C. S. Lim, Y. Lu, J. Wang, J. Xu, H. Chen, C. Zhang, M. Hong and X. Liu, *Nature*, 2010, **463**, 1061–1064.
- [200] H.-X. Mai, Y.-W. Zhang, R. Si, Z.-G. Yan, L.-D. Sun, L.-P. You and C.-H. Yan, *J. Am. Chem. Soc.*, 2006, **128**, 6426–6436.
- [201] S. Wojtkiewicz, P. Sawosz, M. Kostecki and A. Sokolowska, *Microelectron Eng.*, 2013, **108**, 121–126.
- [202] V. Kale, M. Lastusaari, J. Holsa and T. Soukka, *RSC Adv.*, 2015, **5**, 35858–35865.
- [203] F. Shi, J. Wang, D. Zhang, G. Qin and W. Qin, *J. Mater. Chem.*, 2011, **21**, 13413–13421.
- [204] S. Zhang, J. Li, G. Lykotrafitis, G. Bao and S. Suresh, *Adv. Mater.*, 2008, **21**, 419–424.

- [205] N. Sakai, Y. Matsui, A. Nakayama, A. Tsuda and M. Yoneda, *J. Phys.: Conf. Ser.*, 2011, **304**, 012049.
- [206] A. Banerjee, A. Berzhkovskii and R. Nossal, arXiv:1411.7348, 2014.
- [207] H. S. Mader, P. Kele, S. M. Saleh and O. S. Wolfbeis, *Curr. Opin. Chem. Biol.*, 2010, **14**, 582–596.
- [208] J. Lan, Y. Liu, L. Li, F. Wen, F. Wu, Z. Han, W. Sun, C. Li and J. Chen, *Sci. Rep.*, 2016, **6**, 1–8.
- [209] E. Blanco, H. Shen and M. Ferrari, *Nat. Biotechnol.*, 2015, **33**, 941–951.
- [210] J.-C. Boyer and F. C. J. M. van Veggel, *Nanoscale*, 2010, **2**, 1417–1419.
- [211] G. Chen, H. Qiu, P. N. Prasad and X. Chen, *Chem. Rev.*, 2014, **114**, 5161–5214.
- [212] F. Wang, R. Deng and X. Liu, *Nature Protocols*, 2014, **9**, 1634–1644.
- [213] H.-S. Qian and Y. Zhang, *Langmuir*, 2008, **24**, 12123–12125.
- [214] Y. Wang, L. Tu, J. Zhao, Y. Sun, X. Kong and H. Zhang, *J. Phys. Chem. C*, 2009, **113**, 7164–7169.
- [215] A. Elhalawany, W. E. Hayenga, S. He, C. Lantigua, N. J. J. Johnson, A. Almutairi and M. Khajavikhan, Plasmonics: Metallic Nanostructures and Their Optical Properties XII, Proceedings of SPIE Vol. 9163, Bellingham, 2014, p. 916331.
- [216] C. Lantigua, S. He, M. A. Bouzan, W. Hayenga, N. J. J. Johnson, A. Almutairi and M. Khajavikhan, *Opt. Lett.*, 2014, **39**, 3710–3713.
- [217] G. Liang, Y. Li, W. Feng, X. Wang, A. Jing, J. Li and K. Ma, *Int. J. Nanomedicine*, 2016, **11**, 6079–6088.
- [218] L. Shang, K. Nienhaus and G. U. Nienhaus, *J. Nanobiotechnology*, 2014, **12**, 1–11.
- [219] A. E. Guller, A. Nadort, A. N. Generalova, E. V. Khaydukov, A. V. Nechaev, I. A. Kornienko, E. V. Petersen, L. Liang, A. B. Shekhter, Y. Qian, E. M. Goldys and A. V. Zvyagin, *ACS Biomater. Sci. Eng.*, 2018, **4**, 3143–3153.
- [220] M. Buchner, P. G. Calavia, V. Muhr, A. Kroninger, A. J. Baeumner, T. Hirsch, D. A. Russell and M. J. Marin, *Photochem. Photobiol. Sci.*, 2019.

- [221] T. Riuttamaki, I. Hyppanen, J. Kankare and T. Soukka, *J. Phys. Chem. C*, 2011, **115**, 17736–17742.
- [222] S. Bhuckory, E. Hemmer, Y.-T. Wu, A. Yahia-Ammar, F. Vetrone and N. Hildebrandt, *Eur. J. Inorg. Chem.*, 2017, **2017**, 5186–5195.
- [223] P. Kim, C. Li, R. E. Riman and J. Watkins, *ACS Appl. Mater. Interfaces*, 2018, **10**, 9038–9047.
- [224] Y. Liu, Q. Ouyang, H. Li, Z. Zhang and Q. Chen, *ACS Appl. Mater. Interfaces*, 2017, **9**, 18314–18321.
- [225] H. Chen and J. Ren, *Talanta*, 2012, **99**, 404–408.
- [226] H. Chen, A. Fang, L. He, Y. Zhang and S. Yao, *Talanta*, 2017, **164**, 580–587.
- [227] J. N. Aronson, *Biochem. Educ.*, 1983, **11**, 68.
- [228] N. Ghosh, R. Mondal and S. Mukherjee, *Langmuir*, 2015, **31**, 8074–8080.
- [229] J.-M. Swiecicki, F. Thiebaut, M. D. Pisa, S. Gourdin-Bertin, J. Tailhades, C. Mansuy, F. Burlina, S. Chwetzoff, G. Trugnan, G. Chassaing and S. Lavielle, *Sci. Rep.*, 2016, **6**, 1–11.
- [230] M. A. Omary and H. H. Patterson, in *Encyclopedia of Spectroscopy and Spectrometry*, ed. J. C. Lindon, G. E. Tranter and D. W. Koppenaal, Academic Press, Oxford, 3rd edn., 2017, vol. 2, ch. Luminescence, Theory, pp. 636–653.
- [231] A. Deshmukh, S. Bandyopadhyay, A. James and A. Patra, *J. Mater. Chem. C*, 2016, **4**, 4427–4433.
- [232] J. L. Colon, C.-Y. Yang, A. Clearfield and C. R. Martin, *J. Phys. Chem.*, 1990, **94**, 874–882.
- [233] J. Yang and M. A. Winnik, *Can. J. Chem.*, 1995, **73**, 1823–1830.
- [234] J. Liu, Y. Zhong, P. Lu, Y. Hong, J. W. Lam, M. Faisal, Y. Yu, K. S. Wong and B. Z. Tang, *Polym. Chem.*, 2010, **1**, 426–429.
- [235] C. Nunes, C. Sousa, H. Ferreira, M. Lucio, J. L. Lima, J. Tavares, A. C. da Silva and S. Reis, *J. Environ. Biol.*, 2008, **29**, 733–738.
- [236] D. K. Singh, P. K. Iyer and P. Giri, *Carbon*, 2012, **50**, 4495–4505.

- [237] L. Mattsson, K. D. Wegner, N. Hildebrandt and T. Soukka, *RSC Adv.*, 2015, **5**, 13270–13277.
- [238] T. A. Beu and A. Farcas, *AIP Conf. Proc.*, 2017, **1916**, 020001.
- [239] K. A. Curtis, D. Miller, P. Millard, S. Basu, F. Horkay and P. L. Chandran, *PLoS One*, 2016, **11**, e0158147.
- [240] D. R. Chang, S. Harden and N. Loverro, *J. Macromol. Sci.-Chem.*, 1986, **23**, 801–804.
- [241] R. Chen, V. D. Ta, F. Xiao, Q. Zhang and H. Sun, *Small*, 2013, **9**, 1052–1057.
- [242] M. J. Ruedas-Rama and E. A. H. Hall, *Anal. Chem.*, 2010, **82**, 9043–9049.
- [243] R. V. Benjaminsen, M. A. Matthebjerg, J. R. Henriksen, S. M. Moghimi and T. L. Andresen, *Mol. Ther.*, 2013, **21**, 149–157.
- [244] Y. Ding, F. Wu, Y. Zhang, X. Liu, E. M. L. D. de Jong, T. Gregorkiewicz, X. Hong, Y. Liu, M. C. G. Aalders, W. J. Buma and H. Zhang, *J. Phys. Chem. Lett.*, 2015, **6**, 2518–2523.
- [245] T. Wu, J.-C. Boyer, M. Barker, D. Wilson and N. R. Branda, *Chem. Mater.*, 2013, **25**, 2495–2502.
- [246] L. M. Wiesholler and T. Hirsch, *Opt. Mater.*, 2018, **80**, 253–264.
- [247] A. K. Varkouhi, M. Scholte, G. Storm and H. J. Haisma, *J. Control. Release*, 2011, **151**, 220–228.
- [248] A. M. Dennis, W. J. Rhee, D. Sotto, S. N. Dublin and G. Bao, *ACS Nano*, 2012, **6**, 2917–2924.
- [249] H. Nie, M. Li, Q. Li, S. Liang, Y. Tan, L. Sheng, W. Shi and S. X.-A. Zhang, *Chem. Mater.*, 2014, **26**, 3104–3112.
- [250] J. Sun, P. Ling and F. Gao, *Anal. Chem.*, 2017, **89**, 11703–11710.
- [251] J. Xia, S. Chen, G.-Y. Zou, Y.-L. Yu and J.-H. Wang, *Nanoscale*, 2018, **10**, 22484–22492.
- [252] A. Andrade-Eiroa, E. Vasquez-Blanco, P. Lopez-Mahia, S. Muniategui-Lorenzo and D. Prada-Rodriguez, *Analisis*, 2000, **28**, 148–154.

- [253] D. S. Richardson, C. Gregor, F. R. Winter, N. T. Urban, S. J. Sahl, K. I. Willig and S. W. Hell, *Nat. Commun.*, 2017, **8**, 1–9.
- [254] B. K. Grillo-Hill, B. A. Webb and D. L. Barber, in *Quantitative Imaging in Cell Biology*, ed. J. C. Waters and T. Wittmann, Academic Press, Burlington, 2014, vol. 123, ch. 23, pp. 429–448.
- [255] J. Huang, L. Ying, X. Yang, Y. Yang, K. Quan, H. Wang, N. Xie, M. Ou, Q. Zhou and K. Wang, *Anal. Chem.*, 2015, **87**, 8724–8731.
- [256] L. He, X. Yang, F. Zhao, K. Wang, Q. Wang, J. Liu, J. Huang, W. Li and M. Yang, *Anal. Chem.*, 2015, **87**, 2459–2465.
- [257] J. Schindelin, I. Arganda-Carreras, E. Frise, V. Kaynig, M. Longair, T. Pietzsch, S. Preibisch, C. Rueden, S. Saalfeld, B. Schmid, J.-Y. Tinevez, D. J. White, V. Hartenstein, K. Eliceiri, P. Tomancak and A. Cardona, *Nat. Methods*, 2012, **9**, 676–682.
- [258] K. W. Dunn, M. M. Kamocka and J. H. McDonald, *Am. J. Physiol. Cell Physiol.*, 2011, **300**, C723–C742.
- [259] J. H. McDonald and K. W. Dunn, *J. Microsc.*, 2013, **252**, 295–302.
- [260] M. H. Teplensky, M. Fantham, P. Li, T. C. Wang, J. P. Mehta, L. J. Young, P. Z. Moghadam, J. T. Hupp, O. K. Farha, C. F. Kaminski and D. Fairen-Jimenez, *J. Am. Chem. Soc.*, 2017, **139**, 7522–7532.
- [261] M. Qu, Q. Lin, S. He, L. Wang, Y. Fu, Z. Zhang and L. Zhang, *J. Control. Release*, 2018, **277**, 173–182.
- [262] A. N. Koo, H. J. Lee, S. E. Kim, J. H. Chang, C. Park, C. Kim, J. H. Park and S. C. Lee, *Chem. Commun.*, 2008, **48**, 6570–6572.
- [263] G. M. Cooper, *The Cell: A Molecular Approach*, Sinauer Associates, Sunderland, 2nd edn., 2000.
- [264] H. Kettiger, A. Schipanski, P. Wick and J. Huwyler, *Int. J. Nanomedicine*, 2013, **8**, 3255–3269.
- [265] L. Kou, J. Sun, Y. Zhai and Z. He, *Asian J. Pharm.*, 2013, **8**, 1–10.
- [266] A. Bhaw-Luximon, in *Engineered Carbohydrate-Based Materials for Biomedical Applications: Polymers, Surfaces, Dendrimers, Nanoparticles, and Hydrogels*, ed. R. Narain, John Wiley & Sons, Hoboken, 2011, ch. 10.

- [267] R. V. Sondergaard, J. R. Henriksen and T. L. Andresen, *Nat. Protoc.*, 2014, **9**, 2841–2858.
- [268] Z.-G. Yue, W. Wei, P.-P. Lv, H. Yue, L.-Y. Wang, Z.-G. Su and G.-H. Ma, *Biomacromolecules*, 2011, **12**, 2440–2446.
- [269] M. Graessmann and A. Graessmann, *Methods Enzymol.*, 1983, **101**, 482–492.
- [270] J. C. Sanford, T. M. Klein, E. D. Wolf and N. Allen, *Particul. Sci. Technol.*, 1987, **5**, 27–37.
- [271] F. Torney, B. G. Trewyn, V. S.-Y. Lin and K. Wang, *Nat. Nanotechnol.*, 2007, **2**, 295–300.
- [272] S. Martin-Ortigosa, J. S. Valenstein, V. S.-Y. Lin, B. G. Trewyn and K. Wang, *Adv. Funct. Mater.*, 2012, **22**, 3576–3582.
- [273] J. Wang, Y. Sun, W. Zhang, Y. Liu, X. Yu and N. Zhao, *Talanta*, 2014, **129**, 241–248.
- [274] Z. Xia and Y. Liu, *Biophys. J.*, 2001, **81**, 2395–2402.
- [275] I. S. Behbahan, M. A. McBrien and S. K. Kurdistani, *Bio-protocol*, 2014, **4**, e1027.
- [276] B. C. Pressman, *Annu. Rev. Biochem.*, 1976, **45**, 501–530.
- [277] T. Prochnicki, M. S. Mangan and E. Latz, *F1000Research*, 2016, **5**, 1–15.
- [278] G. A. Altenberg and L. Reuss, in *Epithelial Transport: A Guide to Methods and Experimental Analysis*, ed. N. K. Wills, L. Reuss and S. A. Lewis, Chapman and Hall, London, 1996, ch. 7, pp. 147–166.
- [279] S. Dwane, E. Durack and P. A. Kiely, *BMC Res. Notes*, 2013, **6**, 1–11.
- [280] A. Linnala, V.-P. Lehto and I. Virtanen, *J. Neurosci. Res.*, 1997, **49**, 53–63.
- [281] F. Xi, F. Sang, C. Zhou and Y. Lin, *Neural Regen. Res.*, 2012, **7**, 2867–2873.
- [282] B. L. Ross, B. Tenner, M. L. Markwardt, A. Zviman, G. Shi, J. P. Kerr, N. E. Snell, J. J. McFarland and J. R. Mauban, *eLife*, 2018, **7**, e35458.
- [283] K. Saito, Noriyuki, Hatsugai, K. Horikawa, K. Kobayashi, T. Matsu-ura, K. Mikoshiba and T. Nagai, *PLoS ONE*, 2010, **5**, e9935.

- [284] J. Jonkman, C. M. Brown and R. W. Cole, in *Quantitative Imaging in Cell Biology*, ed. J. C. Waters and T. Wittmann, Academic Press, Burlington, 2014, vol. 123, ch. 7, pp. 113–134.
- [285] A. Sedlmeier, D. E. Achatz, L. H. Fischer, H. H. Gorris and O. S. Wolfbeis, *Nanoscale*, 2012, **4**, 7090–7096.
- [286] M. H. Lee, J. H. Han, J. H. Lee, N. Park, R. Kumar, C. Kang and J. S. Kim, *Angew. Chem. Int. Ed.*, 2013, **52**, 6206–6209.
- [287] Y. Bao, H. D. Keersmaecker, S. Corneillie, F. Yu, H. Mizuno, G. Zhang, J. Hofkens, B. Mendrek, A. Kowalczyk and M. Smet, *Chem. Mater.*, 2015, **27**, 3450–3455.
- [288] S. Bolte and F. P. Cordelieres, *J. Microsc.*, 2006, **224**, 213–232.
- [289] R. Gupta, P. Mishra and A. Mittal, *Austin J. Radiol.*, 2015, **2**, 1031.
- [290] S. E. A. Gratton, P. A. Ropp, P. D. Pohlhaus, J. C. Luft, V. J. Madden, M. E. Napier and J. M. DeSimone, *PNAS*, 2008, **105**, 11613–11618.
- [291] *Bulk Transport*, <https://www.khanacademy.org/science/biology/membranes-and-transport/bulk-transport/a/bulk-transport>, accessed Apr 2019.
- [292] H. Foster, A. Reynolds, G. Stenbeck, J. Dong, P. Thomas and E. Karteris, *Mol. Med. Rep.*, 2010, **3**, 27–35.
- [293] K. G. Rothberg, J. E. Heuser, W. C. Donzell, Y.-S. Ying, J. R. Glenney and R. G. Anderson, *Cell*, 1992, **68**, 673–682.
- [294] N. A. Monteiro-Riviere, A. O. Inman and L. W. Zhang, *Toxicol. Appl. Pharmacol.*, 2009, **234**, 222–235.
- [295] *AlamarBlue Cell Viability Assay Protocol*, <https://www.thermofisher.com/uk/en/home/references/pro-and-tissue-analysis/cell-proliferation-assay-protocols/cell-viability-with-alamarblue.html>, accessed Jul 2018.
- [296] B. Kong, J. H. Seog, L. M. Graham and S. B. Lee, *Nanomedicine*, 2011, **6**, 929–941.
- [297] S. N. Rampersad, *Sensors*, 2012, **12**, 12347–12360.
- [298] A. Kroll, M. H. Pillukat, D. Hahn and J. Schnekenburger, *Eur. J. Pharm. Biopharm.*, 2009, **72**, 370–377.

- [299] *Trypan Blue Exclusion Protocol*, <https://www.thermofisher.com/uk/en/home/references/gibco-cell-culture-basics/cell-culture-protocols/trypan-blue-exclusion.html>, accessed Jul 2018.
- [300] G. Sivaraman, B. Vidya and D. Chellappa, *RSC Adv.*, 2014, **4**, 30828–30831.
- [301] M. J. Ruedas-Rama, J. D. Walters, A. Orte and E. A. Hall, *Anal. Chim. Acta*, 2012, **751**, 1–23.
- [302] S. Y. Lee, M. Lin, A. Lee and Y. I. Park, *Nanomaterials*, 2017, **7**, 411.
- [303] A. Orte, J. M. Alvarez-Pez and M. J. Ruedas-Rama, *ACS Nano*, 2013, **7**, 6387–6395.
- [304] M. Eisenstein, *Nat. Methods*, 2018, **15**, 19–22.
- [305] F. Weeber, S. N. Ooft, K. K. Dijkstra and E. E. Voest, *Cell Chem. Biol.*, 2017, **24**, 1092–1100.
- [306] *Nat. Methods*, 2018, **15**, 1.
- [307] A. C. Rios and H. Clevers, *Nat. Methods*, 2018, **15**, 24–26.
- [308] M. Ohring, *Engineering Materials Science*, Academic Press, San Diego, 1995.
- [309] J. Kenkel, *Analytical Chemistry for Technicians*, CRC Press, Boca Raton, 4th edn., 2014.
- [310] D. Zhao, Y. Wan and W. Zhou, *Ordered Mesoporous Materials*, Wiley-VCH, Weinheim, 2013.
- [311] T. E. Weirich, in *Electron Crystallography: Novel Approaches for Structure Determination of Nanosized Materials*, ed. T. E. Weirich, J. L. Labar and X. Zou, Springer, Dordrecht, 2006, ch. C.1, pp. 235–258.
- [312] Z. Hou, C. Li, P. Ma, G. Li, Z. Cheng, C. Peng, D. Yang, P. Yang and J. Lin, *Adv. Funct. Mater.*, 2011, **21**, 2356–2365.
- [313] G. Chen, T. Y. Ohulchanskyy, R. Kumar, H. Agren and P. N. Prasad, *ACS Nano*, 2010, **4**, 3163–3168.
- [314] A. Kumar, *Introduction to Solid State Physics*, PHI Learning, Delhi, 2nd edn., 2015.
- [315] M. He, X. Pang, X. Liu, B. Jiang, Y. He, H. Snaith and Z. Lin, *Angew. Chem. Int. Ed.*, 2016, **55**, 4280–4284.